UNIVERSIDAD DE GRANADA

Programa Oficial de Doctorado Interuniversitario en Dinámica de los Flujos Biogeoquímicos y sus Aplicaciones

TESIS DOCTORAL

ESTUDIO DE PROCESOS EN LA DESEMBOCADURA DEL GUADALQUIVIR Y GOLFO DE CÁDIZ: VARIABILIDAD ESPACIO-TEMPORAL MEDIANTE TELEDETECCIÓN

Isabel Caballero de Frutos

Cádiz, 2014

UNIVERSIDAD DE GRANADA

Programa Oficial de Doctorado Interuniversitario en Dinámica de los Flujos Biogeoquímicos y sus Aplicaciones

Estudio de procesos en la desembocadura del Guadalquivir y Golfo de Cádiz: variabilidad espacio-temporal mediante teledetección

TESIS DOCTORAL

Isabel Caballero de Frutos

Cádiz, 2014

Editor: Universidad de Granada. Tesis Doctorales
Autor: Isabel Caballero De Frutos
ISBN: 978-84-9125-057-9
URI: http://hdl.handle.net/10481/39864

La doctoranda Isabel Caballero de Frutos y el director de la tesis Gabriel Navarro Almendros garantizamos, al firmar esta tesis doctoral, que el trabajo ha sido realizado por la doctoranda bajo la dirección del director de la tesis y hasta donde nuestro conocimiento alcanza, en la realización del trabajo, se han respetado los derechos de otros autores a ser citados, cuando se han utilizado sus resultados o publicaciones.

Puerto Real, 19 de noviembre 2014

Director de la Tesis | Doctoranda

Fdo.: Gabriel Navarro Almendros | Fdo.: Isabel Caballero de Frutos

Esta Tesis Doctoral ha sido realizada gracias a la concesión de una Beca de Formación de Personal Investigador del Proyecto de Excelencia de la Junta de Andalucía titulado "Estudio de los eventos de turbidez en la desembocadura del Guadalquivir mediante teledetección y su conexión con procesos meteorológicos y oceanográficos" (P09-RNM-4853). El trabajo de investigación se ha llevado a cabo dentro del Departamento de Ecología y Gestión Costera del Instituto de Ciencias Marinas de Andalucía (ICMAN) en Puerto Real, perteneciente al Consejo Superior de Investigaciones Científicas (CSIC), bajo la supervisión del Dr. Gabriel Navarro.

Lista de acrónimos

Acrónimo	*Significado*
ACP	*Atmospheric Correction Procedure*
ANOVA	*ANalysis Of VAriance*
AVHRR	*Advanced Very High Resolution Radiometers*
B	*Bias*
CDOM	*Coloured Disolved Organic Matter*
Chl	*Clorofila*
COSTZ	*Solar zenith angle approximation*
CSIC	*Consejo Superior de Investigaciones Científicas*
CTD	*Conductivity, Temperature, Depth*
CV	*Coeficiente de Variación*
CZCS	*Coastal Zone Color Scanner*
d_{max}	*Máximo clorofila*
DMCII	*DMC International Imaging*
DN	*Digital Number*
DOS	*Dark Object Subtraction*
ENVISAT ETM	*ENVironmental* SATellite *Enhanced Thematic Mapper*
EOF	*Empirical Orthogonal Function*
Er	*Relative Error*
ESA	*European Space Agency*
ETM	*Estuarine Turbidity Maximum*
EU-WFD	*European Union Water Framework Directive*
FNU	*Nephelometric Turbidity Units*
FRS	*Full Resolution*
F_0	*Constante solar*
G	*Gain*
GMT	*Greenwich Mean Time*
GOCI	*Geostationary Ocean Color Imager*
GODAS	*Global Ocean Data Assimilation System*
HICO	*Hyperspectral Imager for the Coastal Ocean*
ICMAN	*Instituto de Ciencias Marinas de Andalucía*
K_d	*Coeficiente de extinción de la luz*
Lsat	*At-satellite spectral radiance*
Lw	*Water-leaving radiance*
MERIS	*MEdium Resolution Imaging Spectrometer*
MLD	*Mixed Layer Depth*
MM	*Componente mensual marea marea*
MODIS	*Moderate Resolution Imaging Spectroradiometer*
MSF	*Componente quincenal marea*
M2	*Componente lunar semi-diurna marea*
n	*Número de elementos*

NAO	*North Atlantic Oscillation Index*
NASA	*National Aeronautics and Space Administration*
NDVI	*Normalized Difference Vegetation Index*
NDWI	*Normalized Difference Water Index*
NIR	*Infrarrojo cercano*
nLw	*Water-leaving radiance*
NOAA	*National Oceanic and Atmospheric Administration*
OC3M	*Ocean Chlorophyll three-band algorithm for MODIS*
OC4Me	*Ocean Chlorophyll three-band algorithm for MERIS*
p	*Coeficiente de Pearson*
PAR	*Photosynthetically-Active Radiation*
PIF	*Pseudo Invariant Features*
r	*Coeficiente de correlación*
r^2	*Coeficiente de determinación*
RGB	*Red Green Blue*
RMSE	*Root Mean Square Error*
ROI	*Region Of Interest*
RR	*Reduced Resolution*
Rrs	*Remote Sensing Reflectance*
RS	*Remote Sensing*
RTC	*Radiance Transfer Codes*
SD	*Standard Deviation*
se	*Error estándar*
SeaDAS	*SeaWiFS Data Analysis System*
SeaWiFS	*Sea-Viewing Wide Field-of-View Sensor*
SHV	*Starting Haze Value*
SPM	*Suspended Particulate Matter*
SPOT	*Satellite for Observation of Earth*
SST	*Sea Surface Temperature*
S2	*Componente Solar Semi-diurna*
TSS	*Total Suspended Solids*
TOA	*Top Of Atmosphere*
U	*Componente zonal del viento*
UTM	*Universal Transverse Mercator*
V	*Componente meridional del viento*
WGS84	*World Geodetic System 84*
$Z_{1\%}$ - Z_{eu}	*Profundidad fótica*
λ	*Longitud de onda*
ρw	*Water-leaving reflectance*

Lista de figuras

CAPÍTULO 1.

CAPÍTULO 2.

CAPÍTULO 3.

CAPÍTULO 4.

CAPÍTULO 5.

CAPÍTULO 6.

Lista de tablas

CAPÍTULO 3.

CAPÍTULO 4.

CAPÍTULO 5.

CAPÍTULO 6.

Resumen

En esta Tesis Doctoral se ha realizado un estudio detallado de los mecanismos que se desarrollan a través de la generación de la pluma de turbidez en la desembocadura del estuario del Guadalquivir y se ha definido su variabilidad mediante el uso conjunto de técnicas de teledetección y datos in situ. El análisis que se aborda en el trabajo ha requerido el uso de numerosos satélites con diferentes características (resolución espacial, temporal y espectral), proporcionando de esta manera información para realizar un análisis multi-sensor. El principal objetivo es determinar los parámetros físico-biogeoquímicos y de calidad de las aguas (sólidos en suspensión, turbidez, clorofila, coeficiente de extinción de la luz, ...) e implementar la metodología para generar los algoritmos empíricos y semianalíticos a partir de datos satelitales de distinta índole. Se examinan los procesos que acontecen en el estuario y región adyacente caracterizando los patrones espacio-temporales e identificando los agentes implicados en las diversas escalas de variabilidad. El forzamiento oceano-meteorológico asociado a las precipitaciones, las descargas de la presa de Alcalá del Río y el índice climático NAO controlan las fluctuaciones estacionales e inter-anuales, mientras que el efecto de la marea (ciclo semi-diario y quincenal) y del viento en la desembocadura modulan la pluma de turbidez a lo largo de todo el año, exhibiendo una variabilidad significativa. Se hace un especial énfasis en diagnosticar el papel que tienen dichos procesos de turbidez sobre los ecosistemas en el entorno de la plataforma continental y golfo de Cádiz, constituyendo, de tal manera, una potente herramienta para los programas de gestión integral de calidad del agua y de los recursos litorales.

Índice de contenidos

Capítulo 1

Introducción

1.1. El estuario del Guadalquivir

Los estuarios son ecosistemas costeros únicos donde los ambientes marino y fluvial interactúan significativamente. Estas zonas de transición corresponden a uno de los espacios más relevantes del mundo debido a su complejidad, vulnerabilidad y su elevada producción biológica (Dyer & Dyer, 1997). Adicionalmente, estos enclaves son vitales para el comercio, transporte, acuicultura, pesquerías, y recientemente, se han convertido en áreas turísticas muy demandadas, generando considerables beneficios socio-económicos para las regiones costeras adyacentes. Todo esto les convierte en emplazamientos altamente valiosos y atractivos, por lo que es fundamental un profundo conocimiento de los procesos y mecanismos que acontecen sobre ellos y la óptima gestión integrada de sus recursos y posibles usos.

En este contexto se enmarca el estuario del Guadalquivir, el cual es un claro ejemplo de ecosistema acuático significativo desde diversos puntos de vista, ocupando un lugar importante en la historia como uno de los sistemas río-estuario-delta más extensos de la Europa occidental. El estuario, con una longitud aproximada de 110 km, se encuentra situado en la costa suroeste de la península ibérica y se extiende desde la presa de Alcalá del Río hasta su desembocadura en la Broa de Sanlúcar. El nacimiento del río se halla en las montañas de Cazorla, a unos 1.400 m sobre el nivel del mar, con una longitud total de 680 km y una cuenca de drenaje de 63.822 km^2 (Granado-Lorencio, 1991). Cabe destacar que a un lado de la desembocadura del Guadalquivir se encuentra el Parque Nacional y Natural de Doñana, el humedal más importante de toda Europa y uno de los hábitats de hibernación más utilizados por las aves del continente. En 1980 la UNESCO clasificó el parque como Reserva de la Biosfera y en 1994 fue declarado Patrimonio de la Humanidad.

Figura 1 Localización del estuario Guadalquivir y ubicación general de las principales actividades y lugares de importancia socioeconómica.

El estuario actúa como fuente de material en suspensión en la plataforma adyacente, generando elevados niveles de turbidez (Navarro *et al.*, 2012b). Adicionalmente, ejerce de fertilizador de nutrientes (Prieto *et al.*, 2009), aumentando los valores de producción primaria (Navarro & Ruiz, 2006), además de ser motor de los recursos pesqueros de la Andalucía occidental (Ruiz *et al.*, 2009). Por otra parte, los numerosos municipios aledaños introducen grandes cargas de materia orgánica y compuestos inorgánicos, sobre todo en la parte alta del mismo (Contreras-Arribas, 2013; Mendiguchía *et al.*, 2007). Por tanto, el estuario tiene un papel primordial en los procesos que se desarrollan en la amplia plataforma continental del golfo de Cádiz, cuenca que conecta el océano Atlántico con el mar Mediterráneo. La productividad de los ecosistemas marinos en la región se rige principalmente por las condiciones hidrológicas y bio-geoquímicas que se presentan en la cuenca, y en particular, en las zonas costeras situadas en la plataforma continental.

La morfología del estuario ha evolucionado significativamente a lo largo de la historia, inicialmente a causa de los procesos naturales y más tarde ocasionado por las modificaciones humanas. Debido a que el terreno que rodea el estuario es prácticamente

plano, la morfología del río, antes de la influencia antrópica, incluía numerosos meandros y ramificaciones. Esta situación no era muy conveniente para la navegación en el puerto de Sevilla, principal centro de intercambios comerciales entre España y el recién descubierto continente americano. Por lo tanto, en el siglo XVIII, la primera y no última gran modificación humana comenzó con la eliminación de los meandros, que se ha prolongado hasta el día de hoy, reduciendo 50 km de longitud entre la desembocadura y el puerto, siendo la actual distancia de 84 km (Ruiz *et al.*, 2014). En el siglo XX, estas alteraciones fueron acompañadas por la presión de las actividades relacionados con la agricultura, que conllevaron el consiguiente drenaje generalizado de las marismas y las modificaciones masivas del régimen de agua dulce. Más del 80% de la superficie original de la marisma fue transformada, lo que representa una de las mayores pérdidas en Europa. Adicionalmente, las crecientes demandas de la agricultura condujeron asimismo a la construcción de numerosos embalses en toda la cuenca de drenaje (55 presas en total). La presa de Alcalá del Río (1930), a tan sólo 110 km de la desembocadura, se encontraba tan próxima de la misma que dio lugar a la transformación de la dinámica de las mareas en el estuario. Las entradas de agua dulce se han reducido en un promedio del 60% (de aproximadamente 5.000 hm^3/año en 1931-1981 a 2.000 hm^3/año en 1981-2000), con una mayor reducción en años secos (Contreras & Polo, 2010). La descarga es un parámetro actualmente controlado casi en su totalidad por las diferentes actuaciones acometidas sobre el cauce del río y sus afluentes, como se desprende del informe "Estudio de impacto medioambiental de las actuaciones de mejora en accesos marítimos al puerto de Sevilla" (2000). Este caudal resulta irregular, tanto a nivel anual (estíos frente a los caudales invernales) como interanual (variabilidad hidrológica de un año a otro), sucediéndose períodos de grandes aportaciones con períodos de fuertes sequías. Recientemente, a raíz de la problemática generada por el accidente minero de Aznalcóllar, las restantes marismas del área de Doñana se aislaron completamente usando diques y compuertas (Contreras & Polo, 2010). La producción de sal y la acuicultura también han contribuido al aislamiento del estuario de su entorno. Como resultado de todas estas modificaciones, el estuario está compuesto de un canal principal con un número pequeño de caños sin una zona de llanos mareales significativa. El canal es dragado periódicamente desde su desembocadura hasta donde se accede al Puerto de Sevilla con el fin de garantizar una profundidad mínima de navegación de 6,5 m. Estas continuas perturbaciones han sido lo suficientemente intensas como para no sólo alterar de manera drástica la dinámica del

estuario, sino también la geomorfología de la zona costera adyacente (López-Ruiz *et al.*, 2012).

Durante el desarrollo del proyecto entre la Autoridad Portuaria de Sevilla y el Consejo Superior de Investigaciones Científicas para el estudio titulado "Propuesta metodológica para diagnosticar y pronosticar las consecuencias de las actuaciones humanas en el estuario del Guadalquivir" se creó una plataforma tecnológica de toma de datos en tiempo real que generó una gran cantidad de información, permitiendo diagnosticar con detalle la dinámica del estuario (Contreras & Polo, 2012; Diez-Minguito *et al.*, 2012, 2013, 2014; Navarro *et al.*, 2011, 2012b). De esta manera, se progresó en el conocimiento científico existente sobre su funcionamiento y entorno. En el estudio hay información medida y examinada que indica que las aguas en más de dos tercios del estuario no presentan un buen estado ecológico la mayor parte del año. Hoy en día, el diagnóstico que se presenta, como consecuencia neta de esta intensa presión antrópica para abastecer correctamente los diversos usos económicos y ambientales, encaja con un estuario en profundo deterioro, con una alteración aguda de numerosos procesos y recursos básicos importantes para mantener su buen estado ambiental (Ruiz *et al.*, 2014). Las sucesivas transformaciones han generado intensas velocidades que favorecen la continua resuspension de los sedimentos y la erosión de la costa, con un alto tiempo de residencia de las aguas que provoca la retención de las mismas dentro del estuario (Díez-Minguito *et al.*, 2013). Además de la intensa influencia de las actividades a la que se encuentra actualmente sometido, el estuario se ve afectado por la aparición de las plumas de turbidez a distintas escalas temporales y espaciales. De hecho, en el estuario del Guadalquivir, la aparición de estos eventos de turbidez es uno de los problemas que recientemente han generado agudos debates y mayor alarma social, dando lugar a intensos conflictos socio-económicos y ambientales. Los niveles elevados de sólidos en suspensión ponen en peligro el ya frágil equilibrio de un ecosistema castigado por la presión de la intervención humana en la zona, dificultando y llegando a imposibilitar el riego de numerosas zonas cultivadas en el estuario, entre otras, los arrozales, y el funcionamiento de las instalaciones dedicadas a la acuicultura (Contreras, 2012). Durante más del 80% de los días del año la descarga fluvial es insuficiente para evitar que las masas de agua estén bien mezcladas, lo que impide su estratificación. En esas condiciones, la elevada turbidez inhibe la transmisión de la luz en el agua, por lo que el fitoplancton es incapaz de crecer significativamente debido a la limitación

lumínica, y se encuentra en un estado extremo (aparentemente próximo a la mera supervivencia), totalmente al contrario de lo que cabría esperar dada la elevada radiación solar incidente que llega al mismo. En la actualidad, el estuario consume más oxígeno del que produce su biota vegetal, y debido a la restricción de la fotosíntesis, afecta al balance entre consumo y producción de materia orgánica, dañando severamente el estado y diversidad ecológica de sus aguas (Ruiz *et al*., 2014). Estos episodios, relativamente recientes, han puesto de manifiesto la necesidad de identificar las fuentes críticas de estos sucesos en sí, y las condiciones que potencian su persistencia. Consecuentemente, considerando el papel que juegan los procesos estuarinos sobre la hidrología y los ecosistemas, el estudio integrado del estuario del Guadalquivir se presenta como una de las piezas clave dentro de la caracterización y gestión sostenible de esta región.

1.2 Teledetección en zonas costeras

La observación de los océanos mediante el uso de sensores a bordo de satélites ha adquirido la madurez necesaria como para formar parte de diversas disciplinas científicas, entre ellas la meteorología y oceanografía. Actualmente, el alto nivel de desarrollo de las técnicas de teledetección y de los métodos de procesamiento han convertido la percepción de "simples imágenes de satélite" en medidas cuantitativas de variables relevantes para estudios marinos. Específicamente, los sensores de color son instrumentos capaces de obtener la señal electromagnética visible proveniente de la superficie marina y convertir dicha señal y su variación en diversos parámetros como abundancia del fitoplancton, concentración de material particulado, material orgánico disuelto, o también permitir la visualización de la velocidad a la que los océanos secuestran dióxido de carbono atmosférico. En los últimos años hemos sido testigos de cómo las mediciones realizadas por estos sensores han revolucionado el modo de contemplar, analizar y comprender la biología y las interacciones fisico-químicas de los océanos a escala mundial. Las primeras observaciones del color del océano desde el espacio se llevaron a cabo con la puesta en órbita del sensor CZCS (Coastal Zone Color Scanner), un radiómetro que operaba en el satélite de investigación Nimbus-7 de la NASA desde 1978 a 1986. Este instrumento sentó las bases científicas para una nueva generación de medidas vía satélite en la década de los 90. Entre estos cabe destacar, enfocados en aplicaciones oceánicas, los sensores SeaWiFS (Sea-Viewing Wide Field-of-View Sensor) y MODIS (Moderate Resolution Imaging Spectroradiometer), ambos de la Agencia Espacial NASA y el sensor MERIS (MEdium Resolution Imaging Spectrometer), lanzado por la Agencia Espacial Europea (ESA).

Una de las grandes ventajas de los productos satelitales reside en la perspectiva panorámica y el carácter sinóptico que ofrecen, que unido al hecho de obtener información de zonas remotas o de difícil acceso, les confiere mayor capacidad que las tradicionales medidas in situ (campañas de campo, muestreos continuos, fondeos de instrumentos, boyas, ...). Los métodos convencionales de muestreo de los parámetros relacionados con la hidrodinámica, biogeoquímica y calidad de las aguas (sólidos en suspensión, turbidez, clorofila, CDOM, temperatura, salinidad, coeficiente de extinción de la luz,...) presentan deficiencias debido tanto a la alta variabilidad espacio-temporal de los procesos que se desarrollan en los sistemas marinos como por su elevado coste.

Sin embargo, estas técnicas de laboratorio o medidas in situ poseen frecuentemente mayor precisión absoluta que los datos satelitales.

Otro aspecto positivo de los sensores remotos atañe a la cobertura global y repetitiva que ofrecen de los océanos, brindando la posibilidad de realizar estudios multi-temporales y seguir la evolución global de fenómenos de naturaleza dinámica y compleja. Cabe destacar que la trasmisión casi inmediata de los datos registrados a los usuarios interesados es otro punto eficaz para su inclusión en modelos y sistemas de predicción. Es por ello por lo que las técnicas de teledetección se han convertido recientemente en una de las herramientas más efectivas, valiosas y potentes a la hora de estudiar estos entornos, ofreciendo de forma sinóptica observaciones de alta resolución espacial y temporal (Chen *et al.,* 2007; Doxaran *et al*., 2002; Hu *et al.,* 2004) y reforzando, de esta manera, los tradicionales métodos de adquisición de datos.

Es importante destacar que, debido al enfoque de la oceanografía óptica en aguas de tipo I, aquellas cuyas propiedades ópticas dependen principalmente de la concentración de fitoplancton y de sus productos asociados (generalmente el océano exterior), existe un vacío referente a los algoritmos para estimar la calidad de las aguas en las zonas costeras, y en particular, los sistemas estuarinos. Estas regiones pertenecen particularmente a aguas de tipo II, es decir, son aguas dominadas por sedimentos inorgánicos en suspensión y materia orgánica disuelta como también fitoplancton (Morel & Prieur, 1977). Además de este inconveniente, la proximidad a costa y contaminación de la señal en zonas someras hacen difícil obtener información satelital precisa y consistente, por lo que es necesario desarrollar primordialmente validaciones y controles de calidad de los datos. Mediante el uso que se pretende hacer de la teledetección y de los diversos sensores ópticos en esta Memoria, se definirán y validarán los algoritmos locales capaces de determinar los parámetros con un alto índice de calidad, rellenando de esta manera el hueco existente en la actualidad para la cuantificación automática mediante datos satelitales sobre esta franja costera. El uso combinado de la información proporcionada por los diversos satélites ofrece la posibilidad de realizar un análisis multi-sensor, el cual se hace imprescindible, ya que no existe en la actualidad un instrumento cuyas propiedades (resolución espacial, temporal y espectral) abarquen todas las necesidades requeridas en el trabajo que engloba esta memoria.

El análisis que se aborda en esta Tesis Doctoral viene motivado, como se ha mencionado anteriormente, por la necesidad de comprender y predecir los procesos estuarinos y los mecanismos que controlan las distintas escalas de variabilidad espacio-temporal de los parámetros de control físico, biogeoquímico y de calidad de las aguas de esta región costera. A raíz de los extremos episodios de incremento de turbidez ocurridos durante los pasados años 2007 y 2008, y de la consecuente problemática generada en el entorno del Guadalquivir, con graves repercusiones sobre la dinámica, morfología y biodiversidad, el estudio científico se hace imprescindible. De hecho, esta Tesis Doctoral se encuentra enmarcada dentro de un Proyecto de Excelencia de la Junta de Andalucía, denominado "Estudio de los eventos de turbidez en la desembocadura del Guadalquivir mediante teledetección y su conexión con procesos meteorológicos y oceanográficos", el cual se ha ejecutado en el Instituto de Ciencias Marinas de Andalucía (ICMAN-CSIC), y del cual Isabel Caballero fue beneficiaria de una beca de doctorado. Para determinar todo el espectro de fluctuaciones del ecosistema es adecuado contemplar la teledetección como un componente esencial, el cual conforma uno de los objetivos subyacentes de este trabajo, que debe emplearse en combinación con la implementación de otros instrumentos o medidas in situ, jugando ambos un papel clave. El estudio abarca distintas facetas multidisciplinares, lo que permitirá una mejora de la información sobre el funcionamiento del estuario mediante una visión global, además de estudiar su interacción con el ecosistema de la plataforma continental sur-atlántica andaluza. Las técnicas que se usarán a lo largo de su desarrollo generarán una herramienta eficaz y precisa de diagnóstico imprescindible para el avance en la gestión óptima del estuario y las actuaciones futuras de las administraciones públicas competentes.

1.3 Objetivos principales

El objetivo general que se plantea en esta Tesis Doctoral es:

Realizar un estudio detallado de los mecanismos que se desarrollan a través de la generación de la pluma de turbidez en la desembocadura del estuario del Guadalquivir y conocer su variabilidad espacio-temporal mediante el uso conjunto de técnicas de teledetección y datos in situ. Se hará un especial énfasis en el papel que tienen dichos procesos sobre el entorno de la plataforma continental y el golfo de Cádiz y las consecuencias y posibles impactos en los valores ecológicos de la región.

Este propósito general se pretende alcanzar a partir de la consecución de los siguientes objetivos específicos como son:

1. Determinar los parámetros de estudio físico-biogeoquímicos y de calidad de las aguas (sólidos en suspensión, turbidez, clorofila, coeficiente de extinción de la luz, ...) e implementar la metodología para generar los algoritmos empíricos y semianalíticos a partir de datos de satélite de distinta índole y de los datos de campo.
2. Describir los procesos que acontecen en el estuario del Guadalquivir y caracterizar los patrones espacio-temporales identificando los agentes forzantes meteorológicos y oceanográficos implicados en las diversas escalas de variabilidad.
3. Diagnosticar la interacción de dichos parámetros con los procesos estuarinos y los efectos sobre la hidrología y los ecosistemas del golfo de Cádiz, constituyendo de tal manera, una potente herramienta para los programas de gestión de la calidad y de los recursos litorales.

1.4 Organización de la memoria

A partir de los objetivos y planteamientos propuestos, la estructura de la presente Tesis Doctoral está organizada en 8 capítulos, como se detalla brevemente a continuación:

En el capítulo actual, **Capítulo 1,** se presenta la descripción detallada del área de estudio, así como el "estado del arte" en el que se centra esta Tesis Doctoral. También se indican la justificación y objetivos generales que se han planteado.

En los siguientes cinco capítulos se recogen la metodología, resultados y discusión de los estudios realizados a lo largo de esta Tesis Doctoral, correspondiendo a las versiones originales de cinco artículos científicos publicados en su mayoría. Específicamente, los Capítulos 2, 3, 5 y 6 se encuentran actualmente publicados, mientras que el Capítulo 4 está en proceso de ser enviado a la revista.

El **Capítulo 2** pone en relieve el uso de un satélite español de alta resolución, DEIMOS-1, en el estudio de diversos procesos costeros en la región, como son la pluma de turbidez en el estuario del Guadalquivir, los niveles de inundación en las marismas de Doñana y la vegetación inter-mareal en la Bahía de Cádiz.

El **Capítulo 3** hace referencia al desarrollo e implementación de la metodología de corrección atmosférica con el satélite DEIMOS-1, dirigido especialmente a caracterizar los TSS en el estuario y desembocadura.

Se proseguirá con el **Capítulo 4,** que se encuentra dedicado a interpretar el conjunto de los resultados del estudio realizado con las imágenes del sensor MERIS FRS, haciendo especial hincapié en la influencia de la marea y el viento sobre la pluma de turbidez.

En el **Capítulo 5** se estudia con detalle la variabilidad estacional e inter-anual de los sólidos en suspensión y clorofila en la zona de la desembocadura y plataforma continental, prestando especial atención a los resultados mediante el análisis EOF (Empirical Orthogonal Function) conjunto.

El **Capítulo 6** evalúa el bloom de fitoplancton en el golfo de Cádiz y los principales mecanismos que controlan los patrones estacionales haciendo uso de los datos de GlobColour.

En el **Capítulo 7** se ofrece una síntesis general de los principales resultados obtenidos durante la presente investigación y su relación con otros trabajos previos, como también la contribución e implicaciones derivadas del mismo.

Finalmente, en el último **Capítulo 8,** se nombran de forma breve y concisa las conclusiones más importantes que se derivan de la presente Tesis Doctoral, y basándonos en ellas, se recomendarán futuras líneas de investigación.

Por último, se presentan las **referencias bibliográficas** utilizadas en esta memoria.

CAPÍTULO 2

DEIMOS-1 SATELLITE PROVIDES IMAGERY FOR COASTAL MANAGEMENT

Isabel Caballero[1], Edward P. Morris[1], Gabriel Navarro[1]

[1] Departamento de Ecología y Gestión Costera, Instituto de Ciencias Marinas de Andalucía, Consejo Superior de Investigaciones Científicas (ICMAN-CSIC), Puerto Real, 11510, España

Sea Technology, 2012, 53, 2, 10-13
Factor de impacto: 0.068 (2012)
Categoría: ENGINEERING, OCEAN
Rango en la categoría: 15
Número total de revistas en la categoría: 15
Quartil en la categoría: Q4

DEIMOS-1 Satellite Provides Imagery for Coastal Management

High Spatial Resolution Satellite Measures River Plume Dynamics, Wetland Flood Levels and Intertidal Vegetation Changes in Spain

By Isabel Caballero
Ph.D. Student
Edward P. Morris
Postdoctoral Researcher, Ph.D.
and
Gabriel Navarro
Research Assistant, Ph.D.
Department of Ecology and Coastal Management
Instituto de Ciencias Marinas de Andalucía Consejo Superior de Investigaciones Científicas (ICMAN-CSIC)
Puerto Real, Spain

Satellite-borne sensors are an ideal tool for remotely assessing a number of water quality parameters that determine the functioning of aquatic ecosystems. For example, chlorophyll and total suspended solids in a body of water are critical variables for determining primary production and can help characterize nutrient loading and sediment dynamics. Remote sensing can also potentially provide a synoptic view of the transport of waterborne materials by tides, river discharges and currents, allowing the examination of the role of coastal hydrodynamics in erosion and deposition processes, phytoplankton primary production and the transport of nutrients and pollutants.

In recent years, there have been significant advances in the availability of satellite sensors that can provide frequent high spatial resolution and extensive coverage of environmental parameters in coastal areas. These capabilities offer a substantial advantage over traditional in-situ observations, which often have limited spatial or temporal coverage and are usually expensive. Hence, remote sensing promises to be a cost-effective technique for monitoring coastal dynamics and fulfilling the monitoring obligations of management agencies, such as the EU Water Framework Directive.

One particular new satellite, DEIMOS-1, is used to study coastal processes in the Gulf of Cádiz. The authors present three examples of how DEIMOS-1 images can be used for coastal management in areas with high ecological value: determining the dynamics of a river plume near a fisheries reserve in the estuary of the Guadalquivir River; measuring flood dynamics in the wetlands of Doñana National Park; and tracking changes in intertidal vegetation at Cádiz Bay Natural Park.

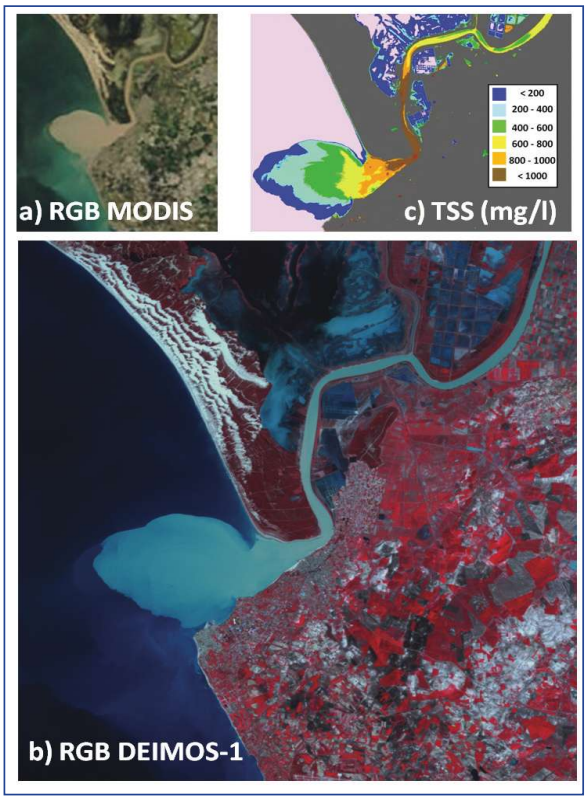

An RGB image captured from NASA's MODIS satellite is shown in (a). An RGB composite from the DEIMOS-1 satellite (b) and a map of TSS concentration at the river mouth defined by band ratio green-red radiances, (c), is shown in a scene captured in March 2011.

DEIMOS-1 Satellite

Developed by Elecnor Deimos Imaging S.L. (Valladolid, Spain), DEIMOS-1 is the first private satellite in Europe that carries a multichannel optical sensor. The satellite is a small automatic spatial platform weighing only 100 kilograms and provides visible and near-infrared (NIR) images split into three wide bands between 510 and 906 nanometers. Designed to obtain terrestrial images, the satellite has a 22-meter spatial resolution that is suitable for studying vegetation cover and a

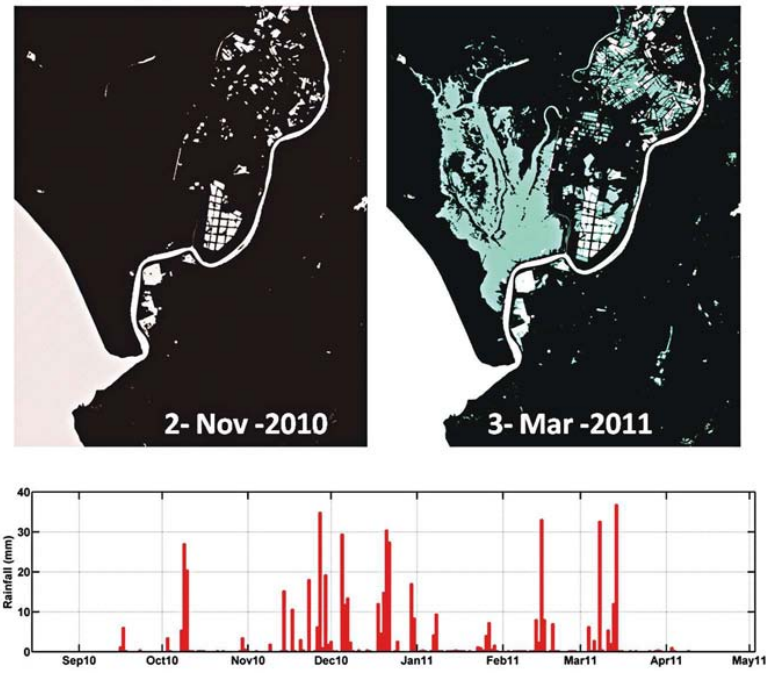

(Above) A map of the flooded area in the Doñana wetlands and water masses defined by the normalized difference water index in November 2010 and March 2011 images, respectively. The blue areas indicate the difference in the range of flooding between both images. The bottom graph shows daily mean precipitation, measured in millimeters at the meteorological station in Almonte, Spain, near Doñana National Park.

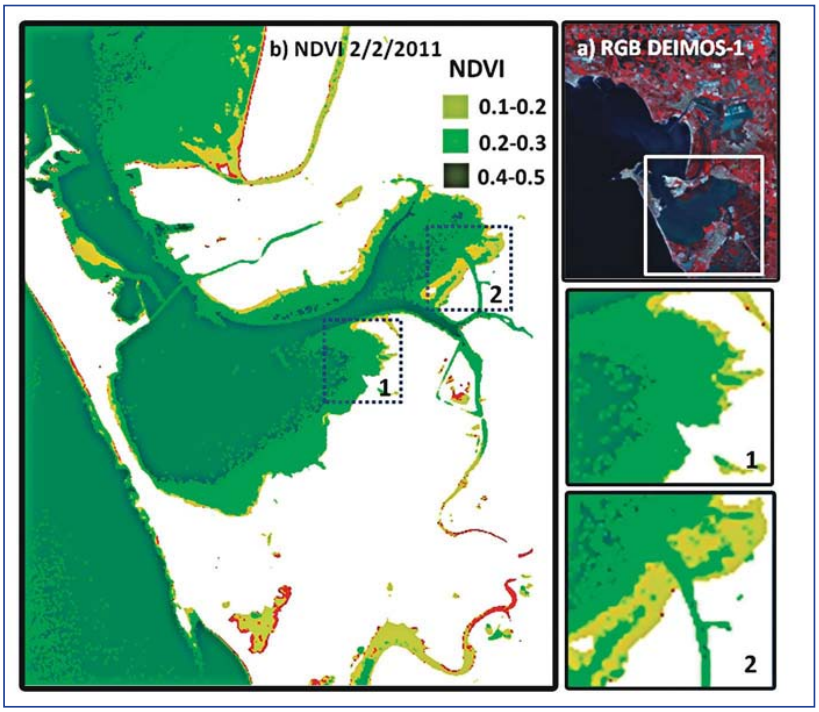

(Right) An RGB DEIMOS-1 composite (a) and normalized difference vegetation index map (b) for DEIMOS-1 data from February 2011 in Cádiz Bay. Images 1 and 2 are zooms of the areas.

600-kilometer extent that allows repeated views of an area at a high temporal resolution.

The coordinate system of the satellite imagery was World Geodetic System 1984 UTM zone 29N. Three bands were available per image: Band 3 (green: 510 to 618 nanometers), Band 2 (red: 614 to 698 nanometers) and Band 1 (NIR: 755 to 906 nanometers). The RGB images for the DEIMOS-1 sensor were composed by merging the three bands.

Guadalquivir River Plume Dynamics

In order to study the spatial dynamics of the river plume of the Guadalquivir estuary, eight DEIMOS-1 images were compared to field measurements of the concentration of milligrams of total suspended solids (TSS) per liter, taken using the gravimetric method.

Water samples were collected in three field campaigns at 20 positions in the region of the river mouth within 30 minutes of DEIMOS-1 satellite overpasses. Sampling positions were recorded with a GPS (accuracy within 5 meters).

Water-leaving radiance was extracted from the images at the corresponding positions and compared to the measured TSS. The band ratio, green-red (GR), gave the strongest linear relationship with TSS, where TSS = -639.46 + 2930 GR. The coefficient of determination of this linear relationship is 0.90 (r^2), where the Pearson product-moment correlation coefficient is $p < 0.001$, and the authors used 55 for in-situ data ($n = 55$).

The high coefficient of determination (r^2) suggests that this simple radiance band ratio can determine water sediment loads with a relatively high accuracy. Thus, in areas affected by river runoff, remote sensing may provide a cost-effective alternative for monitoring water quality.

This algorithm was used to calculate TSS of the Guadalquivir River plume after an extended period of heavy rains. The high spatial resolution of the DEIMOS-1 sensor and the GR band ratio's sensitivity to TSS allows the visualization of detailed structure within the plume.

The most intense water sediment loads were observed in

the final stretch of the river, which is surrounded by wetlands. Sediment dispersion and the irregular shape of the plume, caused by the prevailing coastal hydrodynamics, were clearly visible. Therefore, DEIMOS-1 images could potentially provide detailed information on estuarine sediment loads.

Regular synoptic observations of the intensity and structure of river runoff in a range of meteorological and oceanographic conditions will improve researchers' understanding of coastal sediment dynamics and contribute to the effective management of transitional waters.

Doñana National Park Flood Levels

The freshwater marshes of Doñana National Park are one of the most important conservation areas in the world. As Europe's largest sanctuary for migrating birds, the area was declared a national park in 1969, a biosphere reserve in 1980, an important wetland site under the Ramsar Convention in 1982 and a natural World Heritage Site in 1994.

The wetland relies on seasonal flooding via a number of rivers and streams, as well as groundwater intrusion. However, much of its catchment area has been affected by human interventions such as channel modifications, dams and groundwater extraction. Understanding how these interventions and any possible remediation strategies affect the functioning of the park requires detailed synoptic overviews of flooding in a range of meteorological conditions.

DEIMOS-1, with a spatial resolution of 22 meters and an NIR band, was demonstrated as an effective tool for mapping flood levels within Doñana National Park. Using the normalized difference water index (NDWI), areas of water were identified: NDWI = (Green - NIR) / (Green + NIR)

Values of NDWI were classified as water for two images, representing November 2010 and March 2011, chosen to represent dry and wet conditions, respectively. The contrast between the images was immediately obvious with the characteristic shape of the flooded wetland clearly visible in the March 2011 image. Small lakes and man-made ponds that are permanently flooded are also easily observed are visible as areas that do not change between the images.

Hence, the extent and distribution of flooding can be assessed using simple image intersection techniques, potentially allowing cost-effective, seasonal monitoring of the wetlands. Combining this information with archived images from other sensors will allow the evaluation of the effects of historical interventions as well as the efficiency of future management plans on environmental flows within the park.

Intertidal Vegetation in Cádiz Bay

Coastal vegetation, such as sea grasses, salt marshes and mangroves, provide many highly valuable services, including carbon sequestration, coastal defense and increasing biodiversity. However, these habitats are also now among the most endangered from increasing development of coastal zones.

Cádiz Bay Natural Park is an area of salt marshes and intertidal flats that has a very long history of human development, starting with the Romans. Declared a natural park in 1989, a Ramsar site in 1992 and an area of special community importance in 2006, it has a rich abundance saltmarshes and is home to three of the four species of European sea grasses. Monitoring the state of this natural resource is a key part in ensuring the environmental quality of local waters.

Synoptic views of the abundance (biomass or coverage) of intertidal vegetation was acquired by using DEIMOS-1 images collected at low tide. A normalized difference vegetation index (NDVI), a quantitative index of chlorophyll containing plant biomass, was calculated for intertidal areas of the park: NDVI = (NIR - Red) / (NIR + Red).

Previous field studies in the bay suggest that NDVI-abundance relationships for marine plants are relatively linear up until high biomasses. By using these relationships, it is possible to cost-effectively map the abundance of vegetation. Discerning between different vegetation types may be a little more tricky, as the sensor only has three bands, and the sea grass species have rather similar reflectance spectra.

Nevertheless, ephemeral green macroalgae mats that cover bare sediment areas in winter do appear to have a distinct spectral signature, suggesting

that at least this potentially nuisance algae may be easily identified using DEIMOS-1.

Conclusions

This work has highlighted the potential of DEIMOS-1 imagery to provide reliable information for using in the optimal management of coastal and transition waters.

DEIMOS-1 is likely to be a very valuable tool that will complement regional monitoring programs, as it has a wide variety of applications in coastal research, including identifying flood areas, estuarine sediment dynamics and coastal vegetation abundance, as well as the ability to collect images on demand.

Acknowledgments

This study has been developed in the context of the P09-RNM-4853 and RPN-049/2010 projects.

References

For a list of references, contact Isabel Caballero at isabel.caballero@icman.csic.es. ■

Isabel Caballero is a marine science graduate student and is pursuing her Ph.D. at the Instituto de Ciencias Marinas de Andalucía Consejo Superior de Investigaciones Científicas (ICMAN-CSIC) with support from the Regional Government of Andalucía. Her research focuses on applying remote sensing techniques to study coastal processes.

Edward P. Morris received his Ph.D. in oceanography and marine biology from the University of Groningen in May 2005. Since 2005, he has been a postdoctoral researcher at the University of Cádiz's biology department. Since September 2011, he has been based in the Department of Ecology and Coastal Management at ICMAN-CSIC.

Gabriel Navarro received a Ph.D. in marine science from the University of Cádiz in 2004. Since June 2005, he has been a research assistant and remote sensing specialist at the Department of Ecology and Coastal Management at ICMAN-CSIC.

CAPÍTULO 3

ASSESSMENT OF SUSPENDED SOLIDS IN THE GUADALQUIVIR ESTUARY USING NEW DEIMOS-1 MEDIUM SPATIAL RESOLUTION IMAGERY

Isabel Caballero[1], Edward P. Morris[1], Javier Ruiz[1], Gabriel Navarro[1]

[1] Departamento de Ecología y Gestión Costera, Instituto de Ciencias Marinas de Andalucía, Consejo Superior de Investigaciones Científicas (ICMAN-CSIC), Puerto Real, 11510, España

Remote Sensing of Environment, 2014, 146, 148-158
doi:10.1016/j.rse.2013.08.047
Factor de impacto: 4.769 (2013)
Categoría: REMOTE SENSING
Rango en la categoría: 1
Número total de revistas en la categoría: 27
Quartil en la categoría: Q1

Remote Sensing of Environment 146 (2014) 148–158

Contents lists available at ScienceDirect

Remote Sensing of Environment

journal homepage: www.elsevier.com/locate/rse

Assessment of suspended solids in the Guadalquivir estuary using new DEIMOS-1 medium spatial resolution imagery

Isabel Caballero *, Edward P. Morris, Javier Ruiz, Gabriel Navarro

Departamento de Ecología y Gestión Costera, Instituto de Ciencias Marinas de Andalucía, ICMAN-CSIC, Puerto Real, 11510 Cádiz, Spain

ARTICLE INFO

Article history:
Received 29 September 2012
Received in revised form 18 July 2013
Accepted 8 August 2013
Available online 12 October 2013

Keywords:
Ocean color
DEIMOS-1
Atmospheric correction
Total Suspended Solids
River plume
Guadalquivir estuary

ABSTRACT

Measurements of Total Suspended concentrations (*TSS*) are critical for monitoring geomorphological processes as well as ensuring the "good status" of transitional and coastal waters. Here, we explore the potential of the new DEIMOS-1, multi-spectral, medium-resolution satellite sensor for quantifying *TSS* dynamics within the large, turbid Guadalquivir estuary (SW Iberian Peninsula). Eight scenes were atmospherically corrected using various image-based procedures (apparent reflectance; Dark Object Subtraction, DOS; and solar zenith angle approximation, COSTZ). In-situ measurements (100 to 1400 mg L^{-1}) from three campaigns coinciding (±15 min) with satellite overpasses were used to assess the semi-analytical algorithm from Nechad et al. (2010) relating water-leaving reflectance (ρ_w) to *TSS*. All bands were very sensitive to *TSS*, however saturation of the visible wavelengths was observed at the highest sediment loads. The best correlation was obtained for the NIR band (755–906 nm) using the simple band-reflectance model at the top of atmosphere reflectance ($\rho_{w(TOA)}$), $TSS\ (\text{mg L}^{-1}) = 21428.77\ \rho_{w(TOA)} / (1 - \rho_{w(TOA)} / 0.21) - 346.17$ ($r^2 = 0.864$, $p < 0.001$, $\varepsilon_r = 25.411\%$, $n = 53$), which was used to generate maps. This approach revealed detailed spatio-temporal variability in sediment concentrations within the river plume, near to shore and far up the river channel. We demonstrate that DEIMOS-1 has a high capability as a valuable tool for the frequent, synoptic monitoring of water-quality parameters needed for the optimum management of coastal and transitional waters.

1. Introduction

Estuaries are one of the most sensitive, complex and biologically productive aquatic environments in the world. They are vital to commerce, transportation, and fisheries, and recently, have acquired increasing social significance for recreation activities, providing economic benefits via tourism (Prandle, 2009; Wolanski & McLusky, 2011). They correspond to buffer protecting zones which are important for coastal geomorphology, whose dynamics are dependent on a subtle balance between sediment inflow from inland waters or the sea and sediment outflow (Volpe, Silvestri, & Marani, 2011). Transport of terrestrial material through estuaries typically follows the seasonality of the local climate and may show marked interannual variability (Chen, Hu, & Muller-Karger, 2007; Doxaran, Froidefond, Lavenderb, & Castainga, 2002), producing plumes over the continental shelf and particularly in inner shelf areas.

The concentration of Total Suspended Solids (*TSS*), also called Total Suspended Matter or Suspended Particulate Matter (*TSM* and *SPM*, respectively) within the water column is an important parameter that when combined with volumetric flow rates, allows the estimation of river-borne sediment transport through transitional waters (i.e., estuaries) into the coastal zone (Nezlin, DiGiacomo, Stein, & Ackerman, 2005; Warrick, Mertes, Washburn, & Siegel, 2004). *TSS* can also give an indication of the extent of nutrient (Mayer et al., 1998) and pollutant loading (Martin & Windom, 1991), as well as directly determine the underwater light climate, and thus indirectly affect primary production (May, Koseff, Lucas, Cloern, & Schoellhamer, 2003). Regular observations of *TSS* in inland, transitional and coastal waters are thus critical for monitoring coastal geomorphological processes as well as ensuring the "good status" of these waters (European Union Water Framework Directive, EU-WFD).

Conventional sampling methods (i.e., filtering water samples) can be costly and time-consuming, making them difficult to apply over large areas at a high temporal resolution. Long-term deployment of instruments, such as optical backscatter devices, allow continuous turbidity measurements (Navarro, Gutiérrez, Díez-Minguito, Losada, & Ruiz, 2011; Navarro et al., 2012), however these can be tricky to calibrate and maintain, again pushing up costs. Remote sensing (RS) offers the possibility of high-spatial resolution measurements of surface water *TSS*, as well as other important parameters (e.g., photosynthetic pigment concentrations, chromatic dissolved organic matter and temperature) at a reasonable cost and high temporal resolution (days to weeks) (Baban, 1993, 1997; Hu et al., 2004; Saldías, Sobarzo, Largier, Moffat, & Letelier, 2012; Tassan, 1994). Hence, the complementary use of RS has been suggested for a number of critical problems in coastal management (Alparslan, Aydöner, Tufekci, & Tüfekci, 2007; Ritchie, Cooper, & Schiebe, 1990; Ritchie, Zimba, & Everitt, 2003).

* Corresponding author. Tel.: +34 956832612.
E-mail address: Isabel.caballero@icman.csic.es (I. Caballero).

0034-4257/$ – see front matter © 2013 Elsevier Inc. All rights reserved.
http://dx.doi.org/10.1016/j.rse.2013.08.047

Satellite-borne sensors have been effectively used to assess the relationship between *TSS* and the water-leaving radiance (L_w) or water-leaving reflectance (ρ_w) of surface waters allowing detailed synoptic views of sediment dynamics in rivers and lakes (Carpenter & Carpenter, 1983; Ritchie & Cooper, 1988), wetlands (Bustamante, Pacios, Díaz-Delgado, & Aragonés, 2009), estuaries (Baban, 1995; Caballero, Morris, & Navarro, 2012; Chen et al., 2007; Doxaran et al., 2002; Hu et al., 2004), harbors (Hellweger, Schlosser, Lall, & Weissel, 2004) and coastal zones (Miller & McKee, 2004; Teodoro, Veloso-Gomes, & Gonsalves, 2008). *TSS* retrieval in Case II waters (Gordon & Morel, 1983; Mobley, 2004; Morel & Prieur, 1977) is particularly difficult due to the presence of a variety of suspended and dissolved materials; such as colored dissolved organic matter (CDOM or yellow substances), phytoplankton and terrestrial debris (Volpe et al., 2011). Moreover, the historical focus of bio-optical oceanography on Case I waters has led to a lack of reliable algorithms for estimating water-column parameters in these complex Case II regions (Morel & Prieur, 1977). Land vicinity as well as the relatively small size and shallow waters of estuaries are other challenging factors that also contribute to the difficulty of RS in coastal regions.

Because the mix of materials found in Case II waters significantly changes the backscattering characteristics of surface waters (Jerlov, 1976; Kirk, 1983), models relating *TSS* to L_w or ρ_w tend to be empirical (Doxaran et al., 2002), accounting for the particular situation of the considered area (Bricaud & Morel, 1987), rather than based on inherent optical properties (IOPs) (Ritchie et al., 2003). A notable exception was provided by Doxaran, Cherukuru, and Lavender (2006), who established empirical quantification relationships from several field data and a reflectance model integrating the mean values of the water constituents' inherent optical properties. Furthermore, semi-analytical approaches and neural network models based on physical knowledge of the relationship between reflectance and *TSS* concentrations have been established in coastal waters (e.g., Nechad, Ruddick, & Park, 2010; Stumpf & Pennock, 1989; Zhang, Pulliainen, Koponen, & Hallikainen, 2002). Suspended sediments increase reflectance throughout the visible and near-infrared (NIR) proportion of the electromagnetic spectrum (Ritchie, Schiebe, & McHenry, 1976). However, in part because of the minimal interference from other constituents, changes in ρ_w (NIR) due to changes in *TSS*, at high turbidity, are often more easily detected (Doxaran et al., 2006). Thus, a number of site-specific algorithms based on the ratio of NIR to visible remote sensing reflectance (R_{rs}) have been developed with some success (Hu et al., 2004; Miller & McKee, 2004). Several studies have demonstrated that these bands have sufficient sensitivity to detect a wide range of *TSS* in coastal and estuarine waters.

The aim of this paper is to estimate total suspended sediment concentrations in the Guadalquivir estuary (SW Iberian Peninsula, Fig. 1) using the DEIMOS-1 satellite sensor. This relatively new satellite can provide multispectral (green, red and NIR) images of medium spatial resolution (22 m) with a large extent (600 km), and offers the opportunity to collect images on demand (repeat time of 1 day). Hence, DEIMOS-1 can potentially be used to regularly map *TSS* and examine the detailed dynamics of river plumes, providing useful information for the optimal management of coastal regions. Here we focus on two key issues to be resolved before DEIMOS-1 data can be routinely applied to examine *TSS* in coastal studies: 1) Atmospheric correction of the data (see Supplementary data for details), and 2) Calibration of a semi-analytical algorithm for the retrieval of *TSS* from water-leaving reflectance. We then go on to demonstrate the potential of these approaches for the retrieval of detailed information about *TSS* dynamics within a large estuary.

2. Material and methods

2.1. Guadalquivir estuary

The Guadalquivir river is located in the southwest of the Iberian Peninsula (Fig. 1a) and flows into the Gulf of Cádiz (Atlantic Ocean). It is one

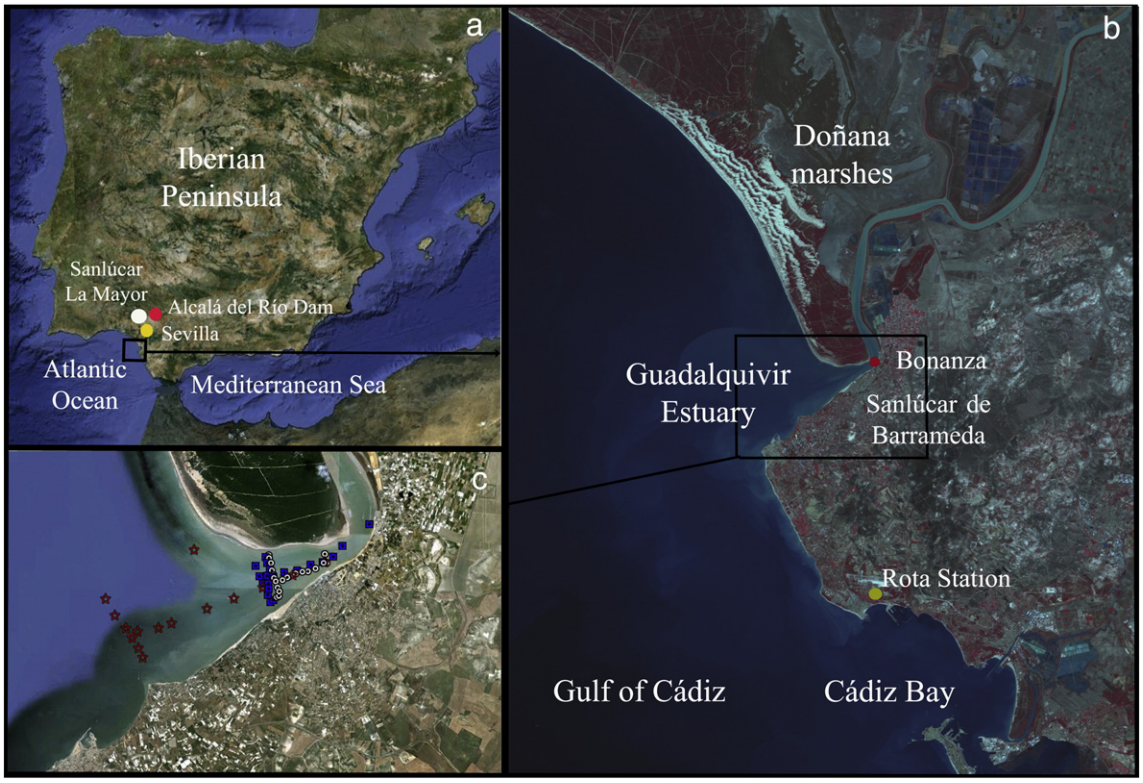

Fig. 1. a) Localization of the study area (SW Iberian Peninsula). b) Map showing the Gulf of Cádiz and the Guadalquivir estuary. c) Dots, squares and stars represent the position of samples collected during 3 campaigns in 16 December 2010, 14 January 2011 and 3 March 2011, respectively (Google Earth).

of the largest rivers in Spain (650 km long). The estuary has a width of 800 m near the mouth to 150 m at the head, and the mean depth is 7.1 m. Tidal influence extends up the Guadalquivir as far as the Alcalá del Río dam (Díez-Minguito, Baquerizo, Ortega-Sánchez, Navarro, & Losada, 2012), 110 km upstream from the river mouth at Sanlúcar de Barrameda (Fig. 1b). The estuary is a well mixed mesotidal system with a longitudinal salinity gradient (Vanney, 1970), a semidiurnal tidal period and maximum tidal range of 3.86 m. The estuary and its coastal fringe are characterized by high current velocities (Navarro et al., 2011), large loads of suspended matter resulting in high turbidity levels (Navarro et al., 2012) and high biological productivity (Navarro & Ruiz, 2006). Important biogeochemical consequences would take place during plume events, considering that the Guadalquivir River spreads its constituents (e.g. pollutants, nutrients, sediments) over a larger area through the Gulf of Cádiz. Specifically, the Guadalquivir estuary plays a relevant role in the regulation of the pelagic ecosystem of the continental shelf of the Gulf of Cádiz and hence in the maintenance of the natural resources of the basin acting as a fertilizer through the pumping of permanent inorganic nutrients that are injected into the basin (Navarro & Ruiz, 2006; Prieto et al., 2009; Ruiz, González-Quirós, Prieto, & Navarro, 2009).

Situated at the mouth of the estuary, isolated from the estuarine tidal flow by walls and floodgates, are the highly-protected wetlands of Doñana National Park (Fig. 1b), which are considered one of the most important conservation areas in the world (UNESCO-MAB Biosphere Reserve). A relatively heavy commercial and tourist traffic, that requires the periodic dredging of a shipping channel, extends from the estuary mouth to the major city of Seville. During the last decades, the adjacent region has undergone substantial changes in agricultural land use, urban development, and fisheries extraction (Ruiz et al., 2009). As a consequence, the current shape of the estuary is characterized by a main channel surrounded by tidal creeks without any significant intertidal zones. Furthermore, the natural transport of material from the river basin has been drastically reduced by a series of dams; 80% of the freshwater discharged to the estuary is regulated by the Alcalá del Río dam. Recently, Díez-Minguito et al. (2012) have described the hydraulic regime of the estuary depending on the fresh water discharges from the Alcalá del Río dam: outflow > 400 $m^3\ s^{-1}$, fluvially-dominated; outflow < 40 $m^3\ s^{-1}$, tidally-dominated and ranging from 40 to 400 $m^3\ s^{-1}$, intermediate situation.

In spite of the socio-economic and environmental significance of the Guadalquivir estuary and its impact on shelf ecosystems, until very recently, only a few studies have been conducted in the zone. The possible overexploitation of the estuary has generated, and is still generating, strong conflicts of interests that make decision-making processes extremely challenging.

2.2. Meteorological and oceanographic data

Daily mean flow rates ($m^3\ s^{-1}$) of the Guadalquivir river at the Alcalá del Río dam (Fig. 1a) were obtained from the "Agencia Andaluza del Medio Ambiente y Agua" (https://www.agenciamedioambienteyagua.es). Daily total rainfall (mm) measured at a meteorological station in Sanlúcar la Mayor (Fig. 1a) was obtained from the Agroclimatic Station network (http://www.juntadeandalucia.es). Hourly wind speed ($m\ s^{-1}$) and direction were acquired from a meteorological station (Fig. 1b) located in Rota (36.63° N, 6.35° W, IANDALUC38, http://www.wunderground.com). Measured hourly water height (m, measured using a Miros Radar at the mouth of the estuary) (Fig. 1b) from the Bonanza tidal gauge (36.80° N, 6.34° W, Mareógrafo de Bonanza, 3332) was obtained from the "Puertos del Estado" monitoring network (http://www.puertos.es).

2.3. TSS measurements

In-situ samples were acquired during three field campaigns (16 December 2010, 14 January and 3 March 2011) arranged to coincide (±15 min) with satellite overpasses (~10:30 GMT) at the mouth of the estuary. Image collection and sampling occurred during clear sky conditions. Between 15 and 20 samples were collected each campaign (total $n = 55$) using a longitudinal–transversal transect design (Fig. 1c, positions recorded using a standard GPS, Garmin, ±5 m). Surface-water was collected by hand using a dark plastic bottle (1 L) over a depth of 0.25 m. The concentration of Total Suspended Solids (*TSS*, $mg\ L^{-1}$) was quantified by filtering (pre-weighed Whatman GF/F filters) a 100 mL aliquot from each sample and weighing the dry (24 h at 60 °C) filters.

2.4. Imagery and processing

DEIMOS-1, developed by Elecnor Deimos Imaging S.L. Valladolid, Spain, is the first private satellite in Europe that carries a multichannel optical sensor. This sun-synchronous satellite can provide multispectral images (three wide bands between 510 and 906 nm, Table 1) with a 22 m spatial resolution, a 600 km extent and a repeat time of 1 day (with the possibility to collect images on demand). Images are available commercially from archive and via rapid tasking (http://www.deimos-imaging.com). Although designed primarily for rapid-response following disasters, DEIMOS-1 has strong potential as a RS platform able to complement studies on coastal and transition waters (Caballero et al., 2012).

The DEIMOS-1 images used in this study consist of eight mostly cloud-free scenes selected to be representative of autumn–winter and spring–summer conditions between 2010 and 2011 (Table 2). The images were supplied as multiband GeoTIFFs of level L1T data, i.e., orthorectified with Ground Control Point (GCP) correction, with a Universal Transverse Mercator (UTM) projection (UTM29N) and the World Geodetic System 84 (WGS84) datum. Metadata for each image was supplied in XML format. Image processing was carried out using the open-source software R 2.14.2 (R Core Development Team 2011) and Quantum GIS 1.7.4 (Development Team 2012). Custom image processing code was written in R using the packages *Landsat* (Goslee, 2011) and *raster* (Hijmans & Etten, 2011), and in Matlab 7.10.0 (R2010a).

2.5. Radiometric and atmospheric image corrections

Radiometric corrections were applied to convert the digital number (*DN*) of each pixel to at-satellite spectral radiance (L_{sat}, $W\ m^{-2}\ \mu m^{-1}\ sr^{-1}$), removing the gain and bias effects introduced by the sensor (Fig. 2I). The gain (G) and bias (B) values for each band were read from the metadata files and L_{sat} was calculated as:

$$L_{sat} = (DN/G) + B. \quad (1)$$

DEIMOS-1 instrument is calibrated by DEIMOS in cooperation with DMC International Imaging Ltd. (DMCII). Absolute and relative calibration are performed yearly, whereas trend monitoring and analysis are undertaken every fifteen days against Landsat reference and using CEOS pseudo-invariant sites. DEIMOS-1 absolute calibration is within 5% accuracy for all bands, whilst the relative calibration with Landsat is within 1–2%. Additional information about the absolute and relative calibration of the DEIMOS-1 sensor can be found on the DEIMOS Imaging website (http://www.deimos-imaging.com) and in the "DCM Data Product Manual" (Crowley, 2010).

Table 1
Spectral bands (in nm) of DEIMOS-1, Landsat ETM+ and Landsat TM.

Band	Number D-1	DEIMOS-1	Landsat ETM+	Landsat TM
Green	3	510–618	508–618	507–619
Red	2	614–698	615–701	622–704
NIR	1	755–906	750–910	750–912

Table 2
DEIMOS-1 image information with image number, date, and in-situ data available for cross-validation procedure.

Image number	Date	In-situ
1	30 August 2010	
2	2 November 2010	
3	16 December 2010	Yes
4	14 January 2011	Yes
5	2 February 2011	
6	3 March 2011	Yes
7	16 April 2011	
8	13 September 2011	

For multi-temporal image sets used to detect changes in environmental parameters it is important to reduce the variation in reflectance associated with the different atmospheric conditions of each scene, i.e., relative scaling of scenes. Furthermore, with the aim of deriving relationships between water quality parameters and ρ_w, it is important to adjust images so that ρ_w of features within a scene represent ground-level ρ_w spectra. These two aims should be accomplished by atmospheric correction procedure (ACP). Owing to its novelty, to our knowledge there are no available studies documenting the effectiveness of ACP for DEIMOS-1 images. Nevertheless, having a sun-synchronous orbit, a spatial resolution and optical bands very similar to Landsat-5 TM, it seems a reasonable assumption that commonly used ACP should be applicable. ACP can be divided into two main categories: physically-based and image-based (Lu, Mausel, Brondizio, & Moran, 2002). Physically-based corrections are the most complex and potentially accurate method (correcting for both additive scattering and the multiplicative transmittance components), but often require gathering in-situ measurements at the time of image acquisition and the use of radiance transfer codes (RTC) to eliminate atmospheric effects. In practice, such corrections have 2 major disadvantages; 1) field data is frequently unavailable or expensive to collect, and 2) the complexity and cost of

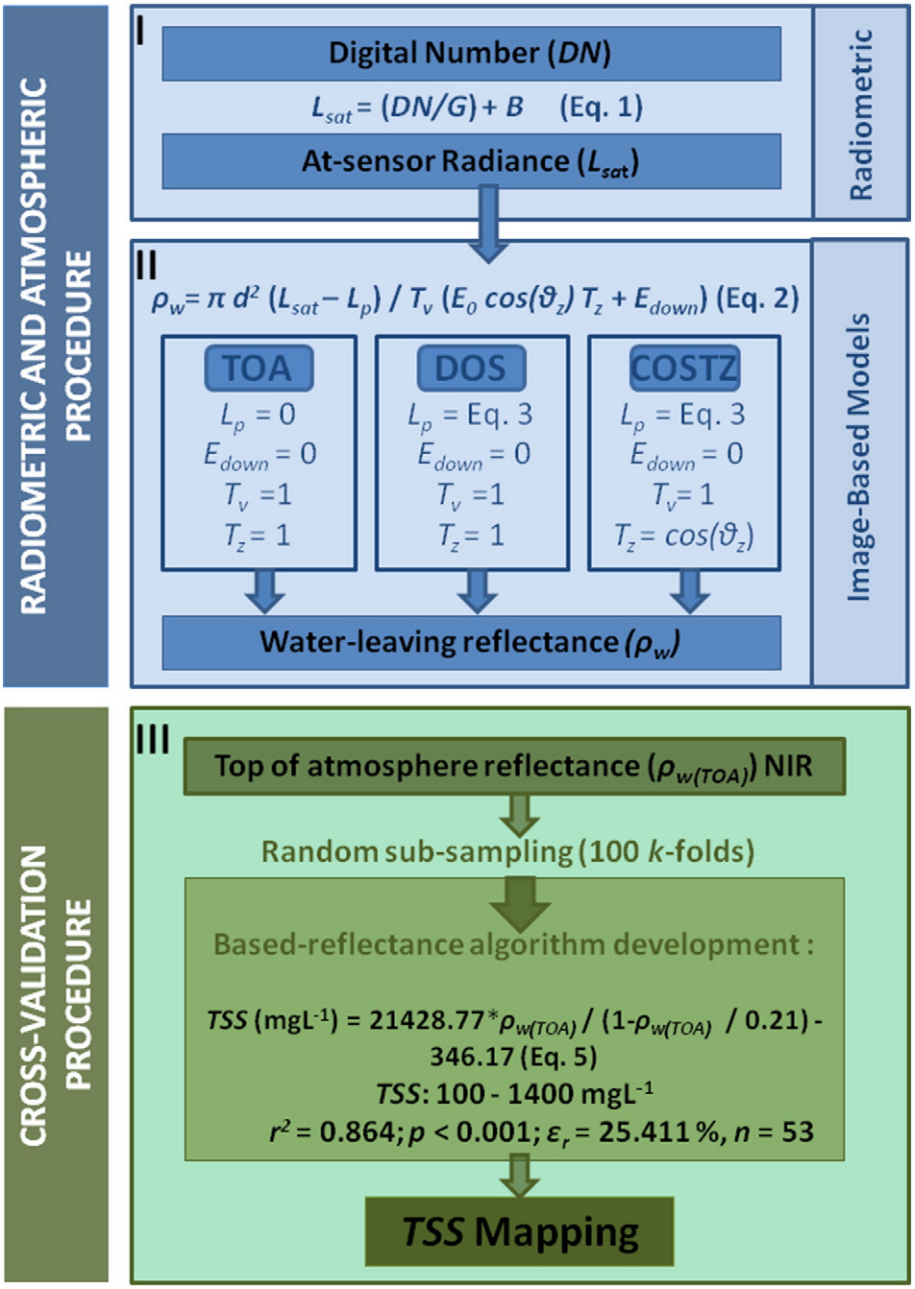

Fig. 2. Scheme of the radiometric and atmospheric procedure of the DEIMOS-1 data, cross-validation procedure and *TSS* algorithm development.

RTC are off-putting to the average user. Image-based ACP has the advantage of being relatively easy to apply and requires no extra information (except the metadata for an image). Indeed, comparisons of ACP for multi-temporal image sets suggest that simple image-based methods often give similar or better results (Lu et al., 2002; Song, Woodcock, Seto, Lenney, & Macomber, 2001). Various ACPs are available, each relying on different simplifying assumptions (Chen et al., 2004; Ritchie et al., 1990; Song et al., 2001; Wang et al., 2010). Here, we apply two simple image-based ACPs; DOS (Dark Object Subtraction or darkest pixel correction) and the improved COST (COSTZ, solar zenith angle approximation) procedures (Chavez, 1988, 1989, 1996; Fraser, Ferraze, Kaufman, Markham, & Mattoo, 1992; Milton, 1994), which are compared to the apparent (or top of atmosphere, TOA) reflectance (Chavez, 1989).

The general equation for conversion of L_{sat} to water-leaving reflectance (ρ_w) is:

$$\rho_w = \pi d^2 \left(L_{sat} - L_p\right) \Big/ T_v(E_0 \cos(\theta_z) T_z + E_{down}) \quad (2)$$

where, L_p is the atmospheric path radiance, T_v the atmospheric transmittance from the target toward the sensor, T_z the atmospheric transmittance in the illumination direction, E_{down} the downwelling diffuse spectral irradiance at the surface due to the scattered solar flux in the atmosphere, E_0 the band-specific exo-atmospheric solar constant, d the earth–sun distance (a factor which corrects for the variation in solar irradiance due to seasonal changes in earth–sun distance), and θ_z the solar zenith angle (derived from the image metadata). The exo-atmospheric solar constant ($W\,m^{-2}\,\mu m^{-1}$) is defined for DEIMOS-1 in the "DMC Data Product Manual" (Crowley, 2010). We used the values derived from the Thuillier 2002 model; 1032, 1537 and 1808 $W\,m^{-2}\,\mu m^{-1}$ for the NIR, red and green bands, respectively.

Top of atmosphere water-leaving reflectance ($\rho_{w(TOA)}$) was calculated by assuming that L_p and E_{down} are equal to zero, and T_v and T_z are equal to one (Table 4). The DOS approach accounts for L_p and implicitly assumes that: 1) The atmosphere is horizontally homogeneous within each scene (Chen et al., 2004; D'Sa, Hu, Muller-Karger, & Carder, 2002; Hu, Carder, & Muller-Karger, 2000; Miller & McKee, 2004), 2) The surface is approximately Lambertian, and 3) The scene contains pixels that have essentially zero reflectance at visible wavelengths (i.e., L_{sat} is mainly caused by the atmospheric path radiance) (Chavez, 1989; Song et al., 2001). Subtracting the L_{sat} value of these "dark objects" from all pixels within a scene thus provides a correction for the contribution of atmospheric path radiance (L_p) (Song et al., 2001) (Table 4). In practice dark objects are not absolutely dark (Chavez, 1988), and are assumed to have a reflectance of 1% (Chavez, 1989, 1996; Moran, Jackson, Slate, & Teillet, 1992), hence L_p was estimated as:

$$L_p = (DN_{min}/G + B) - 0.01 T_v(E_0 \cos(\theta_z) T_z + E_{down})/\pi d^2 \quad (3)$$

Table 3
The mean, minimum and maximum values of root mean squared error (*RMSE*, mg L^{-1}), coefficient of determination (r^2) and mean relative error (εr, %) obtained after 100 *k*-folds cross-validation procedure (top of atmosphere reflectance, NIR band). Coefficients of determination were always statistical significant ($p < 0.001$).

Statistic	100 *k*-folds
Mean *RMSE*	105.630
Min *RMSE*	53.909
Max *RMSE*	157.200
Mean r^2	0.864
Min r^2	0.442
Max r^2	0.968
Mean ε_r	25.411
Min ε_r	11.204
Max ε_r	49.491

Table 4
Parameter values defined for the different atmospheric correction models in Eq. (2) (Apparent reflectance or top of atmosphere; Dark Object Subtraction, DOS; and solar zenith angle approximation, COSTZ), where *SHV* corresponds to the Starting Haze Value (L_p in Eq. 3).

ACP method	L_p	T_v	T_z	E_{down}
Apparent reflectance	0	1	1	0
DOS	*SHV*	1	1	0
COSTZ	*SHV*	1	$cos(\theta_z)$	0

where, DN_{min} is the minimum DN value, selected by constructing a cumulative frequency distribution of DN values for each band of each scene and looking up the minimum DN with at least 1000 pixels. The scenes used in this study contained large areas of deep water > 10 km offshore that provided plenty of potentially suitable dark pixels. The COSTZ procedure also accounts for L_p and uses the cosine of the solar zenith angle as an estimate for the multiplicative transmittance component, $T_z = \cos(\theta_z)$, whilst assuming E_{down} is zero and T_v is equal to one (Chavez, 1996) (Table 4). The exact implementations of the DOS and COSTZ ACPs (Fig. 2II), and other options for atmospheric correction, can be viewed in detail within the function *radiocor* of the R package *Landsat* (Goslee, 2011).

To assess the effect of the ACPs we selected a number of pseudo-invariant features (PIFs), i.e., spatially well defined and spectrally stable features, such as deep water, sandy beaches, bare ground and man-made structures (Hall, Strebel, Nickson, & Geotz, 1991; Schott, Salvaggio, & Volchok, 1988; Song et al., 2001). We assumed that multi-temporal ρ_w values of these PIFs should have low variation after applying ACPs. PIFs were selected using a semi-supervised procedure; the coefficient of variation (CV) of the seven *DN* images without clouds (January 2011 excluded) was calculated for every pixel of each band separately. CV images for each band were thresholded (<0.2 quantile) and combined, to provide a single image indicating features with low CV in all 3 bands. This image was visually examined along with the original scenes and 19 easily identifiable PIFs ranging from bright to dark were selected for the extraction and analysis of ρ_w values.

2.6. Relationship between ρ_w and TSS

A single band algorithm for *TSS* retrieval based on the semi-analytical, non-linear model developed by Nechad et al. (2010) for turbid waters was applied and calibrated using DEIMOS-1 ρ_w and in-situ *TSS* measurements. The advantages of this algorithm are its strong theoretical background, taking into account assumptions about spatial and temporal variability of specific inherent optical properties (IOPs) and its simple application to multiple bands of any ocean color sensor (Nechad et al., 2010). The mathematical formulation of the model is defined as:

$$TSS = A^{\rho}\rho_w/(1-\rho_w/C^{\rho}) + B^{\rho} \quad (4)$$

where, ρ_w corresponds to the water-leaving reflectance, C^{ρ} (dimensionless) represents the asymptotic limit of the model and has a minor impact on model calibration, hence it is defined utilizing "standard" IOP data computed from the literature (for the DEIMOS-1 NIR band $C^{\rho} = 0.21$, see Table 1 in Nechad et al., 2010), B^{ρ} in theory represents the non-zero reflectance of sediment-free waters, but in practice represents measurement errors in both reflectance and *TSS*, and A^{ρ} represents the calibration parameter relating reflectance to *TSS*. For this analysis both A^{ρ} and B^{ρ} were derived by non-linear regression.

The DEIMOS-1 NIR band (Table 1) centered at $\lambda = 830.5$ nm was used for calibration. This band was selected because the high values of pure water absorption at the longer wavelengths guarantee that *TSS* concentrations in highly turbid waters can be precisely quantified. The frequently ρ_w algorithm saturation beyond a certain *TSS* concentration for a specified short wavelength (red, green and blue) should be

avoided, allowing retrieval of large *TSS* values. Furthermore, the nearly negligible influence of CDOM and phytoplankton absorption in the NIR spectral range provides an easy relation between ρ_w (NIR) and the backscattering and absorption by *TSS* (Nechad et al., 2010). The disadvantage of using the NIR band is its low resolution (minimum *DV* value of 1), making it insensitive to low sediment concentrations. Hence, for the very turbid Guadalquivir estuary (Navarro & Ruiz, 2006) this band is appropriate, but may not be so for other coastal regions.

Each of the individual calibration campaigns (3 in total) sampled different ranges of in-situ *TSS* (low, medium and high); we chose to calibrate the Nechad model using the data from all 3 campaigns pooled together, thus avoiding problems associated with regressions across limited data ranges. Two samples (0.16 km and 0.26 km from the coast, situated above shallow sand bars) were removed from the data set as we suspected that they were contaminated with bottom reflectance. Hence, the final data set included 53 observations collected during 3 different sampling campaigns, each on a different day, with 15–20 observations per campaign.

Non-linear robust weighted regression was used to find the best-fit values for the coefficients A^ρ and B^ρ (Eq. 4). This robust fitting procedure is insensitive to outliers. To improve the fit, considering the log-normal distribution of *TSS*, we utilized the Cauchy Weight Function, $w = 1 / (1 + res^2)$, where *res* is the residual. The calibrated Nechad model presented here is the best fit of the full data set ($n = 53$). Estimation of model prediction error was derived using a statistical cross-validation procedure.

2.7. Cross-validation

Stratified *k*-fold cross-validation was used to assess the accuracy of the calibrated model predictions (Picard and Cook, 1984, Schlerf et al., 2005) i.e., the model was calibrated using a subset of the data (training set) and the model predictions evaluated using an independent data set (validation or test set). Training and test sets were assigned using stratified-random selection; for each individual campaign 75% of the observations were randomly assigned to the training set (total $n = 40$) and 25% assigned to the test set (total $n = 13$). This assignment was repeated 100 times (folds) with the condition that test sets could not overlap i.e., each set was unique. For each fold, the model was calibrated using the training data set and the prediction compared to the test set, allowing derivation of error statistics (root mean squared error, *RMSE*; coefficient of determination, r^2; and mean relative error ε_r). A final assessment of the accuracy of model prediction was derived by averaging the error statistics over all folds (see Supplementary data for sensitivity analysis of the cross-validation procedure).

2.8. Synoptic multi-temporal maps of TSS

The normalized difference water index (*NDWI*) (McFeeters, 1996) was used to create a threshold mask allowing the separation of water and land in each atmospherically corrected image. The calibrated Nechad $\rho_{w(TOA)}$–*TSS* model was then applied to all water pixels producing synoptic gray-scale images of *TSS*. A color table was applied to the images to aid in visualization.

3. Results

3.1. Atmospheric correction

In order to help assess the effectiveness of simple image-based atmospheric correction procedures (ACPs) we selected a number of pixels ranging in brightness that could be reasonably assumed to be Pseudo Invariant Features (PIFs) (Table 5). We assumed that multi-temporal ρ_w values of these PIFs should have relatively low variation after applying ACPs and used the criterion of a low coefficient of variation (CV) to help us select which ACP to use for subsequent ρ_w–*TSS* modeling. Conversion to top of atmosphere water-leaving reflectance ($\rho_{w(TOA)}$) resulted in CV ranging from 20 to 30% (Table 5). Using both DOS and COSTZ ACPs did not appear to provide any clear improvements in PIF CV. The COSTZ ACP did appear to extend the dynamic range of reflectance values, however without ground-truth data, we do not have any means of validating if these are 'more' representative of ground-reflectance values. Temporal variation was similar for all PIFs using all ACPs (data not shown), and in general values tended to be higher in autumn–winter compared to spring–summer. The highest values were observed in the December scene, which had some cloud coverage. Appreciating we lack vital ground-truth data and the image-based ACPs did not appear to correct for seasonal differences in atmospheric conditions, we decided to use the simplest option, i.e., conversion of *DN* to $\rho_{w(TOA)}$.

After atmospheric correction, we can identify which model shows the most significant relationship with the *TSS* concentration. Statistical analysis of ρ_w derived from the three schemes can be used to evaluate *TSS* product accuracy. The cross-validation and the consequently based-reflectance model by Nechad et al. (2010) were applied to the apparent reflectance, DOS and COSTZ data sets, producing a series of *RMSE*, r^2 and ε_r, and the calibration curve (A^ρ and B^ρ parameters) was then taken with the statistics calculated as the mean of the values. The Supplementary data presents supplementary information about the results and the errors addressed in terms of *TSS* retrieval due to the different atmospheric procedures. The simplistic atmospheric correction schemes appear to be effective for the range of sky conditions that occurred during the sample dates. The outcomes in the different approaches indicated that they were somewhat effective in removing the stripping effects of atmospheric variations. The algorithms yielded significant differences: the correlation between *TSS* and $\rho_{w(TOA)}$ and $\rho_{w(DOS)}$ were similar and reasonably good, but the relationship is less clear between *TSS* and $\rho_{w(COSTZ)}$. We found that for relatively clear scenes, correction for TOA (solar zenith angle and earth–sun distance) and also DOS (the scattering and absorption) gave sufficient accuracy to enable retrieval of *TSS* from the satellite data (r^2 and ε_r of 0.864–25.411% and of 0.881–24.173%, respectively, with $p < 0.001$). The shape of the curve remains relatively unchanged and therefore the two fits derived were nearly identical. These image-based techniques are ideal procedures for atmospheric correction based solely on the digital image, requiring no in-situ field measurements during the satellite over-flight. The COSTZ utilization does not lead to improved precision in the results, with a r^2 of 0.591 and introducing larger errors ε_r of 39.963%. All ρ_w values computed from the COSTZ adjustment were higher in the 53 samples (0.18 to 0.5) than from the other two (0.9 to

Table 5
Summary of the mean and coefficient of variation, CV (%) of 3 classes of Pseudo Invariant Features (PIFs) extracted from 8 DEIMOS-1 images between 2010 and 2011, before (*DN*), after radiometric correction (L_{sat}) (W m^{-2} μm^{-1} sr^{-1}), after conversion to water-leaving (w) ($\rho_{(w)TOA}$) and after 2 types of image-based atmospheric correction procedure ($\rho_{(w)DOS}$, and $\rho_{(w)COSTZ}$).

PIF	Mean					CV (%)				
	DN	L_{sat}	$\rho_{(w)TOA}$	$\rho_{(w)DOS}$	$\rho_{(w)COSTZ}$	*DN*	L_{sat}	$\rho_{(w)TOA}$	$\rho_{(w)DOS}$	$\rho_{(w)COSTZ}$
Bright buildings	126.9	73.6	0.36	0.35	0.80	16.2	37.9	22.4	23.1	27.1
Beach sand	70.5	42.9	0.21	0.20	0.46	16.6	35.7	19.6	20.6	25.1
Offshore deep water	6.8	8.2	0.04	0.03	0.07	58.4	41.3	30.2	48.0	50.0

0.25). The incorporation of the multiplicative transmittance effect in COSTZ scheme (in addition to the additive scattering effect of DOS) has not resulted in more adequate *TSS* retrieval.

3.2. Relationship between $\rho_{w(TOA)}$ and TSS

The cross-validation procedure and the robust non-linear regression analysis showed that NIR band of $\rho_{w(TOA)}$ extracted from the corrected images were significantly related to *TSS* ($n = 53$). Fig. A1 (Supplementary data) illustrates the prediction performance (*RMSE*, r^2 and ε_r) of the cross-validation for each of the 100 *k*-fold subsets. The outcomes indicate that the values range with an averaged *RMSE* of 105.630 mg L^{-1}, r^2 of 0.864 ($p < 0.001$) and ε_r of 25.411%. Table 3 presents the mean, minimum and maximum values for the three statistics determined by the 100 *k*-folds. In most cases coefficient of determination values were high ($r^2 > 0.80$, $p < 0.001$), except for some of the folds with a minimum value of $r^2 = 0.442$ ($p < 0.001$).

Subsequently, the definitive calibration parameters (A^ρ and B^ρ) for Eq. (4) were calculated with the entire 53 samples (Fig. 3):

$$TSS = 21428.77\rho_{w(TOA)} / \left(1 - \rho_{w(TOA)}/0.21\right) - 346.17 \left(\text{mg L}^{-1}\right) \quad (5)$$

3.3. Mapping TSS concentrations

Using Eq. (5) all 8 $\rho_{w(TOA)}$ NIR images were processed to derive synoptic maps of *TSS* at the mouth of the Guadalquivir river (Fig. 4). The high spatial resolution of the DEIMOS-1 sensor and the sensitivity of the NIR band to high *TSS* allowed the visualization of detailed structure within the river plume. Sediment dispersion and the irregular shape of the plume, caused by the prevailing coastal hydrodynamics, were clearly visible (Fig. 4). Throughout the study period, the most intense water sediment loads were observed in the final stretch, where water from the surrounding wetlands enters the river. Lower concentrations were observed toward the ocean and along the coastline either side of the river mouth. The highest *TSS* (>1000 mg L^{-1}) were observed in winter and spring, the seasons with highest land runoff (Díez-Minguito et al., 2012; Navarro et al., 2011, 2012). Lower values (400–1000 mg L^{-1}) were observed in the channel during the dryer seasons (summer–autumn).

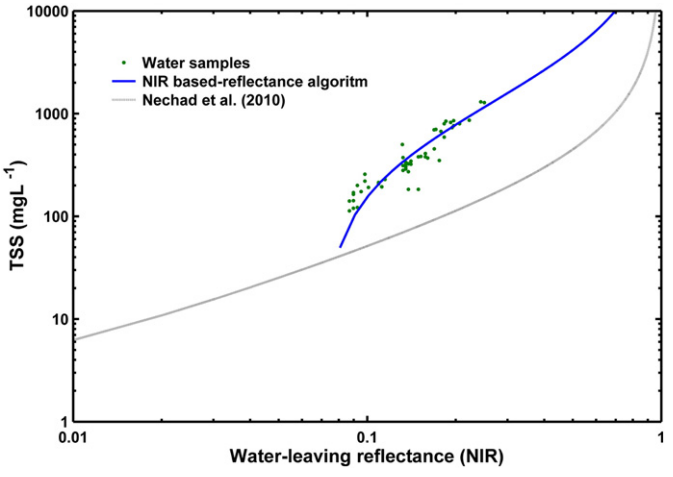

Fig. 3. NIR band algorithm for *TSS* retrieval based on the reflectance model developed by Nechad et al. (2010) using DEIMOS-1 top of atmosphere reflectance ($\rho_{w(TOA)}$). The robust non-linear regression defined the final calibration coefficients: $A^\rho = 21428.77$ (mg L^{-1}) and $B^\rho = -346.17$ (mg L^{-1}) of Eq. (5), with an averaged *RMSE* of 105.630 mg L^{-1}, r^2 of 0.864 ($p < 0.001$), ε_r of 25.411% and $n = 53$ from the cross-validation procedure (blue line, logarithmic scales). Black dashed line represents the fit from Nechad et al. (2010) at this wavelength.

The NIR-*TSS* algorithm developed here was particularly effective for defining the large winter plume of sediment observed after episodic storms with moderate rains (Fig. 2 in Navarro et al., 2012) in March 2011 (Fig. 5). On 3 March 2011, at the time of image acquisition (10:59 GMT), a light NE–ENE wind (<4 m s^{-1}) was blowing, after a calm period the previous night and a medium NE wind (5 m s^{-1}) the day before. The river flow rate was 272.54 m^3 s^{-1} at the time of satellite overpass and had been decreasing from a maximum of >1000 m^3 s^{-1} observed two weeks before. The tide was rising (tidal coefficient 0.82 m, high tide at 15:00 GMT) and there was no substantial rainfall in the last 2 weeks. Hence, the estuary could be classified as an intermediate hydraulic situation between fluvially- and tidally-dominated (Díez-Minguito et al., 2012). A well developed plume was observed with a regular, rounded shape that extended westwards from the river mouth. The high *TSS* values within the plume were in strong contrast compared to the low values (essentially below the detection limit of the algorithm presented here) observed in the surrounded waters. *TSS* was higher in the river mouth (>1200 mg L^{-1}), increasing to a maximum situated 1–3 km upstream. At the offshore edge of the plume, isolines of concentration were nearly circular. In the final stretch of the river, a transversal gradient of *TSS* appears with larger concentrations in the middle corresponding to the river channel.

The MODIS false color composites collected on the same day (Fig. 5c and d, TERRA and AQUA at 11:30 GMT and 13:10 GMT, respectively) show a displacement of the plume north of the river mouth in 2 h after the DEIMOS-1 overpass. This displacement of the plume to the north was also observed in other DEIMOS-MODIS imagery sequences from other days (data not showed here).

The high spatial resolution of DEIMOS-1 and the ample width of the Guadalquivir river also allow to examine upstream variations in *TSS* for purposes such as water quality monitoring (Fig. 6). Using an image from the 16th April 2011, *TSS* values were extracted along a longitudinal profile 50 km upstream of the river mouth (Fig. 6). Two peaks in *TSS* could clearly be observed; one situated approximately at the river mouth with *TSS* values of 200 mg L^{-1}, values then declined to <100 mg L^{-1} at about 5–14 km and increased until another wide maximum (with values ranging between 400 and 550 mg L^{-1}) was reached at the point where "Brazo de la Torre", which drains the agricultural land to the north, joins the Guadalquivir (about 25 km upstream). *TSS* then declined to between 100 and 200 mg L^{-1} for the rest of the upstream region (50 km, the end of the scene).

4. Discussion

4.1. Atmospheric correction

The good relationship between *TSS* concentration and water-leaving reflectance (NIR) highlights the suitability of image-based ACPs for correcting DEIMOS-1 images. The top of atmosphere $\rho_{w(TOA)}$ (corrected from solar zenith angle and earth–sun distance) and water-leaving reflectances from DOS $\rho_{w(DOS)}$ (corrected from the scattering and absorption, which are very important because the path radiance has serious effects on them) work best in providing a quantification of *TSS* from RS data. This process is important not only to transform to water-leaving reflectance, but also for temporal and spatial atmospheric correction so that the ρ_w has the consistency and comparability among different dates of images generating a common scale (Lu et al., 2002). The COSTZ model takes the atmospheric scattering and absorption into account (path radiance), correcting also the effects caused by the atmospheric transmittance, which has multiplicative influences on the image and directly changes the reflectance (Lu et al., 2002); but its utilization does not enhanced accuracy in *TSS* retrieval. In this study, the apparent reflectance procedure (TOA normalization) was used to correct and normalize the multi-temporal set of scenes. The great agreement obtained offers a potential tool that can be utilized for most of the DEIMOS-1 data applications. Notwithstanding, this assessment is not

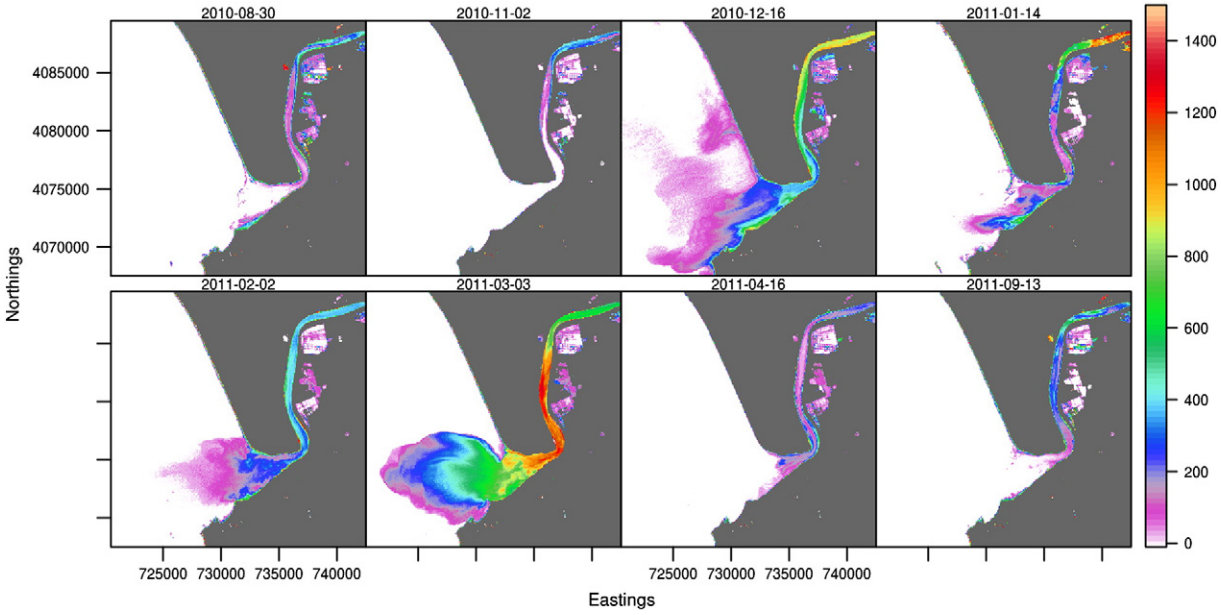

Fig. 4. *TSS* mapping (in mg L^{-1}) for all 8 DEIMOS-1 images analyzed.

related to which absolute atmospheric method provides the most accurate estimates of reflectance, but about the precision of how the radiometric measurements were set on a mutual relative scale to retrieve *TSS* maps.

The quality of DEIMOS-1 imagery appeared to be greatly improved by the atmospheric correction, which is indispensable in the establishment of highly significant, predictive models (Lavery, Pattiaratchi, Wyllie, & Hick, 1993). The estimates of ρ_w are not only useful for calculating the *TSS* concentration, but they can also be related to many oceanographic variables which are significant in studying the optical properties of sea water and the attenuation coefficients derived can be used to classify different water masses (Aranuvachapun & LeBlond, 1981; Jerlov, 1968). Further studies will be carried out to evaluate more complex ACP for improving the accuracy of surface reflectance values.

4.2. Algorithm development

We have shown that the DEIMOS-1 NIR band can be utilized to predict a wide range (100 to 1400 mg L^{-1}) of *TSS* concentrations in the surface waters of the Guadalquivir estuary (Eq. 5, Fig. 3). Satellite estimates of *TSS* by the semi-analytical algorithm achieved mean relative

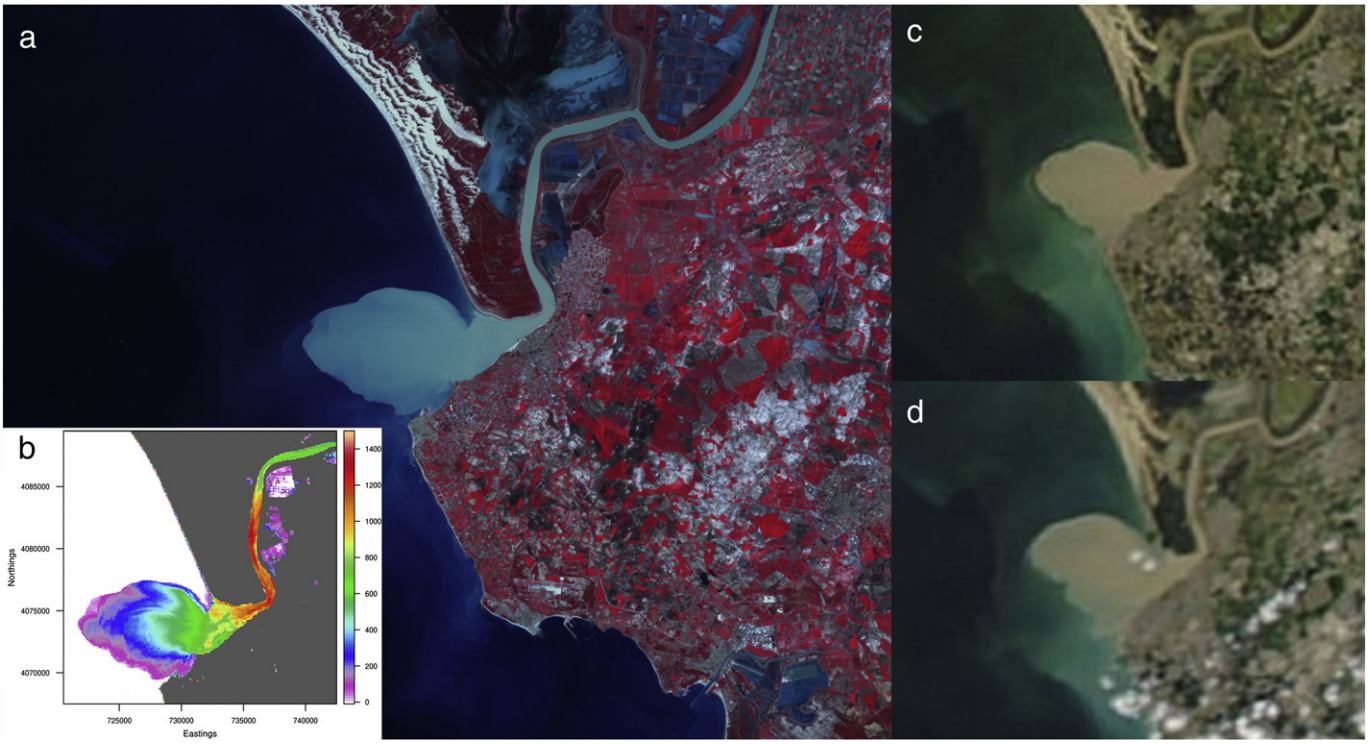

Fig. 5. a) Image of DEIMOS-1 RGB (10:59 GMT), b) map of *TSS* (mg L^{-1}), c) MODIS RGB TERRA (11:30 GMT) and d) AQUA (13:10 GMT) for the scene of 3 March 2011. MODIS images were downloaded from the National Aeronautics and Space Administration (NASA) server (http://lance-modis.eosdis.nasa.gov).

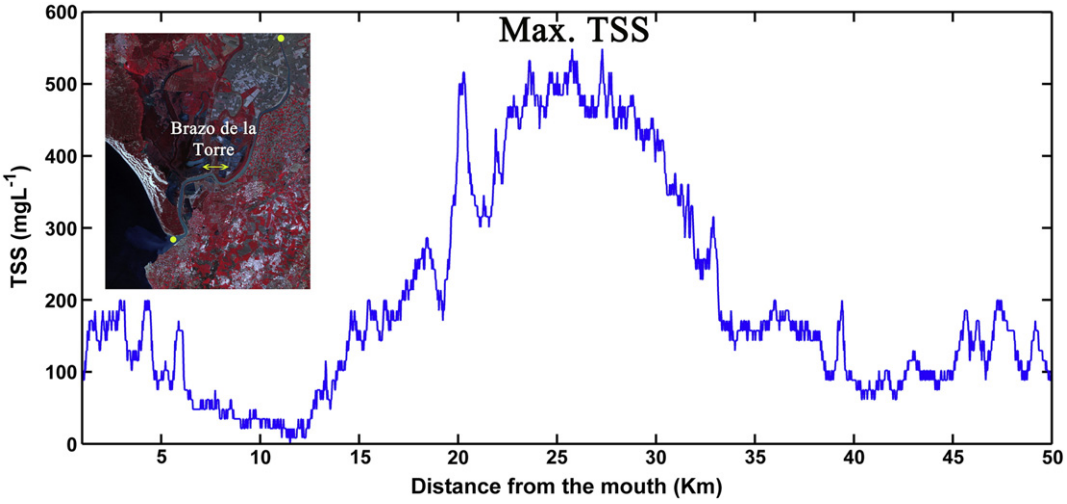

Fig. 6. *TSS* values along a longitudinal river transect of 50 km of image 16 April 2011. Yellow circles mark the beginning and end of the profile, and the arrow the situation of the maximum *TSS* concentration.

errors (ε_r) and coefficients of determination (r^2) of 25% and 0.86, respectively (see Table 3 and Supplementary data for additional results).

Applying our calibrated algorithm to images of the lower reaches of the Guadalquivir estuary and coastal zone for the full 8 scenes collected between 2010 and 2011 (Fig. 4) suggested that this *TSS* range was suitable for quantifying the typical temporal–spatial variation in the estuary. Hence, the routine application of DEIMOS-1 images for monitoring water quality and sediment export in large turbid estuaries seems promising.

The physical basis of the Nechad algorithm with its reduced number of calibration coefficients, provides a useful framework for the intercomparison of *TSS*–ρ_w relationships derived for different spectral bands and, importantly, between different sensors. This should contribute to the more effective use of the wide range of satellite platforms available, in routine monitoring of water quality in coastal zones.

Nevertheless, the calibration coefficients A^ρ and B^ρ derived in this study are quite different from those reported by Nechad at $\lambda = 830.0$ nm ($A^\rho = 2125.12$ mg L^{-1}, $B^\rho = 1.72$ mg L^{-1}). This discrepancy may be due to various reasons; 1) the Nechad et al. (2010) calibration was conducted using in-situ reflectance measurements, avoiding issues with atmospheric effects that are included in our $\rho_{w(TOA)}$ values, 2) the suspended sediment in the Guadalquivir region may have a different mass-specific backscatter coefficient compared to the North Sea, caused by distinct particle types, size, density and composition, and 3) the ranges of sediment concentrations considered were very different, with the Nechad et al. (2010) calibration focusing on values < 100 mg L^{-1}, hence statistical artifacts related to fitting non-linear relationships over different ranges may play a role. These issues mean that in practice true interoperability between sensor platforms and *TSS*–ρ_w relationships between different regions is still subject to limitations.

For high-spatial resolution sensors (such as Landsat, DEIMOS-1, SPOT, Quickbird and IKONOS), the lack of openly accessible, easy to use, ACPs effective for scenes including turbid coastal waters is an issue. Furthermore, the low data-resolution of NIR bands (generally designed for land operations) means differentiation of low sediment concentrations in coastal waters is often not possible. After the correction procedures, very little information was available in the NIR band below a value of 0.05–0.08 (corresponding to 1 *DN*). Similar information has been recovered in the work by Hu et al. (2000, 2004), showing the sensibility of Landsat-7 ETM + band 3 (630–690 nm) for aquatic scenes equal to a radiance value of 0.0635 mW cm^{-2} μm^{-1} sr^{-1} corresponding to 1 *DN*. Concerning this point, this feature restricts to some extent the applications of the sensors compared for example to the high MODIS sensibility. Nevertheless, whilst it is clear that DEIMOS-1 is likely to be unreliable for detecting lower TSS (<100 mg L^{-1}), for extremely turbid coastal regions, such as the Guadalquivir (Navarro & Ruiz, 2006), it may be a useful tool.

Theoretically the relationship between ρ_w and *TSS* is not linear (Ondrusek et al., 2012; Ritchie, Schiehe, & Cooper, 1989; Ritchie et al., 1990). This coupling is dependent on both wavelengths and *TSS* levels, meaning that signal saturation and decline of sensitivity of the green, red and NIR bands occurs at progressively higher particle concentrations (Shen et al., 2010). Hence the ρ_w at shorter wavebands is more sensitive to low *TSS* whilst at longer wavebands is more adequate to measure variations over turbid waters. These phenomena are partly responsible for the variety of algorithms using different regions of the electromagnetic spectrum available for quantifying surface water *TSS* (Baban, 1995; Carpenter & Carpenter, 1983; Chen et al., 2007; Hellweger et al., 2004; Hu et al., 2004; Miller & McKee, 2004; Ritchie & Cooper, 1988; Teodoro et al., 2008). Algorithms using the NIR bands tend to be more common in high turbidity water bodies (Doxaran et al., 2002; Mertes, Smith, & Adams, 1993; Ritchie et al., 1976; Wang, Lu, & Zhou, 2007), reducing large errors in *TSS* estimates but with the inconvenience of restricted sensitivity to low concentrations.

For the purpose of examining highly turbid estuaries such as the Guadalquivir, the NIR wavelengths are optimal for accurate *TSS* concentration quantifications. Primarily, in the NIR spectral range, pure water absorption is more significant and is better able to avoid events of radiance saturations compared to visible bands, which begin to saturate depending on the wavelength (Shen et al., 2010). The NIR band showed no signs of signal saturation at the moderate-elevated *TSS* values observed here, being more sensitive to variations in *TSS*. In addition, the contribution of CDOM and phytoplankton absorption is indeed negligible in the NIR bands, so in areas of high CDOM absorption as especially river plumes, it is necessary to choose a suitably wavelength for retrieval such that the pure water is the dominant absorbing component. Subsequently, with the NIR spectral range, a simplified relationship between ρ_w and the backscattering and absorption by *TSS* is produced and great CDOM absorption is not likely to be a problem (Doxaran et al., 2006; Nechad et al., 2010). In this sense, due to the aim of our work that is to develop an algorithm capable of quantifying *TSS* within the plume, the NIR band (755–906 nm) of DEIMOS-1 sensor corresponds to the best selection to appropriately and precisely retrieve *TSS* over the turbid waters of the Guadalquivir estuary.

For the quantification of low concentrations with green and red bands, a control of the noise signal should be performed to check if over clearer waters the estimation of accurate water-leaving reflectance from DEIMOS-1 is assessed with little noise associated, as it is also

important to analyze if the optical signature of other constituents and their variability (phytoplankton and CDOM) are no more negligible. Further work may allow the adoption of multi-band derivation of *TSS* in a wider range of coastal situations (i.e., in low to moderate turbidity systems). However, careful validation of region-specific *TSS* algorithms in other localities (types of Case II waters) with different combinations of water IOPs and concentration range is suggested to ensure their regular use for large scale synoptic monitoring of coastal zones achieving accurate retrieves.

4.3. TSS mapping

DEIMOS-1 NIR data (Eq. 5) showed a strong relationship with the location and spatial extent of the river plume in the Guadalquivir coastal region. Consistent plume patterns were recognized in the high spatial resolution *TSS* maps and also supported by true-color MODIS (TERRA and AQUA) and DEIMOS-1, showing particularly interesting features related to dynamics and transport processes. Sedimentary flows are predominant features in the estuary and move within the surface waters, and DEIMOS-1 data can be used to rapidly locate the *TSS* maximum, erosion and deposition areas. Moreover, the identification of the *TSS* gradients in the river may be very useful to characterize the spatial patterns of suspended sediments within the channel.

The intense resuspension events play a dominant role in determining the morphodynamic evolution of estuaries and lagoons (Volpe et al., 2011). The episodes with large surface plume coverage occur during the scene 3 March 2011 (Fig. 5) are coincident with high runoff rates and river discharge (Fig. 2 in Navarro et al., 2012). On the image, the circular patterns of the sediment plume are observed, presenting a well defined boundary and contoured plume with a peak around the mouth, then dissipate slowly with a rounded shape. The main gradients are sloping in the offshore direction, where the surface patterns seem to be oriented toward the west. During the intermediate regimes of the estuary, river flow, wind velocity, duration and direction as well as the tidal conditions could play a relevant role in the development and behavior of the plume.

On the other hand, dry seasons and negligible discharges from the dam are often associated with weak plume signals and low *TSS* mean records, presented in a narrow and minimum zone near the mouth as can be observed in the tidally-dominated situation on April 2011 image, also founded in Ondrusek et al. (2012). The inter-annual variability of the plumes in this region during the recent years may reveal the negative NAO phases and trace their influence on flood events, river discharges and coastal oceanography (Prieto et al., 2009). The study area is subject to inter-annual patterns associated with climatic oscillations that control turbidity and chlorophyll distributions and therefore, the fertilization of the Gulf of Cádiz. Hence, *TSS* values in this case can be used to highlight the potential interannual changes experienced within the estuary.

The imagery of 16 April 2011 was acquired during a period of low river flow and according to the hydrodynamic knowledge of the estuary it corresponds to a tidally-dominated regime (Díez-Minguito et al., 2012). The longitudinal section in Fig. 6 has revealed that the highest *TSS* concentrations are found along the channel and the maximum values would have been located between 20 km and 25 km from the mouth. These observations are in good agreement with previous tidal data and results are found in Díez-Minguito et al. (2012), showing that the longitudinal variation of the semi-diurnal harmonic constituents M2, S2 and N2 for the along-channel velocity presents a local maximum in the first stretch, especially in M2, approximately at km 20. Therefore, as can be observed in Fig. 6, the larger *TSS* coincide in position where semi-diurnal tide currents reach their maximum values. These outcomes are also consistent with the harmonic analysis carried out in the estuary (Navarro et al., 2012), particularly in the inner node, where turbidity patterns were associated to the tidal constituents of semidiurnal signals (M2 and S2 group the most energetic).

5. Conclusions

The DEIMOS-1 sensor has a strong potential for quantifying medium-scale spatio-temporal variations in *TSS* within large, turbid estuaries, such as the Guadalquivir. The potentially $\rho_w(NIR)$–*TSS* relationship presented here is a consequence of applying image-based atmospheric correction procedures, which can easily be used with DEIMOS-1. Whilst our aim was to provide estimates of *TSS* in very turbid waters, the NIR band was found to be a good indicator within the wide range of concentrations 100–1400 mg L^{-1} yielding accurate retrieves ($r^2 = 0.864$, $p < 0.001$, $\varepsilon_r = 25.411\%$, $n = 53$), but with the inconvenience of restricted sensitivity to low concentrations. Remote sensing of *TSS* can be used as part of the cost-effective management of coastal and transitional waters, e.g., in the application of the EU water framework directive. Furthermore, synoptic views of *TSS* may successfully provide important and unique information for applications such as hydrodynamic modeling of coastal zones. Hence, these data will present challenges to researchers establishing a valuable tool that will complement a wide variety of regional monitoring programs contributing to the understanding of coastal environments.

Acknowledgments

We thank the DEIMOS Imaging for distributing the DEIMOS-1 data used in this study. We would like to gratefully thank the free meteorological and oceanographic data of the Agencia Andaluza del Medio Ambiente y Agua, Agroclimatic Station network, Wunderground and Puertos del Estado. The authors also wish to thank Antonio Moreno for the assistance during the cruises and to María Ferrer for the help in the laboratory. The authors would like to thank the anonymous reviewers for their suggestions that have significantly improved the manuscript. Isabel Caballero is supported by a grant from the Junta de Andalucía PhD fellowship program. EPM is supported by a contract (JAE DOCTORES 2010) co-funded by the CSIC and the European Social Fund (ESF2007-2013). This research was supported by the projects P09-RNM-4853, 049/2010 and DMI-COR-LTR753-S funded by the Regional Government of Andalucia, the Spanish Ministry for Agriculture, Food and Environment and DEIMOS company, respectively.

Appendix A. Supplementary data

Cross-validation and Atmospheric Correction Procedures. Supplementary data associated with this article can be found in the online version, at http://dx.doi.org/10.1016/j.rse.2013.08.047. These data include Google maps of the most important areas described in this article.

References

Alparslan, E., Aydöner, C., Tufekci, V., & Tüfekci, H. (2007). Water quality assessment at Ömerli Dam using remote sensing techniques. *Environmental Monitoring and Assessment*, *135*(1–3), 391–398.

Aranuvachapun, S., & LeBlond, P. H. (1981). Turbidity of coastal water determined from Landsat. *Remote Sensing of Environment*, *11*, 113–132.

Baban, S. M. J. (1993). Detecting water quality parameters in Norfolk Broads, UK., using Landsat imagery. *International Journal of Remote Sensing*, *14*, 1247–1267.

Baban, S. M. J. (1995). The use of Landsat imagery to map fluvial sediment discharge into coastal waters. *Marine Geology*, *123*(3–4), 263–270.

Baban, S. M. J. (1997). Environmental Monitoring of estuaries; estimating and mapping various environmental indicators in Breydon Water Estuary, U.K., using Landsat TM imagery. *Estuarine, Coastal and Shelf Science*, *44*, 589–598.

Bricaud, A., & Morel, A. (1987). Atmospheric corrections and interpretation of marine radiances in CZCS imagery: Use of a reflectance model. *Oceanologica Acta, SP*, *7*, 33–50.

Bustamante, J., Pacios, F., Díaz-Delgado, R., & Aragonés, D. (2009). Predictive models of turbidity and water depth in the Doñana marshes using Landsat TM and ETM+ images. *Journal of Environmental Management*, *90*, 2219–2225.

Caballero, I., Morris, E. P., & Navarro, G. (2012). DEIMOS-1 satellite provides imagery for coastal management. *Sea Technology*, *53*(2), 10–13.

Carpenter, D. J., & Carpenter, S. M. (1983). Modeling inland water quality using Landsat data. *Remote Sensing of Environment*, *13*(4), 345–352.

Chavez, P.S., Jr. (1988). An improved dark-object subtraction technique for atmospheric scattering correction of multispectral data. *Remote Sensing of Environment*, *24*, 459–479.

Chavez, P.S., Jr. (1989). Radiometric calibration of Landsat Thematic Mapper multispectral images. *Photogrammetric Engineering and Remote Sensing*, *55*, 1285–1294.

Chavez, P.S., Jr. (1996). Image-based atmospheric corrections—Revisited and improved. *Photogrammetric Engineering and Remote Sensing*, *62*, 1025–1036.

Chen, T., Hu, C., & Muller-Karger, F. (2007). Monitoring turbidity in Tampa Bay using MODIS/Aqua 250-m imagery. *Remote Sensing of Environment*, *109*, 207–220.

Chen, X., Li, Y., Liu, Z., Yin, K., Li, Z., Wai, O., et al. (2004). Integration of multi-source data for water quality classification in the Pearl River estuary and its adjacent coastal waters of Hong Kong. *Continental Shelf Research*, *24*, 1827–1843.

Crowley, G. (2010). *DMC Data Product Manual. 0115056, 02.* UK: DMC International Imaging Ltd.

Development Core Team, R. (2011). *R: A language and environment for statistical computing.* Vienna, Austria: R Foundation for Statistical Computing. 3-900051-07-0.

Díez-Minguito, M., Baquerizo, A., Ortega-Sánchez, M., Navarro, G., & Losada, M.A. (2012). Tide transformation in the Guadalquivir estuary (SW Spain) and process-based zonation. *Journal of Geophysical Research*, *117* (C03019, 14 pp.).

Doxaran, D., Cherukuru, N., & Lavender, S. J. (2006). Apparent and inherent optical properties of turbid estuarine waters: Measurements, empirical quantification relationships, and modeling. *Applied Optics*, *45*(10), 2310–2324.

Doxaran, D., Froidefond, J. M., Lavenderb, S., & Castainga, P. (2002). Spectral signature of highly turbid waters. Application with SPOT data to quantify suspended particulate matter concentrations. *Remote Sensing of Environment*, *81*, 149–161.

D'Sa, E. J., Hu, C., Muller-Karger, F. E., & Carder, K. L. (2002). Estimation of colored dissolved organic matter and salinity fields in case 2 waters using SeaWiFS: Examples from Florida Bay and Florida Shelf. *Proceedings of the Indian Academy of Science*, *111*(3), 197–207.

Fraser, R. S., Ferraze, R. A., Kaufman, Y. J., Markham, B.L., & Mattoo, S. (1992). Algorithm for atmospheric correction of aircraft and satellite imagery. *International Journal of Remote Sensing*, *13*, 541–557.

Gordon, H. R., & Morel, A. Y. (1983). *Remote assessment of ocean color for interpretation of satellite visible imagery.* New York: Springer-Verlag.

Goslee, S.C. (2011). Analyzing remote sensing data in R: The landsat package. *Journal of Statistical Software*, *43*(4), 1–25.

Hall, F. G., Strebel, D. E., Nickson, J. E., & Geotz, S. J. (1991). Radiometric rectification toward a common radiometric response among multidate, multisensor images. *Remote Sensing of Environment*, *35*, 11–27.

Hellweger, F. L., Schlosser, P., Lall, U., & Weissel, J. K. (2004). Use of satellite imagery for water quality studies in New York Harbor. *Estuarine, Coastal and Shelf Science*, *61*(3), 437–448.

Hijmans, R. J., & Etten, J. (2011). *raster: Geographic analysis and modeling with raster data.* R package version 2.0-12 (http://CRAN.R-project.org/package=raster)

Hu, C., Carder, K. L., & Muller-Karger, F. E. (2000). Atmospheric correction of SeaWiFS imagery over turbid coastal waters: A practical method. *Remote Sensing of Environment*, *74*, 195–206.

Hu, C., Chen, Z., Clayton, T., Swarzenski, P., Brock, J., & Muller-Karger, F. (2004). Assessment of estuarine water-quality indicators using MODIS medium-resolution bands: Initial results from Tampa Bay, FL. *Remote Sensing of Environment*, *93*, 423–441.

Jerlov, N. G. (1968). *Optical oceanography.* New York: Elsevier.

Jerlov, N. G. (1976). *Marine optics.* New York: Elsevier.

Kirk, J. T. O. (1983). *Light and photosynthesis in aquatic ecosystems.* Cambridge, United Kingdom: Cambridge University Press.

Lavery, P., Pattiaratchi, C., Wyllie, A., & Hick, P. (1993). Water quality monitoring in estuarine waters using the Landsat Thematic Mapper. *Remote Sensing of Environment*, *3*, 268–280.

Lu, D., Mausel, P., Brondizio, E., & Moran, E. (2002). Assessment of atmospheric correction methods for Landsat TM data applicable to Amazon basin LBA research. *International Journal of Remote Sensing*, *23*(13), 2651.2671.

Martin, J. M., & Windom, H. L. (1991). Present and future roles of ocean margins in regulating marine biogeochemical cycles of trace elements. In R. F. C. Mantoura (Ed.), *Ocean margin processes in global change* (pp. 45–67). New York: Wiley.

May, C. L., Koseff, J. R., Lucas, L. V., Cloern, J. E., & Schoellhamer, D. H. (2003). Effects of spatial and temporal variability of turbidity on phytoplankton blooms. *Marine Ecology Progress Series*, *254*, 111–128.

Mayer, L. M., Keil, R. G., Macko, S. A., Joye, S. B., Ruttenberg, K. C., & Aller, R. C. (1998). The importance of suspended particulates in riverine delivery of bioavailable nitrogen to coastal zones. *Global Biogeochemical Cycles*, *12*, 573–579.

McFeeters, S. K. (1996). The use of the Normalized Difference Water Index (NDWI) in the delineation of open water features. *International Journal of Remote Sensing*, *17*(7), 1425–1432.

Mertes, L. A. K., Smith, M.O., & Adams, J. B. (1993). Estimating suspended sediment concentrations in surface waters of the Amazon River wetlands from Landsat Images. *Remote Sensing of Environment*, *43*, 281–301.

Miller, R. L., & McKee, B.A. (2004). Using MODIS Terra 250 m imagery to map concentrations of total suspended matter in coastal waters. *Remote Sensing of Environment*, *93*, 259–266.

Milton, E. J. (1994). Teaching atmospheric correction using a spreadsheet. *Photogrammetric Engineering and Remote Sensing*, *60*, 751–754.

Mobley, C. D. (2004). *Light and water—Radiative transfer in natural waters* (CD ed.).

Moran, M. S., Jackson, D., Slate, P. N., & Teillet, P.M. (1992). Evaluation of simplified procedures for retrieval of land surface reflectance factors from satellite sensor output. *Remote Sensing of Environment*, *41*, 169–184.

Morel, A., & Prieur, L. (1977). Analysis of variation in ocean color. *Limnology and Oceanography*, *22*, 709–722.

Navarro, G., Gutiérrez, F. J., Díez-Minguito, M., Losada, M.A., & Ruiz, J. (2011). Temporal and spatial variability in the Guadalquivir estuary: A challenge for a real-time telemetry. *Ocean Dynamics*, *61*(6), 753–765.

Navarro, G., Huertas, I. E., Costas, E., Flecha, S., Díez-Minguito, M., Caballero, I., et al. (2012). Use of a real-time remote monitoring network (RTRM) to characterize the Guadalquivir estuary (Spain). *Sensors*, *12*(2), 1398–1421.

Navarro, G., & Ruiz, J. (2006). Spatial and temporal variability of phytoplankton in the Gulf of Cádiz through remote sensing images. *Deep-Sea Research II*, *53*, 1241–1260.

Nechad, B., Ruddick, K. G., & Park, Y. (2010). Calibration and validation of a generic multisensor algorithm for mapping of total suspended matter in turbid waters. *Remote Sensing of Environment*, *114*, 854–866.

Nezlin, N.P., DiGiacomo, P.M., Stein, E. D., & Ackerman, D. (2005). Stormwater runoff plumes observed by SeaWIFS radiometer in the Southern California Bight. *Remote Sensing of Environment*, *98*, 494–510.

Ondrusek, M., Stengel, E., Kinkade, C. S., Vogel, R. L., Keegstra, P., Hunter, C., et al. (2012). The development of a new optical total suspended matter algorithm for the Chesapeake Bay. *Remote Sensing of Environment*, *119*, 243–254.

Picard, R., & Cook, D. (1984). Cross-Validation of Regression Models. *Journal of the American Statistical Association*, *79*(387), 575–583.

Prandle, D. (2009). *Estuaries: Dynamics, mixing, sedimentation and morphology.* University of Liverpool, Cambridge University Press.

Prieto, L., Navarro, G., Rodríguez-Gálvez, S., Huertas, I. E., Naranjo, J. M., & Ruiz, J. (2009). Oceanographic and meteorological forcing of the pelagic ecosystem on the Gulf of Cádiz shelf (SW Iberian Peninsula). *Continental Shelf Research*, *29*, 2122–2137.

Ritchie, J. C., & Cooper, C. M. (1988). Comparison of measured suspended sediment concentrations with suspended sediment concentrations estimated from Landsat MSS data. *International Journal of Remote Sensing*, *9*, 379–387.

Ritchie, J. C., Cooper, C. M., & Schiebe, F. R. (1990). The relationship of MSS and TM digital data with suspended sediments, chlorophyll, and temperature in Moon lake, Mississippi. *Remote Sensing of Environment*, *33*, 137–148.

Ritchie, J. C., Schiebe, F. R., & McHenry, J. R. (1976). Remote sensing of suspended sediment in surface water. *Photogrammetric Engineering and Remote Sensing*, *42*, 1539–1545.

Ritchie, J. C., Schiehe, F. R., & Cooper, C. M. (1989). Landsat digital data for estimating suspended sediment in inland water. *International Association of Hydrological Sciences*, *182*, 151–158.

Ritchie, J. C., Zimba, P. V., & Everitt, J. A. (2003). Remote sensing techniques to assess water quality. *Photogrammetric Engineering and Remote Sensing*, *69*, 69–704.

Ruiz, J., González-Quirós, R., Prieto, L., & Navarro, G. (2009). A Bayesian model for anchovy: The combined pressure of man and environment. *Fisheries Oceanography*, *18*, 62–76.

Saldías, G. S., Sobarzo, M., Largier, J., Moffat, C., & Letelier, R. (2012). Seasonal variability of turbid river plumes off central Chile based on high-resolution MODIS imagery. *Remote Sensing of Environment*, *123*, 220–233.

Schlerf, M., Atzberger, C., & Hill, J. (2005). Remote sensing of forest biophysical variables using HyMap imaging spectrometer data. *Remote Sensing of Environment*, *95*(2), 177–194.

Schott, J. R., Salvaggio, C., & Volchok, W. J. (1988). Radiometric scene normalization using pseudoinvariant features. *Remote Sensing of Environment*, *26*, 1–26.

Shen, F., Salama, M., Zhou, Y., Li, J., Su, Z., & Kuang, D. (2010). Remote-sensing reflectance characteristics of highly turbid estuarine waters – a comparative experiment of the Yangtze River and the Yellow River. *International Journal of Remote Sensing*, *31*(10), 2639–2654.

Song, C., Woodcock, C. E., Seto, K. C., Lenney, M. P., & Macomber, S. A. (2001). Classification and change detection using Landsat TM data: When and how to correct atmospheric effects? *Remote Sensing of Environment*, *75*, 230–244.

Stumpf, R. P., & Pennock, J. R. (1989). Calibration of a general optical equation for remote sensing of suspended sediments in a moderately turbid estuary. *Journal of Geophysical Research*, *94*(C10), 363–371 (14).

Tassan, S. (1994). Local algorithms using SeaWiFS data for the retrieval of phytoplankton, pigments, suspended sediment, and yellow substance in coastal waters. *Applied Optics*, *33*(12), 2369–2378.

Teodoro, A.C., Veloso-Gomes, F., & Gonsalves, H. (2008). Statistical techniques for correlating total suspended matter concentration with seawater reflectance using multispectral satellite data. *Journal of Coastal Research*, *24*, 40–49.

Vanney, J. R. (1970). *L' Hydrologie du bass Guadalquivir.* Madrid: C.S.I.C.

Volpe, V., Silvestri, S., & Marani, M. (2011). Remote sensing retrieval of suspended sediment concentration in shallow waters. *Remote Sensing of Environment*, *115*, 44–54.

Wang, H. Q., Hladik, C. M., Huang, W. R., Milla, K., Edmiston, L., Harwell, M.A., et al. (2010). Detecting the spatial and temporal variability of chlorophyll—A concentration and total suspended solids in Apalachicola Bay, Florida using MODIS imagery. *International Journal of Remote Sensing*, *31*(2), 1366–5901.

Wang, J., Lu, X., & Zhou, Y. (2007). Retrieval of suspended sediment concentrations in the turbid water of the Upper Yangtze River using Landsat ETM+. *Chinese Science Bulletin*, *52*(II), 273–280.

Warrick, J. A., Mertes, L. A. K., Washburn, L., & Siegel, D. A. (2004). A conceptual model for river water and sediment dispersal in the Santa Barbara Channel, California. *Continental Shelf Research*, *24*(17), 2029–2043.

Wolanski, E., & McLusky, D. (2011). *Treatise on estuarine and coastal science.* Amsterdam: Elsevier Inc978-0-08-087885-0.

Zhang, Y., Pulliainen, J., Koponen, S., & Hallikainen, M. (2002). Application of an empirical neural network to surface water quality estimation in the Gulf of Finland using combined optical data and microwave data. *Remote Sensing of Environment*, *81*, 327–336.

Assessment of suspended solids in the Guadalquivir estuary using new DEIMOS-1 medium spatial resolution imagery

Isabel Caballero, Edward P. Morris, Javier Ruiz and Gabriel Navarro

Supplementary Data: Cross-validation and Atmospheric Correction Procedures

Departamento de Ecología y Gestión Costera, Instituto de Ciencias Marinas de Andalucía, ICMAN-CSIC, Puerto Real, 11519, Cádiz, Spain, Pho: +34 956832612; *isabel.caballero@icman.csic.es*

This Supplementary Data presents the methodology and results to calibrate the based-reflectance model using the cross-validation procedure (random sub-sampling) with the water-leaving reflectances (ρ_w) (NIR band). To reduce variability, multiple rounds (k) of cross-validation were accomplished using different partitions (40 and 12 samples for the training and testing datasets, respectively). A 100-k random sub-sampling was developed regarding the finite number of observations (n = 53). The error rates or predictive accuracy on the different iterations were averaged to yield an overall error rate, or predictive accuracy. The mean root mean squared error (*RMSE*), coefficient of determination (r^2), and mean relative error (ε_r) were computed to evaluate the performance of the based-reflectance algorithm (see equations below). This technique was applied to the products derived from the schemes of apparent reflectance ($\rho_{w(TOA)}$), DOS model ($\rho_{w(DOS)}$) and COSTZ model ($\rho_{w(COSTZ)}$) to assess *TSS* accuracy. Initially, the random sub-sampling was used with reflectances determined with the apparent reflectance correction. Fig. S1 gives details of the statistic indicators of the 100 separate estimates for the cross-validation scheme using the top of atmosphere reflectance ($\rho_{w(TOA)}$).

$$RMSE = \sqrt{\frac{1}{N}\sum_{i=1}^{N}\left(\mathrm{TSS}_i^{\mathrm{satellite}} - \mathrm{TSS}_i^{\mathrm{in-situ}}\right)^2}$$

$$\varepsilon_r = \frac{1}{N}\sum_{i=1}^{N}\frac{\left[\mathrm{TSS}_i^{\mathrm{in-situ}} - \mathrm{TSS}_i^{\mathrm{satellite}}\right]}{\mathrm{TSS}_i^{\mathrm{in-situ}}}$$

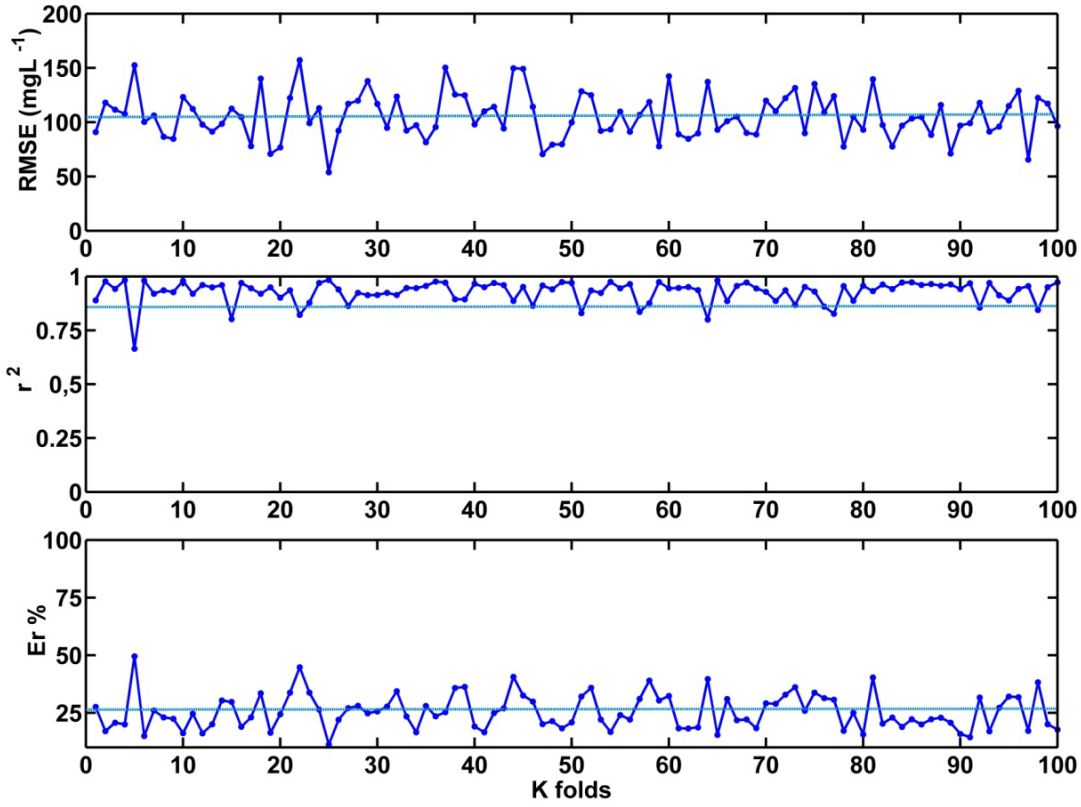

Figure S1. *RMSE*, r^2 and ε_r values for each of the 100 *k*-folds splits; dashed lines correspond to the averaged estimates for the total 100 folds (*RMSE* = 105.630 mgL^{-1}, ε_r = 25.411 % and r^2 = 0.864, $p < 0.001$).

Figure S2 to S6 show the histograms of both calibration parameters (A^{ρ} and B^{ρ}), and the statistics obtained (*RMSE,* r^2 and ε_r) for the 100 iterations. The coefficients and *RMSE* get close to a normally distribution.

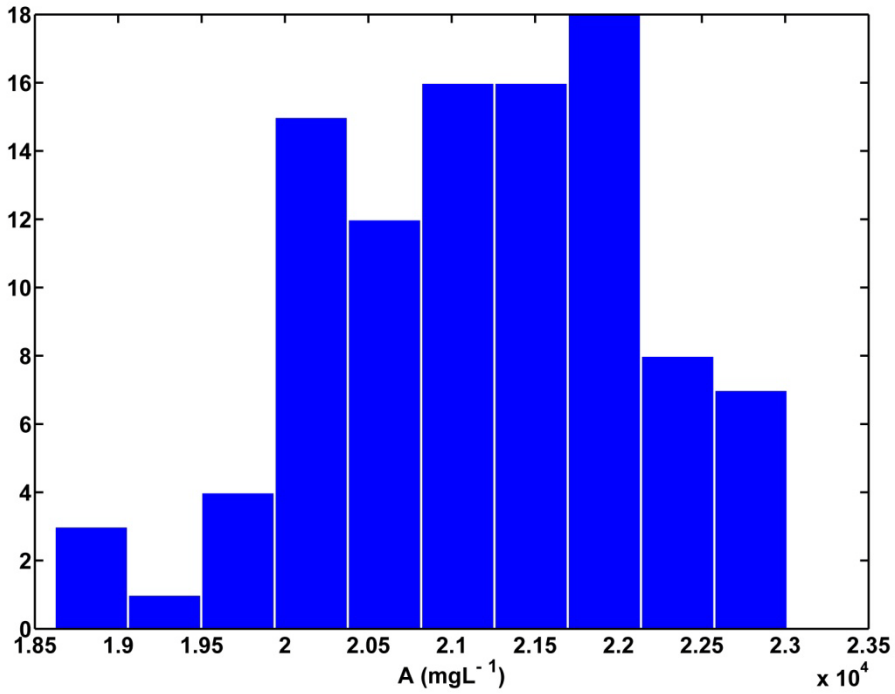

Figure S2. Histogram of parameter A^{ρ} from the 100-*k* folds cross-validation (mgL^{-1}).

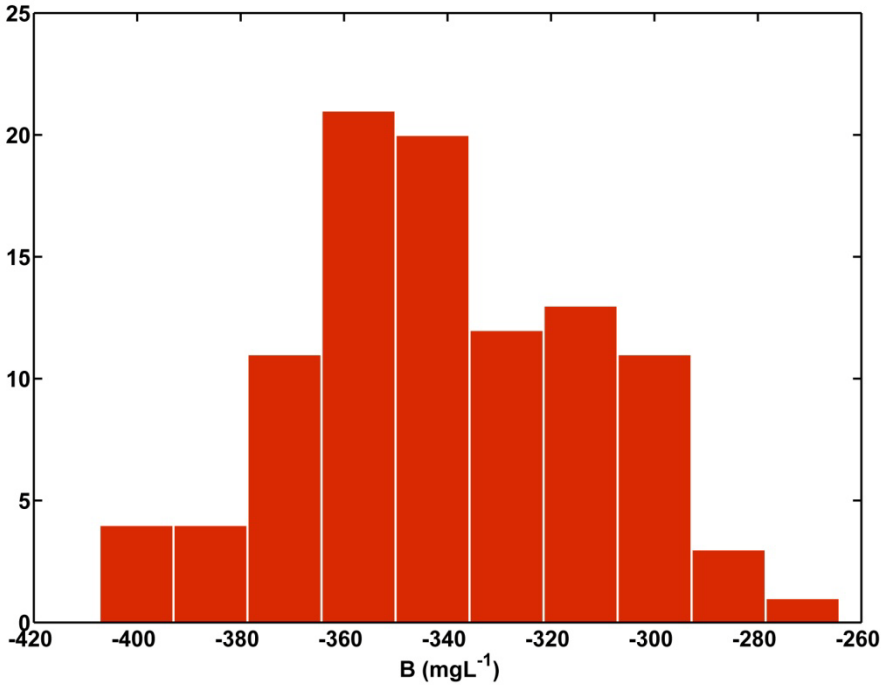

Figure S3. Histogram of parameter B^{ρ} from the 100-*k* folds cross-validation (mgL^{-1}).

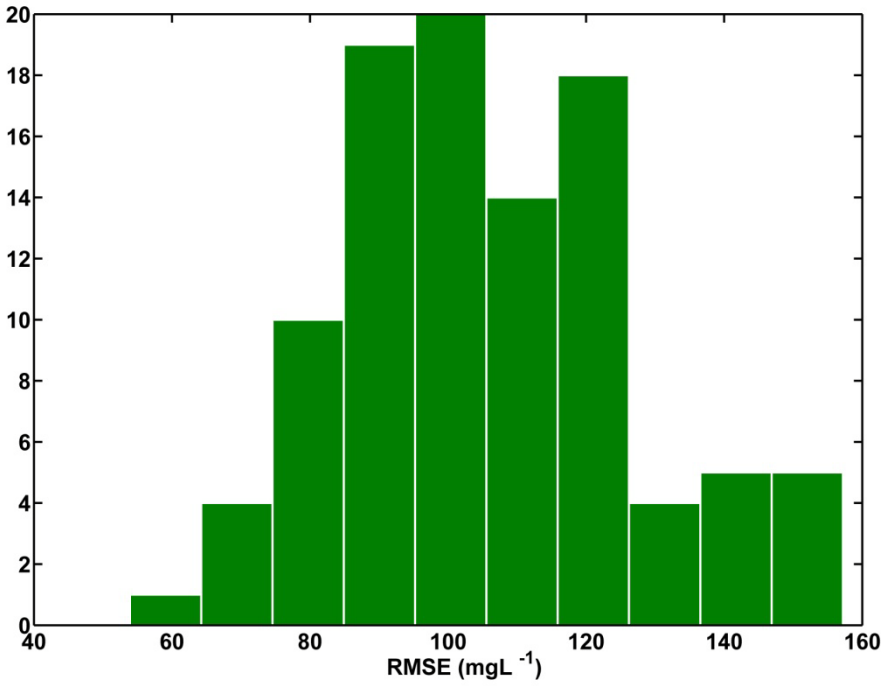

Figure S4. Histogram of parameter *RMSE* from the 100-*k* folds cross-validation (mgL^{-1}).

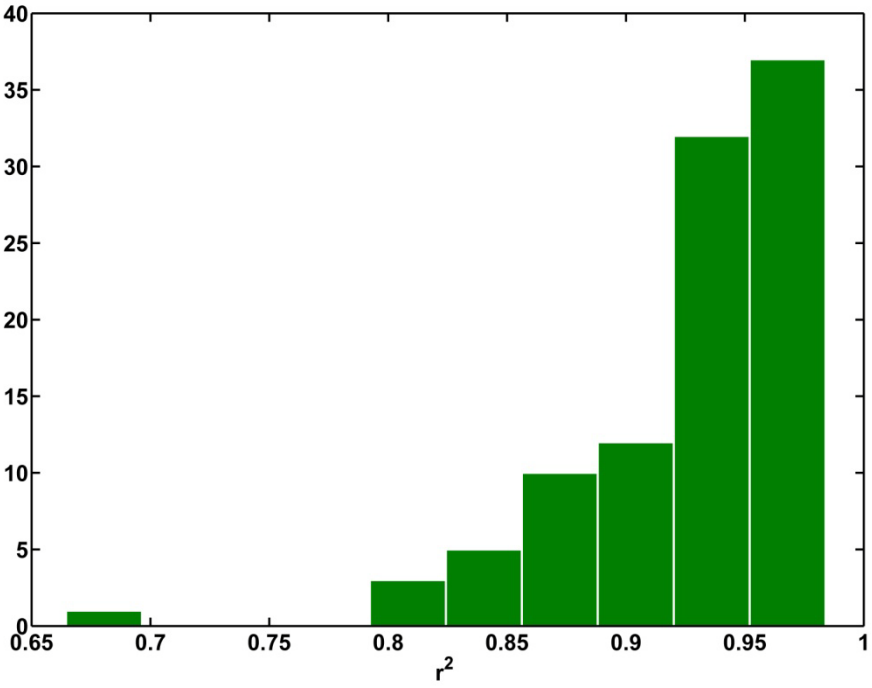

Figure S5. Histogram of parameter r^2 from the 100-*k* folds cross-validation (mgL^{-1}).

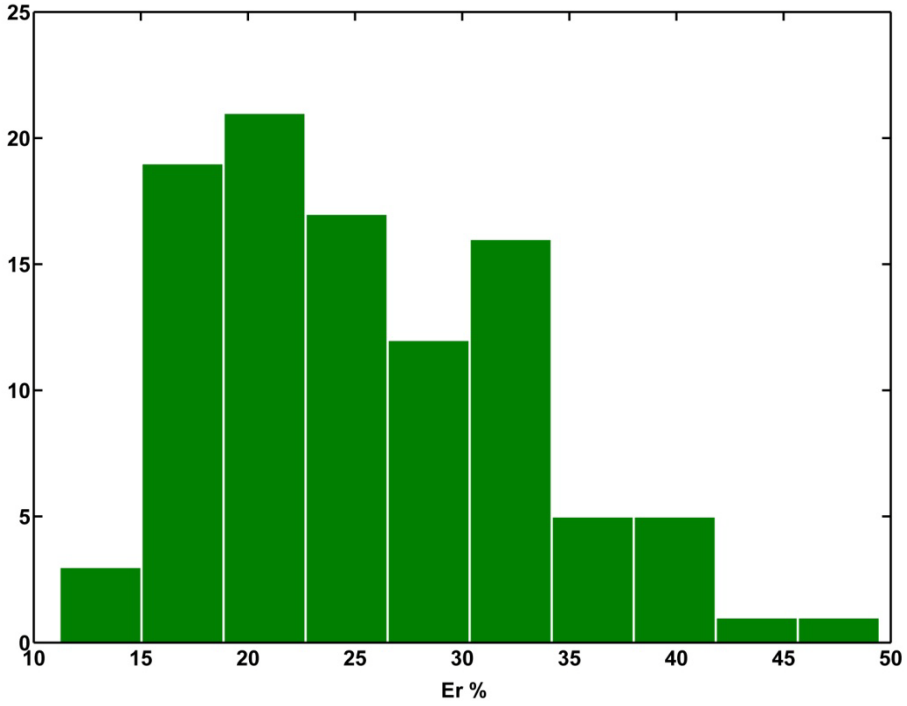

Figure S6. Histogram of parameter ε_r from the 100-*k* folds cross-validation (%).

Moreover, an attempt is made to analyze the sensitivity of the procedure in order to estimate the errors and differences in the cross-validation outcomes using different *k*-folds for the TOA reflectances ($\rho_{w(TOA)}$). According, we have evaluated the random sub-sampling for a major number of iterations, in this case $k = 200$, to compare against the results obtained with the 100 splits. As indicated by the resulting estimates (Table S1), the differences are very small with respect to the 200 splits, regarding a discrepancy of *RMSE* (2,104 mgL^{-1}), r^2 (-0.003) and ε_r (0.311 %) in the mean rates. Taking into account the slight variations of the statistics, errors in the derived reflectance and *TSS* are not significant for the different number of *k*-folds iterations (mean relative error of 25.411 % and 25.100 % for 100 and 200 *k*-folds, respectively), henceforth the procedure was defined for 100 *k*-folds to fix the predictive accuracy of the model.

Table S1. Cross-validation results of *RMSE* (mgL^{-1}), r^2 and ε_r (%) for both 100 and 200 *k*-folds random sub-sampling.

Statistic	**100 *k*-folds**	**200 *k*-folds**
Mean *RMSE*	**105.630**	**103.526**
Min *RMSE*	53.909	53.034
Max *RMSE*	157.200	157.200
Mean r^2	**0.864**	**0.868**
Min r^2	0.442	0.442
Max r^2	0.968	0.975
Mean ε_r	**25.411**	**25.100**
Min ε_r	11.204	10.500
Max ε_r	49.491	48.000

A similar cross-validation procedure is performed to estimate the errors in the derived *TSS* resulting from the DOS and COSTZ water-leaving reflectances ($\rho_{w(DOS)}$ and $\rho_{w(COSTZ)}$, respectively). The based-reflectance algorithm was tested through the 100-*k* random sub-sampling to account for *TSS* precision. Figure S7 and S8 illustrate the values of *RMSE* (mgL^{-1}), r^2 and ε_r (%) for each iteration of the cross-validation with DOS and COSTZ approaches, respectively. Table S2 lists the computed mean, minimum and maximum *RMSE* (mgL^{-1}), r^2 and ε_r (%) for the ρ_w after DOS and COSTZ models. Figure S9 and S10 illustrate the histograms of calibration parameters (A^ρ and B^ρ), *RMSE,* r^2 and ε_r for the 100 iterations of DOS and COSTZ schemes, respectively. Figure S11 and S12 show the robust non-linear regression of the datasets from DOS and COSTZ approaches. The definitive calibration parameters were calculated with the entire 53 samples to establish the model performance:

DOS: $A^\rho = 18890.02$ (mgL^{-1}) and $B^\rho = -198.18$ (mgL^{-1})

COSTZ: $A^\rho = 4868.45$ (mgL^{-1}) and $B^\rho = -97.13$ (mgL^{-1})

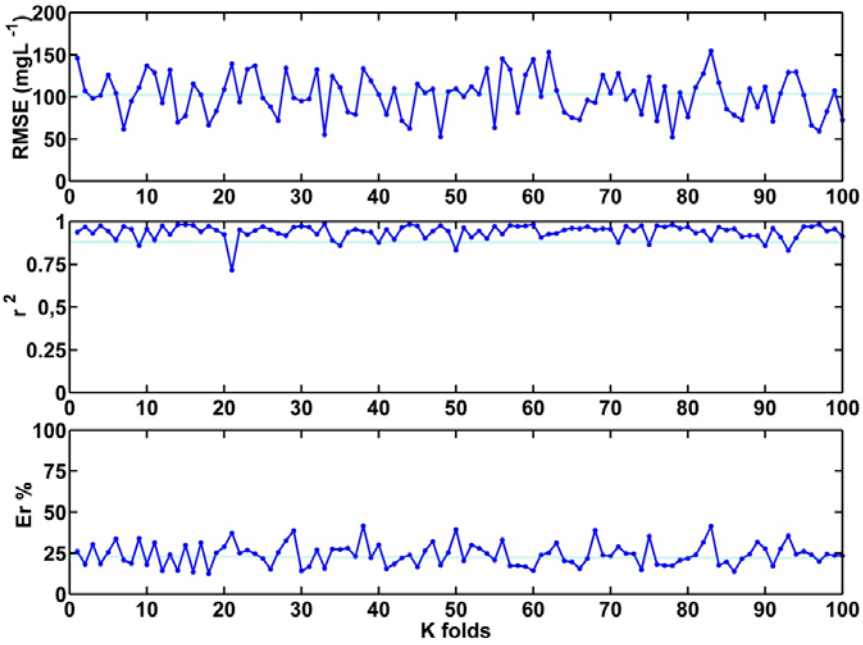

Figure S7. *RMSE*, r^2 and ε_r values for each of the 100 *k*-folds splits (DOS approach); dashed lines correspond to the averaged estimates for the total 100 folds (*RMSE* = 102.020 mgL^{-1}, ε_r = 24.173 % and r^2 = 0.881, $p < 0.001$).

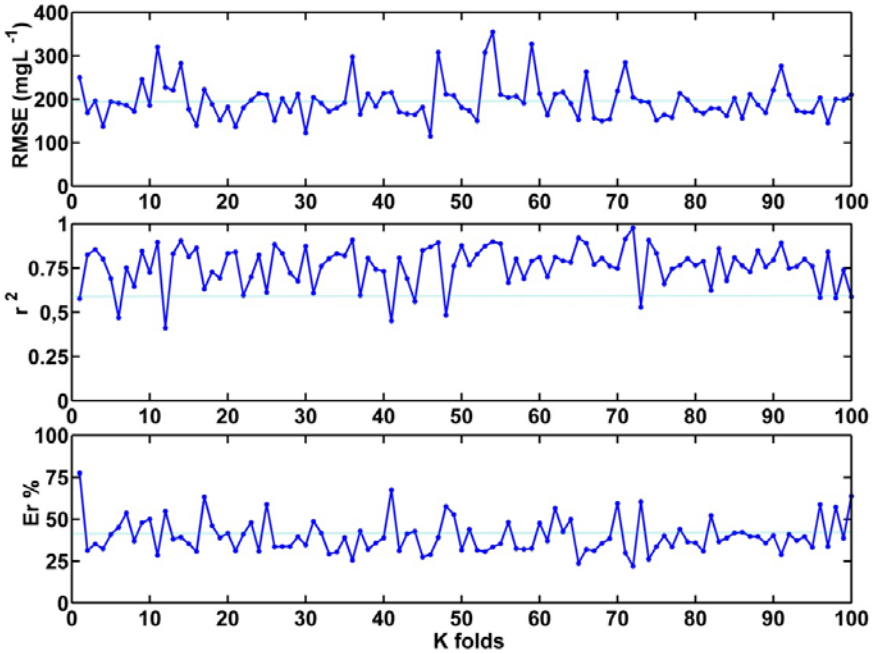

Figure S8. *RMSE*, r^2 and ε_r values for each of the 100 *k*-folds splits (COSTZ approach); dashed lines correspond to the averaged estimates for the total 100 folds (*RMSE* = 197.128 mgL^{-1}, ε_r = 39.963 % and r^2 = 0.591, $p < 0.001$).

Table S2. Cross-validation results of *RMSE* (mgL^{-1}), r^2 and ε_r (%) for both DOS and COSTZ models (100-*k* random sub-sampling).

Statistic	**DOS**	**COSTZ**
Mean *RMSE*	**102.020**	**197.128**
Min *RMSE*	52.066	114.991
Max *RMSE*	154.718	355.254
Mean r^2	**0.881**	**0.591**
Min r^2	0.510	0.169
Max r^2	0.971	0.955
Mean ε_r	**24.173**	**39.963**
Min ε_r	12.408	21.889
Max ε_r	41.637	77.408

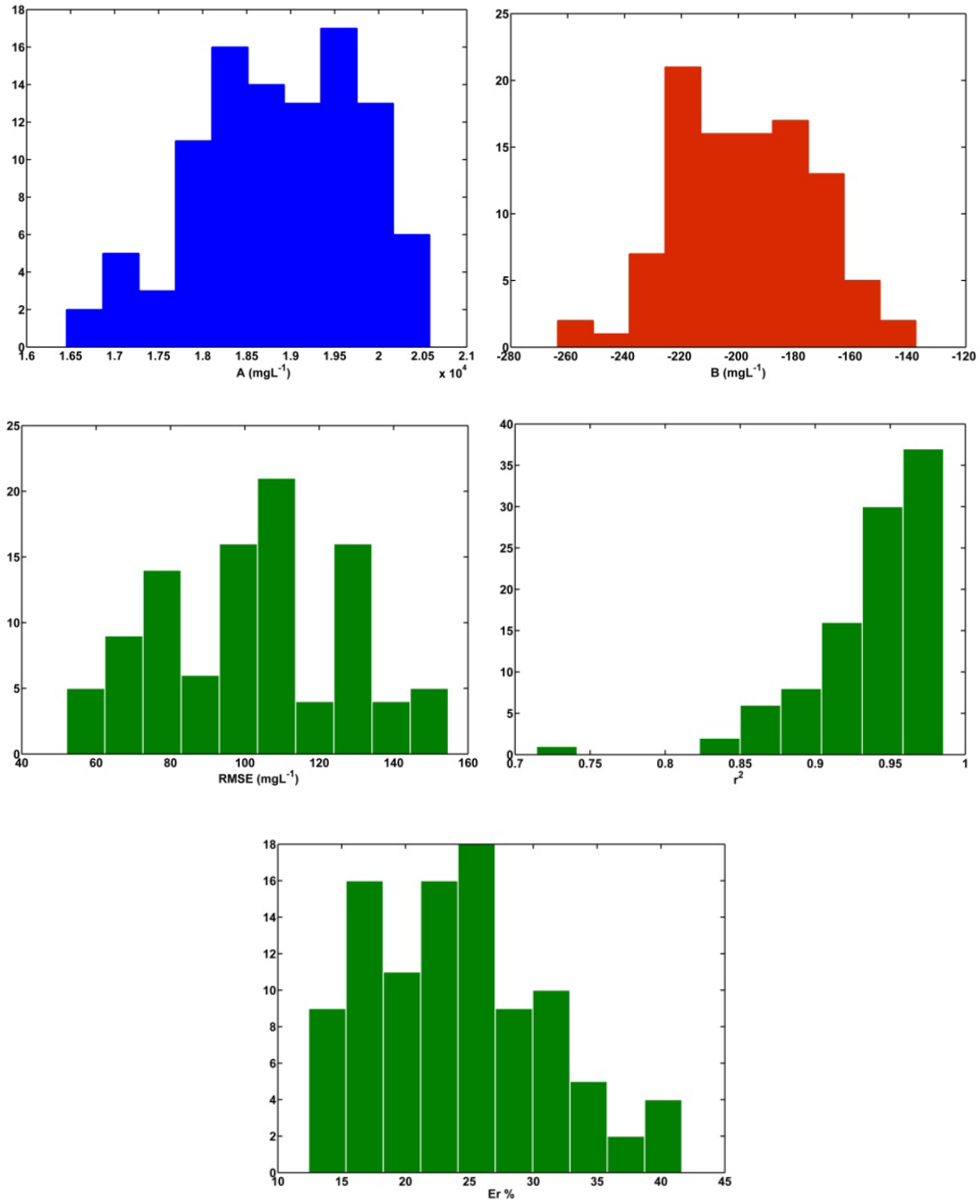

Figure S9. Histograms of parameters A^o (mgL^{-1}), B^o (mgL^{-1}), *RMSE* (mgL^{-1}), r^2 and ε_r (%) from the 100-*k* folds cross-validation (DOS model).

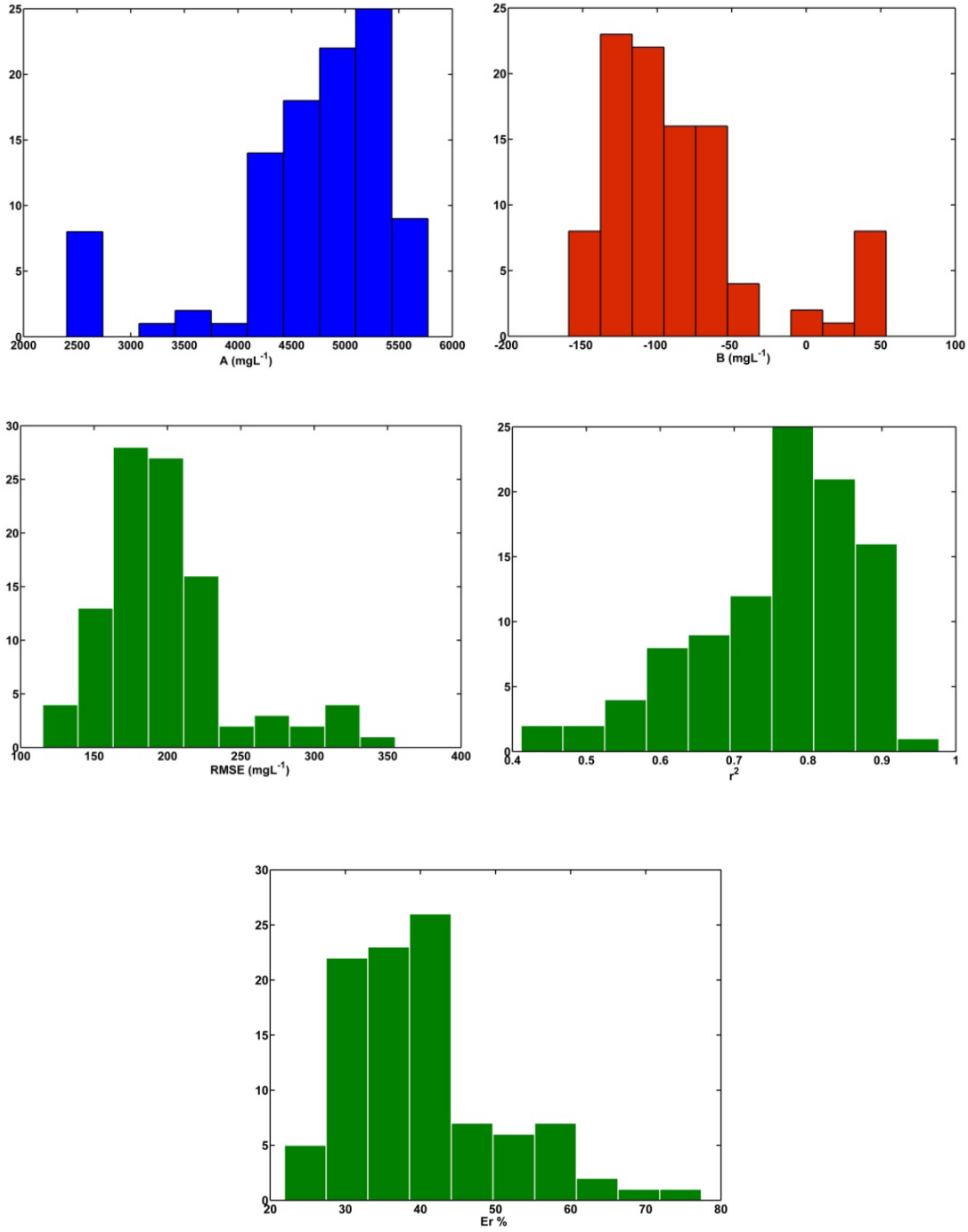

Figure S10. Histograms of parameters A^{ρ} (mgL^{-1}), B^{ρ} (mgL^{-1}), *RMSE* (mgL^{-1}), r^2 and ε_r (%) from the 100-*k* folds cross-validation (COSTZ model).

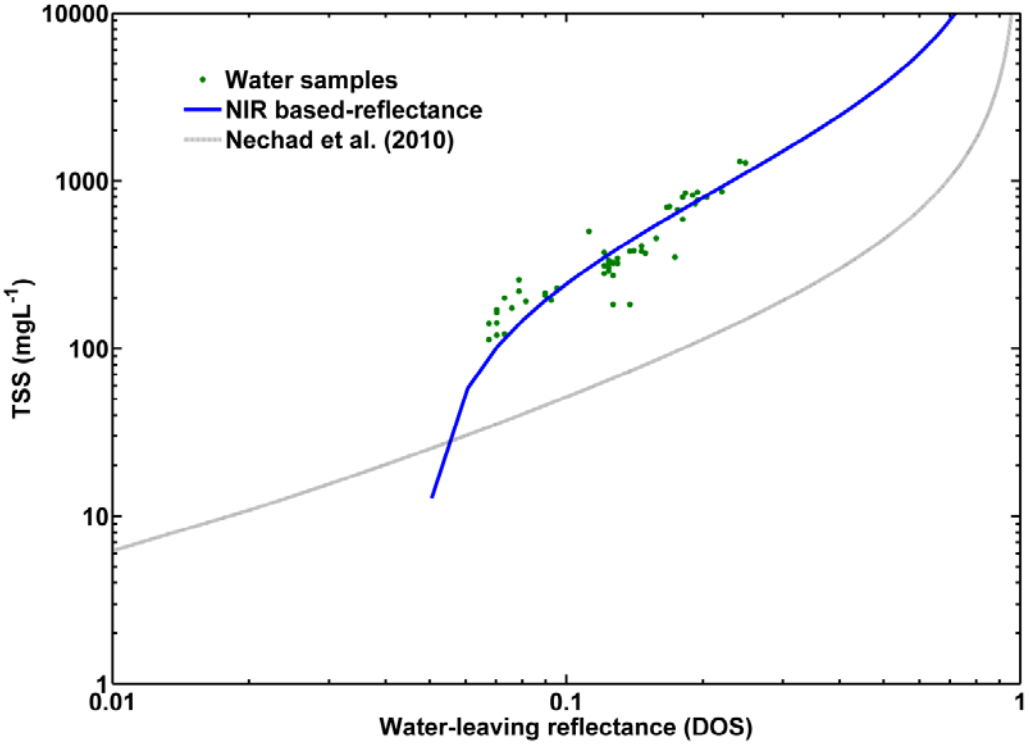

Figure S11. NIR band algorithm for *TSS* retrieval based on the reflectance model developed by Nechad et al. (2010) using DEIMOS-1 water-leaving reflectance derived from DOS model ($\rho_{w(DOS)}$). The robust non-linear regression defined the final calibration coefficients: A^{ρ}= 18890.02 (mgL^{-1}) and B^{ρ} = -198.18 (mgL^{-1}) of Eq. 4, with an averaged *RMSE* of 102.020 mgL^{-1}, r^2 of 0.881 ($p < 0.001$), ε_r of 24.173 % and n = 53 from the cross-validation procedure (blue line, logarithmic scales). Black line represents the fit from Nechad et al. (2010) at this wavelength.

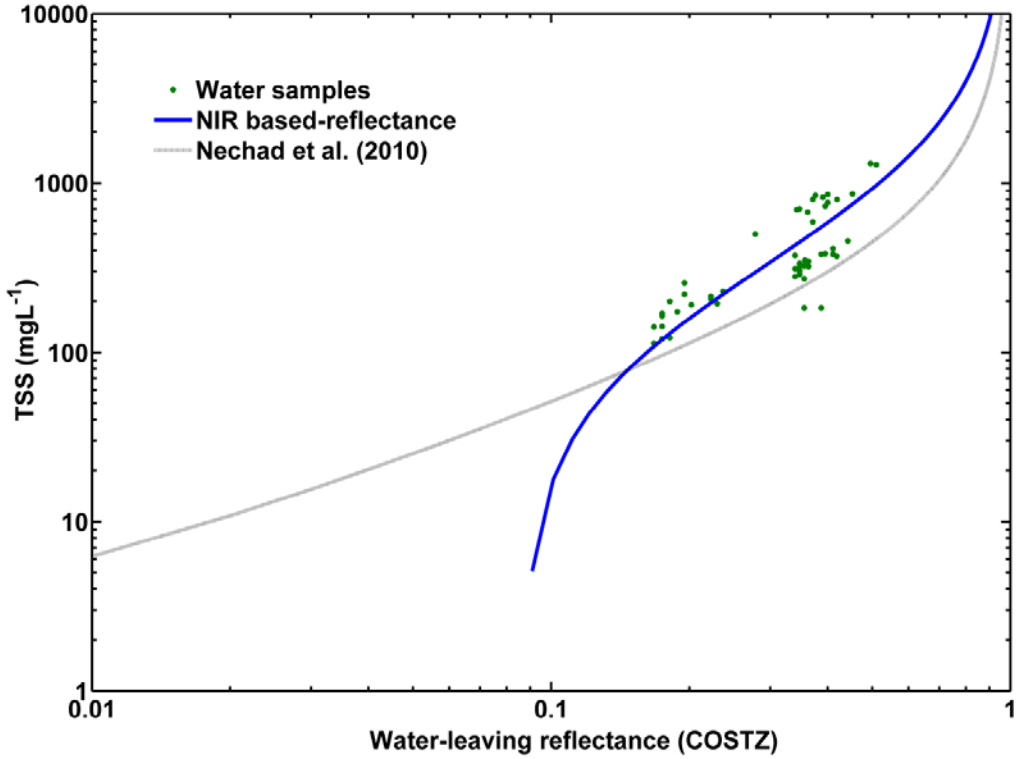

Figure S12. NIR band algorithm for *TSS* retrieval based on the reflectance model developed by Nechad et al. (2010) using DEIMOS-1 water-leaving reflectance derived from COSTZ model ($\rho_{w(COSTZ)}$). The robust non-linear regression defined the final calibration coefficients: A^{ρ} = 4868.45 (mgL^{-1}) and B^{ρ} = -97.13 (mgL^{-1}) of Eq. 4, with an averaged *RMSE* of 197.128 mgL^{-1}, r^2 of 0.591 ($p < 0.001$), ε_r of 39.963 % and n = 53 from the cross-validation procedure (blue line, logarithmic scales). Black line represents the fit from Nechad et al. (2010) at this wavelength.

CAPÍTULO 4

DYNAMICS OF THE TURBIDITY PLUME IN THE GUADALQUIVIR ESTUARY COASTAL REGION: OBSERVATIONS FROM IN SITU TO REMOTE SENSING DATA

Isabel Caballero[1], Gabriel Navarro[1]

[1] Departamento de Ecología y Gestión Costera, Instituto de Ciencias Marinas de Andalucía, Consejo Superior de Investigaciones Científicas (ICMAN-CSIC), Puerto Real, 11510, España

El capítulo íntegro está en proceso de ser enviado a la revista Progress in Oceanography para su publicación.

Dynamics of the turbidity plume in the Guadalquivir estuary coastal region: Observations from in situ to remote sensing data

Isabel Caballero[*] and Gabriel Navarro

Department of Ecology and Coastal Management, Instituto de Ciencias Marinas de Andalucia (ICMAN-CSIC), Puerto Real, 11510, Cadiz.

* Corresponding author: isabel.caballero@icman.csic.es, 0034 627379716

Keywords:

Guadalquivir estuary; turbid plume; spatio-temporal variability; tide; fortnightly cycle; wind; MERIS.

Abstract

High concentrations of suspended particulate matter in coastal waters directly affect or govern numerous water column and benthic processes. In the case of the marine region influenced by the Guadalquivir estuary, turbidity is one of the primary threats to the health of this complex environment. Ten-year ocean color observations between 2002 and 2012 from the MEdium Resolution Imaging Spectrometer (MERIS, 300m) onboard the Envisat multispectral platform are used to quantitatively assess the variability of sediment properties in the Guadalquivir estuary and adjacent region. The combination of high-frequency observations from automated sensors and in situ data in addition to synoptic satellite imagery resulted in an excellent complement to better study water quality parameters. The turbid plume has been detected by the backscattering characteristics of the surface waters in the vicinity of the estuary mouth. Remote Sensing Reflectances at 665 wavelength and turbidity reveal the effects of physical processes governing both the spatial and temporal distribution of the plume.

The findings of this work indicate that both respond to seasonal and inter-annual variations of rainfall and mainly, the freshwater discharges from Alcalá del Río dam. These patterns represent a crucial factor governing phytoplankton primary productivity in the pelagic ecosystem of the Eastern Gulf of Cadiz. Furthermore, our results suggest that the Guadalquivir plume varies on fortnightly scales, presenting smaller dimensions at neap tides and achieving higher dimensions during and after spring tides. Additionally, an asymmetric behavior of plume signal in connection with the semidiurnal tidal cycle (flood and ebb tide) is also founded, with maximum values at low tide. Both fortnightly and semidiurnal cycles appear to be superimposed on the large time-scale variability, and present throughout the year. Moreover, the turbid area is associated with wind direction and intensity, primarily with the meridional component at high frequencies. This study demonstrates that tidal forcing is one of the important ocean processes that drive significant changes of the turbidity plume in the coastal waters, better characterizing its variability and advancing our understanding of sediment dynamics in highly variable estuaries.

Introduction

The Guadalquivir estuary is one of the largest and most productive estuarine systems of the west coast of Europe. Located in the southwest coast of the Iberian Peninsula (Fig. 1), its waters mix with those of the Gulf of Cádiz (Atlantic Ocean). The estuary extends 110 km inland from its mouth at Sanlúcar de Barrameda to the Alcalá del Río dam, the upstream tidal limit (Alvarez *et al.,* 2001). The tides are semidiurnal with amplitudes that range from about 1 m at neap tides to about 3.5 m at spring tides (mesotidal category). The Guadalquivir River is the main source of freshwater inputs and nutrients to the estuary and adjacent shelf, regulating the high biological productivity of the basin (Navarro & Ruiz, 2006; Prieto *et al.,* 2009; Navarro *et al.,* 2012). The river discharge (controlled by Alcalá del Río dam, Fig. 1) usually shows a pronounced dry/wet season signal as well as large interannual variation (Navarro *et al.,* 2011; Caballero *et al.,* 2014b). The dynamics of the turbidity plume are important for the functioning of the estuary and the adjacent coastal region, where high turbidity habitually produces negative effects on water quality, and thus on economy and society. Recently, several episodes of high turbidity during long periods with almost no

freshwater discharge from the upstream dam originated hypoxia and inhibition of phytoplankton growth (Navarro *et al.*, 2012; Caballero *et al.*, 2014b).

Most research of the estuary has focused on its hydrological description (Vanney, 1970), with studies centered attention on hydrodynamic aspects (Álvarez et al., 2001), flow regimes (Costa *et al.*, 2009) or general circulation of the shelf of the Gulf of Cádiz (García-Lafuente *et al.*, 2006). Recently, Ruiz *et al.* (2014) have described the functioning of the estuarine ecosystem based in a holistic approach, including its physical and biogeochemical dynamics and how these act to control biodiversity. A description of its hydraulic regime depending on the freshwater discharges from the dam has been recently established by Díez-Minguito *et al.* (2012): the estuary becomes fluvially-dominated when discharge exceeds 400 m^3/s (fluvial currents are of the same magnitude or larger than the maximum tidal velocities), tidally-dominated when outflow is less than 40 m^3/s (dynamics are dominated by tidal regime and the river contribution to the water level is negligible), and intermediate when discharges range between 40-400 m^3/s. Regional and seasonal variability of water optical, biological, and biogeochemical properties have been studied in the Gulf of Cadiz with long-term satellite observations (Navarro & Ruiz, 2006; Navarro *et al.*, 2011). In addition, significant interannual variability of the Guadalquivir plume patterns has been observed from the Moderate Resolution Imaging Spectroradiometer (MODIS) images on the satellite Aqua, notably related to the synoptic climate variability (Caballero *et al.*, 2014b).

Estuaries are highly dynamic environments where rivers, winds, tides, and turbulence can interact to determine physical, chemical, and biological variability. These forcing factors lead to a wide range of spatio-temporal scales of sediment variability (Cloern, 1991; Roegner *et al.*, 2002). Wind pulses modify estuarine circulations and water levels and generate waves and currents that suspend sediments (Schoellhamer, 1995) and mix nutrients (Largier *et al.*, 2006). In these complex regions, tide also has significant effects on marine ecosystem and is responsible of large fluctuations (Schoellhamer, 1996; Sharples et al., 2007; Valente & da Silva, 2009). Like most of the estuaries, tide is an important ocean process affecting the Guadalquivir enviroment, where tidal resuspension of sediments was distinguished and the Estuarine Turbidity Maximum (ETM) was attributed to tidal current change (Díez- Minguito *et al.*, 2012, 2014).

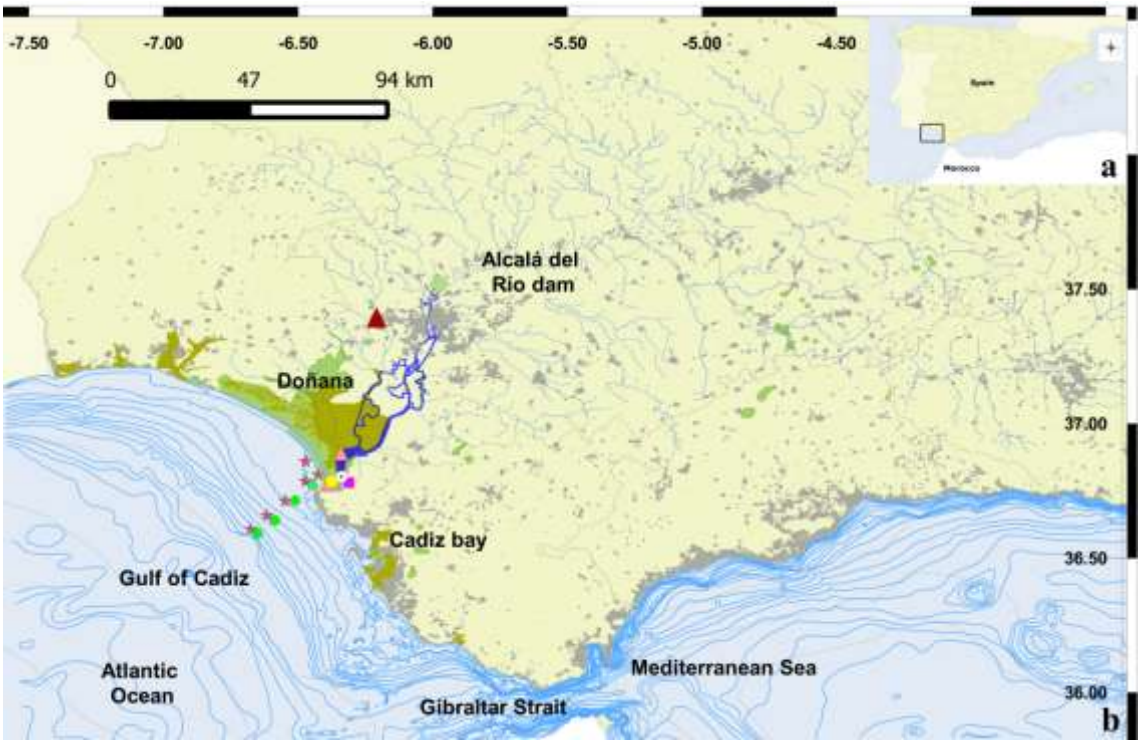

Figure 1. a) Location of the study area (SW Iberian Peninsula); b) Map showing the Gulf of Cadiz coastal region and the Guadalquivir estuary. Green dots and pink stars correspond to the stations of Reserva and Fluctuaciones oceanographic cruises, respectively. Orange marks are both inner and outer nodes (09 and 89, respectively). Yellow mark corresponds to Junta de Andalucía station within the estuary mouth. Green diamond, red triangle and blue star correspond to Alcala del Rio dam, Sanlucar La Mayor meteorological station and SeaWatch buoy in the Gulf of Cadiz. Black rectangle delimits the Region Of Interest (ROI).

There are very few attempts to examine the relationship of the turbidity plume between the Guadalquivir River and the continental shelf with tide influence, while this interaction is known to be critical. While traditional ship-based surveys may not resolve the temporal plume fluctuations and have limitations on monitoring its extent, satellite images can provide frequent, large-scale, synoptic overviews of the coastal zone, enabling a more effective analysis of the temporal and spatial dynamics of these plumes. Satellite observations of the optical properties of coastal surface waters can be used to distinguish turbid plume water from ambient water masses, particularly based on increased concentrations of suspended material within the plumes (Otero & Siegel,

2004; Dzwonkowski & Yan, 2005; Nezlin & DiGiacomo, 2005; Nezlin *et al*., 2005). Although short-term variability in sediment has been documented using optical and/or acoustic sensors (Schoellhamer, 1995; Li & Amos, 2001), no study has been conducted to investigate the wide tidal effects on the Guadalquivir region with satellite observations.

In this work, we use long-term full spatial resolution (FRS) satellite and in situ data to addressed and quantify the seasonal and interannual as well as the short-term variability of suspended sediments in the estuary coastal ecosystem. The main purpose is to understand underlying mechanisms responsible for the spatio-temporal plume patterns and discuss implications of variability. We further want to demonstrate ocean colour images indeed contain tidal information over fortnightly and semidiurnal scales in comparison to the oscillations caused by other driving forces like rainfall and river discharge.

Material and methods

Satellite images

Satellite ocean color images were obtained from the European Space Agency (ESA) MEdium Resolution Imaging Spectrometer (MERIS) on board the Envisat multispectral platform. All available images of chlorophyll concentration (*Chl*, mg/m^3) and Remote Sensing Reflectances at different wavelengths (*Rrs*, 1/sr), both at full spatial resolution (FR, 300 m), covering the region of interest and spanning the complete mission (2002 to 2012), were ordered and downloaded via-ftp from the Ocean Color Website (http://oceancolor.gsfc.nasa.gov). The Level 2 products are the result of the sensor calibration and atmospheric correction, consisting of derived geophysical variables generated from a corresponding Level 1A product using the standard NASA processing methodologies. The MERIS overpass time for central Europe is between 9:30 and 11:00 UTC, with a global coverage every 3 days. Moreover, true-color MODIS 250 m images (TERRA and AQUA) were downloaded from the Earthdata web (https://earthdata.nasa.gov/).

SeaDAS image analysis software (SeaWiFS Data Analysis System, version 6.; http://seadas.gsfc.nasa.gov) was used to read and remap the data to a Mercator projection at 300 m resolution. This sensor typically provides high coverage of the Gulf

of Cádiz study area (overpass at GMT of ~ 10:30 am); however, cloudy and/or foggy conditions result in patchy spatial coverage and temporal gaps. On downloading MERIS data to a local system, the data were displayed and checked to assess image quality. We used the standard SeaDAS algorithm with the ‘‘LAND’’ and ‘‘CLOUD’’ flags to remove the data unintentionally interpolated among others applied as masks with L2_flags, indicating if any algorithm failure or warning conditions occurred for any pixel. These additional and relevant quality control tests were used to discard all suspicious and low-quality data points ensuring that only the most reliable data were retained for analysis (see Table 1 for specific information). They correspond to the flags masked during NASA Level 3-ocean color processing. These generated data files were edited and analyzed using MATLAB 7.10.0 - R2010a (c) software, and the study area was then subset from the images to a Region Of Interest (ROI) with geographic extents of 36.64º N - 36.86º N latitude and 6.36º W - 6.6º W longitude.

Visible bands have been successfully used to estimate *TSS* (Otero & Siegel, 2004; Nezlin & DiGiacomo, 2005; Thomas & Weatherbee, 2006; Caballero *et al.*, 2014b). The red channel (~650 nm) is frequently utilized to asses *TSS* due to the signal of this band is most sensitive to the amount of suspended particles and least influenced by organic matter in relation with other visible bands (Stumpf *et al.*, 1993; Miller & Mckee, 2004; Chen *et al.*, 2010). Analysis of a generic multi-sensor algorithm (Nechad *et al*., 2010) correlating *TSS* and *Rrs* was made, but results were unsatisfactory (not showed here). Then, a regression model for estimating *TSS* from MERIS reflectances in the Guadalquivir estuary was developed. *Rrs* at 665 nm (*Rrs665*) was identified with the best fit (data not shown here), so this channel was then choose for the subsequent study, similar to previous works. Here, we used spectral values of *Rrs665* as a proxy for *TSS*. For each scene, the plume extent was delimited by thresholding the *Rrs665* image. The threshold between "plume boundary" and adjacent waters was defined as 0.007 1/sr, equivalent to the standard normalized water-leaving reflectance (*nLw)* value of 1.3 mW/cm^2 μm sr (Otero & Siegel, 2004; Nezlin & DiGiacomo, 2005; Nezlin *et al.*, 2005; Valente & Silva, 2009; Caballero et al., 2014b). Visual inspection of a subset of images proposed this limit appropriately outlines the river plume (data not shown). Moreover, quantitative estimation of the plume area was made by counting the number of pixels with *Rrs665* > 0.007 1/sr and multiplying by the pixel size (0.09 km^2). This processing is applied over the entire period from 2002 to 2012 that then serves to compute the daily

instantaneous composites and monthly climatology. Exclusively images with more than 30% cloud free pixels in the ROI were used in the 11-year time series. Only pixels with [*Chl*] $\leq$ 20 mg/m^3 were considered, i.e., lower or equal than the highest values occurring in the region (maximum value of the field campaigns).

In addition, an analysis of image properties was carried out using the MATLAB tool "regionprops". A set of properties for the plume shape was calculated in each daily image taking into account that a turbid pixel corresponds to *Rrs665* values > 0.007 1/sr. The plume attributes defined were: Area (number of pixels in the region), Eccentricity (eccentricity of the ellipse , between 0 and 1), Orientation (angle between the *x*-axis and the major axis of the ellipse, in degrees ranging from -90º to 90º), MajorAxixlength (length in pixels of the major axis of the ellipse), and MinorAxislength (length in pixels of the minor axis of the ellipse). The Orientation parameter was used to select plume orientation into Meridional (N-S direction, values between 45º/90º and -45º/-90º) or Zonal (E-W direction, values ranging between -45º745º). This methodology was further utilized for comparison of plume properties and wind variables (Intensity, Direction, and Meridional (Northern and Southern, N and S respectively) and Zonal wind components (Eastern and Western, E and W respectively), to determine wind influence in plume patterns and morphology in the coastal region.

Ancillary data

Ground truth measurements acquired during a series of oceanographic campaigns in the Gulf of Cádiz were employed to define the quality of satellite-derived products in the coastal waters of the Guadalquivir estuary. Surface water samples were collected with a rosette sampler (maximum of 5 m below water surface). Only near-shore samples in the estuary were considered (1km to 25km offshore). *Chl* analysis was performed by filtering samples through Whatman GF/F glass fiber filters (0.7 mm pore size), extracting in 90% acetone, and measuring the [*Chl*] by standard fluorometric methods (Parsons *et al.,* 1984) using a Turner Designs Model 10. The fluorometer was calibrated using pure chlorophyll-a from the cyanobacterium *Anacystis nidulans* (Sigma Chemical Co.) with the concentration determined spectrophotometrically. *TSS* were measured gravimetrically on preweighted Whatman GF/F filters after rinsing with distilled water according to JGOFS protocols (UNESCO, 1994). Field observations were filtered based on metadata indications of data quality. This selection criterion removed samples at

certain situations: depth > 5m, evidence of measuring problems and defective filters. At last, coastal *Chl* and *TSS* information was selected from the "Fluctuaciones" and "Reserva" cruises. Additional information on *TSS* was obtained from the Junta de Andalucía "Monitoring Network of Conductivity and Turbidity in the Guadalquivir estuary" (http://www.es/medioambiente). This was formed by 11 manual sampling stations spread between Alcalá del Río dam and Sanlúcar de Barrameda. The closest station to the mouth was taken for validation proposes (GQ200, Fig. 1). Water samples were collected at the surface (to about 1 m water depth). Detailed information regarding in situ data is presented in Table 2.

Table 1. List of L2_flags used in the masking process to assure the quality control of MERIS datasets retained for analysis (flags at NASA Level 3-ocean color processing).

Flag	Condition
LAND	pixel is over land
CLOUD	cloud contamination
ATMFAIL	atmospheric correction failure
HIGLINT	high sun glint
HILT	total radiance above knee
HISATZEN	large satellite zenith
CLDICE	clouds and/or ice
COCCOLITH	coccolithophores detected
HISOLZEN	large solar zenith
LOWLW	very low water-leaving radiance
CHLFAIL	chlorophyll algorithm failure
NAVWARN	questionable navigation
MAXAERITER	maximum iterations of NIR algorithm
CHLWARN	chlorophyll out of range
ATMWARN	atmospheric correction is suspect

Table 2. Oceanographic field cruises and sampling conducted in the Gulf of Cadiz region. Specifications of data for Total Suspended Solids (*TSS*), turbidity and chlorophyll (*Chl*) validation purposes.

Campaign	Zone	Type	Date	Measurements	Depth
Reserva	Coastal	RV Regina Maris	Jul2002-Sep2004	*TSS - Chl*	*< 5m*
Fluctuaciones	Coastal	RV Regina Maris	May2005-May2007	*TSS - Chl*	*< 5m*
GQ200	River mouth	Manual sampling	Apr2008-May2011	*TSS*	*< 1m*
Node 09	Inner Estuary	RTRM network	May2008-Nov2010	*Turbidity*	*< 1m*
Node 89	River mouth	RTRM network	May2008-Nov2010	*Turbidity*	*< 1m*

In addition, turbidity data was obtained by the real-time remote monitoring (RTRM) network operated by the Instituto de Ciencias Marinas de Andalucía (ICMAN-CSIC) which provide meteorological, hydrographic and water quality information for 3 years (Navarro *et al.,* 2011; 2012). The instrument corresponded to a Turbidimeter Cyclops-7 (Turner Designs) with an operational range of 0-3.000 Nephelometric Turbidity Units-FNU (accuracy of 0.04 FNU). The two water quality stations studied were located in the inner part of the estuary (node 09, 36.89º N - 6.34º W) and in the river mouth (node 89, 36.77º N - 6.39º W) (Fig.1). Navarro *et al.* (2011) established a robust relationship between *TSS* (measured by gravimetric method) and turbidity (FNU units), *TSS* = 1.6015* turbidity (r^2 = 0.93, n = 25 samples).

Daily mean discharge at the Alcalá del Río dam, the main freshwater input to the Guadalquivir estuary, was obtained from the Junta de Andalucia "Regional Water Management Agency" (http://www.chguadalquivir.es/saih/) at station code E60 (37.51º N - 5.97º W, Fig. 1). Daily precipitation measured at an automatic meteorological station in Sanlúcar la Mayor at station code 13 (37.42º N - 6.25º W, Fig. 1) was acquired from the regional Agroclimatic Station Network (http://www.-juntadeandalucia.esagriculturaypesca-/ifapa/ria). Daily wind data were obtained from the nearby meteorological station located in Sanlucar de Barrameda (36.78° N - 6.31° W, Fig. 1) which belongs to the Agroclimatic Stations of the Junta de Andalucía (http://www.juntadeandalucia.es/). In addition, wind information was also obtained from the SeaWatch buoy located in the Gulf of Cádiz (36.48º N - 6.96º W, 54.4 km from coastline; Fig. 1) which belongs to Puertos del Estado (http://www.puertos.es/). Wind data in this station were available at hourly intervals, and were partitioned into

alongshore (North-South or meridional wind, *V*) and cross-shore components (East-West or zonal wind, *U*).

To characterize and quantify tidal effects on the Guadalquivir estuary ecosystem, long-term water level data was recorded with a tidal gauge property of Puertos del Estado placed in the port of Bonanza (36.80° N - 6.34° W, Fig. 1). The sampling interval was 1 h. The current data were processed in MATLAB for performing harmonic analysis of the tide using the "T_tide" Toolbox (Pawlowicz *et al.*, 2002). The software "Tidex" (Tidex 2000, Version 1.1) developed by the Department of Applied Physics of the University of Cádiz (Spain), was used to obtain predicted tidal values at the study area. Tidal harmonic analysis could be performed to determine the approximate amplitudes and phases of the diurnal, semi-diurnal, and higher harmonic tidal constituents of the detrended sea-surface elevations by a least-squares fit. The in situ water level were used to validate the simulated tidal level that was generated from the regional tidal model. The intention of using the tidal model, after exhibiting a good agreement between the model and field information (data not showed here), is to fill the gaps of the observed in situ tidal measurements.

Validation

Statistical validation of these products is essential to verify the accuracy met by the satellite. Careful consideration of measurement scale is critical when comparing remote sensors with in situ observations, particularly because the large spatio-temporal variability of estuarine and coastal water properties influencing those measurements. In this work, data match-ups were made by selecting *Rrs665* and *Chl* values for the corresponding pixel, and average the surrounding grid nodes using a pixel box of 25 pixels, centered on the coordinates of the field measurements. Time difference between satellite overpasses and in situ sampling was < 1.5h. For all match-ups considered, the following statistical parameters were calculated to define the error associated with MERIS estimations; coefficient of correlation (*r*), root mean square error (*rmse*), *bias*, maximum, and minimum values. In the *TSS* - *Rrs665* regression process, an exponential adjustment was utilized because it helps with possible overcorrection for atmospheric effects at large *TSS* values, when the reflectance contribution from the water may no longer be negligible at larger wavelengths (Stumpf *et al.*, 1993; Ruddick *et al.*, 2000).

To estimate [*Chl*] retrieval, we performed a linear regression of in situ data against MERIS *Chl* observations (OC4Me algorithm, O'Reilly *et al.*, 1998).

Results

Validation of water constituents

Even though a large number of in situ measurements were potentially available for the region only a total of 27 and 25 pairs for *TSS* and *Chl*, respectively were found (according to quality flags and validation procedure in Section 2). Spatial distribution of the match-ups for *TSS* and *Chl* assessments is shown in Fig. 1. The stations sampled during the different surveys showed [*TSS*] ranging between 8.0 and 327.5 mg/L while *Rrs665* varied between 0.00004 to 0.0265 1/sr. In general, *Rrs665* in Guadalquivir surface waters increased with large *TSS* levels. High correlation between both variables was observed from the scatter plot (r = 0.89) and the t-test for significance yielded p-values of $p < 0.001$. The non-linear predictive function for [*TSS*] (*TSS* (mg/L) = 20.29*exp(100.1**Rrs665*)) was the best-fit curve, presenting a standard error for RS-derived estimates of 38.3 mg/L (Fig. 2a). The in situ data explained 80% of the variation in the MERIS data, giving correct estimations for this area.

Fig. 2b shows the relationship between *Chl* for these particular data sets (linear equation was logarithmically transformed). In situ and RS-derived [*Chl*] ranged from 0.06 to 1.59 mg/m^3 and 0.20 to 4.59 mg/m^3, respectively and were positively correlated (r = 0.81, $p < 0.0001$). Linear regression between observed and predicted values revealed a *bias* of 0.77 mg/m^3 and *rmse* of 1.19 mg/m^3 (2.2 mg/m^3 intercept and 0.21 slope). The MERIS algorithm OC4Me (O'Reilly et al. 1998) yielded reasonable *Chl* retrievals for this region, where the field data explained 66% of the variation.

In brief, both [*TSS*] and [*Chl*] seemed to be predicted with relatively good precision in the near shore regions of the Guadalquivir estuary. The match-up analysis presented significant agreement between MERIS and in situ data, however satellite steadily overestimated *Chl* at all range of concentrations.

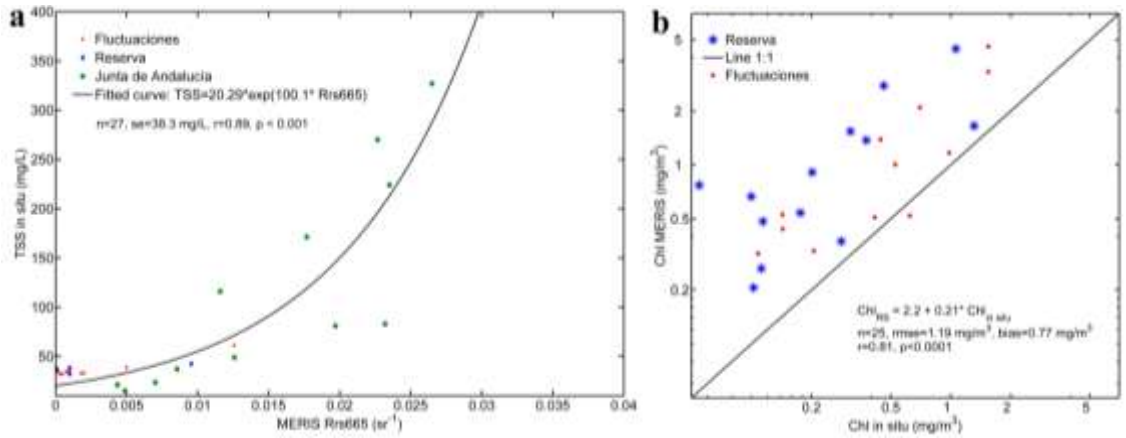

Figure 2. a) Exponential relationship between *Rrs665* (sr^{-1}) and in situ *TSS* (mg/L) from Fluctuaciones (red dotsReserva (blue stars) and Junta de Andalucía (green crosses) coastal campaigns; b) Scatter plot showing the comparison between in situ and at-sensor chlorophyll concentrations (*Chl*, mg/m^3) for Fluctuaciones (red dots) and Reserva (blue stars) cruises (logarithmic axis applied).

Long-term variability

Satellite and field available data allowed the examination of the turbidity plume over several time scales from tidal to seasonal and interannual variability. In addition, the most significant contributing factors had been assessed to determine their influence. Our intent was to identify the fluctuations throughout the study period and describe the dynamics in the coastal region (long and short-term variability). In particular, monthly time series of number of turbid pixels and *Chl* extracted within the ROI (2002-2012) were related with daily rainfall, freshwater discharge and wind speed and direction records (Fig. 3). Rainfall (mm) evidenced a clear pattern with highest values in late fall-winter periods (sometimes beginning of spring) and lower during spring-summer. Discharge from Alcalá del Río dam (m^3/s) exhibited an annual cycle, maximum during late winter-beginning spring and minimum in late summer-beginning fall. The signal presented different annual peak values (maximum in 2010 and 2011, ~ 3000 and 3400 m^3/s respectively) noting a marked interannual variability. A slightly interannual variability compared with discharge is noted in rainfall. The Guadalquivir sediment plume would, thus, be expected to alter seasonally as a result of these cycles. Wind data (speed and direction) varied significantly during the study period, where Western winds ("Ponientes") obviously predominated in comparison with Eastern ("Levantes"). Total

percentage of appearance correspond to 21.4%, 8.9%, 25.2% and 44.5% for North, East, South and West winds, respectively. Highest intensities varied between 8-12.7 m/s while minimum records were around 0.5 m/s.

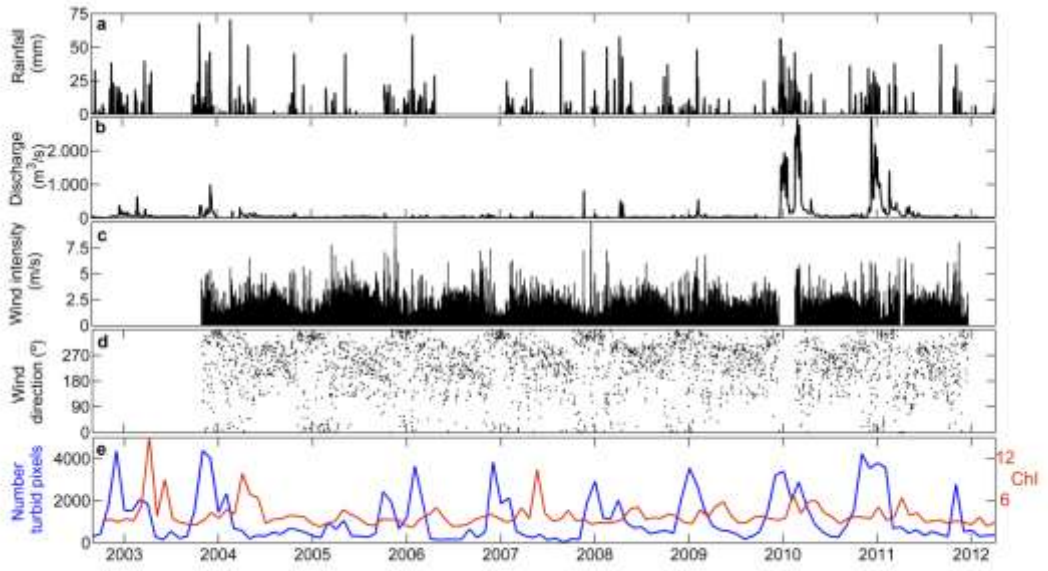

Figure 3. Time series of: a) Daily rainfall at the meteorological station Sanlucar La Mayor (mm); b) Daily river discharge from Alcalá del Río dam (m^3/s); c) Daily wind intensity at the meteorological station Sanlucar de Barrameda (m/s); d) Daily wind direction (º); e) Monthly average of the number of turbid pixels (blue line) and *Chl* arithmetic mean within the ROI (red line, mg/m^3).

A seasonal signal was obvious in the vicinity of the estuary, large plume extensions were consistently observed during late fall and winter (~395 Km^2), while in contrast, small scale or nonexistent plumes were noted in late spring and specifically, summer, regardless of the stream flow scenario. Pronounced plumes occurred at the same time that high river discharges and particularly, parallel to high precipitation rates. During the wet period, greater freshwater discharge may gradually increase and peak the number of turbid pixels. Conversely during dry months (summer), results still showed a distinct signal but the average plume extent decreased (minimum ~1.2 Km^2). It is clear that the data were following a straightforward seasonal trend as might have been expected. The close correspondence between these variables indicated that *TSS* were largely influenced by the fluvial delivery of freshwater in the coastal region. Therefore, the patterns of improving water clarity with decreasing inflow and sediment

input are reported for the transition from the high-flow months to the drought conditions. In this sense, the tidal influence can be significantly filtered out on monthly-averaged plume area.

Chl levels appeared fairly low between summer and fall, while major increases were common during late winter and spring. [*Chl*] was generally above 4 g/m^3 during blooms, in association with an increase of precipitation rates. These peaks coincided with periods where plume area started decreasing from late winter onward. It was however noteworthy that [*Chl*] was low during the major turbid plumes. The phytoplankton bloom pattern occurring after *TSS* peaks was reinforced by the *r* value obtained between both time series, resulting in the highest correlation for 1 month of time lag ($r = 0.49$, $p < 0.0001$), using 8-day TSS and Chl.

Fig. 4 depicts the monthly climatology of MERIS *Rrs665* throughout the region for the years 2002 to 2012. The inherent natural spatio-temporal variability in plume patterns can be detected. The greatest levels along the entire monthly composites were focus on the estuary mouth, suggesting that the high *TSS* observed in this region may be attributable in part to a persistent signal contribution from the river. From the seasonal perspective, months from November to March (wet period) were associated with large areas extended across and along-shore, where the turbid signal reached Cadiz Bay. Generally, during 'low-flow' months (summer to beginning of fall), plume area was relatively small (located within the estuarine mouth and the inner Cadiz Bay) and clear adjacent waters were found.

Short-term variability

Tidal influence

During the second part of this study, plume patterns were investigated based on ocean colour measurements and in situ data. To study the effects of short-term, such as tidal and wind effects, daily imagery was more appropriate than monthly averages. Fig. 5 presents the water level (m) and the meteorological tide (cm) from Bonanza tidal gauge, the river discharge from Alcalá del Río dam (m^3/s), turbidity from both node 09 and 89 (FNU), [*TSS*] records from Junta de Andalucía (mg/L) on the right and the concurrent mean *Rrs665* value in the ROI (1/sr) on the left from May 2008 to December 2010. It is clear that there was a strong relationship between discharge and turbidity signal at both nodes. The most obvious example corresponded to the period from

January to April 2010, where maximum discharges (~3000 m^3/s) were associated with the largest turbidity signals at the outer node 89 (8500 FNU) and one of the highest at the inner node 09 (8200 FNU).

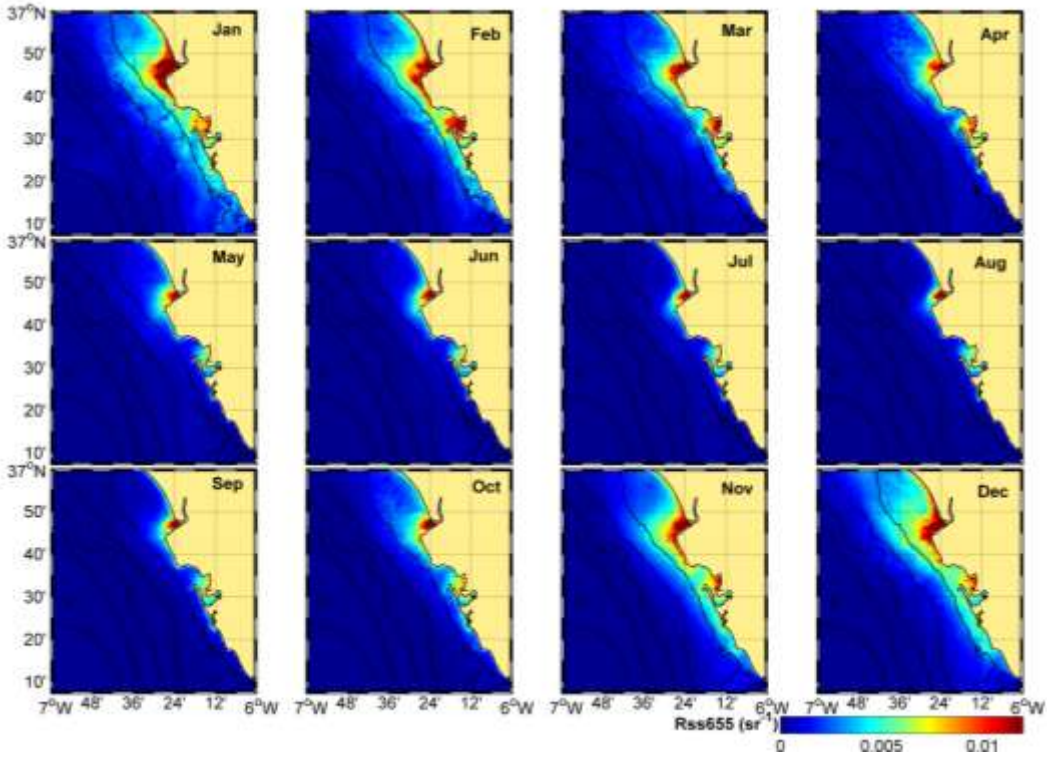

Figure 4. Monthly climatology (2002-2012) of MERIS remote sensing reflectance at 665 nm (*Rrs665*, sr^{-1}). Lines represent bathymetric isolines for the Gulf of Cádiz at the intervals of 20m, 50m, 100m, 200m and 500m.

Moreover, during another pulse in February 2009 (~575 m^3/s), turbidity peaked at both nodes but most dramatically at node 09, causing the more extended turbidity levels within the river channel (8500 FNU). Turbidity at node 09 increased intensely with moderate discharges (e.g.: fall 2008) showing strong spiking. Generally, turbidity is lower at the inner shelf and seems to increase gradually upstream. Furthermore, this behavior was reinforced by the *TSS* records where maximum concentrations were simultaneous to both 2009 and 2010 outflow events, ranging between 1000 and 3000 mg/L. After the initial increase in turbidity during the outflow events, both stations generally were on a downward trend afterwards. During May 2008 high levels were presented at both nodes, reinforced by the high [*TSS*] (1500 mg/L). This episode was generated by a freshwater outflow at the end of April 2008 (Fig. 3), the same order that the one occurred in February 2009 (500 m^3/s). *TSS* were strongly driven by river

discharge, with peaks coincident with maximum discharge pulse. The variations in meteorological tide were generated by changes in weather conditions such as river discharge; during the outflow events, the meteorological tide increased compared to the most stable tidally and intermediate situations. Major discharges in winter 2010 were not presented since data gaps existed at that time but can be still observed during the peak outflow in February 2009.

It appeared that over the sampling period turbidity and *TSS* depended on the seasonal scale related to river outflow but a very strong connection with tidal amplitude seemed to take place, in specific with the fortnightly tidal cycle. In this sense, more significant variations were found at node 09 than at 89 during low river discharge periods, the tidally dominated hydrodynamic states (e.g., summer 2008, 2009 and 2010). A secondary influence on turbidity has been recognized as the spring-neap cycle (Fig. 5), indeed impacted by the strength of the tidal amplitude, showing periodic variations in a lunar cycle.

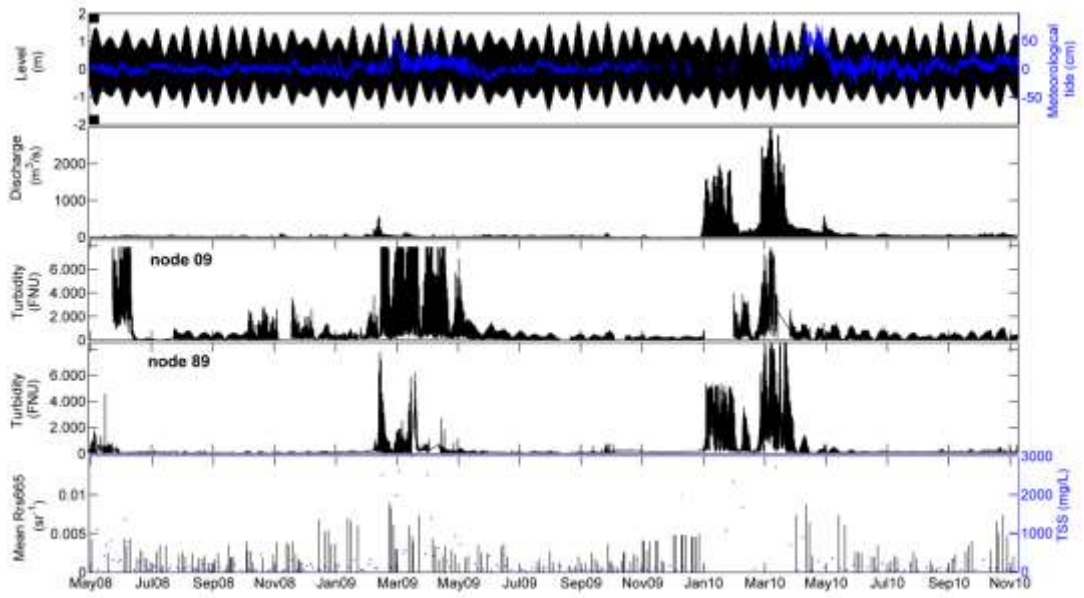

Figure 5. Time series from May 2008 to December 2010 of: a) Water level (m) predicted at Bonanza tidal gauge (black line) and Meteorological tide (cm) measured at Bonanza tidal gauge (blue line); b) Daily river discharge from Alcalá del Río dam (m^3/s); c) Turbidity recorded at the inner node 09 each 30 minutes (FNU); d) Turbidity recorded at the outer node 89 each 30 minutes (FNU); e) Mean *Rrs665* value (sr^{-1}) from MERIS within the ROI (black bars) and *TSS* concentration (mg/L) measured by the Junta de Andalucía during several campaigns in station GQ200 (blue dots).

Fig. 6 displays an example of water-surface elevation and turbidity of both nodes during summer 2010 (discharge < 40 m^3/s, tidally dominated regime; Díez-Minguito *et al.*, 2012). The fortnightly signal (MSF) was included in both records to allow the inspection of the influence of the spring-neap cycle. The astronomical tidal constituent, referred to as MSF (lunar-solar), had low frequency with a tidal period of 14.77 days. The evolution throughout 4 consecutive spring and neap tides further distinguished the relationship detected previously, where turbidity signal presented periodic fluctuations following the lunar cycles. The two nodes showed nearly identical variability but differing in magnitude (higher turbidity at node 09). Maximum turbid waters were found on the interval following the spring tide with peaks during the two major events (13-15 June and 13-15 July, 600 FNU and 370 FNU at node 09 and 89, respectively). In contrast, turbidity intensely dropped during neap tide, as for example on 20 June and 6 July. The MSF lines perfectly described turbidity patterns and seemed to be superimposed to the major fluctuations, indeed being more apparent at node 09 with analogous variability. For node 89, the fortnightly tidal effects were still identifiable even though they were not as significant as at node 09. In that sense, the progression from spring to neap tide was in general, constant. This actually reflected that turbidity values in the region changed according to the fortnightly tidal phases, leading to different variations. In comparison, turbidity at node 09 varied from ~20-700 FNU during spring tide while during the neap tide ranged between 0-250 FNU. In addition, water levels exposed semidiurnal oscillations with maxima-minima around 3.4-1m. The low and high tides can be easily detected. A common tendency of turbidity was that maximum levels in both the river channel and outer estuary occurred at low tide (slack after ebb tide) and at the first instants of flooding, especially during spring tides, but also recognizable during neap tides at both nodes. For instance, during the first spring tide (13-15 June) blue lines indicated that low tide was parallel to peaked turbidity at both nodes (more accentuated at the inner station). In the same way, these features can be also distinguished during neap tides like the example during July, green lines denoted greater turbidity records occurring simultaneously to low tide stage. Accordingly, turbidity ranged with the semidiurnal signal of the tide (M2, S2, N2) showing similar fluctuations as water level.

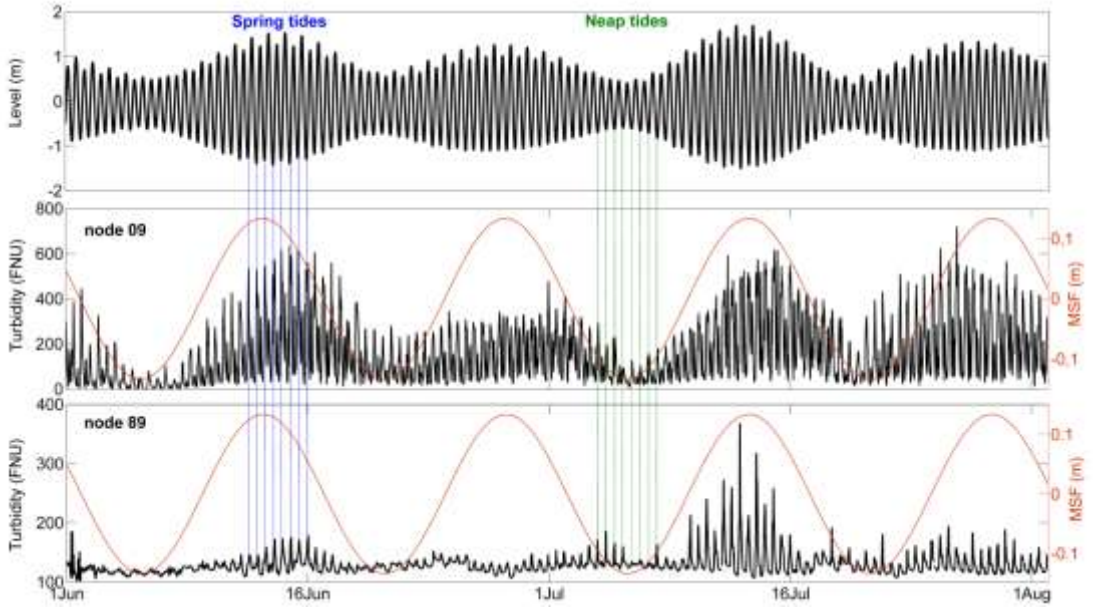

Figure 6. Time series from 1 June to 31 July 2009: a) Water level predicted in Bonanza (m); b) Turbidity at the inner node 09 (FNU); c) Turbidity at the outer node 89 (FNU). Example of turbidity fluctuations at spring and neap tides from both nodes, blue and green lines, respectively. The calculated fortnightly tidal signal (MSF) was superimposed to the turbidity records.

To determine whether the remote sensing data were influenced by tidal amplitude and the spring-neap cycle, an analysis with daily imagery was realized. Fig. 7 presents the histogram of the different situations regarding MERIS images (only < 30% cloud coverage were included). In order to examine distinct cases, each image was selected regarding: 1) the hydrodynamic regime of the estuary which depended on discharge: tidally dominated (<40 m^3/s), intermediate stage (40-400 m^3/s) and fluvially dominated (>400 m^3/s); 2) the fortnightly tidal cycle determined by the MSF: spring (interval of ±7.5 days from spring tide) or neap tide (interval of ±7.5 days from neap tide). Tidally episodes were the most detectable over the 11 year study period (34% and 37% for both spring and neap cycle) while fluvially stages were scarce (~2.5% for both tidal situations). Besides, intermediate cases were also common in the region for both spring and neap tides (around 12.5%). Concerning the eminent importance of the spring-neap cycle over the plume patterns (specially during low freshwater events), it was to some degree relevant to remark the large occurrence of the tidally dominated regime respect

to the others. This involved that the estuary was extremely dependent on tidal effects also in the long-term temporal analysis.

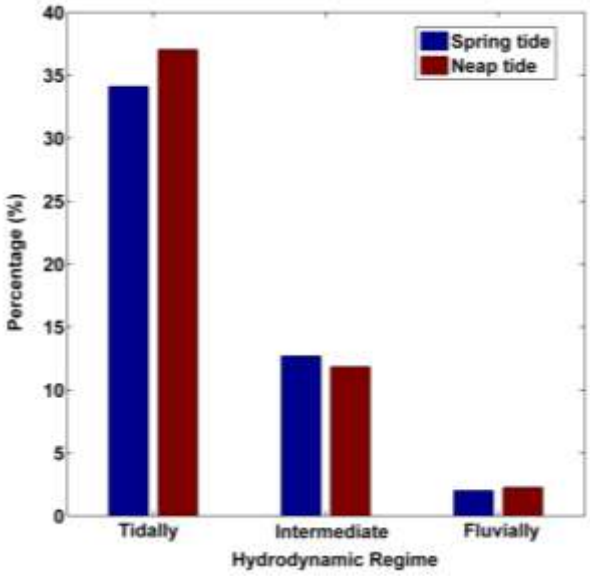

Figure 7. Histogram presenting the percentage of occurrence of the different situations in the estuary regarding the hydrodynamic regime (tidally, intermediate or fluvially dominated) and the fortnightly tidal cycle (spring or neap tides, blue and red lines respectively) in the MERIS imagery (2002-2012). Images with more than 30% of cloud coverage were eliminated.

Using the sea level datasets provided by the tidal gauge, the time difference between each MERIS passing time over the Guadalquivir estuary was computed and the tidal characteristics of each image were defined (tidal stage and MSF cycle). Ocean color images between 2002 and 2012 were grouped regarding the tidal fortnightly cycle (spring or neap tide) and the hydraulic stage recently described by Díez-Minguito *et al.* (2012). Only tidally and intermediate stages were selected for further evaluation since fluvially cases were regularly dominated by river discharges and can modulate or mask tidal influence. Moreover, only the interval of ±3 days from spring and neap tides were further examined. The same procedure was accomplished taking into account all the days between spring and neap tide (±7.5 days) but similar results were obtained (data not showed here). Finally a climatologic composite with all the individual scenes of

each group was estimated as the representative for each specific case study. The division between spring and neap tides in both hydrodynamic situations was calculated. Fig. 8 provides the final climatologic distribution to better quantify ocean properties in a lunar cycle, where the spring-neap cycle apparent in the turbidity sensor was also visible in the satellite images (the percentage of appearance of each situation over the entire period is displayed). Highest *Rrs665* levels were located in the mouth of the river, decreasing further along and across-shore. Areas with enhanced *Rrs665* appeared on spring tide scenarios for both tidally and intermediate situations (Fig. 8 a-d, respectively). In contrast, pronounced diminish in terms of *Rrs665* magnitude and coverage were observed during neap tides (Fig. 8 b-e). These were confined to a small geographic region close to the coast with minimum levels around neap cycle. In disagreement of the coastal region, no notable difference could be identified in the offshore waters. Therefore, the spring-neap turbidity variations were important in the coastal region, while in the open ocean appeared to be insignificant. *Rrs665* patterns indicated noticeable tide-driven fluctuations for both stages. In comparison, intermediate scenarios exhibited less variation (~ 1.5-2) than tidally situations (~ 3). For the tidally-spring case, the estuary mouth was consistently dominated by high *Rrs665* and the typical rounded plume shape was most defined that in the neap case. This characteristic can be also noted in the division, dominated by the spring signal (Fig. 7 c). The same behavior was prevalent in the intermediate cases.

Fig. 9 shows four satellite images (RGB composites from MODIS) during spring tides (15 and 31 July) and neap tides (18 July and 3 August), illustrating the spatial distribution of the turbid plume in the upper water column (tidally dominated regime). On 15 and 31 July, water level was low in both cases at the same time of satellite overpass (-1.26 and -0.90 m, respectively), while images on 18 July and 3 August corresponded to ebb situation (-0.24 and -020 m, respectively). The scenes highlighted the effect of the different characteristics regarding the spring-neap cycles. On 15 July satellite image (large spring tides) showed greater plume area throughout the estuary with slightly larger turbidity in the mouth compared with the image on 31 July (lower spring tides). Contrary, during the ebb period on 18 July and 3 August images, where the tide amplitude was approximately the same on both scenes (difference of 0.04 m), weak plume patterns were exhibited along the region, with slightly major signal during the first one, which corresponded to higher neap tides. These images indicated the significant variability in turbidity distribution over the fortnightly cycle.

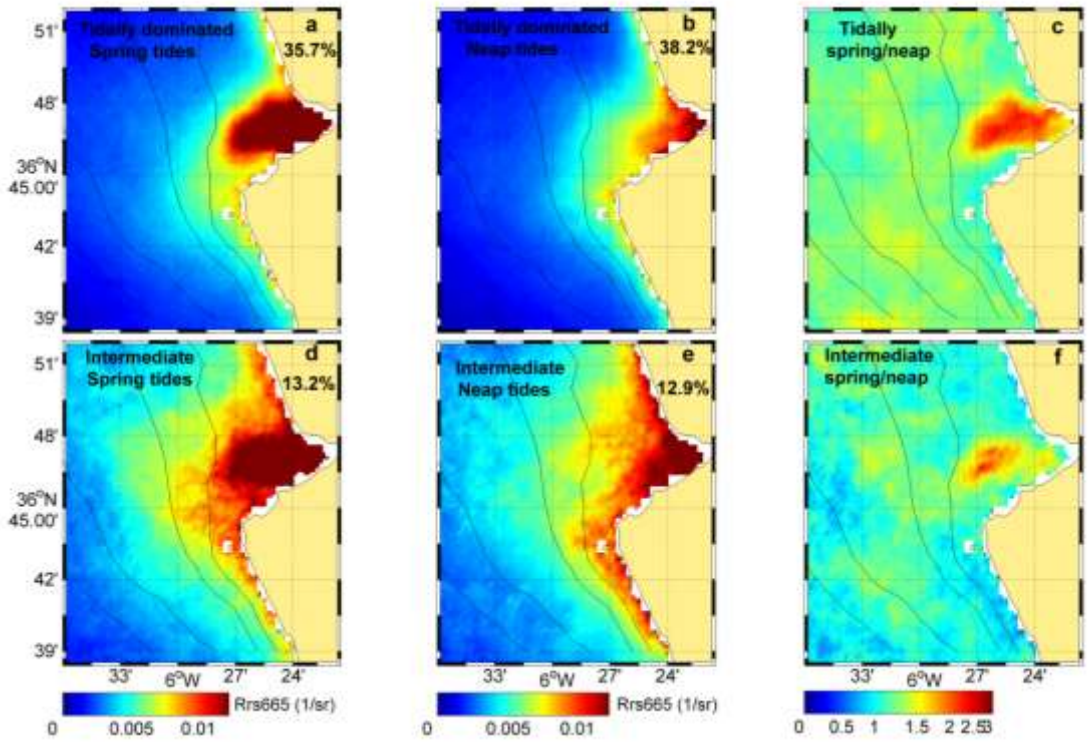

Figure 8. Climatologic *Rrr665* composite derived from MERIS images from 2002 to 2012 for different hydrodynamic and fortnightly tidal regimes: a) Tidally dominated during spring tide; b) Tidally dominated during neap tide; d) Intermediate situation during spring tide; e) Intermediate situation during neap tide; c) Division between spring and neap tide in tidally scenarios (a/b); f) Division between spring and neap tide in intermediate scenarios (d/e). Percentage of occurrence in each study case is noted. Only images with cloud coverage <30% were included.

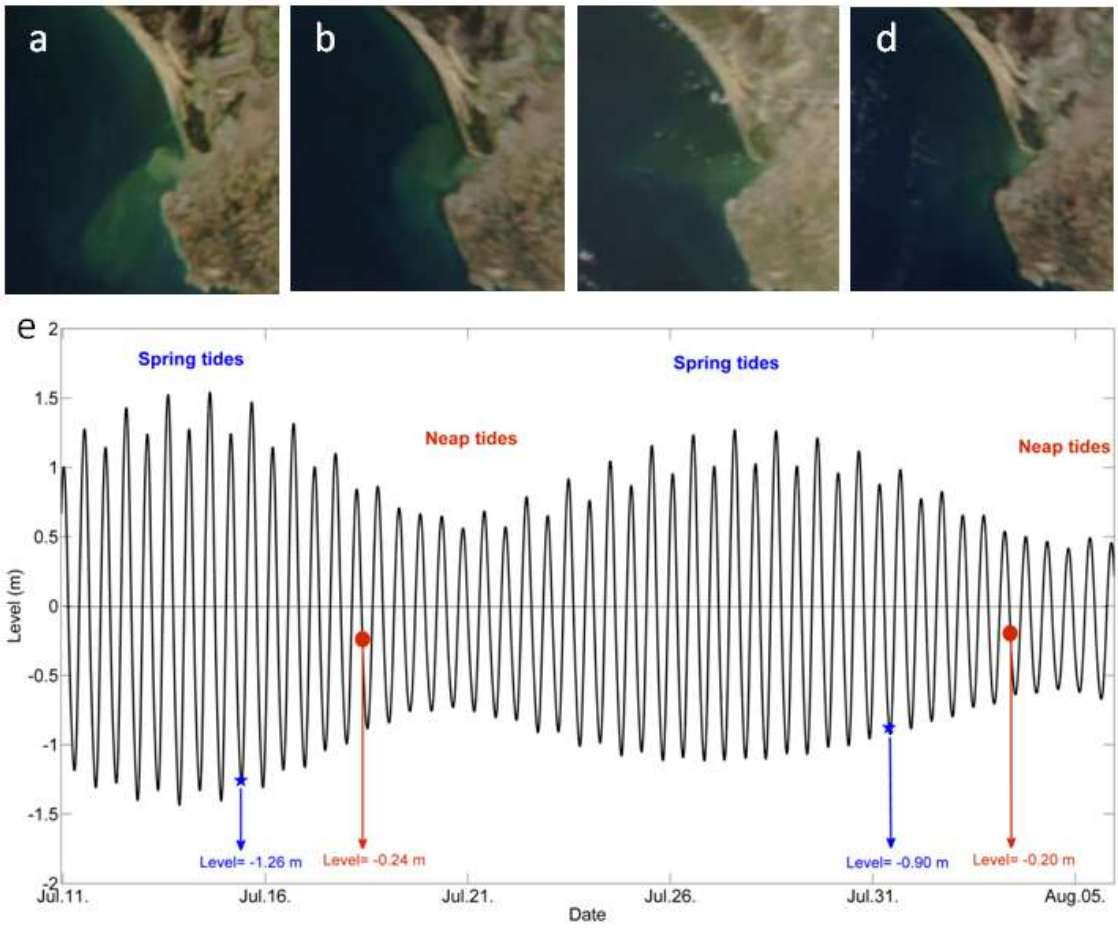

Figure 9. MODIS RBG composites (250 m) on: a) 15 July (10:35h), and b) 18 July (10:39); c) 31 July (10:32h) ; d) 3 August (10:38h); e) Water level at Bonanza tidal gauge (m) from 11 July to 5 August 2010 within one fortnightly tidal sequence and the semidiurnal tidal variations (tidally hydrodynamic regime). Blue stars and red dots represent spring and neap tides cases, respectively.

To further quantify and assess the impact of the low-high tidal effects on ocean optical properties in the Guadalquivir estuary, the regional averaged *Rrs665* values as a function of the semidiurnal tidal fluctuations were included (Fig. 10 and 11). In this case, similar to Fig. 8, each MERIS image was divided following hydrodynamic regime, the fortnightly cycle and additionally, the semidiurnal tidal cycle (high or low tide). The climatology *Rrs665* in each condition was derived from the specific group of satellite images corresponding to the same interval as described previously. Results in Fig. 10 refer to the spring cycle indicating the percentage of appearance of each case. The outcomes show that for the tidally situations, enhanced turbidity signal was

observed in low tide stages compared to high tide. This peculiarity was evident in the division between low and high tide (maximum of 2 particularly within the estuary mouth, Fig. 10c). Contrary, variance in the intermediate cases was noticeable less within the estuary mouth (~ 1, Fig. 10f) but higher offshore (~ 2.5-3). Plume shape was slightly irregular than the typical rounded extent of spring tides.

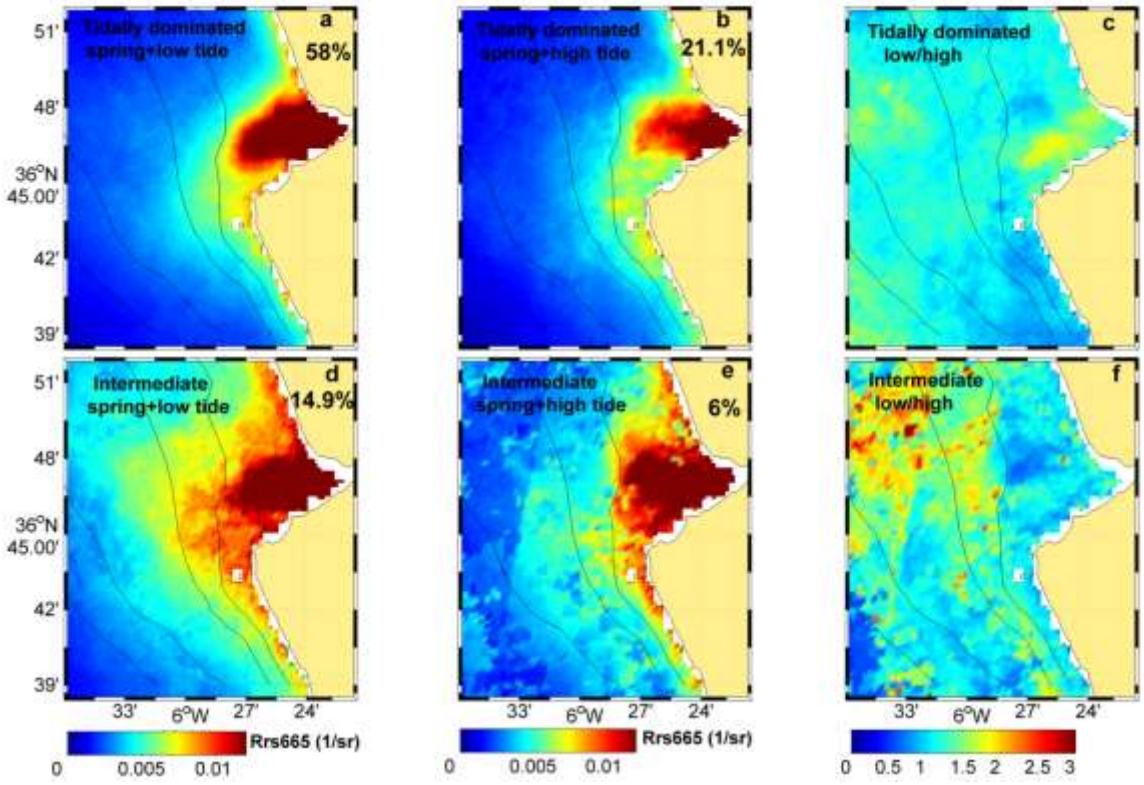

Figure 10. Climatologic *Rrr665* composite derived from MERIS images from 2002 to 2012 for different hydrodynamic regimes and semidiurnal tidal stages during spring tides: a) Tidally dominated during low tide, b) Tidally dominated during high tide, d) Intermediate situation during low tide, e) Intermediate situation during high tide, c) Division between low and high tide in tidally scenarios (a/b), and f) Division between low and high tide in intermediate scenarios (d/e). Only images with cloud coverage <30% were included. Percentage of occurrence in each study case is indicated.

Fig. 11 represents the same procedure accomplished in Fig. 10 but exclusively with neap tide scenarios, showing the percentage of occurrence. In this regard, more episodes of high tide in both regimes were encountered contrary to the spring tide situations. Variations of the water level in the tidally dominated regime did not lead to

significant changes in plume patterns in comparison to the spring tide cases (Fig. 10). The *Rrs665* change was moderate between low and high tide (~ 1.5-2). Contrary, in the intermediate scenarios, particular higher values were observed in the low tide climatologic with maximum differences centered at the mouth (~ 2.5-3). It was also noted that slightly enhanced turbidity typically occurred at low water level within a tidal cycle, especially during ebb or early flood tides regardless the hydrodynamic regimen of the estuary. Concerning the offshore waters, it seemed like during intermediate stages the plume extent was larger compare to the tidally situations where plume was confined to the mouth. This point was coherent since higher discharges leaded to the input of large *TSS* into the estuary which further modulated tidal influence. In the tidally dominated case, due to limited sediment availability prior to the freshwater pulses, plume area was restricted to the estuary mouth.

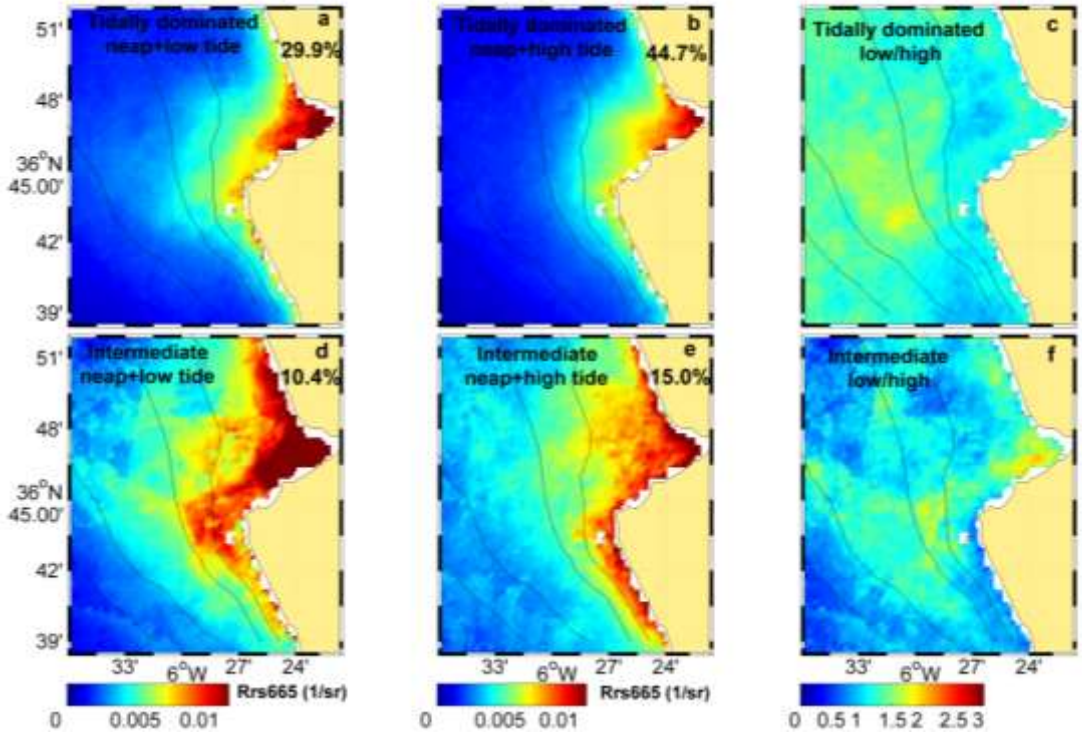

Figure 11. Climatologic *Rrs665* composite derived from MERIS images from 2002 to 2012 for different hydrodynamic regimes and semidiurnal tidal stages during neap tides: a) Tidally dominated during low tide, b) Tidally dominated during high tide, d) Intermediate situation during low tide, e) Intermediate situation during high tide, c) Division between low and high tide in tidally scenarios (a/b), and f) Division between low and high tide in intermediate scenarios (d/e). Percentage of occurrence in each study case is indicated. Only images with cloud coverage <30% were included.

Wind influence

Previous section outlined the main plume features regarding tidal effects. In addition, wind regime was also examined in this work in order to establish a relationship with plume variation. Wind intensity and direction at Sanlucar de Barrameda meteorological station is shown in Fig. 3 (November 2003 to December 2011). Cross-shore and alongshore wind fluctuations were mostly dominated by synoptic scale variability (3-5 days). Winds coming from the West were dominant during the study period (44.5%) comparing to Easters winds (8.9%). Continuous westerly winds generally prevailed throughout the seasons, particularly during summer and fall, occasionally interrupted by Eastern events in winter and early spring. Both downwelling-favorable and upwelling wind events appeared to be alternated by periods of relaxation.

Daily *Rrs665* imagery from MERIS were used to assess the connection between wind (SeaWatch buoy) and turbidity plume. For this purpose, several parameters were calculated within the ROI: number of turbid pixels, mean *Rrs665* and maximum *Rrs665* (images <30% cloud coverage, n = 205). These variables were compared with the 24 hours average (before MERIS overpass) wind intensity, direction, and the zonal U (N-S) and meridional V (E-W) wind components. Table 3 presents the results were the correlation coefficient (r) and the P-value were displayed for each combination. The parameters were strongly correlated with the intensity and the meridional components of the wind, yielding similar r values and statistically significant ($p< 0.001$). Contrary, neither the zonal component W nor wind direction showed a clear relationship with plume estimation, with the exception of E winds.

Moreover, the image properties characterized by the plume shape analysis were further compared with wind parameters (SeaWatch buoy). Table 4 presents the results regarding three different wind situations: 24, 48 and 72 hours prior to satellite overpass in the region (~ 10:30 GMT). Meridional winds (N-S) were only compared to plume scenarios were plume orientation was also meridional, the same for zonal winds (E-W). In this case, information about wind effects can be recognized in each situation. The best correlations corresponded to the wind 24 hours prior to plume scene, generally with deteriorated associations at 48 and 72 hours before. The first case showed high r between intensity and meridional (N) and zonal (E-W) winds with Area, Major and Minor axis. Contrary, S winds only correlated with Area, presenting low r values (p >

0.1) with both Major and Minor axis. No clear relationship was found neither with combinations of eccentricity in each of the 3 examples. As expected, the outcomes highlighted plume patterns indeed were impacted by the strength and direction of the wind, specifically the North-South component.

Fig. 12 shows four examples of the image processing analysis with *Rrs665*: 17 July 2003, 8 October 2003, 15 November 2010 and 11 June 2011. In the first 4 rows (Fig. 12 a-d-g-j) the *Rrs665* values are exhibited (1/sr), then the mask is used with the selection of the turbid pixels with *Rrs665 > 0.*007 1/sr (red area) and the conversion to a *.png* image format (Fig. 12 b-e-h-k). Finally, the "*regionprops*" toolbox is applied with the output exhibited in Fig. 12 c-f-i-l, defining Area (number of pixels in the white region), and MajorAxixlength (red line) and MinorAxislength (green line) corresponding to the length in pixels of the major and minor axis of the ellipse in red.

Additionally, MODIS RGB composites (TERRA) showed strong and quick response of plume circulation to wind changes. Plume variability in these images was similar to the remote-sensing reflectance (Caballero *et al.*, 2114). For illustrating this concern, three typical examples representative of the system variability were selected (February 2009, 2010 and 2004, Fig. 13). The first event (Case 1, Fig. 13 a-c) spanned from 12 to 21 February 2009 during weak northwesterly winds, which slightly confined the plume to the southern coast (see Table 5 for specific information about hydrodynamic and tidal state). A clear plume pattern was recognized in the images where the successive pulses from the river were transporter further south along the coast. The second case (Case 2, Fig. 13 d-f) corresponded to an offshore and northerly plume expansion during 22-24 February 2010 associated with an intense southwesterly wind event. Contrary to Case 1, the marked turbid coverage spread out a great portion of the Guadalquivir estuary and adjacent coast. Even though these situations were mainly controlled by river discharges (fluvially dominated regime), the wide plume displacement succeeded along the northern coast was perfectly distinguished. The last episode was referred to zonal winds (Case 3, Fig. 13 g-i), where plume expansion to the south parallel to an evident confinement induced by a moderate westerly event was detected during three consecutive days (27-29 February 2004). During this particular episode, a buoyant plume and highly turbid waters were clearly present on the coastal zone. These sediments, resuspended during the windy period simultaneous to satellite flyover, could have remained in suspension mostly due to the more energetic wind effects. Due to the low occurrence of Eastern wind episodes, no significant cases were

detected partly because during winter and spring cloud coverage was substantially greater.

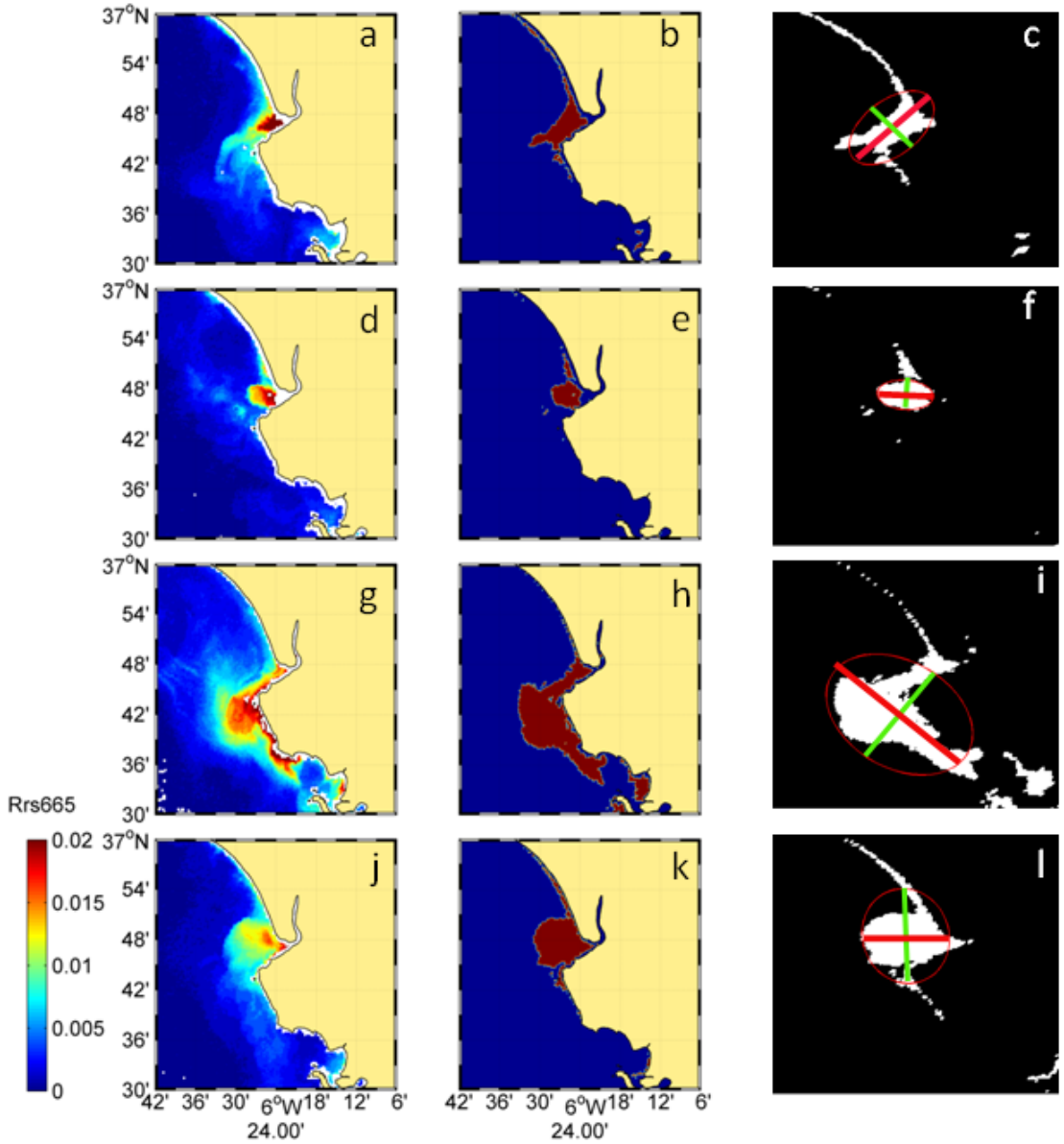

Figure 12. Examples of four images during property analysis procedure: 17 July 2003, 8 October 2003, 15 November 2010 and 11 June; a) d) g) j) Corresponded to *Rrs665* values, b) e) h) k) Turbid mask applied (red region); and c) f) i) l) Shape form showing the ellipse (red) and orientation, and Major (red line) and Minor (green line) axis, respectively.

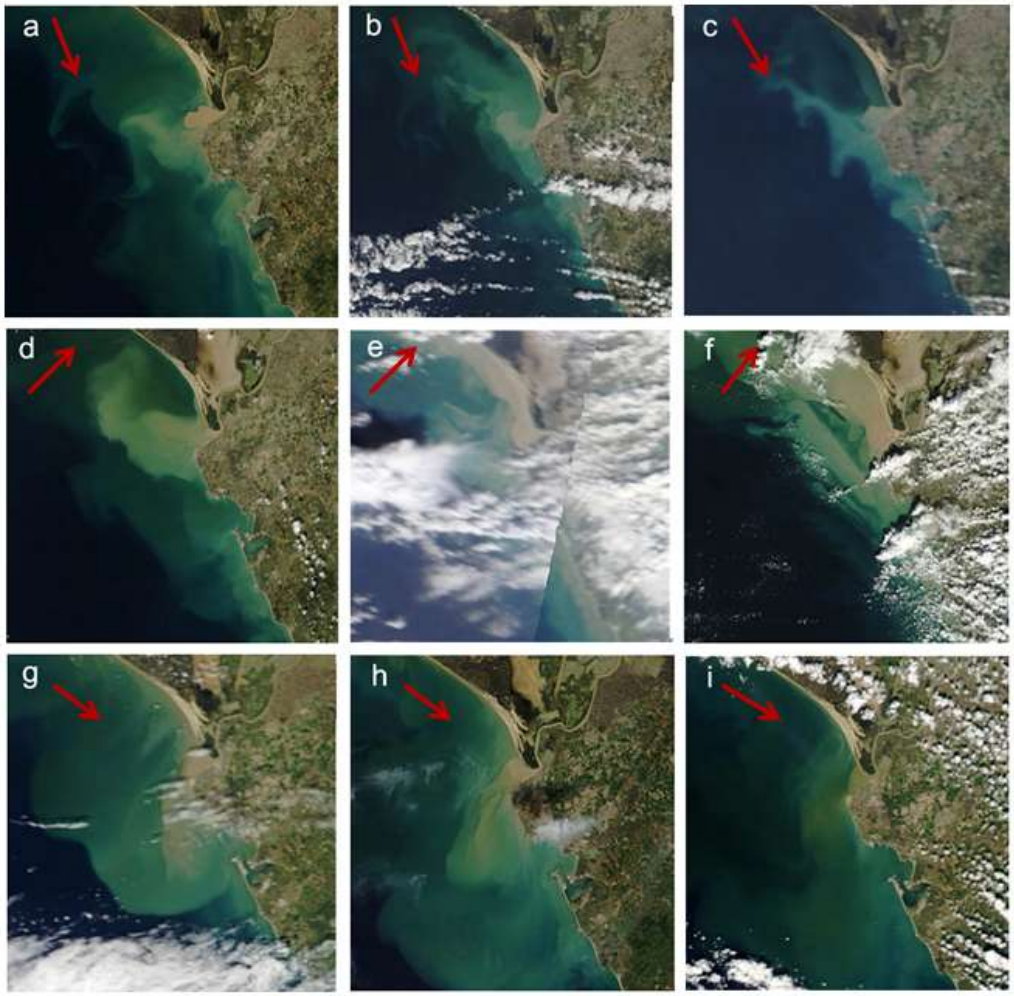

Figure 13. RGB MODIS images (250 m) captured during the three examples related to wind influence: a) Case 1 corresponding to 12, 16 and 21 February 2009 (North wind event), b) Case 2 on 22, 23 and 24 February 2010 (South wind event), and c) Case 3 during 27, 28 and 29 February 2004 (Western wind episode). Red arrows indicate wind direction. More detail information regarding the situation of each image can be noted in Table 4.

Table 3. Correlation coefficient (*r*) and P-value for the different comparisons between wind and plume parameters within the ROI (*n* = 205).

ROI /Wind	Intensity	Direction	N	S	E	W
Number of turbid pixels	0.38*	0.07	0.53 *	0.45 **	0.20 **	-0.09
Mean Rrs665	0.335	0.001	0.51*	0.47 **	0.23 **	-0.01
Maximum Rrs665	0.29*	0.002	0.48 *	0.49 **	0.22 **	-0.02

* p<0.00001

**p<0.001

No mark p>0.1

Table 4. Correlation coefficient (*r*) and P-value for the different comparisons between wind: Intensity, Meridional winds N-S, Zonal winds E-W; and plume parameters determined with the image analysis method: Area, Major axis, Minor axis and Eccentricity (*n* = 926).

24 h before	Area	Major axis	Minor axis	Eccentricity
Intensity	0.39 *	0.44 *	0.39 *	-0.09
N	0.48 **	0.45 *	0.49 ***	-0.15
S	0.37 **	0.14	0.18	-0.02
E	0.25**	0.29 **	0.22 *	0.04
W	0.37 *	0.36 *	0.39 *	-0.02 *
48 h before	Area	Major axis	Minor axis	Eccentricity
Intensity	0.33 *	0.37 *	0.31 *	-0.02
N	0.1	0.17	0.13	0.03
S	-0.008	-0.11	-0.02	-0.07
E	0.16 **	0.23*	0.16 **	0.01
W	0.29 *	0.34 *	0.29 *	0.02
72 h before	Area	Major axis	Minor axis	Eccentricity
Intensity	0.30 *	0.35 *	0.29 *	-0.009
N	-0.34 ***	-0.23	-0.20	0.07
S	0.24	0.15	0.11	0.12
E	0.12 ***	0.15 ***	0.07	0.02
W	0.22*	0.26*	0.24*	-0.06

* p<0.00001

** p<0.001

***p<0.05

No mark p>0.1

Table 5. Description of the different oceanographic and meteorological variables related to the three examples of wind influence in the Guadalquivir estuary adjacent coast. The days correspond to the MODIS RGB composites used.

Date	Example	Event	Intensity (m/s)	Direction (º)	Discharge (m^3/s)	Hydrodynamic Regime	Fortnightly cycle
12 February 2009	Case 1	North	1.0	345	68	Intermediate	Spring
16 February 2009	Case 1	North	1.1	347	56	Intermediate	Spring
21 February 2009	Case 1	North	2.1	339	36	Tidally	Neap
22 February 2010	Case 2	South	5.1	224	2212	Fluvially	Neap
23 February 2010	Case 2	South	4.2	217	2419	Fluvially	Neap
24 February 2010	Case 2	South	1.2	212	2663	Fluvially	Neap
27 February 2004	Case 3	West	3.9	302	0	Tidally	Neap
28 February 2004	Case 3	West	2.6	301	0	Tidally	Neap
29 February 2004	Case 3	West	2.4	290	0	Tidally	Neap

Discussion

Ocean Colour Validation

Fig. 2a presents the exponential relation with good correspondence between *Rrs665* and *TSS*. Validation analyses demonstrate successful *TSS* retrieval using this sensor in coastal waters (overall standard error of 38.3 mg/L and 80% of variance). Nevertheless, caution should be taken in applying this approach outside this region, due to Inherent Optical Properties tend to vary between coastal seas (Babin *et al.*, 2003). In this regard, the optical features of the water masses (size, composition, density, particle type,...) may differ as well as the *TSS* ranges contemplated. Previous studies have exposed a clear connection between at-sensor backscattering products and field *TSS* (Walker, 1996; Miller & Mckee, 2004; Cui *et al.*, 2010; Ondrusek *et al*., 2012). Earlier *TSS* validation with MODIS water-leaving radiance at 555 nm data has shown good agreement in the coastal region of the Guadalquivir estuary, being *TSS* the dominant source of variation in the optical properties (Caballero *et al.*, 2014b).

Chl comparison between MERIS products and the in situ counterparts exhibited the algal product from the standard processor (OC4Me algorithm) systematically overestimates *Chl* (*bias* = 0.77 mg/m^3), describing 66% of the variance. The substantial degree of scatter about the 1:1 line was founded over all [*Chl*] ranges (Fig. 2b). Moreover, this general overestimation of satellite retrieval was also established herein using MODIS data (Caballero *et al.,* 2014b). The tendency of *Chl* algorithms to overestimate [*Chl*] on account of estuarine and terrestrial materials is a peculiarity reported by other authors in several coastal turbid domains (Zhang *et al.,* 2006; Cui *et al.,* 2010).

This work confirms MERIS optical data offer information for the water quality monitoring with reasonable accuracy, exhibiting strong correlations between sensor and field observations. Satellite imagery are sensitive for detecting variations in *TSS* and *Chl*. Moreover, the seasonal relationships are consistent from year-to-year during our study period (2002-2012), which sustain the regression is time independent. The point that the sampling stations are located across the region illustrated the variability of MERIS retrieval over the wide range of concentrations. The uncertainty detected was partially due to the mismatch in sampling size between the *in situ* (~1m^2) and satellite (~0.09 km^2) measurements and the small-scale, high-frequency variability in geophysical properties in the Guadalquivir estuary compared with open-ocean waters. These issues, together with atmospheric correction failure in the turbid coastal area could account, to some extent, for the discrepancy in the validation results.

Plume variability and forcing mechanisms

River discharge and rainfall influence

TSS seasonal patterns were strongly controlled by discharge rates from Alcala del Rio dam reservoir, frequently coincident with winter maximum. Consistently, the diminish of storm passage and accordingly, riverine inputs allowed clear shelf waters to move further inshore. *TSS* have to follow a sharp seasonal pattern due to the climate seasonality in which the estuary is framed. Discharge varies significantly on an interannual basis as a result of the highly variable rainfall events across the catchment, which will vary depending on drought or wet years. Equivalent relationship has been reported in several coastal environments (Otero & Siegel, 2004; Nezlin & DiGiacomo,

2005; Thomas & Weatherbee, 2006; Brodie *et al.*, 2010). The patent lower variance in the mouth region suggested that high *TSS* were a relatively prominent feature, contrary to offshore waters. Moreover, turbidity signal reinforced this notably seasonal behavior for both inner and outer stations (09 and 89, respectively); maxima observed during high runoff and vice versa (Fig. 5). In this regard, more obvious relationship is generally encountered at the inner node (e.g.: winter 2009). *TSS* fluctuations are similar to that of the turbidity because both variables strongly correlate in the Guadalquivir estuary (Navarro *et al.,* 2011). This variability is generally consistent with previously reported large-scale, time-averaged patterns of turbidity and surface *TSS* in the Guadalquivir region (Navarro *et al.,* 2012; Ruiz *et al.,* 2013). Caballero *et al.* (2014b) detected a comparable seasonal cycle of *TSS* for the region using MODIS imagery; improved water clarity with decreasing inflow and rainfall rates.

It is worth noting that the temporal lag of *Chl* maximum, following high turbid events, suggests a coupling between sediment resuspension and phytoplankton blooms (Fig. 3). *Chl* annual peak is associated with the diminishing of the turbid plume fairly coincident with the end of the wet season (spring). The observed variations are generally consistent with those described in Caballero *et al.* (2014b) using MODIS data at the scale of the Gulf of Cadiz coastal environment. Consequently, the seasonal shift in hydrology from fluvially dominated (generally in winter) to tidally dominated (summer) regime is therefore, the main factor regulating suspended matter fluctuations, which also can constrain phytoplankton blooms.

Fortnightly tidal effects

Results indicated plume behavior is controlled by both dominant agents (rainfall and discharges), but can also be widely modulated by other oceanographic and meteorological factors such as tidal and wind effects. A close examination of both in situ and remote sensing datasets suggests a potential link to tidal stirring, documenting how the spring-neap cycle regulates plume patterns throughout Guadalquivir estuary coastal region. Turbidity tends to increase during spring tides and diminishes during neap tides at both inner and outer nodes (09 and 89, respectively; Fig. 5 and Fig. 6). This pattern is most obviously manifested at inner station than in the outer estuary (e.g., summertime of 2008, 2009 and 2010, Fig. 5). In addition, there is not notable variation on peaked turbidity signal at node 09 while at node 89 a slightly difference exists during

spring tides. This feature is associated to the fact that inner node is located along the river channel (~20 km from node 09) and also close to one of the maximum turbidity zones (Díez-Minguito *et al.*, 2012, 2014; Caballero *et al.*, 2014a), while node 89 is situated within the mouth (Fig. 1). Hence, turbidity at node 89 can be more affected by the offshore conditions (wind, wave or currents), while node 09 presents more stable variability with respect to the fortnightly cycle. This issue can be distinctly illustrated during June and July 2009 (Fig. 6), where turbidity fluctuations are intimately described by the dominant spring-neap cycle (MSF signal superimposed). As we mentioned above, this relationship is clearly manifested at the inner node at both low and high tidal stage.

Rrs665 climatologic maps from MERIS also supported the same variability than in situ observations, demonstrating *Rrs665* patterns are also attributed to the fortnightly tidal oscillations. For the two hydrodynamic stages, *Rrs665* signal appeared to be prevailing in both magnitude and size during spring tides, as the division illustrated (Fig. 8 c-e). This obviously indicated the control of spring tides on *Rrs665*. During neap tides, significant *Rrs665* drops can be observed along the coastal region, and the sediment plumes featured with strengthened *Rrs665* in the estuary mouth can be hardly discriminated. The concentrations during spring tides are a factor two or three larger than those observed in neap tides. This feature was also distinguished within estuary by Díez-Minguito *et al.*, (2014), suggesting that estuary signals appeared to influenced in the offshore coastal region. The entire coverage of the turbid waters is greater in the tidally scenarios, with larger difference between spring and neap tides. This is comprehensible since at intermediate situations, fluvial effect is larger and can overcomes tide, distorting the spring-neap influence on plume patterns (only a slight tidal modulation can be seen in the images). The study also reveals that lunar cycle effects on the ocean color observations are significant in the coastal regions and negligible for the open ocean. Fig. 9 provides an additional evidence of the considerably fortnightly tidal oscillations in four different MODIS RGB composites during tidally-dominated period. The effects of the differences in spring tides magnitude on turbidity are exposed; a clear turbidity plume within the mouth during large spring tides while inappreciable sign of plume appeared during small spring tides, both at low tides cases. This particular example is also recurrent throughout the study period and detected in several situations by visual analysis (data not showed here).

Consequently, the turbid plume exhibited significant variability within a fortnightly cycle. This demonstrates that this plume is locally generated, and tidal forcing is one of the major ocean processes that drive turbidity changes. Regardless of the occurrence percentage of both situations (73.8% and 26.1% for tidally and intermediate cases, respectively), the same behavior is founded. In addition, the fact that the appearance of both spring and neap tides is quite similar in both regimes permit us to confirm that the dissimilarity is not caused by distinct number of images in each map. Since satellite imagery to generate composite maps are also evenly distributed in different seasons with long-term MERIS measurements (11 years), hence the effect of seasonal signal is largely averaged out and negligible. This suggests to imply one of the strongest factors on the long-term variability of ocean colour measurements in this region. It is also noted that the *Rrs665* variation during a spring-neap cycle reflects not only the change of the sediment concentration in the water column, but also the possible changes of the particle size, density and optical properties (Babin *et al.,* 2003).

These fluctuations allow deductive assumptions about the spring-neap oscillations captured in both satellite and in situ data, generated by a fortnightly erosion-sedimentation cyclic variation in the strength of the currents. Current velocity and the magnitude of the transport in spring tides almost double the neap tides values (Díez-Minguito *et al.*, 2012, 2014), leading to enhanced tidal amplitudes, vertical mixing rates and an overall widespread plume. Advective transport capacity of the tidal flow seems to be the dominant tidal process affecting *TSS*; spring tides probably increased resuspension of bottom sediment reaching larger turbulence (higher bed shear stress at the bottom), as tidal range decreases, sediments are gradually deposited, leading to more accumulation. These results are consistent with our findings, presence of greater plume during the spring tides and weakening around neap tides. The relationship seemed valid throughout the year and outweighed other long-term variations, including the seasonal cycle of *TSS* which had been reported previously (Navarro *et al.,* 2012; Caballero *et al.*, 2014b). Similar coupling between fortnightly tidal cycle and plume variability has been established in other regions such as in the Tagus estuary (Valente & da Silva, 2009), San Francisco Bay (Schoellhamer, 1996; Ruhl *et al.,* 2001) and a Belgian estuary (Fettweis *et al.,* 1998).

Semidiurnal tidal effects

Furthermore, this coastal region exhibits an asymmetric behavior of turbidity and *TSS* in connection with flood and ebb tide. This feature is clearly marked in the turbidity signal, both inner and outer nodes present maximum values between the period of low tide and the first moment of flooding during spring (blue lines) and neap (green lines) tides (Fig. 6). However, this pattern is more accentuated at the inner node, specially during neap tides. In addition, a second turbidity peak (~half value of the maximum) is observed at node 09 during flood interval. This statement is confirmed by MERIS imagery (spring tide); turbidity signal is greater at low tide during tidally dominated regimes (factor ~2, Fig. 10). The same characteristic is distinguished in neap tide stages with less contrast at the estuary mouth (Fig. 11). Contrary, intermediate scenarios revealed irregular patterns at both high and low tide. This response is the result of the considerable large fluvial impact during these situations, which mask tidal forcing along the semidiurnal cycle. One interesting point corresponds to the inspection of the different percentage of occurrence of low and high tides in both spring (larger during low tide) and neap (lower during low tide) scenarios. In either of them, larger plume signal is constantly detected at low tide, thus final variability is not dependent on the total number of images of each climatologic map. The images also helped interpret the observations that could not be accounted for only by in situ data. For example, the significant expansion or confinement of the turbid plume can be clearly examine with the synoptic satellite images. Neither in the in situ stations nor in the campaigns data the progression of the river plume from the river mouth to the adjacent continental shelf could be analyze.

These tide-associated sediment variations (relatively high sediment during low tides and vice versa during high tides) are consistent with the distinctive sediment gradients in the region. Within a tidal cycle water masses are at their maximum seaward extent at low tide and at their maximum landward extent at high tide. It would be plausible to assume that the interval between ebb and low tide is the period when the plume area is expected to be larger. This characteristic may be the reason why the plume is well detected during low tide in satellite images. Díez-Minguito *et al.* (2012, 2014) have founded that upstream the estuary the amount of sediment suspended in the water column is larger after the occurrence of the maximum flood. This peculiarity is partially associated to the fact that floods are typically shorter than ebbs, leading to

stronger velocities during the flood tide, thereby indicating that the estuary is flood-dominant according to Speer & Aubrey (1985). In the case of the estuary mouth and inner node, during flood periods clean waters from offshore regions enter to the estuary with lower turbidity signal. Contrary, during the ebb tide, after the higher tidal erosive fluxes of the flood stage and maximum resuspension, the plume expanded outside the estuary with higher turbidity. This aspect is reinforced by the work of Díez-Minguito *et al.* (2014), which determined erosion dominates over sedimentation in the stretches nearest to the mouth, being the amount of sediment discharged from upstream substantially smaller that the generated downstream. For turbidity records at the inner node, a double-peak feature is also attributable to the effects of ebbing and flooding tides on the deposition and resuspension of suspended sediments. Hence, high-frequency turbidity variations are also tidally driven in the Guadalquivir estuary and adjacent zones. Similar tidal control has been demonstrated in other estuaries (Cloern, 1996; Li & Smayda, 2001; Roegner *et al.*, 2002).

Fig. 9 further illustrates that it thereby appears unlikely that plume extent on 6 June would be just a result of the ebb-flood semidiurnal cycle, since intense turbidity occurs during flood interval in the coastal region. Therefore, it will be more reasonable to describe the observations in relation to the fortnightly cycle, suggesting that the noted developed plume is chiefly due to the turbidity increase inside the estuary during the spring tide, and not attributed to the semidiurnal variability. Tidal effects are most significant during spring tides when both tidal excursion and tidal erosive fluxes are sufficiently large to transport elevated [*TSS]* to the estuary. The climatologic imagery actually reflected the predominance of high turbidity gradients and spatially non-uniform plume patterns along this coastal region, exposing the plume shift interacting between semidiurnal and fortnightly tidal cycle. Spectral analysis by Navarro *et al.* (2012) indicated that the greatest energy of variation in turbidity within the Guadalquivir estuary was associated with the semidiurnal (M2, S2 and N2) and the sub-tidal frequencies (monthly and fortnightly constituents, MM and MSF, respectively), similar to the water level spectrum (Díez-Minguito *et al.*, 2012). This demonstrates that high frequency sediment variation is associated with both the semidiurnal and the fortnightly tidal cycle. Navarro *et al.* (2012) established that the harmonic analysis explicates greater tidal variability in the inner estuary than in the river mouth, with also larger fortnightly constituents. This confirms the evidence of the different turbidity response at both inner and outer nodes related to tidal forcing in this work.

Wind influence

The outcomes of this work indicate the dispersal of turbidity plumes also responded effectively to wind forcing. The sub-tidal sediment variation of the plume parameters is controlled by local winds, both the meridional or along-shore component and the zonal or across-shore component as correlation analyses revealed (Table 3 and 4). This denoted the importance, regardless of the hydrodynamic stage, of the wind constituent, being a key factor in plume variability over the Guadalquivir coastal region. The image analysis carried out with the MERIS imagery exhibited the close link between plume motion and wind direction and intensity. In this sense, the three plume parameters (Area, Major and Minor axis) where better correlated with the 24 h previous wind conditions than 48 or 72 h, pointing out the changing state of plume patterns regarding the external conditions.

Additionally, MODIS imagery have shown that plume shape and trajectory can be particularly sensitive to wind direction (Fig. 13); indicating directly confinement of the plume to the coast during prevailing westerly winds, and offshore and along-shore expansion by northerly or southerly-winds (southward and northward flow, respectively). Plume distance was greatest with an increased frequency/intensity of meridional winds, but zonal constituent indeed drives plume patterns (specially dominant westerlies). Then, this mechanism may be responsible for the plume extent, moving northward or southward with the wind-driven circulation, depending on the direction and intensity of the wind. The plume during ebb tide is gradually ejected into the coastal zone and can remain in the region until it is totally mixed with ocean water. The offshore dispersal of surface sediments can also be induced by Ekman dynamics, but the previous wind conditions and the duration of the event may determine plume behavior. Our results show that spatial variations could introduce significant variability in plume-influenced shelves, where impact of wind and waves would be expected to be more pronounced. This observation is consistent with those from other estuarine and coastal waters (Piñones *et al.,* 2005; Fauchot *et al.,* 2008; Otero *et al.,* 2008), where wind can force near-shore waters far offshore, also modulated by tides.

Conclusions

The findings achieved in this work indicate MERIS imagery clearly revealed the spatio-temporal patterns of sediment variation and demonstrated how synoptic satellite images complement high-frequency observations at a fixed station to properly assess plume dynamics. The Guadalquivir River plume is a highly dynamic feature; sediments discharged from the river may be dominant seasonally throughout the wet seasons, while tide and wind-induced action leading to large turbidity signals may occur throughout the year. The results evidence that the low frequency or sub-tidal scale (fortnightly cycle) and semidiurnal tidal effects are also critical ocean processes that drive the synoptic-scale of water clarity in this coastal environment. Hence, tidal forcing corresponds to one of the most significant periods of variability, of the same order as seasonal and inter-annual fluctuations. The permanence of high concentrations in the estuary and in the continental shelf mostly depends on the dominance of each of the hydrodynamic regimes, tidally or fluvially, and on the interference of meteorological factors such as wind (direction and speed). These forcing mechanisms control the resulting sediment transport towards the final stretch or otherwise the water retention within the estuary, and the final export and dispersion of the plume in the Gulf of Cádiz basin. Conclusively, this work further confirms the combination of physical forcing in modulating sediment resuspension, expanding our understanding of the processes and the scale of the agents governing turbidity.

Acknowledgements

We would like to gratefully thank the ESA for distributing the MERIS data used in this study and the Junta de Andalucia for in situ data. The authors also thank the crews of the R.V. Regina Maris and B.I.O. García del Cid for support during the cruises. IC is supported by a grant of the Junta de Andalucia PhD fellowship program. This work was financially supported by the Junta de Andalucia Projects P09-RNM-4853 and PR11-RNM-7722.

References

Álvarez, O., Tejedor, B., & Vidal, J. (2001). La dinámica de marea en el estuario del Guadalquivir: un caso peculiar de 'resonancia antrópica'. Física de la Tierra, 13, 11-24.

Babin, M., Stramski, D., Ferrari, G. M., Claustre, H., Bricaud, A., Obolensky, G., et al. (2003). Variations in the light absorption coefficients of phytoplankton, nonalgal particles, and dissolved organic matter in coastal waters around Europe. Journal of Geophysical Research: Oceans (1978–2012), 108(C7).

Brodie, J., Schroeder, T., Rohde, K., Faithful, J., Masters, B., Dekker, A., et al. (2010). Dispersal of suspended sediments and nutrients in the Great Barrier Reef lagoon during river-discharge events: conclusions from satellite remote sensing and concurrent flood-plume sampling. Marine and Freshwater Research, 61(6), 651-664.

Caballero, I., Morris, E. P., Ruiz, J., & Navarro, G. (2014). Assessment of suspended solids in the Guadalquivir estuary using new DEIMOS-1 medium spatial resolution imagery. Remote Sensing of Environment, 146, 148-158.

Caballero, I., Morris, E., Prieto, L., & Navarro, G. (2014). The influence of the Guadalquivir river on spatio-temporal variability of suspended solids and chlorophyll in the Eastern Gulf of Cadiz. Mediterranean Marine Science (in press).

Chen, Z., Hu, C., Muller-Karger, F. E., & Luther, M. E. (2010). Short-term variability of suspended sediment and phytoplankton in Tampa Bay, Florida: observations from a coastal oceanographic tower and ocean color satellites. Estuarine, Coastal and Shelf Science, 89(1), 62-72.

Cloern, J. E. (1991). Annual variations in river flow and primary production in the South San Francisco Bay Estuary (USA) James E. Cloern US Geological Survey, MS-496, 345 Middlefield Road, Menlo Park, CA 94025, USA. Estuaries and coasts: Spatial and temporal intercomparisons, 19, 91.

Cloern, J. E. (1996). Phytoplankton bloom dynamics in coastal ecosystems: a review with some general lessons from sustained investigation of San Francisco Bay, California. Reviews of Geophysics, 34(2), 127-168.

Costa, S., Gutiérrez Mas, J., & Morales, J. (2009). Establecimiento del régimen de flujo en el estuario del Guadalquivir, mediante el análisis de formas de fondo con sonda multihaz. Revista de la Sociedad Geológica de España, 22(1-2), 23-42.

Cui, T., Zhang, J., Groom, S., Sun, L., Smyth, T., & Sathyendranath, S. (2010). Validation of MERIS ocean-color products in the Bohai Sea: A case study for turbid coastal waters. Remote Sensing of Environment, 114(10), 2326-2336.

Díez-Minguito, M., Baquerizo, A., Ortega-Sánchez, M., Navarro, G., & Losada, M. (2012). Tide transformation in the Guadalquivir estuary (SW Spain) and process-based zonation. Journal of Geophysical Research: Oceans (1978–2012), 117(C3).

Díez-Minguito, M., Baquerizo, A., de Swart, H.E., Losada, M. A. (2014). Structure of the turbidity field in the Guadalquivir estuary: Analysis of observations and a box model approach (in press).

Dzwonkowski, B., & Yan, X.-H. (2005). Tracking of a Chesapeake Bay estuarine outflow plume with satellite-based ocean color data. Continental Shelf Research, 25(16), 1942-1958.

Fauchot, J., Saucier, F. J., Levasseur, M., Roy, S., & Zakardjian, B. (2008). Wind-driven river plume dynamics and toxic< i> Alexandrium tamarense</i> blooms in the St. Lawrence estuary (Canada): A modeling study. Harmful algae, 7(2), 214-227.

Fettweis, M., Sas, M., & Monbaliu, J. (1998). Seasonal, neap-spring and tidal variation of cohesive sediment concentration in the Scheldt Estuary, Belgium. Estuarine, Coastal and Shelf Science, 47(1), 21-36.

García-Lafuente, J., Delgado, J., Criado-Aldeanueva, F., Bruno, M., del Río, J., & Miguel Vargas, J. (2006). Water mass circulation on the continental shelf of the Gulf of Cádiz. Deep Sea Research Part II: Topical Studies in Oceanography, 53(11), 1182-1197.

Largier, J. L., Lawrence, C., Roughan, M., Kaplan, D., Dever, E., Dorman, C., et al. (2006). WEST: A northern California study of the role of wind-driven transport in the productivity of coastal plankton communities. Deep Sea Research Part II: Topical Studies in Oceanography, 53(25), 2833-2849.

Li, M. Z., & Amos, C. L. (2001). SEDTRANS96: the upgraded and better calibrated sediment-transport model for continental shelves. Computers & Geosciences, 27(6), 619-645.

Li, Y., & Smayda, T. (2001). A chlorophyll time series for Narragansett Bay: assessment of the potential effect of tidal phase on measurement. Estuaries, 24(3), 328-336.

Miller, R. L., & McKee, B. A. (2004). Using MODIS Terra 250 m imagery to map concentrations of total suspended matter in coastal waters. Remote Sensing of Environment, 93(1), 259-266.

Navarro, G., & Ruiz, J. (2006). Spatial and temporal variability of phytoplankton in the Gulf of Cádiz through remote sensing images. Deep Sea Research Part II: Topical Studies in Oceanography, 53(11), 1241-1260.

Navarro, G., Gutiérrez, F., Díez-Minguito, M., Losada, M., & Ruiz, J. (2011). Temporal and spatial variability in the Guadalquivir estuary: a challenge for real-time telemetry. Ocean Dynamics, 61(6), 753-765.

Navarro, G., Huertas, I. E., Costas, E., Flecha, S., Díez-Minguito, M., Caballero, I., et al. (2012). Use of a Real-Time Remote Monitoring Network (RTRM) to Characterize the Guadalquivir Estuary (Spain). Sensors, 12(2), 1398-1421.

Nechad, B., Ruddick, K., & Park, Y. (2010). Calibration and validation of a generic multisensor algorithm for mapping of total suspended matter in turbid waters. Remote Sensing of Environment, 114(4), 854-866.

Nezlin, N. P., & DiGiacomo, P. M. (2005). Satellite ocean color observations of stormwater runoff plumes along the San Pedro Shelf (southern California) during 1997–2003. Continental Shelf Research, 25(14), 1692-1711.

Nezlin, N. P., DiGiacomo, P. M., Stein, E. D., & Ackerman, D. (2005). Stormwater runoff plumes observed by SeaWiFS radiometer in the Southern California Bight. Remote Sensing of Environment, 98(4), 494-510.

Ondrusek, M., Stengel, E., Kinkade, C. S., Vogel, R. L., Keegstra, P., Hunter, C., et al. (2012). The development of a new optical total suspended matter algorithm for the Chesapeake Bay. Remote Sensing of Environment, 119, 243-254.

Otero, M. P., & Siegel, D. (2004). Spatial and temporal characteristics of sediment plumes and phytoplankton blooms in the Santa Barbara Channel. Deep Sea Research Part II: Topical Studies in Oceanography, 51(10), 1129-1149.

Otero, P., Ruiz-Villarreal, M., & Peliz, A. (2008). Variability of river plumes off Northwest Iberia in response to wind events. Journal of Marine Systems, 72(1), 238-255.

Pawlowicz, R., Beardsley, B., & Lentz, S. (2002). Classical tidal harmonic analysis including error estimates in MATLAB using T_TIDE. Computers & Geosciences, 28(8), 929-937.

Piñones, A., Valle-Levinson, A., Narváez, D., Vargas, C., Navarrete, S., Yuras, G., et al. (2005). Wind-induced diurnal variability in river plume motion. Estuarine, Coastal and Shelf Science, 65(3), 513-525.

Prieto, L., Navarro, G., Rodríguez-Gálvez, S., Huertas, I. E., Naranjo, J., & Ruiz, J. (2009). Oceanographic and meteorological forcing of the pelagic ecosystem on the Gulf of Cadiz shelf (SW Iberian Peninsula). Continental Shelf Research, 29(17), 2122-2137.

Roegner, G. C., Hickey, B. M., Newton, J. A., Shanks, A. L., & Armstrong, D. A. (2002). Wind-induced plume and bloom intrusions into Willapa Bay, Washington. Limnology and Oceanography, 47(4), 1033-1042.

Ruddick, K. G., Ovidio, F., & Rijkeboer, M. (2000). Atmospheric correction of SeaWiFS imagery for turbid coastal and inland waters. Applied optics, 39(6), 897-912.

Ruhl, C. A., Schoellhamer, D. H., Stumpf, R. P., & Lindsay, C. L. (2001). Combined Use of Remote Sensing and Continuous Monitoring to Analyse the Variability of Suspended-Sediment Concentrations in San Francisco Bay, California. Estuarine, Coastal and Shelf Science, 53(6), 801-812.

Ruiz, J., Macías, D., Losada, M., Díez-Minguito, M., & Prieto, L. (2013). A simple biogeochemical model for estuaries with high sediment loads: Application to the Guadalquivir River (SW Iberia). Ecological Modelling, 265, 194-206.

Ruiz, J., Polo, M.J., Díez-Minguito, M., Navarro, G., Morris, E.P., Huertas, E., Caballero, I., Contreras, E., Losada, M.A. (2014). The Guadalquivir Estuary: A Hot Spot for Environmental and Human Conflicts. Environmental Management and Governance: Advances in Coastal and Marine Resources, Springer International Publishing Switzerland, 8, 199-232.

Schoellhamer, D. H. (1995). Sediment resuspension mechanisms in old Tampa Bay, Florida. Estuarine, Coastal and Shelf Science, 40(6), 603-620.

Schoellhamer, D. H. (1996). Factors affecting suspended- solids concentrations in South San Francisco Bay, California. Journal of Geophysical Research: Oceans (1978–2012), 101(C5), 12087-12095.

Sharples, J., Tweddle, J. F., Mattias Green, J., Palmer, M. R., Kim, Y.-N., Hickman, A. E., et al. (2007). Spring-neap modulation of internal tide mixing and vertical nitrate fluxes at a shelf edge in summer. Limnology and Oceanography, 52(5), 1735-1747.

Stumpf, R. P., Gelfenbaum, G., & Pennock, J. R. (1993). Wind and tidal forcing of a buoyant plume, Mobile Bay, Alabama. Continental Shelf Research, 13(11), 1281-1301.

Thomas, A. C., & Weatherbee, R. A. (2006). Satellite-measured temporal variability of the Columbia River plume. Remote Sensing of Environment, 100(2), 167-178.

Valente, A. S., & da Silva, J. C. (2009). On the observability of the fortnightly cycle of the Tagus estuary turbid plume using MODIS ocean colour images. Journal of Marine Systems, 75(1), 131-137.

Vanney, J. (1970). Lhidrologie du Bas Guadalquivir Publicaciones del Dep. de Geograffa Aplicada. CSIC. Madrid.

Walker, N. D. (1996). Satellite assessment of Mississippi River plume variability: causes and predictability. Remote Sensing of Environment, 58(1), 21-35.

Zhang, C., Hu, C., Shang, S., Müller-Karger, F. E., Li, Y., Dai, M., et al. (2006). Bridging between SeaWiFS and MODIS for continuity of chlorophyll-< i> a</i> concentration assessments off Southeastern China. Remote Sensing of Environment, 102(3), 250-263.

CAPÍTULO 5

THE INFLUENCE OF THE GUADALQUIVIR RIVER ON SPATIO-TEMPORAL VARIABILITY OF SUSPENDED SOLIDS AND CHLOROPHYLL IN THE EASTERN GULF OF CADIZ

Isabel Caballero[1], Edward P. Morris[1], Laura Prieto[1], Gabriel Navarro[1]

[1] Departamento de Ecología y Gestión Costera, Instituto de Ciencias Marinas de Andalucía, Consejo Superior de Investigaciones Científicas (ICMAN-CSIC), Puerto Real, 11510, España

Mediterranean Marine Science (en prensa) 15, 4
doi: 10.12681/mms.844
Factor de impacto: 1.734 (2013)
Categoría: MARINE & FRESHWATER BIOLOGY
Rango en la categoría: 43
Número total de revistas en la categoría: 103
Quartil en la categoría: Q2

The influence of the Guadalquivir River on the spatio-temporal variability of suspended solids and chlorophyll in the Eastern Gulf of Cadiz.

Caballero I.*, Morris E.P., Prieto L. and Navarro G.

Department of Ecology and Coastal Management, Instituto de Ciencias Marinas de Andalucia (ICMAN-CSIC), Puerto Real, 11510, Cadiz.

* Corresponding author: isabel.caballero@icman.csic.es

Keywords

Water quality, remote-sensing, MODIS, EOF analysis, Gulf of Cadiz, Guadalquivir estuary.

Abstract

This study examines the spatio-temporal variability of the turbidity plume and phytoplankton biomass (in terms of chlorophyll) in the marine region influenced by the Guadalquivir estuary using ocean colour images over a period of 11 years (2003-2013). The area of the turbidity plume was calculated using water-leaving radiance at 555 nm (*nLw555*). Climatologic and monthly averages showed recurrent high *nLw555* levels in winter and high chlorophyll in spring. Similar variability was confirmed by Empirical Orthogonal Function (EOF) analysis of 8-day composite images, illustrating the existence of different regions with similar behaviour. The first EOF mode explained 60.7% and 31% of the variability in *nLw555* and chlorophyll, respectively, and was associated with enhanced Total Suspended Solids (*TSS*) in autumn-winter and phytoplankton blooms in winter-spring periods. The results confirmed that the development of the turbidity plume and subsequent phytoplankton blooms were strongly regulated by river discharges and precipitation. Indeed, inter-annual variation in *nLw555* was consistent with changes in the large-scale climate index, the North Atlantic Oscillation, a proxy for regional rainfall patterns. In the case of phytoplankton biomass, the second EOF mode revealed differentiation between offshore and near shore areas, the latter characterized by delayed development of phytoplankton blooms due to light limitation by high *TSS*. This suggests that the stability of the water column, via its influence on phytoplankton light-limitation, also influenced the timing and magnitude of phytoplankton bloom events. The dynamics of the Guadalquivir estuary turbidity plume is a crucial factor for the pelagic ecosystem of the Eastern Gulf of Cadiz, governing phytoplankton productivity.

Introduction

The Guadalquivir river is one of the largest rivers in Spain with a total length of 680 km and a drainage basin of 63822 km^2 (Granado-Lorencio, 1991). Located on the South-western coast of the Iberian Peninsula, the last 110 km of the river is the Guadalquivir estuary (Fig. 1), with a width of 800 m near its mouth, 150 m at the head, and a mean depth of 7.1 m. The estuary is a well-mixed mesotidal system with a longitudinal salinity gradient (Vanney, 1970), a semidiurnal tidal period and maximum tidal range of 3.5 m during spring tides (Díez-Minguito *et al.*, 2012). Tidal influence extends up the Guadalquivir as far as the Alcala del Rio dam, 110 km upstream from the river mouth at Sanlucar de Barrameda (Fig. 1). The original transport of material from the river basin has been drastically diminished by the construction of numerous reservoirs (the actual number of dams is 55). Annual discharges from Alcala del Rio dam have been strongly altered since the 1970s, in conjunction with the development of intensive agriculture and increased water demands. Terrestrial contributions to the estuary have decreased by about 60%, from 158.55 m^3/s (1931–1981) to 63.42 m^3/s (1981–2000) (Navarro *et al.*, 2012b). Discharges from Alcala del Rio dam represent approximately 80% of the estuary's freshwater supply. The substantial fluvial inputs associated with the discharge of Guadalquivir and also major rivers such as Guadalete, Guadiana and Tinto-Odiel are the main supply of the continental shelf of the Gulf of Cádiz (about 50 km wide from the East of Cape Santa Maria to the West of the Bay of Cadiz). The outer estuary and its coastal fringe are characterized by large loads of suspended matter resulting in high turbidity levels (Navarro *et al.*, 2012b) and high biological productivity (Navarro & Ruiz, 2006; Prieto *et al.*, 2009). This estuarine environment is ecologically and socio-economically important, resulting in high levels of pressure from numerous stakeholders (Bhat & Blomquist, 2004; Ruiz *et al.*, 2014). In addition, the Gulf of Cadiz region is characterized by strong seasonality and important synoptic weather events (Prieto *et al.*, 2009), which largely control chlorophyll concentrations and suspended material. Hence, there is a need for comprehensive studies on the natural functioning of the region so as to allow assessment of the potential consequences of anthropogenic actions. Enhancing knowledge about the factors influencing plume and bloom dynamics is important for coastal decision-makers, who are responsible for the challenging short-term management and long-term policy decisions to protect water quality and human health.

Estuarine plumes in coastal regions are significantly influenced by land-derived discharge emanating from an estuary (Morris *et al.*,1995). As a result, the turbidity plume may be biogeochemically characterized by the significantly inorganic nutrients and dissolved trace heavy metal enrichment compared with offshore waters (Mendiguchía *et al.*, 2007). At the same time,

sediment load and other substances from the rivers diminish light transmittance in the sea. Chemical transport and biogeochemical interactions within these areas may be key factors in several important processes, including phytoplankton production, eutrophication and global geochemical cycling. Estuarine plume region is usually located in the lower reaches of an estuary, where conditions are favourable for phytoplankton growth, resulting in enhanced biological activity. As a consequence, chlorophyll blooms in estuarine plumes (impacting adjacent coastal areas) can be potentially higher than in nearby ocean regions (Pennock, 1985). However, in turbid environments, light availability plays a fundamental role as the energy source for phytoplankton growth (Cloern, 1987), and it also influences phytoplankton community structure and algal competition (Reynolds, 1998).

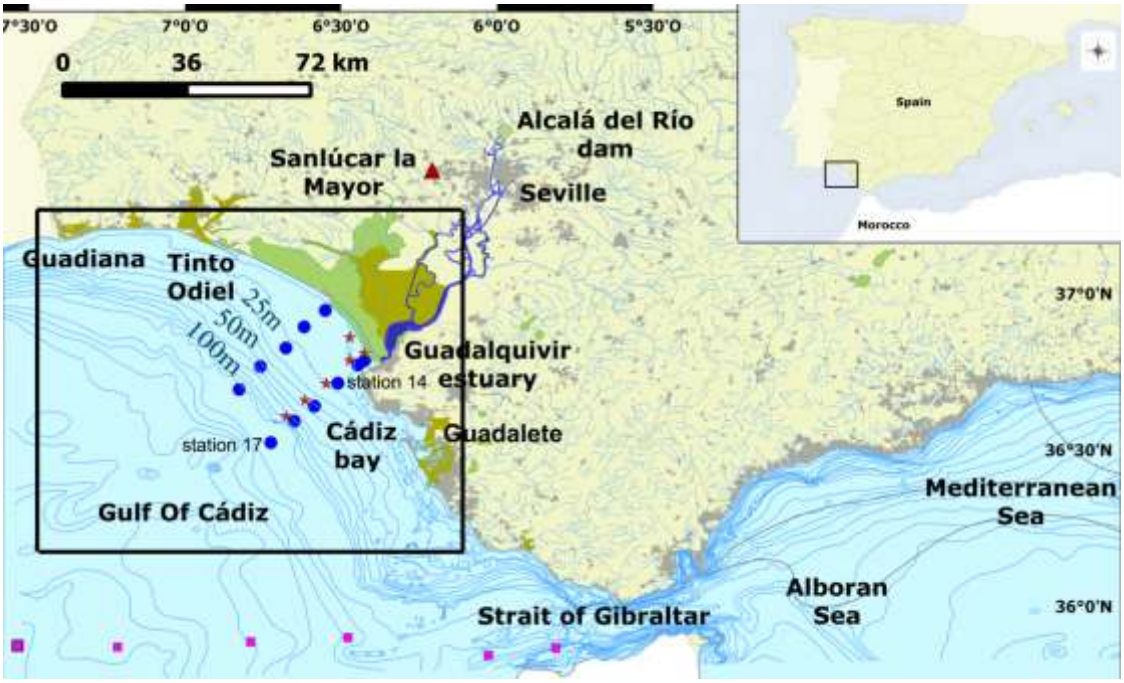

Figure 1. a) Location of the study area (SW Iberian Peninsula). b) Map showing the Gulf of Cadiz coastal area and the Guadalquivir estuary. Blue cycles, red stars and cyan squares correspond to the stations of Fluctuaciones, Reserva and SESAME oceanographic cruises, respectively. Green diamond is Alcala del Rio dam and red triangle is Sanlucar La Mayor meteorological station. Black rectangle delimits the Region Of Interest (ROI).

Furthermore, water clarity or transparency is important for the functioning of estuarine and coastal ecosystems; directly influencing primary productivity and acting as an indicator of nutrient loading and sediment dynamics (Ruiz *et al.*, 2013). Three main types of material are responsible for

the colour and transparency of the water: phytoplankton and suspended particles related to algal activity, non-algal suspended solids (Total Suspended Solids, *TSS*), and humic substances (Coloured Dissolved Organic Matter, *CDOM*). Sources of *TSS* include terrestrial inputs from river basins and anthropogenic discharges, such as industrial or urban effluents, fringing estuarine habitats, such as salt marshes, and resuspension of sediments. Often, these inputs are enriched with organic matter and nutrients (organic and inorganic), and depending on their source, may include potentially toxic compounds, such as heavy metals and pharmaceuticals (González-Mazo *et al.*,1998; Kidd *et al.*, 2007; Mendiguchía *et al.*, 2007). Hence, tracing the dynamics of river-estuary plumes within coastal zones can also assist in understanding the effects of a range of other potential stressors.

Integrated management of transitional and coastal waters is a priority, e.g. to comply with the EU water framework directive (WFD); however cost-effective methods to monitor water quality at large synoptic scales are lacking. Tools that can provide recurrent, widespread, and consistent observations, allowing the detection of changes in water conditions are sorely needed. Frequent synoptic information on suspended matter and chlorophyll is difficult to obtain using in situ monitoring networks, since the spatial distribution of suspended matter (such as chlorophyll) is highly heterogeneous. Furthermore, standard monitoring programs can be costly and time-consuming. As a consequence, sparse spatial and temporal data resolution is obtained, without guaranteeing a representative coverage of the variability in complex heterogeneous environments such as coastal waters and estuaries. During the past two decades, there have been significant advances in the development of satellite-borne sensors that can provide synoptic views of environmental parameters in coastal zones. Ocean colour remote sensing is now recognized as a suitable and cost-effective technique for the large-scale control of coastal water quality, based on optically active water characteristics. The collection and interpretation of earth observation imagery from optical sensors provides a unique set of capabilities for monitoring the state and trend of the environment, with great potential to overcome some of the spatial and temporal uncertainties inherent in in-situ measurements. However, satellite platforms also have limitations with respect to adequate spatial resolution, correct sensitivity, sensor calibration and image processing software; such limitations become more apparent when the data obtained are applied to specific coastal environments. Other limiting factors are atmospheric correction and bio-optical algorithms, since they are generally devised to convert ocean observations to consistent and accurately retrieved water-quality parameters only in specific regions (Sathyendranath, 2000; Miller *et al.*, 2005). The ocean colour of the Guadalquivir estuary is affected by a variety of processes typical of environments with Case-II waters (i.e. the optical properties do not co-vary with chlorophyll

content), including phytoplankton blooms, sediment plumes, and other episodic phenomena, such as runoff events (Morel *et al.*, 2006).

The aim of the present study is to use Moderate Resolution Imaging Spectroradiometer (MODIS) imagery to derive water-quality parameters (Total Suspended Solids and chlorophyll) related to phytoplankton dynamics and the pelagic ecosystem in the coastal zone adjacent to the Guadalquivir estuary. The work is motivated by the need to understand and predict the phenomena that control the exchange of riverine-estuarine material with the coastal region. Results of the validation of remotely-sensed observations and in situ measurements are presented, allowing the evaluation of the effectiveness of the MODIS sensor for monitoring key water quality parameters in the vicinity of a large highly turbid estuary. We then investigate the turbidity plume and phytoplankton bloom dynamics using more than 11 years of high temporal resolution satellite observations. Finally, by matching the major modes of spatio-temporal variability derived from the images with meteorological and oceanographic data sources, we provide indications as to how local climatology and physical oceanography modulate the role of the Guadalquivir river in the regional pelagic ecosystem of the Eastern Gulf of Cadiz.

Materials and Methods

Satellite Imagery

Satellite ocean colour images were obtained from the MODIS sensor on the Aqua multispectral platform. This sensor provided daily or better coverage of the Gulf of Cadiz study area, although clear-sky images were obtained for about half of the days during the period of interest. All available images of chlorophyll concentration ([*Chl*], mg/m^3), Remote Sensing Reflectance of the 555 nm wavelength band (*Rrs555*, sr^{-1}), diffuse attenuation coefficient for downward irradiance at 490 nm wavelength (Kd_{490}, m^{-1}), and the Photosynthetically-Active Radiation (PAR, Einstein / m^2 / day) at medium spatial resolution (1 km), covering the region of interest and spanning the years from 2003 to 2013, were ordered and downloaded via-ftp from the Ocean Color Website (http://-oceancolor.gsfc.nasa.gov). The MODIS algorithm to retrieve [*Chl*] corresponds to OC3M (O'Reilly *et al*., 2000).

SeaDAS image analysis software (SeaWiFS Data Analysis System, version 6. (http://-seadas.gsfc.nasa.gov) was used to read and remap the data to a Mercator projection at 1 km resolution. Upon downloading MODIS data to a local system, the data were displayed to assess image quality. During data processing, checks are made for different defined conditions. We used the standard SeaDAS algorithm with the ''LAND'' and ''CLOUD'' flags to remove the data unintentionally interpolated among others applied as masks with L2_flags, indicating whether any

algorithm failure or warning conditions occurred for any pixel. These additional and relevant quality control tests were used to discard all suspicious and low-quality data points, thus ensuring that only the most reliable data were retained for analysis (see Table 1 for specific information). They correspond to the flags masked during Level 3-ocean colour processing.

Table 1. List of L2_flags used in the masking process to assure the quality control of the data retained for analysis. These correspond to the flags masked at Level 3-ocean colour processing.

Flag	Condition
LAND	pixel is over land
CLOUD	cloud contamination
ATMFAIL	atmospheric correction failure
HIGLINT	high sun glint
HILT	total radiance above knee
HISATZEN	large satellite zenith
CLDICE	clouds and/or ice
COCCOLITH	coccolithophores detected
HISOLZEN	large solar zenith
LOWLW	very low water-leaving radiance
CHLFAIL	chlorophyll algorithm failure
NAVWARN	questionable navigation
MAXAERITER	maximum iterations of NIR algorithm
CHLWARN	chlorophyll out of range
ATMWARN	atmospheric correction is suspect

These generated data files were edited and analyzed using MATLAB 7.10.0 - R2010a (c) software, and the study area was then subset from the images to a Region Of Interest (ROI) with geographic coordinates 36.25º N - 37.25º N, 7.5º W - 6.1º W (Fig. 1). *Rrs555* images were converted to the normalized water-leaving radiance (*nLw555*, mW/cm^2 μm sr, normalized to a zenith viewing geometry at the mean Earth-Sun distance) as $nLw555 = F_0 \times Rrs555$, where F_0 is the annual spectral mean extraterrestrial solar irradiance, also called the solar constant. For the Aqua 545-565 nm band, the F_0 value corresponds to 186.09 mW/cm^2 μm (Neckel, 1984).

In this work, the river plume was operationally defined as a water mass with optical properties clearly different from those of the water masses in the vicinity of the estuary mouth. For this backscattering resulting in high values of upwelling radiation in the green-yellow band (λ = 555 nm) was used. The *nLw555* product is commonly utilized to distinguish river plumes, and was

strongly correlated with *TSS* concentration ([*TSS*]) in near-surface waters (Lahet *et al.*, 2001; Loisel *et al.*, 2001; Toole & Siegel, 2001; Otero & Siegel, 2004; Nezlin & Di Giacomo, 2005; Nezlin *et al.*, 2005; Thomas & Weatherbee, 2006). For each scene, the plume extension was delimited by thresholding of the *nLw555* image. The threshold between "plume boundary" and coastal waters was defined as 1.3 mW/cm^2 μm sr (Otero & Siegel, 2004; Nezlin & DiGiacomo, 2005; Nezlin *et al.*, 2005; Valente & da Silva, 2009). Visual examination of a subset of images suggested that this value adequately defined the river plume (data not shown). Hence, this work has focused on the plume areas using indicator *nLw555* values as a proxy of [*TSS*]. Quantitative estimation of the plume extent was made by counting the number of pixels with *nLw555* values >1.3 mW/cm^2 μm sr and multiplying by the pixel size (1 km^2).

The diffuse attenuation coefficient for photosynthetically active radiation (Kd_{PAR}) can be routinely derived from present day remote sensing based on estimates of Kd_{490}. Kd_{PAR} and was calculated by two relationships (Morel *et al.*, 2007; Pierson *et al.*, 2008). Kd_{PAR} was used to estimate the lower limit of the euphotic zone (defined as the depth where PAR represents 1% of surface radiation- $Z_{1\%}$) ($Z_{1\%}$=4.6/ Kd_{PAR}), following the Lambert-Beer law (Kirk, 1983). This procedure was performed for two stations (Fig. 1): nearshore station 14 (36.7133º N- 6.5100ºW, 14 km distance to coast and ~25 m depth) and offshore station 17 (36.4983º N- 6.7583ºW, 43 km distance to coast and >200 m depth). *Bias* and *rmse* (root mean square error) were noticeably similar for both equations (*bias* of -0.32 m and 1.08 m and *rmse* of 0.65 m and 2.66 m, for station 14 and 17, respectively) and therefore $Z_{1\%}$ by Morel *et al*. (2007) was the only one presented.

Only images with more than 85% cloud free pixels in the ROI were used in the 11-year time series. The final products corresponded to the images ([*Chl*] and *nLw555*) after the comprehensive filtering, which are used in the validation process. Only pixels with [*Chl*] $\leq$ 20 mg/m^3 were considered, i.e. lower than or equal to the highest values occurring in the region (maximum value of the field campaigns). Extremely high chlorophyll values are not usually detected in the area (Sánchez-Lamadrid *et al.*, 2003; Prieto *et al.*, 2009). Daily images were further combined into 8-day and monthly means, as well as monthly climatologies and a total climatology for the 11-year period.

In-situ data

Water samples were collected near the surface (depths < 5 m) with a rosette sampler during several oceanographic field cruises in the Gulf of Cadiz (see Table 2 for detailed information). One sample for each station was collected, which were located within the first optical depth. At each sampling site, a CTD cast was performed with a Seabird Electronics Inc (Bellevue, WA, USA) CTD-SBE19plus to measure temperature, conductivity and depth. Chlorophyll analysis was performed by filtering samples through Whatman GF/F glass fiber filters (0.7 mm pore size),

extracting in 90% acetone, and measuring the [*Chl*] by standard fluorometric methods (Parsons *et al.*, 1984) using a Turner Designs Model 10. The fluorometer was calibrated using pure chlorophyll from the cyanobacterium *Anacystis nidulans* (Sigma Chemical Co.) with the concentration determined spectrophotometrically. Samples to measure [*Chl*] were filtered on board and immediately deep-frozen. Pigment concentrations were subsequently determined at the ICMAN-CSIC (Marine Science Institute of Andalucia, Cadiz) laboratory within a few days of the survey. Total concentrations of suspended solids were measured gravimetrically on pre-weighted Whatman GF/F filters after rinsing with distilled water according to JGOFS protocols (UNESCO, 1994). In situ observations were chosen based on metadata indications of data quality. This selection criterion removed samples at certain situations: depth > 5m, evidence of measuring problems and defective filters. As a result, coastal [*Chl*] and [*TSS*] information was selected from the "Fluctuaciones" and "Reserva" cruises. In the "SESAME" oceanic campaign, only [*Chl*] measurements were carried out. The distance between coastline and sampling stations ranged from 3 km to 35 km (average of 19 km) in the case nearshore campaigns (Reserva and Fluctuaciones) and from 10 km to 140 km in the case of the SESAME oceanic campaign. The depth at these positions varied from 15 m minimum to 150 m maximum (>1000 m in SESAME). Moreover, the Mixed Layer Depth (MLD) was estimated from the temperature and density profiles of the CTD. Several criteria have been used in the literature for the definition of MLD and a simple one is based on the changes in the properties of temperature or density with depth (Kara *et al.*, 2000). We have used the property difference in this work to define MLD for both temperature and density (difference of 0.5º and 0.125σ, respectively) since they are widely used (Kara *et al.*, 2000). In addition, MLD data have been obtained from the operational datasets routinely produced by the Global Ocean Data Assimilation System (GODAS) downloaded at http://www.esrl.noaa.gov/psd//gridded. The binary datasets corresponded to a monthly composite from 2003 to 2013. The arithmetic mean was calculated for the pixels corresponding to the study region (2º latitude x 0.6º longitude).

Table 2. Oceanographic field cruises conducted in the Gulf of Cadiz region. Specifications of data for Total Suspended Solids (*TSS*) and chlorophyll (*Chl*) validation purposes.

Campaign	**Zone**	**Vessel**	**Date**	**Measurements**
Reserva	Coastal	RV Regina Maris	July 2002-September 2004	*TSS - Chl*
Fluctuaciones	Coastal	RV Regina Maris	May 2005-May 2007	*TSS - Chl*
SESAME I	Ocean	RV Regina Maris	April 2008	*Chl*
SESAME II	Ocean	BIO García del Cid	September 2008	*Chl*

Daily mean discharge at the Alcala del Rio dam (Fig. 1, the main freshwater input to the Guadalquivir estuary), was obtained from the "Agencia Andaluza del Agua" (http://www-.chguadalquivir.es/saih/, station code E60). Daily precipitation measured at an automatic meteorological station in Sanlucar la Mayor (Fig. 1, 37.422º N-6.254º W, station code 13) were obtained from the regional Agroclimatic Station Network (http://www-.juntadeandalucia.es/agriculturaypesca/ifapa/ria).

Data on the North Atlantic Oscillation (NAO), a climatic phenomenon that greatly contributes to variability in the weather system in the North Atlantic and Europe, was provided by the Climate Analysis Section (NCAR, Boulder, USA), (http:// www.cgd.ucar.edu/cas/jhurrell/indices.html) (Hurrell, 1995). The winter (December through March) index of the NAO is based on the difference of normalized sea level pressure (SLP) between Lisbon, Portugal and Stykkishol- mur/Reykjavik, Iceland since 1864.

Validation of satellite information

To determine the quality of satellite-derived estimations of [*Chl*] and [*TSS*] in coastal waters, validation was carried out using in situ ground truth measurements acquired during several oceanographic field cruises (Table 2). The high spatio-temporal variability of estuarine water properties means that matching in situ observations with images is challenging. In this regard, different levels of spatial-temporal averaging were tested. Data match-ups were made by selecting *nLw555* and [*Chl*] values for the corresponding pixel, and also averaging the surrounding grid nodes using a 1x1 and 2x2 pixel box centred on the coordinates of the field measurements. Time differences between satellite overpasses and in situ sampling were grouped into time intervals of <1.5h, 1.5-3h, and 3-5h. These validation procedures are similar to validation works carried out by other authors (Bailey & Wang, 2001; Sá *et al*., 2008; Jamet *et al.*, 2011). Testing suggested that improved correlations between Remote Sensing (RS) and in situ-derived [*Chl*] and [*TSS*] values were observed when the shortest temporal separation window (1.5h) and smallest spatial scale (a single pixel) were used (data not shown). Hence, validation presented here only uses this limited number of higher quality match-ups. For all match-ups considered, the following statistical parameters were calculated to define the error associated with MODIS estimations; Pearson's coefficient of correlation (*r*), root mean square error (*rmse*), *bias*, maximum, and minimum values:

$$rmse = \sqrt{\frac{\Sigma(x_s - x_i)^2}{n}}$$

$$bias = \frac{\sum[\![(x]\!]_s - x_i)}{n}$$

where x_i and x_s correspond to the in situ and satellite values, respectively.

An exponential adjustment was utilized in the *TSS* - *nLw555* regression because, for large [*TSS*] levels the fit is not linear. This procedure helps with possible overcorrection for atmospheric effects at high [*TSS*] values, when the water reflectance contribution may no longer be negligible at larger wavelengths (Ruddick *et al*., 2000). We performed a linear regression of in situ data against MODIS [*Chl*] observations to estimate the precision of retrieval. In addition, we also compared MODIS data with the offshore cruises ("SESAME" I and II, >30km from estuary mouth) in order to characterize the quality of satellite products both in coastal waters and offshore. A previous validation exercise conducted by Navarro & Ruiz (2006) between in situ [*Chl*] measurements at 10 m (2000-2002) and Sea-viewing Wide Field-of-view Sensor (SeaWiFS) data exhibited good correlation.

Empirical Orthogonal Function (EOF) analysis

Composites of *nLw555* and [*Chl*] (8-day composite means from January 2003 to June 2013) were analyzed by decomposing their variability using the EOF (Lorenz, 1956). This methodology simplifies the dimensions of large datasets, including ocean colour images (Baldacci *et al.,* 2001; Brickley & Thomas, 2004; Xu *et al*., 2011), to a few significant orthogonal (spatially uncorrelated) modes of variability. This procedure was used to study the Gulf of Cadiz offshore region with [*Chl*] imagery from SeaWiFS imagery (Navarro & Ruiz, 2006). EOF procedures assume the data to be complete, i.e. without gaps. Therefore, previous to performing the analysis, gaps were filled by inserting the mean of the surrounding 8 pixels or 24 pixels. The final data set resulted in a total of 482 8-day composite images. The software used was MATLAB 7.10.0 with the code "*pcatool*" (Björnsson & Venegas, 1997).

EOF analysis has been extremely useful for examining ocean colour images, which have long time series and significant spatial variability, like the data sets used in this study. The importance of the EOF modes for the spatial and temporal variability was tested following the methodology by North *et al.* (1982). The interpretation of EOF modes is not always obvious, especially with difficult non-periodic signals, and should be explained with caution. Typically, the smallest modes explain much of the variance and their associated patterns are the simplest to interpret. In order to examine in detail the temporal variability of the amplitudes of each mode and identify the forcing factors, diverse oceanographic and meteorological variables have been studied and further analyzed to detect the main mechanisms of each mode. 8-day and monthly averages of the variables were contrasted with the temporal amplitudes of each mode. Statistics for each pair include the

correlation determined by Pearson's coefficient of correlation (*r*) and p-value to test if the correlation is statistically significant.

Results

Validation of remotely retrieved Total Suspended Solids and Chlorophyll

One of the objectives of this study was to validate MODIS-derived water-quality parameters in the coastal region influenced by the Guadalquivir estuary. Even though a large number of in situ measurements were potentially available for the region, only 53 and 66 pairs (match-ups) for [*TSS*] and [*Chl*], respectively, were considered suitable for validation following the selection procedure and quality control of both in situ and satellite data described in Materials and Methods.

In situ [*TSS*] ranged between 28.1 and 130.4 mg/L and *nLw555* ranged between 0.1861 and 4.8011 mW/cm^2 μm sr. Both variables were highly positively correlated (Fig. 2a, $r = 0.96$, $p < 0.001$) and a non-linear predictive function for [*TSS*] (*TSS* (mg/L) =26.68*exp(0.3283**nLw555*)) gave a standard error for RS-derived [*TSS*] estimates of 5.0 mg/L. Hence, [*TSS*] appeared to be predicted with relatively good accuracy in both the offshore and nearshore regions close to the Guadalquivir estuary.

In situ and RS-derived [*Chl*] ranged from 0.055 to 4.18 mg/m^3 and 0.095 to 4.99 mg/m^3, respectively, and were positively correlated (Fig. 2b, $r = 0.79$, $p < 0.001$). Linear regression of observed and predicted values (Fig. 2b, logarithmic scale applied) revealed a *bias* of 0.63 mg/m^3 and *rmse* of 1.10 mg/m^3 (slope = 1.19). To highlight the increasing *bias* observed for nearshore to offshore RS-derived [*Chl*], a subset of 12 pairs at least 30 km offshore from the estuary mouth were also compared (Fig. 2b, "SESAME"). Whilst maximum [*Chl*] values (0.82 mg/m^3) were lower for this subset, the range of values appeared relatively comparable to nearshore values. Pairs fell close to the 1:1 line, *bias* was insignificant (*bias* ~ 0 mg/m^3) and the derived *rmse* was an order of magnitude smaller (0.086 mg/m^3).

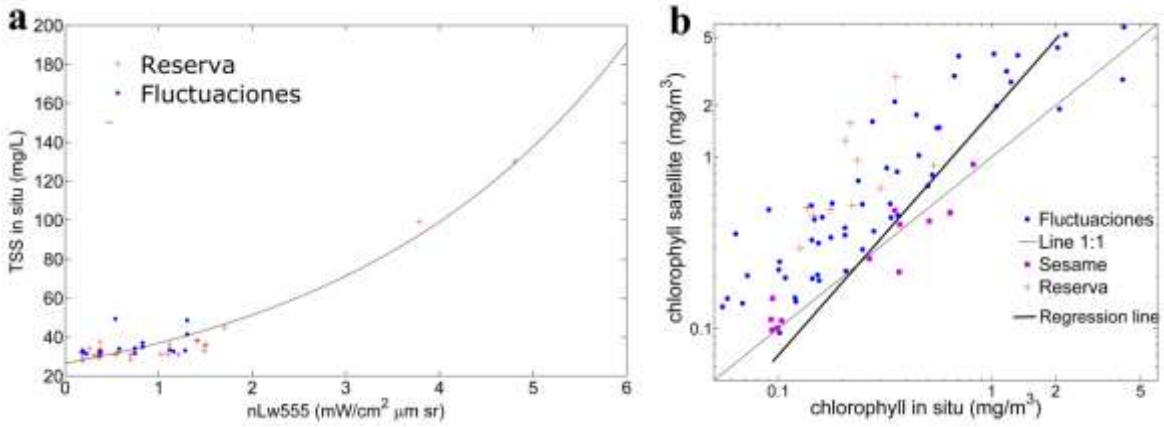

Figure 2. a) Exponential relationship between at-sensor normalized water leaving reflectance at 555 nm *(nLw555*, mW/cm^2 µm sr) and in situ Total Suspended Solids (*TSS*, mg/L) from Fluctuaciones (dots) and Reserva (crosses) coastal campaigns. Fitted curve: *TSS* (mg/L) = 26.68*exp(0.3283**nLw555*), *n* = 53, *standard error* = 5.0 mg/L, *r* = 0.96 ($p < 0.001$). b) Scatter plot showing the comparison between in situ and at-sensor chlorophyll concentrations (*Chl*, mg/m^3) for Fluctuaciones (dots) and Reserva (crosses) coastal cruises (logarithmic axis). Regression line: *Y* = 0.49 + 1.28* *X* , *n* = 66, *rmse* = 1.10 mg/m^3, *bias* = 0.63 mg/m^3, *r* = 0.79 ($p < 0.001$). Squares correspond to SESAME offshore stations. The line corresponds to 1:1 ratio.

Total Suspended Solids and Chlorophyll variability patterns

Regional satellite climatology of the Gulf of Cadiz was computed on the basis of the mean annual cycle for eleven years of MODIS data (2003-2013). Maximum *nLw555* values were located within the vicinity of the Guadalquivir and Guadalete river mouths (Fig. 3a, 4.2 and 3.9 mW/cm^2 µm sr, [*TSS*] of 103.6 and 92.2 mg/L respectively) whereas minimum values were detected offshore (0.24 mW/cm^2 µm sr, [*TSS*] = 28.7 mg/L). The typical salient pattern indicated that water clarity was usually low in the external part of the mouth, and increased offshore. The monthly climatology clearly shows the seasonal strengthening and weakening of this general pattern (Fig. 4). In winter and early spring (November- March), high values in the Guadalquivir estuary and Cadiz Bay extended along and offshore from the coastline to form a band (plume) (>1.3 mW/cm^2 µm sr). During spring and summer, ambient waters generally had low *nLw555* values with highly localized plumes restricted to the river mouth. The extent of riverine discharges during storm flood events can also be assessed using this limit, with the largest plumes found near the river mouth and further south. Extreme turbid episodes during the study period took place during autumn and winter 2007 and throughout 2010 and 2011.

Total [*Chl*] climatology (Fig. 3b) showed that maximum concentrations (around 14 mg/m^3) were observed close to the coast (specially near the estuary), with values decreasing to a minimum of about 0.3 mg/m^3 offshore. Examining the monthly climatology (Fig. 5) revealed that higher [*Chl*] values tended to be observed in the North of the study region near the coast, especially near the Guadalquivir estuary, and lower values usually occured South of Cadiz Bay. Monthly mean [*Chl*] values peaked during March to May within the region in terms of magnitude and coverage (bloom ~40 km offshore). In addition, the offshore region presented highest [*Chl*] values (more than 0.5 mg/m^3) during March, indicating an extensive phytoplankton bloom throughout the region. During summer, offshore [*Chl*] values were low and high values were confined to shallow regions near the coast.

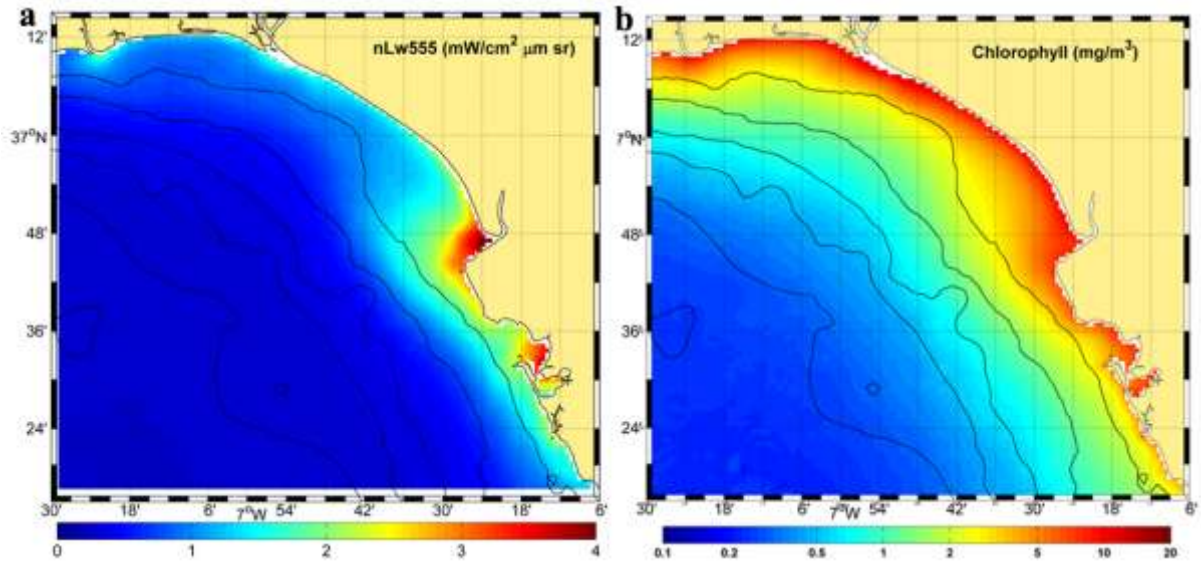

Figure. 3. Total climatology of MODIS (2003-2013): a) Normalized water leaving reflectance at 555 nm (*nLw555*, mW/cm^2 µm sr), b) Chlorophyll (*Chl*, mg/m^3). Lines represent bathymetric isolines for the Gulf of Cádiz at the intervals of 20m, 50m, 100m, 200m and 500m.

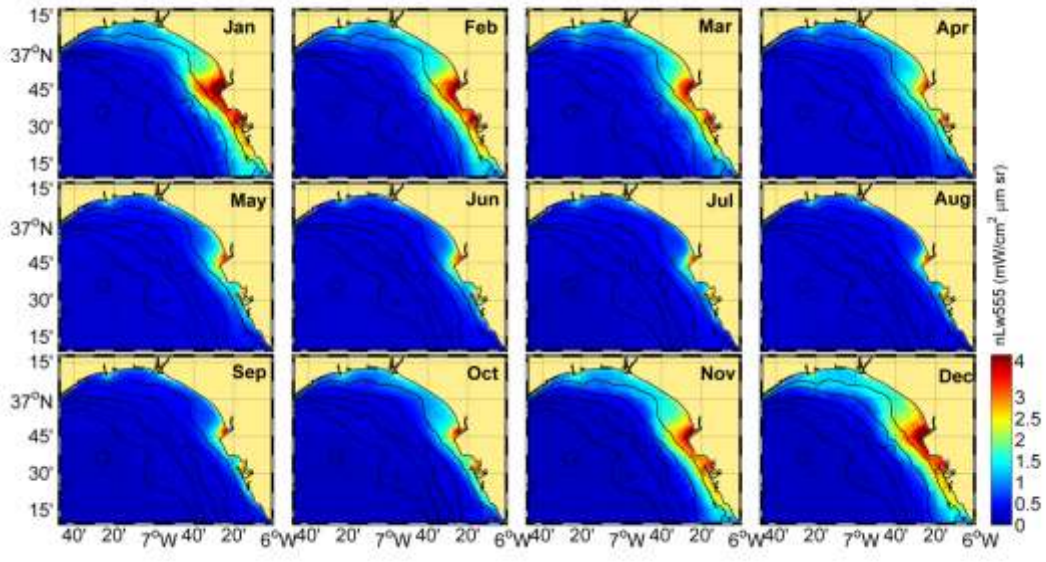

Figure. 4. Monthly climatology (2003-2013) of MODIS normalized water leaving reflectance at 555 nm (*nLw555*, mW/cm^2 µm sr). Lines represent bathymetric isolines for the Gulf of Cádiz at the intervals of 20m, 50m, 100m, 200m and 500m.

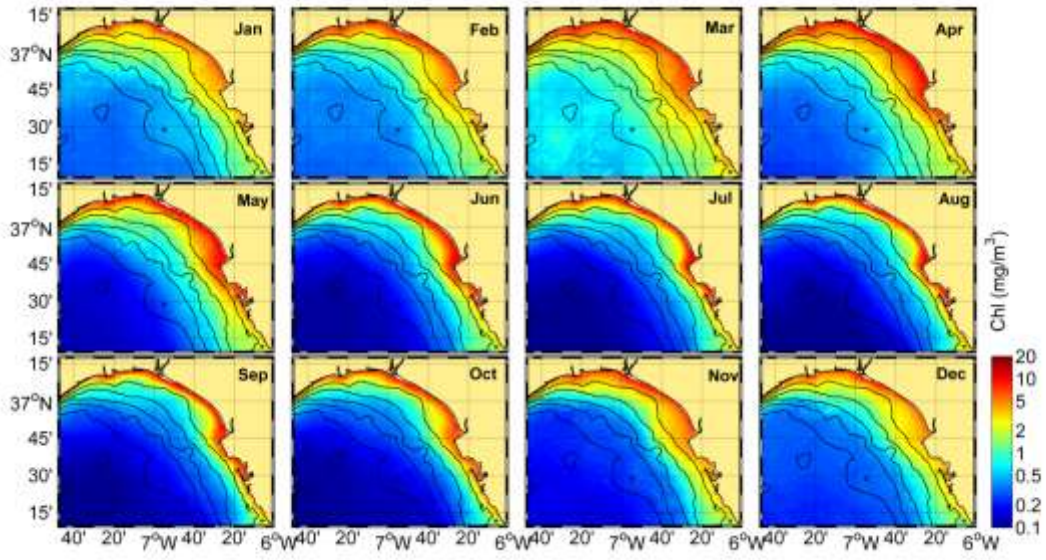

Figure. 5. Monthly climatology (2003-2013) of MODIS chlorophyll (*Chl*, mg/m^3). Lines represent bathymetric isolines for the Gulf of Cádiz at the intervals of 20m, 50m, 100m, 200m and 500m.

Modal analyses of nLw555

EOF analysis revealed three significant (North *et al.*, 1982) modes for *nLw555*, each explaining 60.7%, 6.5% and 4.7% of the variance, respectively (71.9% of the total variance, Fig. 6). Spatial coefficients of the three modes are plotted in Fig. 7, where colour intensity is directly related to the amplitude of the coefficient (intensity of the phenomenon). Temporal amplitudes of the EOF modes are presented in Fig. 8.

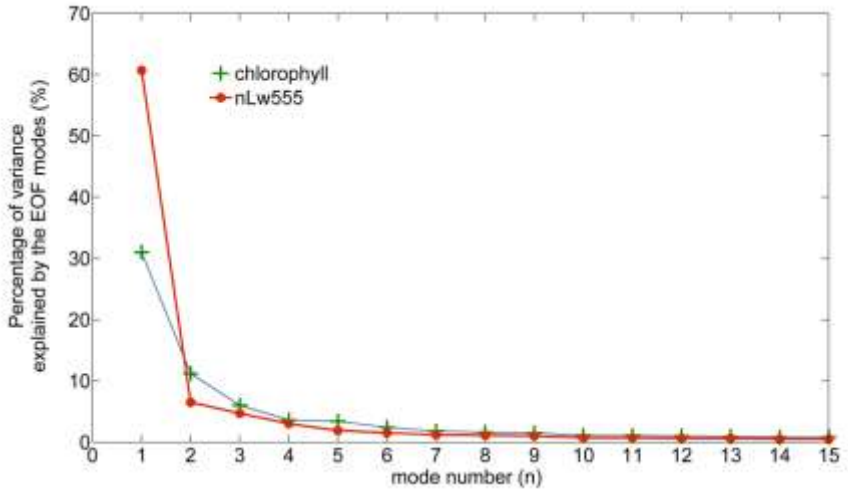

Figure. 6. Percentage of variance explained by the EOF modes 1-3 for normalized water leaving reflectance at 555 nm (*nLw555*) and chlorophyll (*Chl*).

The first *nLw555* EOF mode was positive throughout the region with the highest values occurring in a wide band extending from North of the Guadalquivir estuary to South of Cadiz Bay (Fig. 7a). Particularly high values were found close to Cadiz bay. Spatial coefficients near zero were observed offshore, implying more stability in *nLw555* values. The amplitude function displayed seasonal oscillations between winter and summer (Fig. 8a), with positive and negative amplitudes generally in autumn-winter and spring-summer, respectively. Inter-annual variation in the magnitude of positive amplitudes was apparent, with the highest values observed in winter 2010 (January and December), whilst the magnitude of negative amplitudes was similar through the time-series. This suggests that more pronounced inter-annual variability during autumn-winter was observed closer to the coast.

The spatial pattern associated with the second *nLw555* mode indicated two zones (Fig. 7b): The first zone (Z_{2S}) had positive coefficients that centred on the region just offshore of the Guadalquivir

estuary mouth and extended further South in a confined coastal fringe. The second zone (Z_{2N}) had negative amplitudes expanding all along the coast further offshore and occupying the region north of Z_{2S}. Offshore waters had values around zero. The temporal time series of the second mode amplitude (Fig. 8b) exhibited a similar seasonal trend to the first mode, but in contrast to the first mode, included inter-annual variations in the magnitude of negative amplitudes, suggesting inter-annual variability during spring-summer in the zone north of the estuary.

The third *nLw555* mode also suggested two main spatial zones (Fig. 7c); from the northwest coast to the mouth of the river, values were negative (Z_{3N}), whereas from the limit of Z_{3N} to the most southerly area, values were positive (Z_{3S}). Whereas minimum values in Z_{3N} were observed near shore, in Z_{3S} maximum values were further offshore. The amplitude function again had a seasonal similarity to the first mode (Fig. 8c), but was more irregular. Maximum positive amplitudes were similar in magnitude to the second mode, whereas negative amplitudes were in between the other modes.

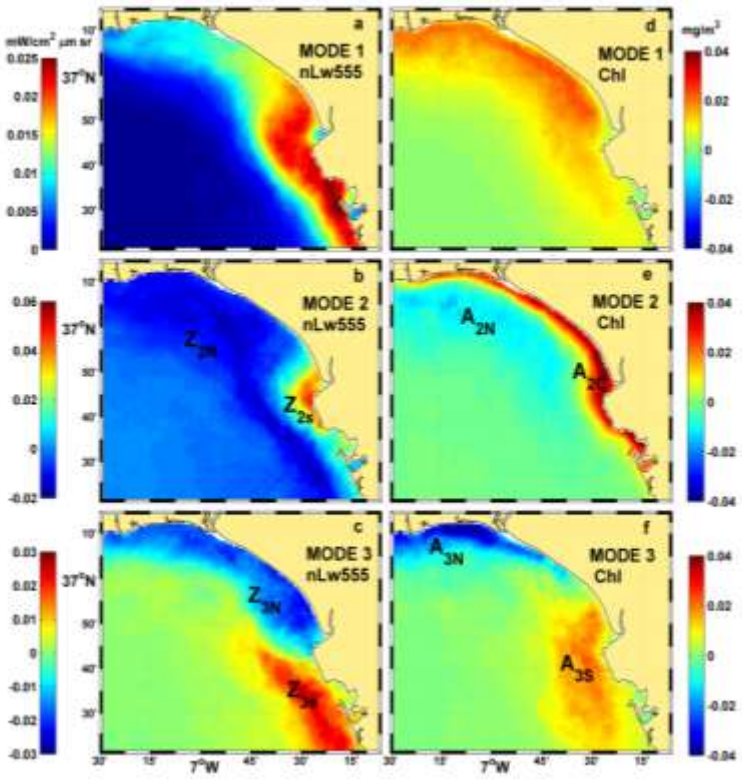

Figure. 7. Spatial coefficient maps corresponding to the a) First, b) Second, and c) Third mode from EOF analysis of normalized water leaving reflectance at 555 nm (*nLw555*, mW/cm^2 μm sr); the same for the d) First, e) Second, and f) Third mode from EOF analysis of chlorophyll (*Chl*, mg/m^3).

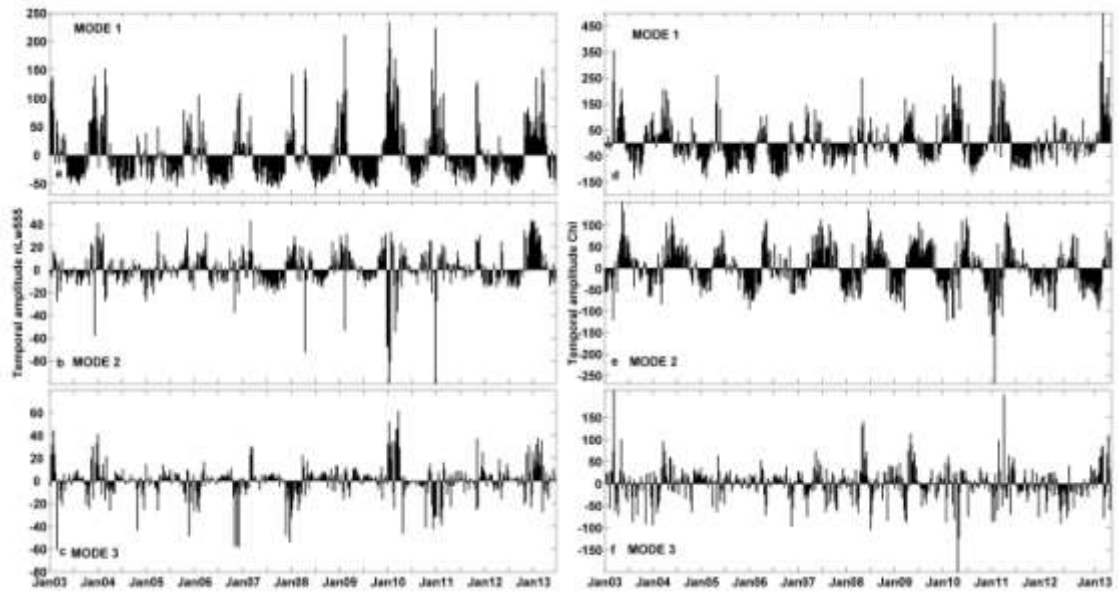

Figure. 8. Amplitude function for the a) First, b) Second, and c) Third mode from EOF analysis of normalized water leaving reflectance at 555 nm (*nLw555*); the same for the d) First, e) Second, and f) Third mode from EOF analysis of chlorophyll (*Chl*).

Table 3. Description of the different zones distinguished by the second and third EOF modes of normalized water leaving reflectance at 555 nm (*nLw555*) and chlorophyll (*Chl*). Further details are given in the text.

Name	Variable	Mode	Region	Spatial Coefficient
$\mathbf{Z_{2N}}$	*nLw555*	2	North	Negative
$\mathbf{Z_{2S}}$	*nLw555*	2	South	Positive
$\mathbf{Z_{3N}}$	*nLw555*	3	North	Negative
$\mathbf{Z_{3S}}$	*nLw555*	3	South	Positive
$\mathbf{A_{2C}}$	*Chl*	2	Coastal	Positive
$\mathbf{A_{2N}}$	*Chl*	2	North	Negative
$\mathbf{A_{3S}}$	*Chl*	3	South	Positive
$\mathbf{A_{3N}}$	*Chl*	3	North	Negative

Comparison of the time-series of *nLw555* first mode amplitudes to daily rainfall (mm), daily discharges from Alcalá del Río dam (m^3/s) and the NAO index (Fig. 9), revealed that positive amplitudes, generally observed in late autumn, winter and early spring, tended to be associated with

periods of high rainfall (r = 0.47, p < 0.001, Table 4), river discharges (r = 0.50, p < 0.001, Table 4) and negative NAO values (r = -0.41 and -0.52, p < 0.001, Table 4). Negative *nLw555* first mode amplitudes generally occurred in the usually drier late spring and summer months. It is noteworthy that low-medium magnitude rainfall events do not tend to match well with discharges to the estuary because of the intense regulation by several reservoirs of the Guadalquivir basin. Furthermore, medium sized discharges may occur without intense local rainfall; for example, see late autumn-winter 2006. However, extreme rainfall events were clearly marked by high discharges from the dam (a protection measure) and clearly coincided with very negative values of the NAO index in 2010, 2011 and 2013 (Fig. 9e). Additionally, a high correlation was found between monthly mean plume area and monthly averaged precipitation (r = 0.63, p < 0.01, Table 4) and monthly river discharge (r = 0.42, p < 0.01, Table 4). Hence, *nLw555* first mode seems to represent variability associated with rainfall and the subsequent terrestrial discharges to the Guadalquivir estuary. The second *nLw555* mode, which showed a similar temporal pattern, was also positively correlated with daily precipitation (r = 0.36, p < 0.02) and discharges (r = 0.41, p < 0.01), suggesting it represented the influence of similar factors.

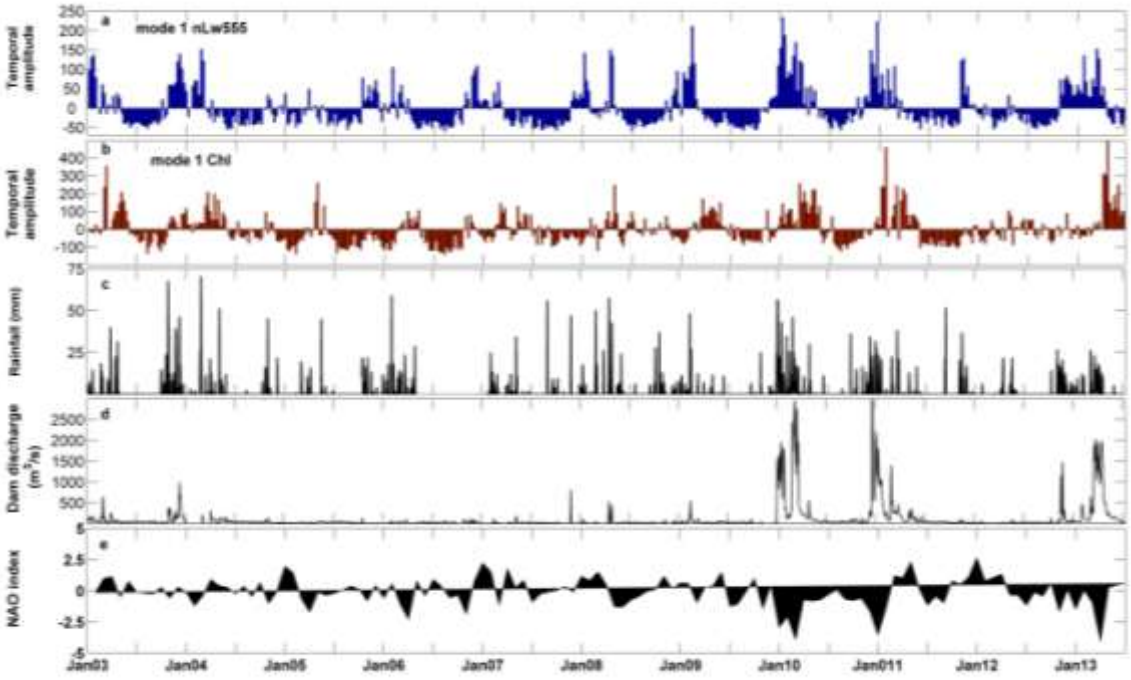

Figure. 9. Time series of: a) Temporal amplitude of EOF mode 1 for normalized water leaving reflectance at 555 nm (*nLw555*, mW/cm^2 μm sr), b) Temporal amplitude of EOF mode 1 for chlorophyll (*Chl*, mg/m^3), c) Daily precipitation average measured at the meteorological station Sanlucar La Mayor (mm), d) Daily river discharge from the Alcala del Rio dam (m^3/s), and e) Monthly time series of North Atlantic Oscillation (NAO) inde

Table 4. Pearson's correlation coefficient (*r*) and p-value among the temporal amplitudes of the EOF modes and precipitation from the meteorological station Sanlúcar La Mayor, discharge from Alcalá del Río dam, the climatic index North Atlantic Oscillation Index (NAO) and plume area. More information is given in the text.

Variables	**Precipitation**		**Discharge**		**NAO**		**Plume area**		**PAR**	
	r	*p*	*r*	*p*	*r*	*p*	*r*	*p*	*r*	*p*
Mode 1 *nLw555*-8-day	0.47	< 0.001	0.50	< 0.001	-		-		-0.59	<0.0001
Mode 1 *nLw555*-monthly	0.46	< 0.001	0.51	< 0.001					-0.62	<0.0001
Mode 2 *nLw555*-8-day	0.36	< 0.02	0.41	< 0.01					-0.18	<0.05
Mode 1 *Chl*-8-day	0.38	< 0.001	0.47	< 0.001	-0.017	< 0.01			0.05	>0.05
Mode 2 *Chl*-8-day	-		-				-0.55	< 0.001	0.67	<0.0001
Mode 2 *Chl*-monthly	-		0.37	< 0.01					0.71	<0.0001
Mode 1 plume area-monthly	0.63	< 0.01	0.42	< 0.01	-0.52	< 0.001				
Mode 1 mean *nLw555*-monthly					-0.41	< 0.001				
Mode 1 mean *Chl*-monthly					-0.017	< 0.01				

Modal analyses of Chlorophyll

EOF analysis of 8-day composite [*Chl*] images revealed three statistically significant modes, explaining 31%, 11% and 6% of total variance, respectively (48% of total variance, Fig. 6). The first spatial mode was positive throughout the region, with maximum values observed nearshore and decreasing values offshore, as well as to the South of the region (Fig. 7d). High and low [*Chl*] values on the continental shelf were associated with positive and negative [*Chl*] first mode coefficients observed in winter-spring and summer, respectively (Fig. 8d). Maximum positive amplitudes showed inter-annual variations, with the highest values observed in winter 2011 and spring 2013, whereas negative amplitudes were of a similar magnitude throughout the time-series.

Similarly to the second *nLw555* mode, the second [*Chl*] mode could be classified into two different zones (Fig. 7e). The first zone (A_{2C}) with positive spatial coefficients was located along the coastal fringe, from Isla Cristina (to the north) to Cadiz Bay (to the south), and coincided with the maximum [*Chl*] observed in the monthly composites (Fig. 3b). The second zone (A_{2N}) was

located further offshore, extending from the North to the Guadalquivir estuary. This zone was characterized by a negative spatial coefficient, suggesting that negative temporal amplitudes represented higher [*Chl*] values, which are associated with the autumn phytoplankton bloom, as observed in the monthly composites (Fig. 5). Coefficients located further offshore (values ~ 0) suggested relative stability in [*Chl*]. [*Chl*] second mode temporal amplitudes showed a marked seasonality; with positive values during spring-summer and negative during the rest of the year (Fig. 8e). As for *nLw555* second mode, inter-annual variation in the magnitude of negative values was observed, whereas positive peaks were rather constant.

The spatial distribution of [*Chl*] third mode also differentiated two zones (Fig. 7f): The first (A_{3S}) corresponded to a wide area from the Guadalquivir mouth to the South, with positive coefficients. The second (A_{3N}), with negative coefficients, was a narrow band along the coast located further North, centred on the mouths of Tinto-Odiel rivers. Offshore waters again suggested relatively stable [*Chl*] compared to the rest of the region. Examination of the temporal amplitudes of this mode (Fig. 8f) suggested an irregular pattern compared with the other modes and large inter-annual variations.

Comparison of the time-series of [*Chl*] first mode amplitudes with daily rainfall (mm), discharges from the Alcala del Rio dam and the NAO index (Fig. 9, Table 4), revealed that positive amplitudes, generally observed in late autumn, winter and early spring, tended to be associated with periods of high rainfall (r = 0.38, p < 0.001), river discharges (r = 0.47, p < 0.001) and, weakly, with negative NAO values (r = -0.017, p < 0.01). The temporal amplitude confirmed that the seasonal timing of [*Chl*] blooms was consistent between years. Nevertheless, important regional inter-annual variability in bloom size was noted, which was related with the magnitude of these storms. Maximum signals of precipitation were linked to high [*Chl*], as can be observed for example in the most recurrent phytoplankton bloom that occurred during winter 2011-2012 and spring 2013.

Regarding the second [*Chl*] mode, amplitudes were also positively correlated with discharges (r = 0.37, p < 0.01), suggesting that river outflow and high [*TSS*] played a role in controlling bloom dynamics in zone A_{2C}, but not A_{2N}. This was illustrated by examining the plume extent in A_{2C} and the variability in [*Chl*] second mode (Fig. 10). During winter periods, an increase in the extent of the plume occurred in parallel with a decrease in [*Chl*] leading to a negative association between [*Chl*] second mode and plume extent (r = -0.55, p < 0.001, Table 4). Regarding this significant pattern, it appears that secondary bloom episodes with less intense [*Chl*] records took place over the

course of the study period. This temporal mode was representative of the semi-annual signal and was coupled with the first mode, presenting a 3-month phase lag supported by the high correlation coefficient between both time series ($r = 0.79$, $p < 0.001$).

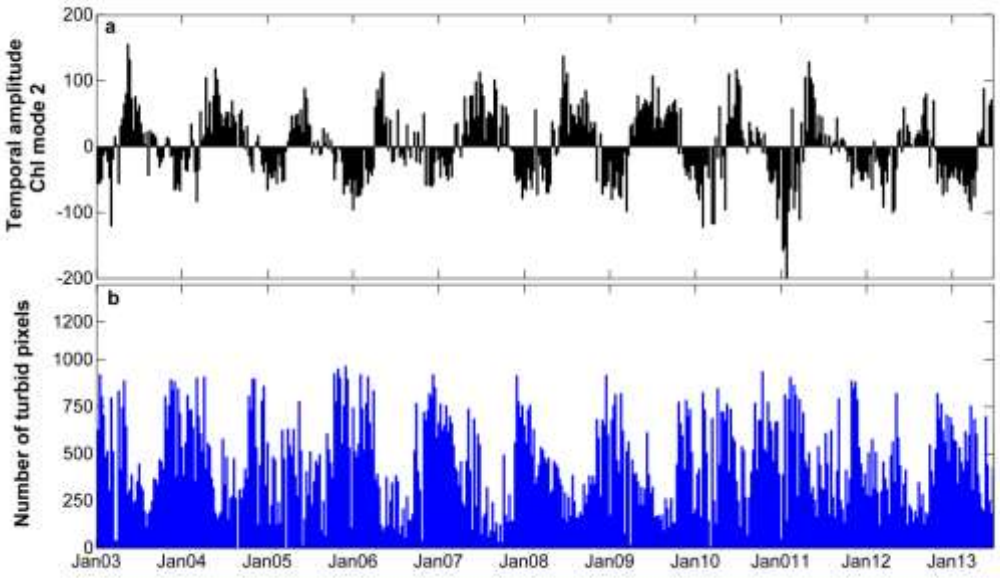

Figure. 10. a) Temporal amplitude of chlorophyll EOF for mode 2, and b) Total number of turbid pixels (*nLw555* values > 1.3 mW/cm^2 μm sr) in the coastal region A_{2C} .

Further indications of the role of [*TSS*] in the control of phytoplankton dynamics in the zone directly in front of the estuary mouth can be observed by examining physical-optical parameters at 2 representative sites (Fig.11), the nearshore station 14, and the offshore station 17 (Fig. 1). Mixed layer depth (MLD, in situ data from May 2005 to August 2007 and via the GODAS model from January 2003 to June 2013) showed annual oscillations that were clearly visible at the offshore station (Fig. 11a). This consisted in a deepening of the mixed layer around winter-early spring (25 m-bottom depth and 180 m, for station 14 and 17, respectively) due to convective mixing caused by the winter cooling. MLD became shallower towards the end of spring and into summer (6 m and 5 m for station 14 and 17, respectively) due to warmer waters that systematically emerged in the region (Vargas *et al.*, 2003; Navarro & Ruiz, 2006). The same seasonal evolution was observed in the GODAS model results (average of a 2º x 0.3º box), which also suggested large inter-annual variability. The correlation between in situ MLD and [*Chl*] was $r = 0.21$ (station 14, $p < 0.05$) and $r = 0.55$ (station 17, $p < 0.005$), whereas correlation with modelled MDL corresponded to $r = -0.0018$ (station 14, $p > 0.05$) and $r = 0.44$ (station 17, $p < 0.0001$). In addition, the relationship with [*Chl*] modes was examined resulting in r values of 0.32 ($p < 0.0001$), -0.47 ($p < 0.0001$) and 0.07 ($p <$

0.4) for modes 1, 2 and 3, respectively. On the other hand, $z_{1\%}$ (Fig. 11b) had maximum values in summer and early autumn (25 m-bottom depth and 129 m, station 14 and 17 respectively) and minimum values towards the end of winter and early spring (2.0 m and 10.4 m). This was equivalent to K_d *(PAR)* values of 0.09 and 0.01 m^{-1} at stations 14 and 17, respectively in summer, and 5.65 and 5.67 m^{-1} in winter. Considering that seasonal variations in daily total PAR ranged from 62 to 20 mol photons/m^2/day in summer and winter, respectively (Fig.11b), the high attenuation at station 14 observed in winter appeared to reduce light availability enough to limit phytoplankton productivity, and thus influence [*Chl*] dynamics (Fig. 11c). Indeed, [*Chl*] at station 14 and 17 were not correlated with daily total PAR (r = 0.07 and 0.03 for station 14 and 17, respectively; $p > 0.5$), whereas they were correlated with $z_{1\%}$ (r = -0.85 and -0.57 for station 14 and 17, respectively; $p < 0.001$, n = 498).

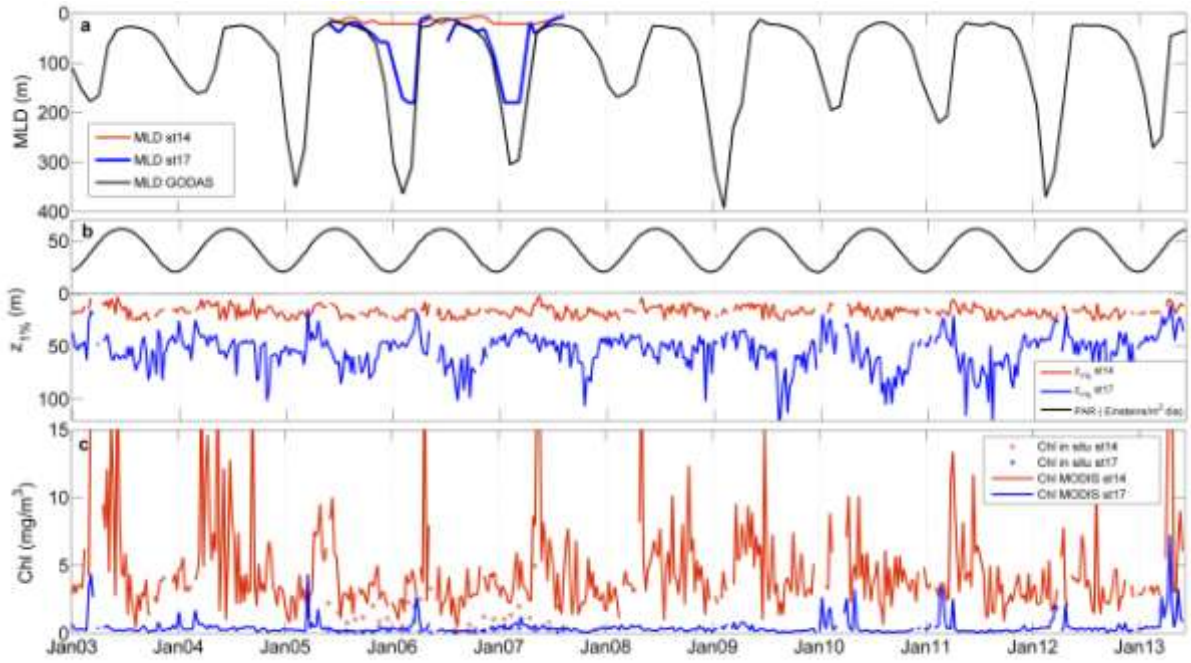

Figure 11. a) Mixed Layer Depth (MLD, m) from in situ data in the coastal station 14 (red line) and offshore station 17 (blue line) and from the GODAS model in the 2ºx0.6º box (black line), b) Euphotic zone ($z_{1\%}$, m) for both station 14 (red line) and station 17 (blue line), and mean Photosynthetically-Active Radiation (PAR, Einstein / m^2 / day) from MODIS data in the ROI, c) *Chl* concentration (mg/m^3) from in situ data in station 14 (red stars) and 17 (blue stars) and from MODIS corresponding pixel for station 14 (red line) and 17 (blue line).

Discussion

Ocean Colour Validation

The exponential relationship between [*TSS*] and the backscattering characteristics of surface waters derived in this study suggests good predictive capacity. Although it must be noted that the relationship is specific for this region and may diverge from other water masses as a consequence of the optical properties of the *TSS*, such as particle types, size, density and composition, as well as due to the *TSS* ranges considered. Comparisons of at-sensor products against field *TSS* or turbidity in coastal areas can be found in the literature (Hu *et al.*, 2004; Otero & Siegel, 2004; Chen *et al*., 2007). There is no agreement about the best class of model to be used. Some suggest it should be logarithmic (e.g. Tassan & Sturm, 1986), log-linear (Chen *et al.*, 1991), linear (Ritchie *et al.*, 1987; Forget & Ouillon, 1998) or exponential (Schiebe *et al.*, 1992; Li & Li, 2000; Hu *et al.*, 2004; Caballero *et al.*, 2014), as used in this study.

A systematic overestimation of MODIS derived [*Chl*] was found in nearshore samples that was not present in the offshore samples. This has been previously observed in other coastal turbid waters (often with large *bias*); indeed the OC3M algorithm (O'Reilly *et al.,* 2000) typically describes 87% of the variance in traditional absorption dominated ocean waters and only 61% in the case of coastal waters. This can be explained by the interference with other absorbing substances such as yellow substance and coloured sediments or detritus (Darecki & Stramski, 2004; Zhang *et al.,* 2006; Werdell *et al.,* 2009). Previous validation exercises conducted by Navarro & Ruiz (2006) between in situ [*Chl*] measurements at 10 m and SeaWiFS data (2000-2002) in the offshore region of Guadalquivir estuary exhibited good correlation (r = 0.85, p < 0.001, n = 304). This relationship indicated less overestimation compared to the results of the nearshore stations in this study, but similar to the offshore stations. These issues, combined with failure to correct for atmospheric and land adjacency effects, help explain the higher uncertainty in retrieving coastal [*Chl*]. Several remote sensing derived-[*Chl*] validation studies in coastal domains exhibit similar results (Ruddick *et al.,* 2000; Toole & Siegel, 2001; Otero & Siegel, 2004); predictive uncertainty in coastal waters is generally higher than in the open ocean. Nevertheless, in terms of cost-effective water quality monitoring, ocean colour algorithms from MODIS provided realistic and high-resolution temporal dynamics of [*TSS*] and [*Chl*]. More importantly, these relationships seem to be stable over 2003 and 2007, reinforcing the hypothesis that the regressions are time-independent and the MODIS-derived values are reasonable estimates. The sampling stations were distributed across the coastal region and throughout four seasons, thus representing an overall consistent relationship over the wide range of concentrations measured offshore and within the plume.

Spatio-temporal variability and driving mechanisms

High *nLw555* values occurred near the coast with the largest values principally found near the Guadalquivir river mouth and Cadiz bay in winter (recurrent presence of sediment plumes), presumably mainly due to sediment-laden terrestrial runoff. Across-coast dispersal distances of 50 to 75 km have been reported for the Guadalquivir estuary plume (Navarro *et al.*, 2012b), which seem to be confirmed by this study. The area south of Guadalquivir, Cadiz bay is also influenced by the Guadalete river and fringing wetlands. Contrary to expectations, relatively low *nLw555* values were found in the vicinity of the other two major rivers located in the north of the region (Tinto-Odiel and Guadiana rivers). Suspended materials released from them are presumably rapidly transported to the southeast, the main prevailing ocean circulation in this region (Criado Aldeanueva *et al.,* 2006; García-Lafuente *et al.,* 2006). Hence, this study supports the previous suggestions that the Guadalquivir is the main source of Holocene sediments (Lobo *et al.,* 2004) and probably, dissolved organic material and nutrients (Ribas-Ribas *et al.,* 2011) to the E. Gulf of Cadiz.

EOF analysis revealed the spatio-temporal structure of the river plume and suggested a close connection between *nLw555* dynamics and meteorological conditions. The *nLw555* first mode appeared to be explained by a combination of rainstorm events and river discharge (Díez-Minguito *et al.,* 2012; Navarro *et al.,* 2011, 2012b; Caballero *et al.,* 2014), both strongly correlated with the NAO index. This index, which also correlates with prevailing winds, has previously been show to be an important indicator of the inter-annual variability in the Gulf of Cadiz (Prieto *et al.,* 2009). The second *nLw555* mode generally showed similar temporal variability to the first mode and was also positively correlated with rainfall and discharges from the Guadalquivir. However, this mode had a more localized distribution of positive values in the vicinity of the estuary mouth and a zone with negative values to the north. The coincidence of the second mode high negative values in winter with the positive values of the first mode (e.g. 2010) suggests the influence of shorter time scale events. A possible candidate could be the influence of onshore westerly winds on local circulation. In this line of thinking, third mode seemed to indicate higher [*TSS*] offshore, particularly in front of Cadiz bay, which may suggest the influence of periods with easterly winds blowing offshore.

The link between river plumes and a large terrestrial runoff event is a regular feature of turbid coastal regions (Otero & Siegel, 2004; Nezlin & DiGiacomo, 2005; Thomas & Weatherbee, 2006; Schroeder *et al.*, 2012). At a significant rain event scale, floods create local modifications of the hydrodynamic conditions in the estuary and, consequently, re-suspension, local erosion of bed and margins, and the deposition of new sediments, influencing coastal waters. Maximum outflow events

due to runoff caused high and persistent turbidity peaks in the region (e.g. winter 2010). These episodes have important consequences for the neighbouring coastal zone, which, in turn, can probably be related to elevated concentrations of nutrients, pollutants, etc. In addition, high levels of suspended solids endanger the already fragile balance of an ecosystem subjected to the pressure of apparent human intervention in the area, hindering the operation of aquaculture facilities and the irrigation of numerous cultivated areas in the estuary (Bhat & Blomquist, 2004; Navarro *et al.*, 2012b). In the E. Gulf of Cadiz, which is dominated by the Guadalquivir estuary, [*TSS]* dynamics appear to be a consequence of the superposition of the seasonal variability of rainfall, the irregular discharges from the Alcala del Rio dam, and to a much lesser extent of the prevailing winds.

Multi-year monthly composites of [*Chl*] showed significant seasonal variability in the region, with the highest values observed in early spring and the lowest in late summer. Similar seasonality was also shown by Navarro (2004) using monthly time series for the entire Gulf of Cadiz. The particularity of this study, is the strip with high [*Chl*] observed along the coast in all composites. This could be an artifact of the higher *bias* found in nearshore waters, as discussed above. On the other hand, the highest [*Chl*] values were observed in the nearshore regions influenced by rivers Guadiana, Tinto-Odiel, Guadalquivir and Guadalete. South of Cadiz bay, the nearshore strip was reduced in intensity and width, suggesting that the observed phenomenon is at least in part related to the fertilizing activity of these major riverine inputs, which promote phytoplankton growth. Indeed, previous studies suggest that these rivers, and in particular the Guadalquivir, constitute the major factor determining the primary productivity and fisheries resources of the region (Prieto *et al*., 2009; Ruiz *et al.,* 2009).

The [*Chl*] first mode appeared to capture this seasonal variability with changes in winter-spring phytoplankton blooms throughout the region (extending out onto the continental shelf), and particularly north of the estuary. This typical seasonality is common to many coastal regions (Peliz & Fiúza, 1999; Thomas *et al.,* 2001; Xu *et al.,* 2011; Le *et al.,* 2013), where nutrient-limitation keeps [*Chl*] low in surface waters during summer. As vertical water structure breaks down in autumn-winter and nutrients become available again, phytoplankton blooms are formed, especially in spring as light availability increases. The correlation of [*Chl*] first mode with precipitation and discharges, suggests that inputs of nutrients from the major rivers, fertilizing the surrounding waters (Peliz & Fiúza, 1999; Navarro & Ruiz, 2006; Navarro *et al.*, 2011), modulate this general pattern. These high-flow events have important consequences for the neighbouring coastal zone, pumping large quantities of nutrients and stimulating the growth of phytoplankton that sustains the food chain (Prieto *et al.,* 2009). In addition, the [*Chl*] trend corresponded to a decline until 2009 and,

from then onwards, an increase that is indicative of nutrient enrichment in the region during recent years. These phenomena are also associated with a precipitation increment due to frequent storm events and consequent river discharge intensification, as has also been observed in the north-eastern Gulf of Cadiz (Prieto *et al.,* 2009; Navarro *et al.,* 2011).

Second mode appeared to distinguish [*Chl*] dynamics between the narrow nearshore strip directly influenced by the rivers (A_{2C}) and the coastal region to the North (A_{2N}). The latter region coincides with the "Huelva Front" (Stevenson, 1977), which is generated by local upwelling as currents flow over the Cape Santa Maria canyon (increasing nutrient supply to surface waters). The increased tendency for an early breakdown of vertical stratification may account for the late summer-autumn phytoplankton blooms predominantly observed in this zone. The EOF analysis of [*Chl*] conducted in the Gulf of Cadiz by Navarro & Ruiz (2006) exhibited the presence of several zones in second mode. In fact, areas A_{2N} and A_{2C}, differentiated by the second mode in the present study, are closely related to Zone 3 and Zone 4 of their study, respectively.

The particularly high [*Chl*] values in the nearshore strip (A_{2C}) were associated with late spring-summer maximum in the second mode, with a time lag of about a month after peaks in the first mode. This suggests that another factor, such as light, rather than nutrients was limiting primary production in this zone (Eppley & Peterson, 1979). Indeed, studies have shown that the Guadalquivir estuary, which has relatively low [*Chl*], despite extremely high nutrient concentrations, is generally severely light-limited due to very high turbidity levels (Navarro *et al.*, 2012a; Ruiz *et al.* 2006; 2013). This is a common feature of other nutrient-replete, highly turbid estuaries (Wofsy, 1983; Cloern, 1987; Irigoien & Castel, 1997). Evidence that this phenomenon extends into the surrounding coastal zone is provided by in situ vertically resolved data on the physical-optical properties of the water column. Maximum [*Chl*] values were observed earlier at the offshore station (around February) compared to the nearshore station located in the estuary mouth (March-April). During this period, MLD at both stations suggests that water column stratification was not significant; however, higher $K_d(PAR)$ levels, resulting in a shallower $z_{1\%}$ were observed at the nearshore compared to the offshore station. This suggests that light limitation due to high [*TSS*] delays the development of the nearshore spring phytoplankton bloom. At both stations, during the stratification period (summer and early autumn), a seasonal thermocline develops, MLD gets shallower, terrestrial inputs decline and nutrient transport to surface waters is restricted (Sarmiento *et al.,* 1998), leading to lower [*Chl*]. The correlation between both in situ and modelled MLD and [*Chl*] suggests a more significant cause-effect connection of MLD-bloom patterns at the offshore station than at the nearshore station. The simultaneous coincidence between MLD and [*Chl*]

maximum suggests that [*Chl*] peaks after the maximum MLD is formed extending below the euphotic zone, confirming the connection established by Navarro *et al.* (2012a). Hence, the relationship existing between both MLD-$z_{1\%}$ depths and upwelling (Fiúza, 1983; Criado-Aldeanueva *et al.*, 2006) and estuarine processes may explain the detected blooms. Finally, [*Chl*] third mode may suggest the influence of strong easterly winds, particularly dominant in the region during summer, which break-down thermal stratification and transport coastal phytoplankton offshore.

Although the Guadalquivir estuary is typically vertically homogeneous (Vanney, 1970), the occurrence of high-flow events could be responsible for strong vertical stratification. Stratification within the plume can trap biomass in distinct layers where light levels can change in just a meter. The influence of the buoyancy plume could diminish the MLD, hence the mean light intensity entering the MLD increases. As stated above, the outstanding effect of light-limitation in turbid environments illustrates the critical significance of mixing properties within buoyant coastal plumes, as it regulates the potential for productivity. In addition, many factors clearly contribute to [*Chl*] degradation, but phytoplankton decay and predator consumption (grazing) are the main sources of phytoplankton mortality in the oceans; zooplankton was found to respond quickly to variations in phytoplankton biomass (Calbet & Landry, 2004). In that sense, the central role of grazing on phytoplankton population dynamics has been recognized in the Gulf of Cadiz (García *et al.*, 2002).

EOF analysis explained 72% and 50% of the variability in *nLw555* and [*Chl*] respectively, suggesting that particularly for [*Chl*], variation at smaller-scales is probably a key feature. Processes not considered here such as tidal dynamics and grazing (García *et al.*, 2002) may help to further explain this variability. Nevertheless, inter-annual and seasonal patterns in [*TSS*] and [*Chl*] appear to be tightly related to terrestrial discharges, particularly from the Guadalquivir estuary, and to the seasonal interaction between water column stratification and light availability. This sustains the significant relevance of the physical conditions and local processes for the biological response in the region. However, in support of future local pollution assessment activities and decision-making needs, higher resolution ocean colour imagery in both time (e.g. sub-diurnal) and space would be required to recognize and predict events adequately. These emerging capabilities would comprehensively sort out and characterize the small-scale variability of the water properties observed in this coastal region. In this regard, the use of airborne sensors or observational platforms will allow regular real-time monitoring and adequate assessment of the ecological impacts of the turbidity plume. Further investigation is necessary to elucidate critical boundaries and the linkages between water quality, turbidity plumes and phytoplankton growth.

Conclusion

This study demonstrates that remote sensing can serve as a tool to estimate [*TSS*] and [*Chl*] in the coastal waters of the Eastern Gulf of Cadiz. Spatio-temporal analyses of both variables permitted the assessment of driving forces and the connection with climate fluctuations. The outcome of EOF analysis suggests that the Guadalquivir river plume is of considerable importance not only because of its effect on nearshore hydrography, but also because of its influence on biological productivity. The seasonal dynamics of total suspended matter are strongly associated with freshwater discharges from the Alcala del Rio dam that follow episodes of heavy precipitation. Furthermore, bloom development in the coastal fringe appears to be delayed by the extended turbidity plumes observed during the rainy season. The combination of variable riverine inputs and mixing processes, with light limitation due to the turbidity plume, creates a dynamic, diverse transition area that may help to explain the very high productivity of the region. Hence, understanding the dynamics of the Guadalquivir river plume is key to managing the coastal resources in the Eastern Gulf of Cadiz.

Acknowledgements

We would like to thank NASA for distributing the MODIS data used in this study and Junta de Andalucia for in situ data. The authors also thank the crews of the R.V. Regina Maris and B.I.O. García del Cid for support during the cruises. IC is supported by a grant of the Junta de Andalucia PhD fellowship program. EPM is supported by a JAE DOCTORES 2010 contract partly funded by the European Union (European Social Fund, ESF2007-2013) and the Spanish Ministry for Economy and Competitiveness. LP is supported by the Ramón y Cajal program of Spanish MINECO. This work was financially supported by the Junta de Andalucia Projects P09-RNM-4853 and PR11-RNM-7722, E.U. MarinERA Project MedEX (CTM2008-04036-E/MAR) and PERSEUS (FP7-287600).

REFERENCES

Bailey, S., Wang, M., 2001. Satellite Aerosol Optical Thickness Match-up Procedures. *NASA Technical Memorandum*, 2001, 70-72. Greenbelt, MD: NASA Goddard Space Flight Center.

Baldacci, A., Corsini, G., Grasso, R., Manzella, G., Allen, J. *et al*., 2001. A study of the Alboran sea mesoscale system by means of empirical orthogonal function decomposition of satellite data. *Journal of Marine Systems*, 29 (1), 293-311.

Bhat, A., Blomquist, W., 2004. Policy, politics, and water management in the Guadalquivir River Basin, Spain. *Water Resources Research*, 40 (8), 1-11.

Björnsson, H., Venegas, S.A., 1997. *A Manual for EOF and SVD Analyses of Climate Data*. Department of Atmospheric and Oceanic Sciences and Centre for Climate and Global Change, McGill University, Technical report, No 97 (1), 52 pp.

Brickley, P.J., Thomas, A.C., 2004. Satellite-measured seasonal and inter-annual chlorophyll variability in the NorthEast Pacific and Coastal Gulf of Alaska. *Deep Sea Research Part II: Topical Studies in Oceanography*, 51 (1), 229-245.

Caballero, I., Morris, E.P., Ruiz, J., Navarro, G., 2014. Assessment of suspended solids in the Guadalquivir estuary using new DEIMOS-1 medium spatial resolution imagery. *Remote Sensing of Environment*, 146, 148-158.

Calbet, A., Landry, M.R., 2004. Phytoplankton growth, microzooplankton grazing, and carbon cycling in marine systems. *Limnology and Oceanography*, 49 (1), 51-57.

Chen, Z., Hanson, J.D., Curran, P.J., 1991. The form of the relationship between suspended sediment concentration and spectral reflectance: its implications for the use of Daedalus 1268 data. *International Journal of Remote Sensing*, 12 (1), 215-222.

Chen, Z., Hu, C., Muller-Karger, F., 2007. Monitoring turbidity in Tampa Bay using MODIS/Aqua 250-m imagery. *Remote Sensing of Environment*, 109, 207-220.

Cloern, J.E., 1987. Turbidity as a control on phytoplankton biomass and productivity in estuaries. *Continental Shelf Research*, 7 (11), 1367-1381.

Criado Aldeanueva, F., García Lafuente, J., Vargas, J.M., Del Rio, J., Vázquez, A. *et al*., 2006. Distribution and circulation of the water masses in the Gulf of Cadiz from in situ observations. *Deep Sea Research II*, 53 (11-13), 1144-1159.

Darecki, M., Stramski, D., 2004. An evaluation of MODIS and SeaWiFS bio-optical algorithms in the Baltic Sea. *Remote Sensing of Environment*, 89 (3), 326-350.

Díez-Minguito, M., Baquerizo, A., Ortega-Sánchez, M., Navarro, G., Losada, M., 2012. Tide transformation in the Guadalquivir estuary (SW Spain) and process-based zonation. *Journal of Geophysical Research*, 117, C03019, doi:10.1029/2011JC007344.

Eppley, R.W., Peterson, B., 1979. Particulate organic matter flux and planktonic new production in the deep ocean. *Nature*, 282 (67), 677-680.

Fiúza, A.F.G., 1983. Upwelling patterns off Portugal. p. 85-98. In: *Coastal Upwelling Its Sediment Record*. Suess, E., Thiede, J., Springer US, New York.

Forget, P., Ouillon, S., 1998. Surface suspended matter off the Rhone river mouth from visible satellite imagery. *Oceanologica Acta*, 21 (6), 739-749.

García, C.M., Prieto, L., Vargas, M., Echevarría, .F., García Lafuente, J., *et al*., 2002. Hydrodynamics and spatial distribution of plankton and TEP in the Gulf of Cadiz (SW Iberian Peninsula). *Journal of Plankton Research*, 24 (8), 817-833.

García-Lafuente, J., Delgado, J., Criado-Aldeanueva, F., Bruno, M., del Rio, J. *et al*., 2006. Water mass circulation on the continental shelf of the Gulf of Cadiz. *Deep Sea Research Part II: Topical Studies in Oceanography*, 53 (11-13), 1182-1197.

González-Mazo, E., Forja, J.M., Gómez-Parra, A., 1998. Fate and distribution of linear alkylbenzene sulfonates in the littoral environment. *Environmental science & technology*, 32 (11),

1636-1641.

Granado-Lorencio, C.,1991. The effect of man on the fish fauna of the River Guadalquivir, Spain. *Fisheries research,* 12 (2), 91-100.

Hu, C., Chen, Z., Clayton, T.D., Swarzenski, P., Brock, J.C. *et al*., 2004. Assessment of estuarine water-quality indicators using MODIS medium-resolution bands: Initial results from Tampa Bay, FL. *Remote Sensing of Environment,* 93, 423-441.

Hurrell, J. W., 1995. Decadal trends in the North Atlantic oscillation. *Science,* 269, 676-679.

Irigoien, X., Castel, J., 1997. Light limitation and distribution of chlorophyll pigments in a highly turbid estuary: the Gironde (SW France). *Estuarine, Coastal and Shelf Science,* 44 (4), 507-517.

Jamet, C., Loisel, H., Kuchinke, C.P., Ruddick, K., Zibordi, G. *et al*., 2011. Comparison of three SeaWiFS atmospheric correction algorithms for turbid waters using AERONET-OC measurements. *Remote Sensing of Environment*, 115 (8), 1955-1965.

Kara, A.B., Rochford, P.A., Hurlburt, H.E., 2000. An optimal definition for ocean mixed layer depth. *Journal of Geophysical Research: Oceans*, 105 (C7), 16803-16821.

Kidd, P., Dominguez-Rodriguez, M., Diez, J., Monterroso, C., 2007. Bioavailability and plant accumulation of heavy metals and phosphorus in agricultural soils amended by long-term application of sewage sludge. *Chemosphere,* 66 (8), 1458-1467.

Kirk, J.T.O., 1983. *Light and Photosynthesis in Aquatic Ecosystems*. Cambridge University Press: Cambridge, MA, USA, 401 pp.

Lahet, F., Forget, P., Ouillon, S., 2001. Application of a colour classification method to quantify the constituents of coastal waters from in situ reflectance sampled at satellite sensor wavebands. *International Journal of Remote Sensing,* 22 (5), 909-914.

Le, C., Hu, C., English, D., Cannizzaro, J., Kovach, C., 2013. Climate-driven chlorophyll-a changes in a turbid estuary: Observations from satellites and implications for management. *Remote Sensing of Environment,* 130, 11-24.

Li, Y., & Li, J., 2000. A suspended sediment satellite sensing algorithm based on gradient transiting from water-leaving to satellite-detected reflectance spectrum. *Chinese Science Bulletin*, *45* (10), 925-931.

Lobo, F., Sánchez, R., González, R., Dias, J., Hernández-Molina, F.J., Fernández-Salas, L. *et al*., 2004. Contrasting styles of the Holocene highstand sedimentation and sediment dispersal systems in the Northern shelf of the Gulf of Cadiz. *Continental Shelf Research,* 24 (4), 461-482.

Loisel, H., Bosc, E., Stramski, D., Oubelkheir, K., Deschamps, P.Y., 2001. Seasonal variability of the backscattering coefficient in the Mediterranean Sea based on satellite SeaWiFS imagery. *Geophysical Research Letters,* 28 (22), 4203-4206.

Lorenz, E.N., 1956. *Empirical orthogonal functions and statistical weather prediction*. Sci. Rep. Statist. Forecasting Proj., Department Meteor., MIT, No 1, 49 pp.

Mendiguchía, C., Moreno, C., García-Vargas, M., 2007. Evaluation of natural and anthropogenic influences on the Guadalquivir River (Spain) by dissolved heavy metals and nutrients. *Chemosphere,* 69 (10), 1509-1517.

Miller, R.L., Del Castillo, C.E., McKee, B.A., 2005. *Remote sensing of coastal aquatic environments: Technologies, techniques and applications*. Springer, Vol. 7, 345 pp.

Morel, A., Gentili, B., Chami, M., Ras, J., 2006. Bio-optical properties of high chlorophyll Case 1 waters and of yellow-substance-dominated Case 2 waters. *Deep Sea Research Part I: Oceanographic Research Papers*, 53 (9), 1439-1459.

Morel, A., Huot, Y., Gentili, B., Werdell, P.J., Hooker, S.B. *et al*., 2007. Examining the consistency of products derived from various ocean color sensors in open ocean (Case 1) waters in the perspective of a multi-sensor approach. *Remote Sensing of Environment*, 111 (1), 69-88.

Morris, A.W., Allen, J.I., Howland, R.J.M., Wood, R.G., 1995. The estuary plume zone: Source or sink for land-derived nutrient discharges? *Estuarine, Coastal and Shelf Science*, 40 (4),

387-402.

Navarro, G., 2004. *Escalas de variabilidad espacio-temporal de procesos pelágicos en el golfo de Cadiz*. MSc Thesis. University of Cadiz, Spain, 224 pp.

Navarro, G., Ruiz, J., 2006. Spatial and temporal variability of phytoplankton in the Gulf of Cadiz through remote sensing images. *Deep Sea Research Part II: Topical Studies in Oceanography,* 53 (11-13), 1241-1260.

Navarro, G., Gutiérrez, F., Díez-Minguito, M., Losada, M., Ruiz, J., 2011. Temporal and spatial variability in the Guadalquivir estuary: a challenge for real-time telemetry. *Ocean Dynamics,* 61 (6), 753-765.

Navarro, G., Caballero, I., Prieto, L., Vázquez, A., Flecha, S. *et al*., 2012a. Seasonal-to-interannual variability of chlorophyll-*a* bloom timing associated with physical forcing in the Gulf of Cadiz. *Advances in Space Research,* 50 (8), 1164-1172.

Navarro, G., Huertas, I.E., Costas, E., Flecha, S., Díez-Minguito *et al*., 2012b. Use of a Real-Time Remote Monitoring Network (RTRM) to Characterize the Guadalquivir Estuary (Spain). *Sensors,* 12 (2), 1398-1421.

Neckel, H., 1984. The solar radiation between 3300 and 12500 Å. *Solar Physics,* 90 (2), 205-258.

Nezlin, N.P., DiGiacomo, P.M., 2005. Satellite ocean color observations of stormwater runoff plumes along the San Pedro Shelf (Southern California) during 1997-2003. *Continental Shelf Research,* 25 (14), 1692-1711.

Nezlin, N.P., DiGiacomo, P.M., Stein, E.D., Ackerman, D., 2005. Stormwater runoff plumes observed by SeaWiFS radiometer in the Southern California Bight. *Remote Sensing of Environment,* 98 (4), 494-510.

North, G.R., Bell, T.L., Cahalan, R.F., Moeng, F.J., 1982. Sampling errors in the estimation of empirical orthogonal functions. *Monthly Weather Review,* 110 (7), 699-706.

O'Reilly, J.E., Maritorena, S., Siegel, D.A., O'Brien, M.C., Toole, D., Mitchell, B.G. *et al*., 2000. Ocean color chlorophyll a algorithms for SeaWiFS, OC2, and OC4: Version 4. *SeaWiFS postlaunch calibration and validation analyses,* 3, 9-23.

Otero, M.P., Siegel, D., 2004. Spatial and temporal characteristics of sediment plumes and phytoplankton blooms in the Santa Barbara Channel. *Deep Sea Research Part II: Topical Studies in Oceanography,* 51 (10), 1129-1149.

Parsons, T.R., Maita, Y., Lalli, C.M., 1984. *A manual of chemical and biological methods for seawater analysis*. Pergamon Press, Oxford, 173 pp.

Peliz, A., Fiúza, A., 1999. Temporal and spatial variability of CZCS-derived phytoplankton pigment concentrations off the Western Iberian Peninsula. *International Journal of Remote Sensing,* 20 (7), 1363-1403.

Pennock, J.R., 1985. Chlorophyll distributions in the Delaware estuary: Regulation by light-limitation. *Estuarine, Coastal and Shelf Science,* 21 (5), 711-725.

Pierson, D.C., Kratzer, S., Strömbeck, N., Håkansson, B., 2008. Relationship between the attenuation of downwelling irradiance at 490 nm with the attenuation of PAR (400 nm–700 nm) in the Baltic Sea. *Remote Sensing of Environment,* 112 (3), 668-680.

Prieto, L., Navarro, G., Rodríguez-Gálvez, S., Huertas, I.E., Naranjo, J. *et al*., 2009. Oceanographic and meteorological forcing of the pelagic ecosystem on the Gulf of Cadiz shelf (SW Iberian Peninsula). *Continental Shelf Research,* 29 (17), 2122-2137.

Reynolds, C.S., 1998. What factors influence the species composition of phytoplankton in lakes of different trophic state. *Hydrobiologia,* 369/370, 11-26.

Ribas-Ribas, M., Gómez-Parra, A., Forja, J.M., 2011. Spatio-temporal variability of the dissolved organic carbon and nitrogen in a coastal area affected by river input: The North Eastern shelf of the Gulf of Cadiz (SW Iberian Peninsula). *Marine Chemistry,* 126 (1), 295-308.

Ritchie, J.C., Cooper, C.M., Yongqing, J., 1987. Using Landsat multispectral scanner data to

estimate suspended sediments in Moon Lake, Mississippi. *Remote Sensing of Environment*, 23 (1), 65-81.

Ruddick, K.G., Ovidio, F., Rijkeboer, M., 2000. Atmospheric correction of SeaWiFS imagery for turbid coastal and inland waters. *Applied optics*, 39 (6), 897-912.

Ruiz, J., Garcia-Isarch, E., Huertas, E., Prieto, L., Juárez, A. *et al*., 2006. Meteorological and oceanographic factors influencing *Engraulis encrasicolus* early life stages and catches in the Gulf of Cadiz. *Deep Sea Research Part II: Topical Studies in Oceanography*, 53 (11), 1363-1376.

Ruiz, J., González-Quirós, R., Prieto, L., Navarro, G., 2009. A Bayesian model for anchovy (*Engraulis encrasicolus*): the combined forcing of man and environment. *Fisheries Oceanography*, 18 (1), 62-76.

Ruiz, J., Macías, D., Losada, M.A., Díez-Minguito, M., Prieto, L., 2013. A simple biogeochemical model for estuaries with high sediment loads: Application to the Guadalquivir River (SW Iberia). *Ecological Modelling*, 265,194-206.

Ruiz, J., Polo, M.J., Díez-Minguito, M., Navarro, G., Morris, E.P. *et al*., 2014. The Guadalquivir Estuary: A Hot Spot for Environmental and Human Conflicts, Chapter 8. Springer International Publishing Switzerland, 199-232.

Sá, C., Da Silva, J., Oliveira, P.B., Brotas, V., 2008. Comparison of MERIS (Algal_1 and Algal_2) and MODIS (OC3M) chlorophyll products and validation with HPLC in situ data collected off the Western Iberian Peninsula. Proceedings *of the 2nd MERIS/(A) ATSR User Workshop*, Frascati, Italy, 22-26.

Sánchez-Lamadrid, A., Ruiz, J., García, E., Juárez, A., Jiménez, T. *et al*., 2003. *Estudio de los recursos pesqueros del Golfo de Cadiz*. Consejería de Agricultura y Pesca, Junta de Andalucia, 35 pp.

Sathyendranath, S., 2000. *Remote Sensing of Ocean Colour in Coastal, and Other Optically-Complex, Waters*. Reports of the International Ocean-Colour Coordinating Group, No 3, 140 pp.

Sarmiento, J.L., Hughes, T.M.C., Stouffer, R.J., Manabe, S., 1998. Simulated response of the ocean carbon cycle to anthropogenic climate warming. *Nature*, 393, 245-249.

Schiebe, F.R., Harrington, Jr., J.A., Ritchie, J.C., 1992. Remote sensing of suspended sediments: the Lake Chicot, Arkansas project. *International Journal of Remote Sensing*, 13 (8), 1487-1509.

Schroeder, T., Devlin, M.J., Brando, V.E., Dekker, A.G., Brodie, J.E. *et al*., 2012. Inter-annual variability of wet season freshwater plume extent into the Great Barrier Reef lagoon based on satellite coastal ocean colour observations. *Marine Pollution Bulletin*, 65 (4), 210-223.

Stevenson, R.E., 1977. Huelva Front and Malaga, Spain, Eddy Chain as defined by Satellite and Oceanographic Data. *Deutsche Hydrographische Zeitschrift*, 30 (2), 51-53.

Tassan, S., Sturm, B., 1986. All algorithm for the retrieval of sediment content in turbid coastal waters from CZCS data. *International Journal of Remote Sensing*, 7, 643-655.

Thomas, A., Carr, M.E., Strub, P.T., 2001. Chlorophyll variability in Eastern boundary currents. *Geophysical Research Letters*, 28 (18), 3421-3424.

Thomas, A.C., Weatherbee, R.A., 2006. Satellite-measured temporal variability of the Columbia River plume. *Remote Sensing of Environment*, 100 (2), 167-178.

Toole, D.A., Siegel, D.A., 2001. Modes and mechanisms of ocean color variability in the Santa Barbara Channel. *Journal of Geophysical Research: Oceans (1978–2012)*, 106 (C11), 26985-27000.

UNESCO, 1994. *Protocols for the Joint Global Ocean Flux Study (JGOFS) Core Measurements. IOC Manuals and Guides*. Paris, UNESCO, 170 pp.

Valente, A.S., da Silva, J.C., 2009. On the observability of the fortnightly cycle of the Tagus estuary turbid plume using MODIS ocean colour images. *Journal of Marine Systems*, 75 (1), 131-137.

Vanney, J., 1970. *Lhidrologie du Bas Guadalquivir*. Publicaciones del Departamento de

Geografía Aplicada, CSIC, Madrid, 176 pp.

Vargas, J., García-Lafuente, J., Delgado, J., Criado, F., 2003. Seasonal and wind-induced variability of sea surface temperature patterns in the Gulf of Cadiz. *Journal of Marine Systems,* 38 (3), 205-219.

Werdell, P.J., Bailey, S.W., Franz, B.A., Harding Jr, L.W.*et al*., 2009. Regional and seasonal variability of chlorophyll-a in Chesapeake Bay as observed by SeaWiFS and MODIS-Aqua. *Remote Sensing of Environment,* 113 (6), 1319-1330.

Wofsy, S., 1983. A simple model to predict extinction coefficients and phytoplankton biomass in eutrophic waters. *Limnology and Oceanography*, 28 (6), 1144-1155.

Xu, Y., Chant, R., Gong, D., Castelao, R., Glenn, S. *et al*., 2011. Seasonal variability of chlorophyll a in the Mid-Atlantic Bight. *Continental Shelf Research,* 31 (16), 1640-1650.

Zhang, C., Hu, C., Shang, S., Müller-Karger, F.E., Li, Y. *et al*., 2006. Bridging between SeaWiFS and MODIS for continuity of chlorophyll-*a* concentration assessments off SouthEastern China. *Remote Sensing of Environment,* 102 (3), 250-263.

CAPÍTULO 6

SEASONAL-TO-INTERANNUAL VARIABILITY OF CHLOROPHYLL-A BLOOM TIMING ASSOCIATED WITH PHYSICAL FORCING IN THE GULF OF CADIZ

Gabriel Navarro[1], Isabel Caballero[1], Laura Prieto[1], Águeda Vázquez[2], Susana Flecha[1], I.E. Huertas[1], Javier Ruiz[1]

[1] Departamento de Ecología y Gestión Costera, Instituto de Ciencias Marinas de Andalucía, Consejo Superior de Investigaciones Científicas (ICMAN-CSIC), Puerto Real, 11510, España

[2] Departamento de Física Aplicada, Universidad de Cádiz, Campus Río de San Pedro, Puerto Real, 11510, España

Advances in Space Research, 2012, 50, 8, 1164-1172
doi:10.1016/j.asr.2011.11.034
Factor de impacto: 1.183 (2012)
Categoría: GEOSCIENCES, MULTIDISCIPLINARY
Rango en la categoría: 103
Número total de revistas en la categoría: 172
Quartil en la categoría: Q3

Available online at www.sciencedirect.com

SciVerse ScienceDirect

Advances in Space Research 50 (2012) 1164–1172

ADVANCES IN SPACE RESEARCH (a COSPAR publication)

www.elsevier.com/locate/asr

Seasonal-to-interannual variability of chlorophyll-*a* bloom timing associated with physical forcing in the Gulf of Cádiz

G. Navarro [a,*], I. Caballero [a], L. Prieto [a], A. Vázquez [b], S. Flecha [a], I.E. Huertas [a], J. Ruiz [a]

[a] Instituto de Ciencias Marinas de Andalucía, ICMAN-CSIC, 11510 Puerto Real, Cádiz, Spain
[b] Departamento de Física Aplicada, Universidad de Cádiz, 11510 Puerto Real, Cádiz, Spain

Available online 4 December 2011

Abstract

Seasonal-to-interannual variability of the winter-spring bloom in the Gulf of Cádiz, eastern North Atlantic, has been investigated using chlorophyll-*a* remote sensing (CHL). These data have been obtained from the GlobColour project; the temporal coverage extends from September 1997 to December 2010. In this study we develop a generic quantitative approach for describing the temporal variability in the shape of the winter-spring bloom within a region. Variability in both the timing and magnitude of the bloom in the basin has been evaluated as a function of physical properties in the water column such as Mixed Layer Depth (MLD, GODAS model), sea surface temperature (SST, from AVHRR radiometers), photosynthetically-active radiation (PAR, from ocean color data) and euphotic depth (Z_{eu}, from ocean color data). The analysis indicated that the timing, size and duration of the phytoplankton bloom in this area are largely controlled by both meteorological and oceanographic conditions at different scales; this means that it is likely to vary widely from one year to another.

Keywords: Gulf of Cádiz; Timing of bloom; Physical–biological forcing

1. Introduction

Ocean phytoplankton is responsible for approximately half the net primary production of the global biosphere (Field et al., 1998). Satellite ocean-color observations have been used for some time to estimate global primary production (Longhurst et al., 1995; Behrenfeld and Falkowski, 1997). Recently, long-term change in global ocean surface chlorophyll-*a* has been shown using satellite data (Martinez et al., 2009); contradictory results have been obtained regarding whether the global ocean biomass increased or decreased from the 1980s to the 2000s (Antoine et al., 2005; Gregg and Conkright, 2002). It has also been reported that the global phytoplankton concentration has declined over the past century (Boyce et al., 2010).

These changes in chlorophyll-*a* concentration and primary production are attributed to variations in physical factors, such as wind, iron deposition and sea surface temperature (SST), associated with global climate changes (Behrenfeld et al., 2006). These studies have concluded that the global annual ocean primary production has decreased in recent years, corresponding with an increase in global SST of 0.2 °C over the same period (Gregg et al., 2003). Warmer ocean temperatures increase stratification of the surface mixed layer, which inhibits the entrainment of nutrients from lower depths to support ocean primary production (Sarmiento et al., 1998). In the North Atlantic Ocean, annual primary production has decreased by 7% over the last two decades, while SST has increased by 0.7 °C and iron deposition decreased by 19% (Gregg et al., 2003).

The initial growth of the phytoplankton bloom has been associated also with variations in incident radiation and wind mixing (Townsend et al., 1994; Henson et al., 2006), in air-temperature (Nezlin and Li, 2003), in sea surface temperature (Thomas et al., 2003), Asian dust (Jo et al., 2007) and in net heat flux (Azumaya et al., 2001); the timing of the bloom is important for the development of zooplankton

* Corresponding author.
E-mail address: Gabriel.navarro@icman.csic.es (G. Navarro).

0273-1177/$36.00 © 2011 COSPAR. Published by Elsevier Ltd. All rights reserved.
doi:10.1016/j.asr.2011.11.034

(Rey et al., 1987), and has implications for higher trophic levels (Platt et al., 2003) and for the seasonality of the biological carbon pump (Eppley and Peterson, 1979). The classic quantitative description of bloom initiation was developed by Sverdrup (1953), who established that the vernal bloom is initiated when the surface mixed layer becomes shallower than the critical depth. Recently, several studies have been carried out in the North Atlantic ocean (Behrenfeld, 2010; Boss and Behrenfeld, 2010), demonstrating that the Critical Depth hypothesis is an inadequate framework for understanding vernal blooms, and replacing it by the Dilution-Recoupling hypothesis (Behrenfeld, 2010); this most recent approach focuses on the balance between phytoplankton growth and grazing, and the seasonally-varying physical processes that influence this balance.

One of the areas where the conditions required by Sverdrup's 1953 hypothesis do not hold is the eastern north Atlantic south of 40°N, where the Gulf of Cádiz is located (Fig. 1). Despite the geographic relevance of the Gulf for oceanographic research, only a few studies of ocean color time-series have been undertaken there with a view to understanding better the phytoplankton blooms using remote sensing data. Sousa and Bricaud (1992) initially described the pigment pattern in the area by analyzing daily images of the Coastal Zone Color Sensor (CZCS). Later, Peliz and Fiúza (1999) reported a complete study investigating the variability of surface pigments derived from the CZCS around the entire Portuguese coast but also briefly including the Gulf of Cádiz. Navarro and Ruiz (2006) analyzed the seasonal variability of chlorophyll-*a* concentration in the continental shelf of the Gulf of Cádiz, and they investigated the differences between the spring bloom in the coastal areas and the winter-spring bloom in the open sea area.

The aim of this study is to analyze the seasonality and the generation of the bloom in the Gulf of Cádiz in the context of the Sverdrup (1953) versus Behrenfeld (2010) hypothesis. This understanding is then used to interpret the interannual variations of this seasonality in the basin associated with physical forcing. The analysis is performed in longer time and greater space resolution than previous studies of the northeastern Atlantic, thus providing more solid grounds on the conclusions obtained.

2. Material and methods

2.1. Ocean color images

Ocean surface chlorophyll-*a* data were downloaded from the GlobColour Project (http://www.globcolour.info/) which produces global ocean color maps (Level-3) by merging the data from the three sensors SeaWiFS, MODIS and MERIS, for the period between 1997 and the end of 2010. Surface chlorophyll-*a* data corresponds to product Chlorophyll-*a* Case I water based on GSM merging method (Maritorena and Siegel, 2005; Maritorena et al., 2010). This method provides the best fit to *in-situ* chlorophyll-*a* concentration and has the added advantages

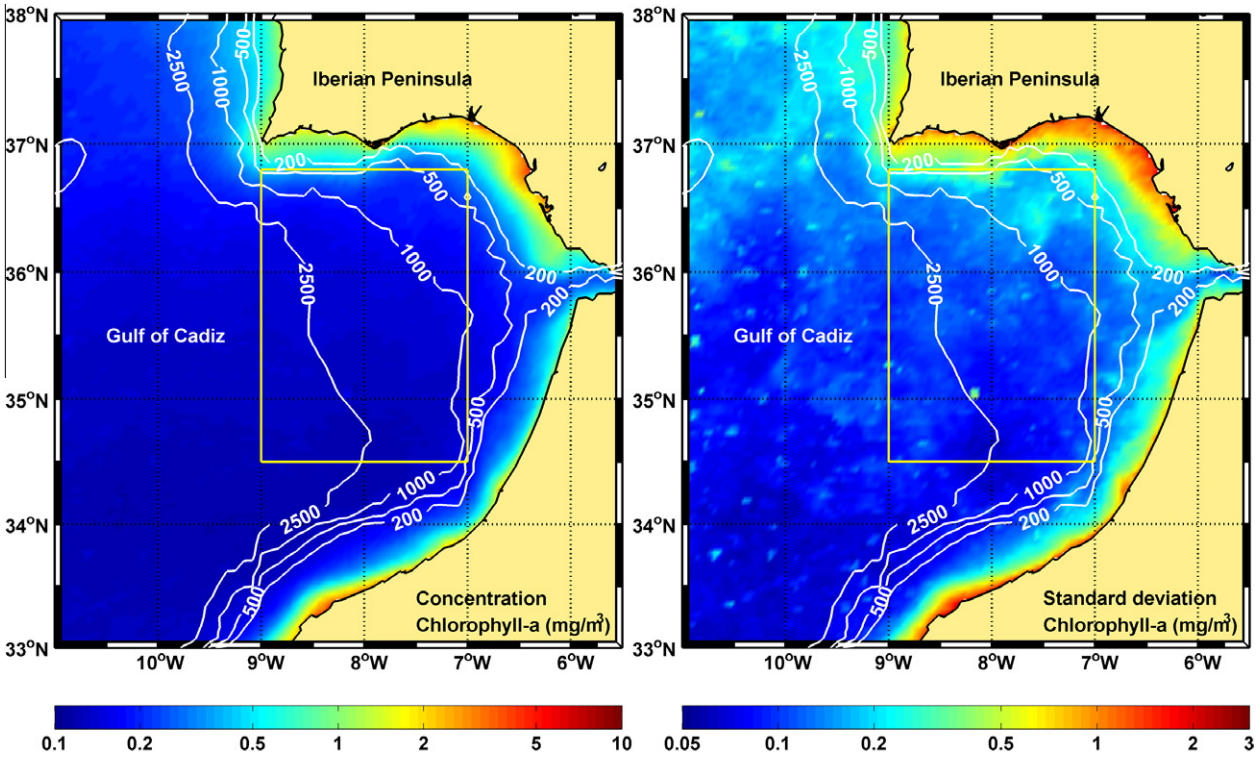

Fig. 1. Images of average chlorophyll-*a* values (left, in mg/m^3) and standard deviation (right, in mg/m^3) for the Gulf of Cádiz between September 1997 and December 2010. The yellow box area represents the ROI for this study. The contour lines represent the bathymetry (in meters). (For interpretation of the references to colour in this figure legend, the reader is referred to the web version of this article.)

of providing other products and allowing to calculate pixel-by-pixel error bars. With these data sets the cloud cover is reduced and, therefore, more useful images become available. Spatial and temporal resolutions of these composite images were 4.6 km and 8 days respectively. The Region of Interest (ROI, 36° 48'–34° 30' N; 9°–7°W, Fig. 1) covers an area of 45,541 km^2 and is located in the center of the Gulf of Cádiz, far from coastal areas that represent Case I water (Caballero et al., 2011). Time series were calculated by averaging arithmetically all valid pixels included in the ROI for each 8-days composite.

To model the annual bloom, 8-day chlorophyll-*a* concentration composite values were fitted to a Gaussian function of time. This function has been used by other authors, first to analyze the vertical pigment profile (i.e. Platt et al., 1988; Bouman et al., 2000; Richardson et al., 2003), and subsequently, the time series of satellite-derived chlorophyll-*a* values during the spring bloom, which also presents a similar distribution with an annual peak (Yamada and Ishizaka, 2006; Platt et al., 2007, 2009). The Gaussian function for describing the time series of satellite-derived chlorophyll-*a* (CHL) values is:

$$\mathrm{CHL}(t) = \mathrm{CHL}_0 + \frac{h}{\sigma\sqrt{2\pi}} * \exp\left[-\frac{(t-d_{\max})^2}{2\sigma^2}\right] \quad (1)$$

where CHL_0 is the base-line chlorophyll-*a* concentration (mg/m^3), $d_{\max}$ (day) is the peak timing, σ (day) is the standard deviation of the Gaussian curve and defines the width of the peak and the peak concentration is defined by ($h/\sigma\sqrt{2\pi}$) where h (mg/m^3 day) is the integral of total satellite derived chlorophyll-*a* values above the base-line. This model was fitted to the chlorophyll-*a* data starting in September and ending in August of the following year, using the nonlinear least-squares method. For this model (Model 1), the initiation of the bloom was calculated as $d_{\max} - 2\sigma$. Moreover, two more model have been implemented to estimate the initiation of the bloom: the approach proposed by Platt et al. (2009) that defines the initiation of the bloom as the time when the amplitude of the fitted curve reaches 20% of the amplitude of the Gaussian (Model 2) and the method by Siegel et al. (2002), which provides a reasonable index for bloom initiation the day in which chlorophyll-*a* rises 5% above the annual median values (Model 3). This method has been also applied by Henson et al. (2006) and Henson and Thomas (2007).

PAR images were obtained from the SeaWiFS sensor (September 1997–December 2007) and from the MODIS sensor (January 2008–December 2010) using individual 8-day Level-3 SMI products, with 9 km of spatial resolution, obtained from NASA's Goddard Space Flight Center (http://oceancolor.gsfc.nasa.gov). Time series were calculated by averaging arithmetically all valid pixels included in the ROI for every 8-days composite.

Net specific growth (r, on d^{-1}) have been calculated from 8-day chlorophyll-*a* satellite data for the ROI, following Behrenfeld (2010):

$$r = \ln\left(\sum \mathrm{CHL}_1 / \sum \mathrm{CHL}_0\right)/\Delta t \quad \text{if MLD is deepening and} > Z_{\mathrm{eu}} \quad (2)$$

$$r = \ln(\mathrm{CHL}_1/\mathrm{CHL}_0)/\Delta t \quad \text{if MLD is shoaling or} < Z_{\mathrm{eu}} \quad (3)$$

where CHL_0 and $\sum\mathrm{CHL}_0$ are the initial chlorophyll-*a* concentration, CHL_1 and $\sum\mathrm{CHL}_1$ are the chlorophyll-*a* concentration after the time interval ($\Delta t = 8$ days) and $\sum\mathrm{CHL} = \mathrm{CHL} * \mathrm{MLD}$, expressed as mg/m^2, which accounts for dilution of the population over a larger volume (Behrenfeld, 2010).

The euphotic depth (Z_{eu}, the depth at which the irradiance has decreased to 1% of the surface value) has been calculated according to the Lambert–Beer law and using the attenuation coefficient (K_d) derived from K490 (Rochford et al., 2001) obtained from the GlobColour Project.

$$K_d = 0.0085 + 1.6243 * \mathrm{K490} \ (\text{where K490} < 1) \quad (4)$$

$$Z_{\mathrm{eu}} = 4.6052/K_d \quad (5)$$

A three-bin running boxcar averaging has been applied to ocean color products (CHL, PAR, r and Z_{eu}) to dampen high frequency variability.

2.2. Sea surface temperature (SST) data

Pathfinder v5 SST data are derived from the five-channel Advanced Very High Resolution Radiometers (AVHRR) on board NOAA polar orbiting satellites. These SST data are a new reanalysis of the AVHRR data stream developed by the University of Miami's Rosenstiel School of Marine and Atmospheric Science (RSMAS) and the NOAA National Oceanographic Data Center (NODC).The product consists of a pair of 8 day-composite global SST (°C) fields at a spatial resolution of 4 km, representing ascending (daytime) and descending (night-time) orbits separately. The data used from September 1997 to December 2009 of descending orbits. Pathfinder SST data are available via an anonymous ftp on the Jet Propulsion Laboratory (JPL) web site (ftp://podaac.jpl.nasa.gov). In the present analysis, the global SST data were sub-sampled to the region of interest including the quality data of the image. SST data were smoothed as described with the ocean color data.

2.3. Mixed Layer Depth (MLD) data

Mixed Layer Depth (MLD) data have been obtained from the operational data sets produced routinely by the Global Ocean Data Assimilation System (GODAS) developed at the National Centers for Environmental Prediction (NCEP). The binary data can be retrieved via ftp cfs.ncep.noaa.gov at directory pub/cfs/godas. The spatial resolution of the MLD data was 0.3° in latitude and 1° in longitude (Behringer and Xue, 2004), and the values were a 5-day composite (pentad). The data run from 1980 to 2010, and were smoothed similarly to ocean color and SST data.

The date and the depth of the maxima MLD for each year were calculated from the times series.

3. Results and discussion

3.1. Seasonal chlorophyll-a dynamics in the Gulf of Cádiz

Fig. 1 displays the climatological chlorophyll-*a* distribution in the basin that was calculated by averaging monthly values of chlorophyll-*a* at each pixel for the whole study period (September 1997–December 2010). Following the general tendency of primary production in the ocean (i.e. Behrenfeld and Falkowski, 1997), this image shows the highest (>10 mg/m^3) concentration and more standard deviation in coastal areas, mainly in the Iberian continental shelf whereas the lowest (<0.1 mg/m^3) chlorophyll-*a* appears in offshore waters, where the standard deviation is the lowest (Fig. 1). These differences are due to the hydrological structures that govern the area. Navarro and Ruiz (2006) described the spatial and temporal patterns of chlorophyll-*a* in several areas over the continental shelf and offshore, and Vargas et al. (2003) defined the anticyclonic structure in the center of the basin that coincides with the oligotrophic area analyzed in this study.

The spatial and temporal pattern of chlorophyll-*a* concentration in the ROI is illustrated in Figs. 2 and 3 respectively. Some common features that are clearly noticeable in the 13-year monthly climatology are the higher concentrations located on the north side with a pronounced north-south decrease. Fig. 3 shows the climatological time series, calculated by averaging 8-days values of the 13 years, and the percentiles (5% and 95%) for chlorophyll-*a* concentration from the GlobColour database in the ROI. The temporal evolution of the chlorophyll-*a* values in the Gulf of Cádiz comprises two distinct regimes over the course of the year: the bloom period from winter to spring (maximum between February and April) and the non-bloom period from May to October, similar to that described in the Alborán Sea (García-Gorriz and Carr, 1999) and western Iberian Peninsula (Peliz and Fiúza, 1999). The mean chlorophyll-*a* concentration fluctuated during the seasonal cycle between 0.1 and 0.35 mg/m^3 over the year, with an overall average concentration of 0.15 mg/m^3. These values reflect the oligotrophic nature of these waters. The greatest differences between percentiles were observed during the winter months, especially between February and April.

3.2. Interannual variations of chlorophyll-a seasonality

Chlorophyll-*a* values from September 1997 to December 2010 clearly showed large variability (Fig. 4). High CHL_{SAT} values were observed in late winter (February and March) each year, and low chlorophyll-*a* concentration always occurred in summer. Chlorophyll-*a* concentration varied from 0.08 to 0.6 mg/m^3, which indicates an oligotrophic area similar to Pacific ocean (Wilson, 2003) and Atlantic ocean (Peliz and Fiúza, 1999). The highest chlorophyll-*a* concentration was observed in late winter in 2009 (≈0.6 mg/m^3).

The use of a Gaussian function to fit the temporal variability of chlorophyll-*a* allows to synthesize the dynamics of the blooming process in the Gulf of Cádiz and, therefore, facilitate its analyses in response to the physical forcing at different scales. Table 1 presents several parameters about the Gaussian fit, including peak amplitude ($h/\sigma\sqrt{2\pi}$), peak timing (d_{max}) and peak width (σ) for each of the 13 years of analysis (Fig. 4). The quality of each curve fitting was assessed by calculating the determination coefficients (R^2; Table 1). These coefficients were very high with a mean value of 0.93 (SD = 0.03). In addition, several models have been used to calculate the initiation of the bloom (see Section 2.1).

This parameterization permits to examine the interannual variations of chlorophyll-*a* seasonality. The background chlorophyll-*a* concentration (CHL_0) generally had very low values (<0.1 mg/m^3) whereas the peak amplitude ranged between 0.1 and 0.55 mg/m^3 throughout the years (Table 1). The width of the bloom peak (σ) varied between 19 and 54 days while the timing of the bloom peak (d_{max}) ranged from the middle of January to the beginning of March, although it usually occurred in February. Mean and standard deviation of peak amplitude and σ were 0.2408 (SD = 0.1187) mg/m^3 and 37 (SD = 9.25) days, respectively.

The timing of the start of the bloom could be an indicator of inter-annual variability in phytoplankton bloom characteristics (Henson et al., 2006). Table 1 shows the dates of the initiation of the bloom calculated by different methods. The earliest bloom was observed in 1997/1998, starting at the end of September, and the latest bloom occurred in 2004/2005, starting on December 10 in 2004. Although individual divergences among models can be observed for some years (Fig. 4; Table 1), there were no overall statistical differences in the date of initiation of the bloom among the three models (ANOVA, $F_{2,36} = 1.51$, $P < 0.2$). Table 1 also evidences differences between Model 3 and the values assigned to this region in the work where this model is first described (Siegel et al., 2002). This discrepancy could emerge from differences in the spatial resolution of the analyses since Siegel et al. (2002) integrated the whole 35°–40°N latitudinal band whereas we only integrated the eastern Atlantic between 36° 48'–34° 30' N. Besides the latitudinal differences involved, also there are longitudinal variations in the initiation of the bloom (Henson and Thomas, 2007).

3.3. Physical forcing of the chlorophyll-a bloom

Fig. 5 shows the temporal pattern of chlorophyll-*a*, *r*, MLD, euphotic depth (Z_{eu}), SST and PAR for the same period than the chlorophyll-*a* time series. There is a seasonal variation in MLD, with decreases in depth from more than 300 m in February–March to 25 m during the summer months. The evolution of MLD shows a large interannual variability (Fig. 5b) although there is a neat coincidence between the timing of MLD and chlorophyll-*a* maxima (d_{max}). A linear correlation analysis between the maximum

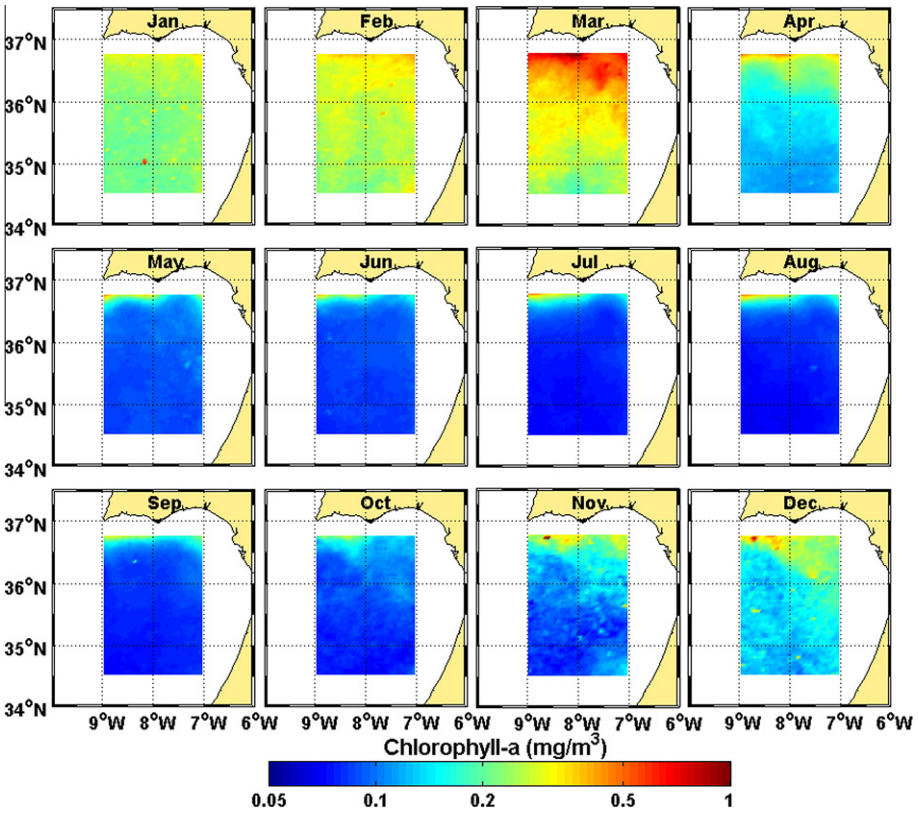

Fig. 2. The 13-year (September 1997–ecember 2010) monthly mean Chlorophyll-*a* (in mg/m^3) distribution for the ROI located at the Gulf of Cádiz.

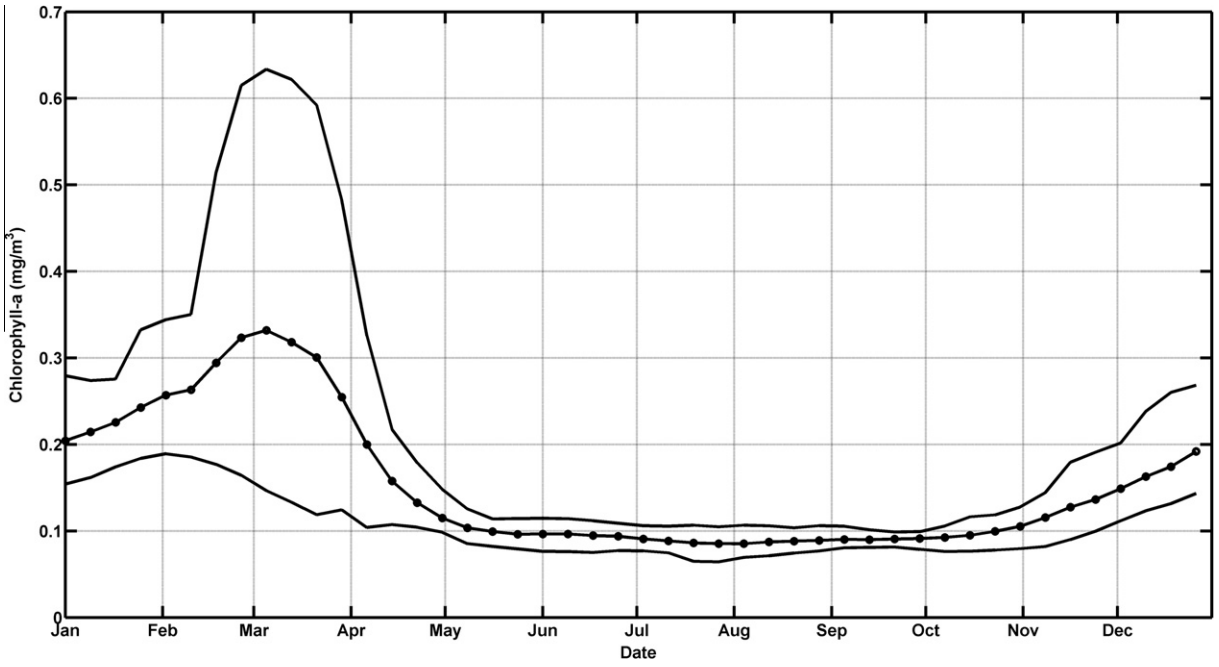

Fig. 3. Annual mean cycle from January to December of chlorophyll-*a* values (open symbol) and 5 and 95 percentiles (solid lines) between September 1997 and December 2010.

depth of the MLD in winter and the peak amplitude of bloom suggests a cause-effect connection between these two parameters ($R = 0.83$ and $P < 0.001$, Table 2), which is also observed between MLD and chlorophyll-*a* integration (h) ($R = 0.54$ and $P < 0.05$, Table 2). In addition, the winter maximum depth is correlated with the duration of the bloom ($R = -0.74$ and $P < 0.01$, Table 2). During several years the initiation of the bloom (mean day of the

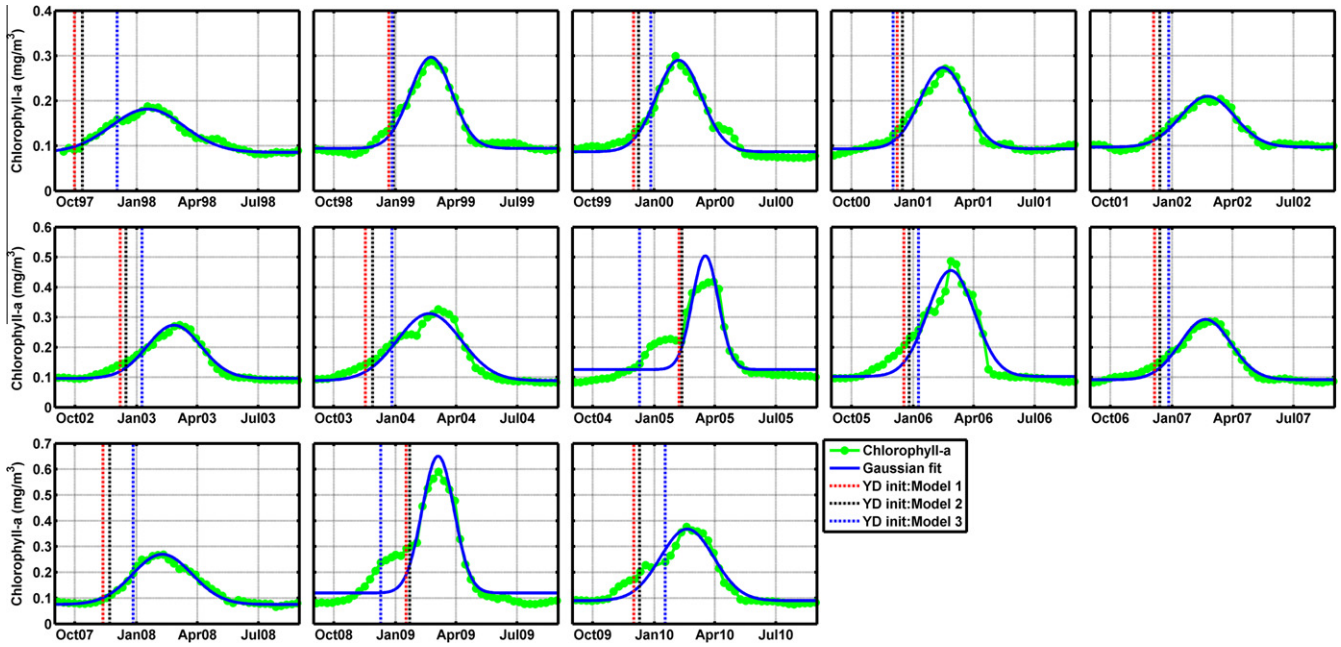

Fig. 4. Thirteen-year record of 8-day chlorophyll-*a* values (green line) and Gaussian function (blue line) fitted to the chlorophyll-*a* data every year bloom (from September to August of the next year). Vertical dashed lines represents the date (YD init) of the initiation of the bloom following several models. Model 1: Yamada and Ishizaka (2006); Model 2: Platt et al. (2009) and Model 3: Siegel et al. (2002). (For interpretation of the references to colour in this figure legend, the reader is referred to the web version of this article.)

Table 1
Parameters obtained from the Gaussian fit for the bloom each year. CHL_o is the base-line chlorophyll-*a* concentration, Peak amplitude ($h/\sigma\sqrt{2\pi}$), σ defines the width of the peak, the date of the initiation of the bloom (dates and Julian day) calculated by three models (Model 1: Yamada and Ishizaka, 2006; Model 2: Platt et al., 2009; and Model 3: Siegel et al., 2002). d_{max} is the date of the peak timing (date and Julian day) and R^2 is the coefficient of determination of the Gaussian fit.

Year of bloom	CHL_0 mg/m^3	Peak mg/m^3	σ days	Start of bloom (date/Julian day)			d_{max} (date)	R^2
				Model 1	Model 2	Model 3		
1997/1998	0.0856	0.0960	54.34	09/30/1997 273	10/12/1997 285	12/03/1997 337	01/17/1998 17	0.94
1998/1999	0.0944	0.2024	31.39	12/21/1998 355	12/29/1998 363	12/27/1998 361	02/22/1999 53	0.96
1999/2000	0.0869	0.2030	33.73	12/01/1999 335	12/09/1999 343	12/27/1999 361	02/06/2000 37	0.94
2000/2001	0.0934	0.1804	33.96	12/08/2000 343	12/16/2000 351	12/02/2000 337	02/14/2001 45	0.93
2001/2002	0.0972	0.1128	40.03	12/04/2001 338	12/14/2001 348	12/27/2001 361	02/22/2002 53	0.97
2002/2003	0.0961	0.1769	40.06	12/07/2002 341	12/16/2002 350	01/09/2003 9	02/25/2003 56	0.95
2003/2004	0.0887	0.2231	47.54	11/17/2003 321	11/28/2003 332	12/27/2003 361	02/20/2004 51	0.89
2004/2005	0.1257	0.3788	19.45	02/06/2005 37	02/11/2005 42	12/10/2004 345	03/17/2005 76	0.87
2005/2006	0.1024	0.3530	34.90	12/18/2005 352	12/26/2005 360	01/09/2006 9	02/25/2006 56	0.90
2006/2007	0.0916	0.2008	37.74	12/06/2006 340	12/14/2006 348	12/27/2006 361	02/19/2007 50	0.96
2007/2008	0.0754	0.1945	44.19	11/12/2007 316	11/22/2007 326	12/27/2007 361	02/08/2008 39	0.97
2008/2009	0.1199	0.5308	23.79	01/16/2009 16	01/22/2009 22	12/10/2008 345	03/05/2009 64	0.89
2009/2010	0.0901	0.2777	39.68	12/01/2009 335	12/10/2009 344	01/17/2010 17	02/18/2010 49	0.91

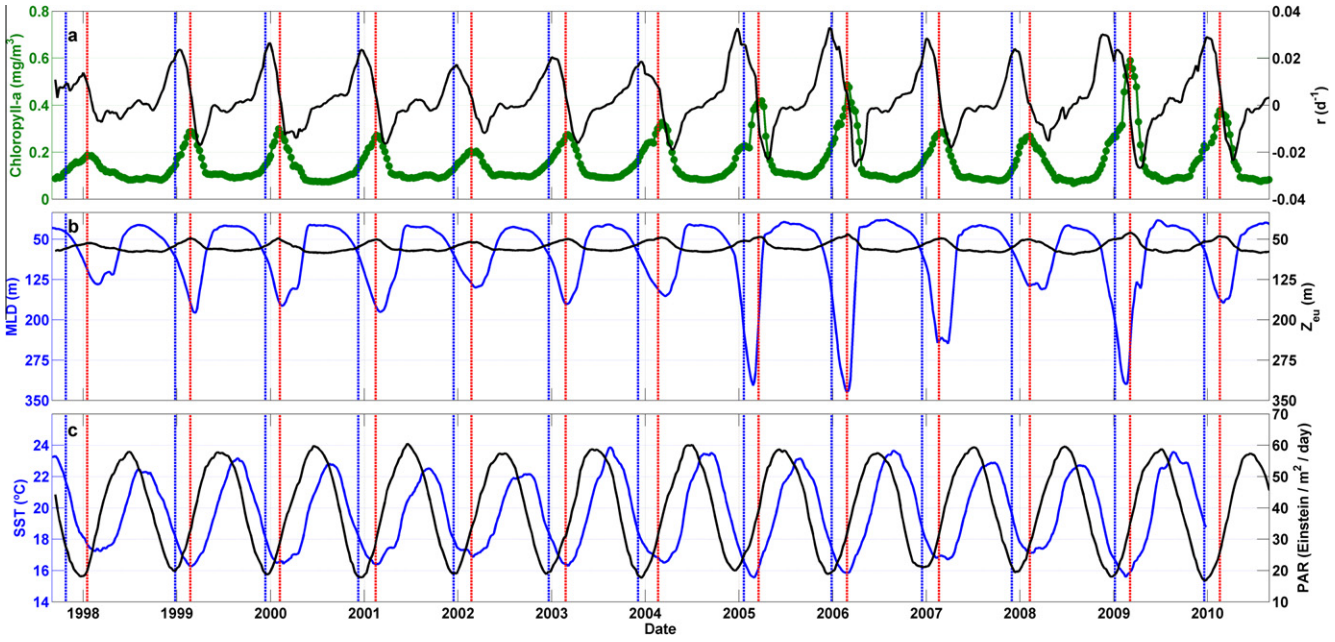

Fig. 5. (a) Time series of chloropyhll-a values (green line, left axis) and phytoplankton net specific growth rate (black line, right axis). (b) Time series of MLD (blue line, left axis) and euphotic depth (black line, right axis). (c) Time series of SST (blue line, left axis) and PAR (black line, right axis). Vertical solid and dashed red lines indicate the timing of the bloom peak (d_{max}) and the start of the bloom (averaged day between the three models) respectively. (For interpretation of the references to colour in this figure legend, the reader is referred to the web version of this article.)

Table 2
Correlation coefficients of (a) maximum MLD to various parameters of Gaussian fit and physical factors (SST_{min}), (b) chlorophyll-*a* peak to the start of the bloom (mean date of the three models) and physical factors (SST_{min}).

(a)	Peak	*h*	σ	SSTmin
MLDmax	0.83 $P < 0.001$	0.54 $P < 0.05$	−0.74 $P < 0.01$	−0.83 $P < 0.001$
(b)		Start of bloom		SSTmin
CHL-a Peak		0.71 $P < 0.01$		−0.85 $P < 0.001$

three models) coincides with the time when the MLD extends below the euphotic layer (Z_{eu}, Fig. 5).

There are some years, such as 2004, 2005, 2006 and 2009, when the determination coefficients have slight deviations (Table 1). For these years with two chlorophyll-*a* peaks, the Gaussian curve fit misses the first chlorophyll-*a* maximum, resulting in an apparent delay in the start of the bloom as reflected by the function parameters. This first peak is followed by events of atypically deep mixed layers (>300 m). Therefore, they can be interpreted as an interruption of the seasonal development of the bloom, owing to dilution and/or light limitations involved in severe entrainment events. The second peak after this interruption is singularly high in connection with an input of deep nutrient-rich waters to the surface (Koeve, 2001; Pätsch et al., 2002). Nutrient enrichment after entrainment can also generates the small rises in chlorophyll-*a* observed in April 1998 and 2000.

The pattern of seasonal variations of SST and PAR in the ROI is illustrated in Fig. 5. Minimum SST in winter is correlated with winter maximum MLD ($R = -0.83$ and $P < 0.001$, Table 2) and peak intensity of bloom ($R = -0.85$ and $P < 0.001$, Table 2). In summer, the MLD minimum also coincides with the SST maximum, when there is maximum stratification in the area (Navarro et al., 2006). PAR intensity (Fig. 5c) does not correlate with peak bloom, duration or timing. These findings indicate that chlorophyll-*a* patterns are not limited by light, and are in agreement with previous reports described in the Atlantic (Siegel et al., 2002) and in the Alborán Sea (García-Gorriz and Carr, 1999) at the same latitude. However, PAR is one of the key signals that govern the seasonal and latitudinal patterns of the phytoplankton biomass, along with the daily integrated light in the mixed layer that also locally modifies the effect of latitude on phytoplankton seasonality (Platt et al., 2009). In fact, there is a positive relationship between the initiation of the bloom (mean date of the three models) and the bloom peak ($R = 0.71$ and $P < 0.01$, Table 2), which indicates that if a blooms starts late, more PAR would be available during the bloom period, as the bloom initiation always occurs later than the PAR minimum in the time series.

The generic mechanism for the initiation of the bloom elucidated by Sverdrup (1953) is related to the rapid

increase of insolation during the spring. However, this is not the case in the ROI latitude, as the PAR is at its minimum levels when the bloom is developing. In addition, Sverdrup (1953) emphasizes that the initiation of the bloom coincides in time with the mixed layer getting shallower in spring, whereas in the Gulf of Cádiz, the chlorophyll-*a* increase occurs while the mixed layer is getting deeper.

Although the time of the maximum depth of MLD is visually correlated with the time of the chlorophyll-*a* peak (d_{max}), it has no effect in either bringing forward or delaying the late winter bloom (no correlation has been found between start and end timing of the bloom and the timing of the maximum depth of MLD). During each seasonal cycle, r remains negative after the time of the bloom peak (d_{max}) until early autumn, to subsequently increase in line with the rise of MLD and the decrease PAR (Fig 5). The maximum chlorophyll-*a* concentration at d_{max} represents the culmination of a positive population growth phase during the phytoplankton bloom, and this phase normally happens while the MLD is getting deeper. These data are consistent with the Dilution-Recoupling hypothesis (Behrenfeld, 2010): when the MLD is greater than the Z_{eu}, the balance between the phytoplankton specific growth rate and grazing is perturbed and the positive net growth phase is initiated for the annual winter bloom in the Gulf of Cádiz.

4. Conclusions

Results presented in this study neatly suggest the dominant role of the seasonal cycle in modulating the chlorophyll-*a* evolution, as compiled by GlobColour time series for open-sea water in the Gulf of Cádiz. The interannual variability in chlorophyll-*a* can be explained by changes in MLD among years. The coupling of MLD and chlorophyll-*a* maxima in the ROI cannot be explained in the framework of the Critical Depth Hypothesis (Sverdrup, 1953). In disagreement with this hypothesis, the initiation of the bloom always occurs earlier than the maxima in the mixed layer during the entrainment period. The analysis of thirteen time series of open ocean oligotrophic waters in the Gulf of Cádiz is more coherent with the Dilution-Recoupling hypothesis recently formulated by Behrenfeld (2010).

Acknowledgments

We thank the ESA for distributing the GlobColour data used in this study, the JPL (NASA) for SST data and the NCEP for MLD data. This work was supported by research projects P09-RNM-4853, PR11-RNM-7722, CTM2008-05680-C02-01/MAR, SESAME (FP6-036949) and MedEX (CTM2008-04036-E/MAR).

References

Antoine, D., Morel, A., Gordon, H.R., Banzon, V.F., Evans, R.H. Bridging ocean color observations of the 1980s and 2000s in search of long-term trends. J. Geophys. Res. 110, C06009, 2005.

Azumaya, T., Isoda, Y., Noriki, S. Modeling of the spring bloom in Funka Bay, Japan. Cont. Shelf. Res. 21, 473–494, 2001.

Behrenfeld, M.J., Falkowski, P.G. Photosynthetic rates derived from satellite-based chlorophyll concentration. Limnol. Ocean. 42 (1), 1–20, 1997.

Behrenfeld, M.J., O'Malley, R.T., Siegel, D.A., McClain, C.R., Sarmiento, J.L., Feldman, G.C., Milligan, A.J., Falkowski, P.G., Letelier, R.M., Boss, E.S. Climate-driven trends in contemporary ocean productivity. Nature 444, 752–755, 2006.

Behrenfeld, M.J. Abandoning Sverdrup's Critical Depth Hypothesis on phytoplankton blooms. Ecology 91 (4), 997–1021, 2010.

Behringer, D., Xue, Y. Evaluation of the global ocean data assimilation system at NCEP: The Pacific Ocean. Eighth Symposium on Integrated Observing and Assimilation Systems for Atmosphere, Oceans, and Land Surface, AMS 84th Annual Meeting, Washington State Convention and Trade Center, Seattle, Washington, 11–15, 2004.

Boss, E., Behrenfeld, M.J. In situ evaluation of the initiation of the North Atlantic phytoplankton bloom. Geophys. Res. Lett. 37, L18603, doi:10.1029/2010GL044174, 2010.

Bouman, H.A., Platt, T., Sathyendranath, S., Irwin, B.D., Wernand, M.R., Kraay, G.W. Bio-optical properties of the subtropical North Atlantic. II. Relevance to models of primary production. Mar. Ecol. Prog. Ser. 200, 19–34, 2000.

Boyce, D.G., Lewis, M.R., Worm, B. Global phytoplankton decline over the past century. Nature 466, 591–596, 2010.

Caballero, I., Ruiz, J., Navarro, G. Dynamics of the turbidity plume in the Guadalquivir estuary (SW Spain): A remote sensing approach, IEEE Oceans 2011, Santander, Spain, 2011.

Eppley, R.W., Peterson, B.J. Particulate organic matter flux and planktonic new production in the deep ocean. Nature 282, 677–680, 1979.

Field, C.B., Behrenfeld, M.J., Randerson, J.T., Falkowski, P. Primary Production of the Biosphere: Integrating Terrestrial and Oceanic Components. Science 281, 237–240, 1998.

García-Gorriz, E., Carr, M.E. The climatological annual cycle of satellite-derived phytoplankton pigments in the Alborán Sea. Geophys. Res. Lett. 26 (19), 2985–2988, 1999.

Gregg, W.W., Conkright, M.E. Decadal changes in global ocean chlorophyll. 29, 15, doi:10.1029/2002GL014689, 2002.

Gregg, W.W., Conkright, M.E., Ginoux, P., O'Reilly, J.E., Casey, N.W. Ocean primary production and climate: global decadal changes. Geophys. Res. Lett. 30, 1809, doi:10.1029/2003GL016889, 2003.

Henson, S.A., Robinson, I., Allen, J.T., Waniek, J.J. Effect of meteorological conditions on interannual variability in timing and magnitude of the spring bloom in the Irminger Basin, North Atlantic. Deep Sea Res. II. 53 (10), 1601–1615, 2006.

Henson, S.A., Thomas, A.C. Interannual variability in timing of bloom initiation in the California Current System. J. Geophys. Res. 112, C08007, doi:10.1029/2006JC003960, 2007.

Jo, C.O., Lee, J.Y., Park, K.A., Kim, Y.H., Kim, K.R. Asian dust initiated early spring bloom in the northern East/Japan Sea. Geophys. Res. Lett. 34, L05602, doi:10.1029/2006GL027395, 2007.

Koeve, W. Wintertime nutrients in the North Atlantic-new approaches and implications for new production estimates. Mar. Chem. 74, 245–260, 2001.

Longhurst, A.R., Sathyendranath, S., Platt, T., Caverhill, C. An estimate of global primary production in the ocean from satellite radiometer data. J. Plankton Res. 17, 1245–1271, 1995.

Maritorena, S., Siegel, D. Consistent merging of satellite ocean color data sets using a bio-optical model. Remote Sens. Environ. 94, 429–440, 2005.

Maritorena, S., d'Andon, O.H.F., Mangin, A., Siegel, D.A. Merged Satellite Ocean Color Data products using a bio-optical model: characteristics, benefits and issues. Remote Sens. Environ. 114, 1791–1804, 2010.

Martinez, E., Antoine, D., Fabrizio, D'Ortenzio., Gentili, B. Climate-driven basin-scale decadal oscillations of oceanic phytoplankton. Science 326 (5957), 1253–1256, 2009.

Navarro, G., Ruiz, J., Huertas, I.E., García, C.M., Criado-Aldeanueva, F., Echevarría, F. Basin-scale structures governing the position of the deep fluorescence maximum in the Gulf of Cádiz. Deep Sea Res. II. 53, 1261–1281, 2006.

Navarro, G., Ruiz, J. Spatial and temporal variability of phytoplankton in the Gulf of Cádiz through remote sensing images. Deep Sea Res. II. 53, 1241–1260, 2006.

Nezlin, N.P., Li, B.L. Time-series analysis of remote-sensed chlorophyll and environmental factors in the Santo Monica-San Pedro Basin off Southern California. J. Marine Syst. 39, 185–202, 2003.

Pätsch, J., Kuehn, W., Radach, G., Santana Casiano, J.M., Gonzalez Davila, M., Neuer, S., Freudenthal, T., Llinas, O. Interannual variability of carbon fluxes at the North Atlantic Station ESTOC. Deep Sea Res. II. 49, 253–288, 2002.

Peliz, A.J., Fiúza, A.F.G. Temporal and spatial variability of CZCS-derived phytoplankton pigment concentrations off the western Iberian Peninsula. Int. J. Remote Sens. 20 (7), 1363–1403, 1999.

Platt, T., Sathyendranath, S., Caverhill, C.M., Lewis, M.R. Ocean primary production and available light: further algorithms for remote sensing. Deep Sea Res. I. 35 (6), 855–879, 1988.

Platt, T., Fuentes-Yaco, C., Frank, K.T. Spring algal bloom and larval fish survival. Nature 423, 398–399, 2003.

Platt, T., Sathyendranath, S., Fuentes-Yaco, C. Biological oceanography and fisheries management: perspective after 10 years. ICES J. Mar. Sci. 64 (5), 863–869, 2007.

Platt, T., White, G.N., Zhai, L., Sathyendranath, S., Roy, S. The phenology of phytoplankton blooms: Ecosystem indicators from remote sensing. Ecol. Model. 2220, 3057–3069, 2009.

Rey, F., Skjoldal, H.R., Slagstad, D. 1987. Primary production in relation to climate changes in the Barents Sea. In: Loeng Bergen, H. (Ed.), The Effect of Oceanographic Conditions on Distribution and Population Dynamics of Commercial Fish Stocks in the Barents Sea. Institute of Marine Research. 29-46

Richardson, A.J., Silulwane, N.F., Mitchell-Innes, B.A., Shillington, F.A. A dynamic quantitative approach for predicting the shape of phytoplankton profiles in the ocean. Prog. Oceanogr. 59, 301–319, 2003.

Rochford, P.A., Kara, A.B., Wallcraft, A.J., Arnone, R.A. Importance of solar subsurface heating in ocean general circulation models. J. Geophys. Res. 106 (C11), 30923–30938, 2001.

Sarmiento, J.L., Hughes, T.M.C., Stouffer, R.J., Manabe, S. Simulated response of the ocean carbon cycle to anthropogenic climate warming. Nature 393, 245–249, 1998.

Siegel, D.A., Doney, S.C., Yoder, J.A. The North Atlantic Spring Phytoplankton Bloom and Sverdrup's Critical Depth Hypothesis. Science 296, 730–733, 2002.

Sousa, F., Bricaud, A. Satellite-derived phytoplankton pigments structures in the Portuguese upwelling area. J. Geophys. Res. 97 (C7), 11343–11356, 1992.

Sverdrup, H.U. On conditions for the vernal blooming of phytoplankton. Journal du Conseil Permanent International Pour L'Exploration de la Mer. 18, 287–295, 1953.

Thomas, A.C., Townsend, D.W., Weatherbee, R. Satellite measured phytoplankton variability in the Gulf of Maine. Cont. Shelf. Res. 23, 971–989, 2003.

Townsend, D.W., Cammen, L.M., Holligan, P.M., Campbell, D.E., Pettigrew, N.R. Causes and consequences of variability in the timing of spring phytoplankton blooms. Deep Sea Res. I. 41 (5-6), 747–765, 1994.

Vargas, J.M., Garcia-Lafuente, J., Delgado, J., Criado, F. Seasonal and wind-induced variability of sea surface temperature patterns in the Gulf of Cádiz. J. Marine Syst. 38 (3–4), 205–219, 2003.

Wilson, C. Late Summer chlorophyll blooms in the oligotrophic North Pacific Subtropical Gyre. Geophys. Res. Lett 30, 1942, doi:10.1029/2003GL017770, 2003.

Yamada, K., Ishizaka, J. Estimation of interdecadal change of spring bloom timing, in the case of the Japan Sea. Geophys. Res. Lett. 33, L02608, doi:10.1029/2005GL024792, 2006.

Capítulo 7

Síntesis general

7.1. Teledetección aplicada a la estimación de los parámetros de calidad de las aguas

Uno de los objetivos fundamentales de esta Tesis Doctoral es estudiar los procesos que acontecen en la desembocadura del Guadalquivir y golfo de Cádiz aprovechando al máximo las capacidades y particularidades que ofrece cada sensor. Las técnicas de teledetección empleadas durante el presente trabajo han resultado favorables y provechosas en la recuperación de información sobre la calidad del agua de la zona de estudio. En concreto, se han analizado los parámetros TSS y Chl de forma especial, además de otros parámetros como el $K_{d,}$ $z_{1\%}$, PAR y Rrs.

Para examinar la variabilidad espacio-temporal del bloom de fitoplancton en el golfo de Cádiz (Capítulo 6), se utilizaron los datos provenientes del Proyecto GlobColour Level 3 (combinación de MODIS, MERIS y SeaWiFS). La baja resolución espacial (4.6 km) fue suficiente para realizar el análisis de la zona oceánica externa al estuario. Sin embargo, para estudiar los procesos oceanográficos que se producen en la zona costera, necesitamos información satelital con mayor resolución espacial. Consecuentemente, en los Capítulos 4 y 5, cuyo objetivo principal era examinar los procesos biogeoquímicos que se producen en la región adyacente al estuario, se utilizaron las imágenes FRS provenientes de MERIS (2002-2012) y del sensor MODIS (2003-2013), con resoluciones espaciales de 300 m y 1 km, respectivamente.

Los resultados obtenidos con los datos proporcionados por el sensor MODIS (Capítulo 5) muestran que mediante el desarrollo del algoritmo empírico de la radiancia de la banda verde (λ=555 nm) se estiman los TSS con gran precisión (se=5.0 mg/L, r=0.96, $p<0.001$). Adicionalmente, este sensor mostraba una alta correlación positiva respecto a la Chl in situ (r=0.79, $p<0.001$), donde la sobreestimación de los datos del satélite se acentuaba desde la zona exterior (bias~0 mg/m^3) hasta la región costera

(bias=0.63 mg/m^3). A medida que nos acercamos a la desembocadura, es necesario aumentar la resolución espacial para analizar los procesos a pequeña escala, y es por ello, por lo que se hizo uso por primera vez de la reciente serie de datos MERIS FRS (*Full Resolution*, 300 m), con mayor resolución que los datos estándar de 1.1 km del mismo sensor (RR, *Reduced Resolution*). Esta mejora en la cobertura espacial favoreció el estudio de la pluma de turbidez y blooms de fitoplancton en una región más próxima al estuario (Capítulo 4). Los resultados certifican el éxito de la estimación de TSS mediante la reflectancia en la banda del rojo (λ=665 nm), describiendo el 80% de la varianza del conjunto de datos (se=38.3 mg/L, r=0.89, $p<0.001$). De igual manera que con el sensor MODIS, la evaluación de Chl fue correcta, alcanzando valores precisos (r=0.81, $p<0.0001$) pero exhibiendo cierta sobreestimación (bias=0.77 mg/m^3). A pesar de este aspecto, cabe indicar que el rango de variabilidad de los datos en este trabajo (Chl ~ 0-20 mg/ m^3) es superior a lo que se presenta en otros estudios y publicaciones, donde el valor máximo no supera los 10 mg/m^3.

Sin embargo, con la información suministrada por estos sensores de color oceánico, sobre todo debido a su resolución espacial, es imposible estudiar los procesos biogeoquímicos que se producen en el interior del estuario. Para ello, se utilizaron imágenes del satélite DEIMOS-1, con una resolución espacial de 22 metros y una resolución espectral de 3 bandas (verde: 510-618 nm, rojo: 614-698 nm e Infrarrojo Cercano: 755-906 nm) y así afrontar el análisis expuesto en los Capítulos 2 y 3. En primer lugar, indicar que debido a su baja resolución espectral, no se pudo cuantificar la concentración de clorofila, aunque si fue posible estimar los TSS. En segundo lugar, mientras que todas las series de datos descritas previamente estaban procesadas tras la corrección atmosférica por parte de las diferentes agencias espaciales (nivel L2, radiancia o reflectancia), con las imágenes DEIMOS-1 se procedió a la implementación de la corrección atmosférica como paso previo a la cuantificación de TSS, puesto que los datos originales se encontraban en Digital Number (L1B, sin corrección atmosférica). Una vez aplicada, se recuperaron los valores de TSS con una precisión excelente (r=0.93, $p<0.001$) mediante el algoritmo semi-empírico de la banda del Infrarrojo Cercano (λ=755-906 nm), a pesar del amplio rango de concentraciones a analizar (100-1400 mg/L).

Como se ha querido mostrar en los diferentes capítulos de esta Tesis Doctoral, es difícil determinar qué instrumento o sensor satelital es "óptimo" para estimar los

parámetros de calidad del agua en las zonas estuarinas y adyacentes a las mismas, y cómo las características del sensor en sí afectan al posterior análisis de la variabilidad espacio-temporal en la región de interés. Por lo tanto, dependiendo de los objetivos del estudio, habrá que elegir que sensor es el idóneo para alcanzar dichos propósitos, dependiendo de las características del satélite, como son la resolución espacial, espectral y temporal. Si se diseñara específicamente un nuevo instrumento para esta zona, debería tener una capacidad de revisita elevada (gran resolución temporal) y así permitir examinar patrones de alta frecuencia (escalas mareales de alta frecuencia, escala meteorológica,...). En este caso, sería una resolución temporal similar al sensor GOCI (Geostationary Ocean Color Imager), que es el primer satélite geoestacionario de color oceánico, con capturas de imágenes horarias. Sin embargo, la escasa resolución espacial (500 metros), similar a la de MERIS o MODIS, restringen el estudio de las zonas propias del estuario y generan pérdida de variación en el promedio espacial. Satélites como DEIMOS-1 (22 m), Landsat (~30 m) o la generación de Spot 6-7 (1.5 m) si permitirían examinar el estuario y analizar procesos de gran resolución espacial. Desventajas de estos instrumentos son su escasa cobertura temporal (de días a semanas) y baja resolución espectral (algunas bandas en la zona del visible). Para aumentar la resolución espectral, lo ideal sería trabajar con instrumentos hiper-espectrales como puede ser el sensor HICO (Hyperspectral Imager for the Coastal Ocean). Las características del número de bandas (128 canales entre 350 nm y 1080 nm) así como la anchura de las mismas (6 nm) posibilitan el análisis de una gran variedad de parámetros de calidad de las aguas en zonas específicamente complejas. Es posible que estos requisitos no se puedan aunar en un solo sensor y se necesite una constelación en su lugar, o como se ha planteado en esta Tesis Doctoral, utilizar numerosos sensores con diferentes características y realizar un análisis multi-sensor.

7. 2. Variabilidad espacio-temporal y mecanismos forzantes

El conjunto de resultados obtenidos en el marco de la presente Tesis Doctoral han permitido abordar la descripción de los procesos de turbidez y blooms de fitoplancton en la zona de la desembocadura del estuario del Guadalquivir y la plataforma continental del golfo de Cádiz, subrayando la importancia del intercambio de propiedades en el tramo final del mismo, entre el estuario y la zona adyacente. Tal como se describe en el trabajo realizado por Díez-Minguito *et al.* (2012), el comportamiento hidrodinámico del estuario se encuentra determinado principalmente por las descargas desde la presa de Alcalá del Río, diferenciando tres regímenes hidrodinámicos que dominan las distintas escalas de variabilidad dependiendo del volumen de la descarga: régimen fluvial (>400 m^3/s), régimen intermedio (40-400 m^3/s) y régimen mareal (<40 m^3/s).

Se ha expuesto repetidas veces a lo largo de esta memoria la estrecha relación existente entre la precipitación y las descargas desde la presa de Alcalá del Río, así como en la distribución de TSS. El papel estacional de ambos factores (precipitación y descarga) genera máximos de TSS particularmente durante los periodos de otoño e invierno, y mínimos durante las épocas estivales. Este aporte de agua dulce río arriba modifica la hidrodinámica inducida por la marea, incrementando la velocidad de sedimentación y capacidad de transporte de la componente fluvial (Díez-Minguito *et al.*, 2012) y por consiguiente, aumentando los TSS a lo largo del estuario (Capítulo 3) y en la plataforma continental (Capítulos 4 y 5). El análisis de nLw555 (estimador de TSS) mediante las EOF revela la estructura espacio-temporal de la pluma y sugiere su estrecha conexión con las condiciones océano-meteorológicas, donde el primer y principal modo de variación (~61% varianza) se asocia a la combinación lluvia-descarga ($r=0.47$ y $r=0.50$ respectivamente, $p<0.001$). Adicionalmente, ambos factores se encuentran estrechamente correlacionados con el índice NAO ($r=-0.52$, $p<0.001$), asociando parte de la variabilidad interanual a este índice climático.

La inspección del régimen intermedio que se llevó a cabo en el Capítulo 4 pone de manifiesto la estrecha interacción de los procesos mareales y fluviales, y como ambos fenómenos gobiernan los patrones de turbidez en relación a cual ejerce mayor dominio

sobre el otro, afectando a la plataforma continental como zona de transición entre las aguas del Guadalquivir y el mar abierto.

Los procesos fluviales gobiernan en el estuario durante épocas determinadas (particularmente en periodos de intensas lluvias y descargas), mientras que el resto del año, son los mecanismos mareales los que regulan el patrón de turbidez. Tal como se ha demostrado en el Capitulo 4 con las imágenes MERIS y datos in situ, la variabilidad de TSS en la plataforma y estuario externo se debe en parte al forzamiento mareal, tanto de la componente quincenal (mareas vivas y muertas) como de la componente semi-diurna (mareas bajas y altas), exhibiendo una variabilidad significativa. Durante mareas vivas se aprecia un notable aumento de TSS con respecto a las mareas bajas, cuyo debilitamiento de la señal de turbidez puede apreciarse entre un factor de ~2-3. Este resultado viene respaldado por el estudio desarrollado por Díez-Minguito *et al.* (2014) en el propio estuario, lo que permite deducir que los patrones estuario adentro son similares de igual medida en la plataforma continental adyacente. Adicionalmente, mientras que en el estuario la fase de inundación domina sobre el reflujo mareal, caracterizándose por mayores TSS (Díez-Minguito *et al.,* 2014), en la desembocadura y plataforma se observan mayores concentraciones tras finalizar el ciclo de vaciante. Gracias al procesamiento de las imágenes DEIMOS-1, se han determinado las zonas de máximo de turbidez típicas de estos enclaves (ETM), examinando para ello el tramo comprendido entre los primeros 50 km cercanos a la desembocadura (Capítulo 3). Se ha descrito la posición del ETM alrededor del km 30, el cual, dependiendo de la descarga de la presa de Alcalá del Río o del estado mareal, mostraba significativas fluctuaciones en la intensidad y localización. Estas conclusiones son confirmadas por trabajos de modelización que han sido desarrollados recientemente (Díez-Minguito *et al.,* 2014), en los cuales se detalla la existencia de otros dos máximos situados a 58 y 80 km aproximadamente desde la desembocadura. La precisa caracterización de los gradientes de TSS genera considerables avances para la monitorización de los parámetros de calidad de las aguas del estuario, ofreciendo nuevas posibilidades complementarias a las redes de medidas utilizadas hasta la fecha (Navarro *et al.,* 2011, 2012b).

La permanencia de la pluma de turbidez depende principalmente del nivel de cada uno de los flujos, el fluvial y mareal, pero en la desembocadura el viento juega un papel primordial en la modulación de la distribución de los sedimentos en cualquiera de los tres regímenes hidrodinámicos analizados. Conforme a la dirección e intensidad del

viento, los sedimentos son transportados para ser finalmente retenidos en la desembocadura o por contrario, exportados y dispersados en el golfo de Cádiz. El análisis de imagen mediante los datos de Rrs665 (proxy de TSS) abordado en el Capítulo 4 muestra la interferencia del viento (componentes zonales o meridionales) sobre los parámetros de forma de la pluma (área, excentricidad, eje mayor y menor), señalando la mejor correlación para la media de 24 horas previas al paso del satélite (con relación menor para 48 y 72 horas). Cada constituyente produce movimientos de las masas de agua en trayectorias diferentes: vientos predominantes de Levante ventilan el estuario y favorecen la progresión de la pluma hacia el Oeste, mientras que los de Poniente arrastran las aguas hacia la costa; entretanto la componente meridional Norte/Sur retira la pluma hacia el Sur/Norte con mejores correlaciones que las zonales ($r=0.49$ y $r=39$ respectivamente, $p<0.001$). Este flujo efectivo resultante de la acción del viento genera diversos escenarios que contribuyen al intercambio estuario-plataforma y a la posible renovación del agua en el sistema estuarino.

Desde esta perspectiva, hay que añadir que la acción irregular del oleaje y su rotura en la desembocadura e inmediaciones puede favorecer la resuspension de sedimentos. Respecto a ello, cabe mencionar que durante esta Tesis Doctoral se llevó a cabo un estudio del oleaje con el radar altimétrico ENVISAT-RA2, caracterizando la altura significante del oleaje mediante el uso de información con mayor resolución espacial y con un procesamiento enfocado hacia las zonas costeras. Los resultados de este trabajo fueron alentadores para futuros análisis de este agente involucrado en los fenómenos de turbidez y transporte de sedimentos (Caballero *et al.,* 2014a).

Las implicaciones ecológicas de los patrones físicos descritos hasta ahora se examinan con detalle en la zona de plataforma adyacente al estuario del Guadalquivir (Capítulo 4 y 5) y golfo de Cádiz (Capítulo 6). Los resultados obtenidos mediante la climatología y el análisis de las EOF (modo 1, 31% varianza) ponen de manifiesto la evidente relación entre la variabilidad estacional de Chl (concentraciones elevadas en invierno-primavera y bajas en verano) y la pluviosidad y entrada de agua dulce, sugiriendo que la fertilización de las aguas circundantes es sensible a los aportes de nutrientes a través del estuario (Prieto *et al.,* 2009), añadido al efecto de grado de mezcla y estratificación de la columna de agua (MLD). El vínculo existente dado entre los altos niveles de TSS y la extensión de la pluma con la disminución de Chl (EOF modo 2) indica que la reducción de disponibilidad y penetración de la luz (descenso de

$z_{1\%}$) ocasiona una severa limitación de la producción primaria y dinámica de fitoplancton en la zona de la desembocadura y plataforma continental. Estos resultados han sido confirmados en los Capítulos 4 y 5, donde se ha encontrado un desfase temporal de aproximadamente 1 mes entre el máximo de turbidez y el bloom de fitoplancton. Lejos del estuario, donde los niveles de turbidez son escasos o no llegan a afectar, no se distingue ese efecto de restricción lumínica y por lo tanto no inhibe la producción primaria, tal y como se muestra en el Capítulo 6. En este caso, los patrones estacionales e interanuales del bloom invernal (magnitud y frecuencia) en las aguas del golfo de Cádiz ponen de manifiesto que es la estructura vertical de la columna de agua y los procesos de mezcla los que controlan el bloom de fitoplancton en la zona offshore.

Por consiguiente, la variabilidad del ecosistema pelágico se encuentra controlada por el forzamiento de los diversos mecanismos en el golfo de Cádiz, y con especial énfasis en la zona de plataforma adyacente a la desembocadura, en un amplio rango de frecuencias que modulan el patrón general. Debido a la complejidad de la zona de estudio y a la dinámica variable de los patrones espacio-temporales, las costosas medidas in situ exhiben notables deficiencias tanto en la resolución espacial, en el caso por ejemplo de las medidas de turbidez correspondientes al Capítulo 4, puesto que no son capaces de ofrecernos la visión general de la pluma y su distribución espacial, como temporal, en el caso de las campañas de campo (Capítulos 3, 4 y 5), las cuales poseen una variabilidad temporal limitada. A este respecto, con la presente contribución y la implementación de las técnicas de teledetección desarrolladas en esta Tesis Doctoral se ofrece una innovadora y valiosa herramienta que podrá complementar una amplia variedad de programas regionales de vigilancia como parte de la óptima gestión integral de la zona estuarina y las aguas de transición.

Capítulo 8

Conclusiones

8.1 Conclusiones generales

A continuación, se resumen las principales conclusiones derivadas de los resultados de investigación que se han presentado a lo largo de la Tesis Doctoral.

- La metodología propuesta mediante el uso de las técnicas de teledetección es una excelente y valiosa herramienta que proporciona de manera sinóptica y económica una extensa cantidad de información con gran precisión relativa al comportamiento de la pluma de turbidez y blooms de fitoplancton en la zona exterior del estuario del Guadalquivir y plataforma continental del golfo de Cádiz.
- Las imágenes de alta resolución espacial del satélite DEIMOS-1, tras la corrección atmosférica, han revelado la capacidad de cuantificar TSS con gran exactitud mediante el algoritmo semi-analítico de la banda del NIR. Asimismo, se ha caracterizado la zona de máximo de turbidez (ETM) a 30 km de la desembocadura y los patrones de TSS en un transecto del estuario.
- Los resultados presentados mejoran el conocimiento actual acerca de las técnicas de teledetección y su aplicación a zonas costeras típicas de aguas de Caso II. Los algoritmos empíricos locales definidos para la estimación de TSS con los sensores de color oceánico MERIS y MODIS (Rrs665 y nLw555, respectivamente) constituyen los primeros trabajos de detalle que se han llevado a cabo en la región de estudio, y han sido capaces de determinar con exactitud el amplio abanico de concentraciones que aparece en las aguas superficiales. A pesar de la sobreestimación de Chl en aguas costeras, no presente en aguas oceánicas, se han obtenido valores precisos para el gran rango de Chl mediante los algoritmos estándares OC3M y OC4Me.
- Los datos ópticos provenientes de los diversos sensores satelitales han caracterizado los patrones de TSS y de la pluma de turbidez, los cuales se encuentran afectados por las intensas precipitaciones y descargas desde la presa de Alcalá del Río, generando una significativa variabilidad estacional e inter-anual asociada con el índice

climático NAO. Adicionalmente, el análisis EOF realizado con las imágenes del sensor MODIS ha contribuido a definir los principales modos de variación de TSS y Chl, y su relación con los principales mecanismos forzantes. Se ha identificado que el forzamiento mareal sobre TSS se establece a lo largo de todo el año, con alteraciones entre el ciclo quincenal de mareas vivas y muertas y el ciclo semi-diurno de mareas bajas y altas (mayores y menores TSS, respectivamente).

- La interacción con el régimen meteorológico de vientos indica que la dimensión, forma y transporte de la pluma aguas afuera de la desembocadura están sujetas a las condiciones de intensidad y dirección del viento de ambas componentes zonales y meridionales. El análisis de imagen mediante los datos del sensor MERIS revela que los Levantes renuevan el estuario y trasladan la pluma hacia el Oeste, mientras que los Ponientes arrastran las aguas hacia la costa con el estancamiento del estuario; entretanto la componente meridional Norte/Sur se encarga de desplazar la pluma a lo largo de la costa.

- El análisis de la naturaleza del ecosistema pelágico ha puesto de manifiesto la directa restricción de producción primaria y retraso del bloom invernal debido a los altos niveles de TSS (limitación de luz) en la desembocadura y aguas circundantes. Por el contrario, los patrones estacionales e inter-anuales de Chl en la plataforma y golfo de Cádiz, donde la pluma de turbidez no tiene impacto, se encuentran regulados por los mecanismos de estratificación y capa de mezcla típicos de esta región.

8.2 Futuras líneas de investigación

Los resultados obtenidos a lo largo de la presente Tesis Doctoral invitan al planteamiento de prometedoras futuras líneas de investigación como complemento y ampliación del trabajo realizado hasta la fecha. A continuación, se enumeran las principales líneas a desarrollar, algunas de ellas ya iniciadas:

- El uso de la teledetección para la estimación de otros parámetros relacionados con la calidad sigue siendo un área de investigación novedosa en esta región costera. Por ello, se hará uso de los datos hiper-espectrales ofrecidos por el nuevo satélite HICO (Hyperspectral Imager for the Coastal Ocean) para estimar los parámetros examinados hasta la actualidad (TSS y Chl) además de otros más específicos como el CDOM (colored dissolved organic matter) y PFT (phytoplankton functional types). Los 128 canales de este sensor (350-1080 nm) contribuirán de manera significante al desarrollo de nuevos algoritmos multi-banda específicos para esta región costera, haciendo hincapié en la diferenciación de la contribución de cada componente en la señal óptica de las aguas superficiales.
- Incorporar como fuente de información satelital la amplia serie de datos CDR (Surface Reflectance Climate Data Record) obtenida mediante los diversos sensores Landsat 4 a Landsat 7 que se extiende desde 1982 hasta la actualidad. Estas imágenes poseen una alta resolución espacial similar a la de DEIMOS-1 (30 m), lo que potenciaría el estudio de procesos de turbidez a pequeña escala en la zona estuarina. Cabe mencionar que las imágenes Landsat-8 (2013-actualidad) no se encuentran corregidas atmosféricamente, por lo que se llevaría a cabo este procedimiento haciendo uso del programa ACOLITE V.20140722.0, implementado en el MUMM y con el cual ya se han realizado diversas pruebas para precisar su idoneidad.
- Profundizar en el análisis detallado de los fenómenos que acontecen en la desembocadura, y como los diferentes procesos forzantes (meteorológicos y oceanográficos) afectan a la pluma de turbidez incluyendo la escala vertical de variación en la medida de lo posible. A partir del estudio de oleaje que se abordó mediante el altímetro ENVISAT RA-2 se abren nuevas líneas de trabajo, en las cuales se analizará

el papel que juega el oleaje en la resuspensión de sedimentos y modificación de la pluma en la desembocadura.

- Incorporación sistemática de observaciones in situ en campañas de oportunidad que surjan en la zona de estudio para medir tanto los parámetros de calidad del agua como las propiedades ópticas de las mismas. Estas últimas se llevarán a cabo mediante un espectroradiómetro, instrumento que proporcionará datos de radiancias y reflectancias para, mediante la aplicación de modelos de inversión, obtener las concentraciones de los diversos parámetros a estudiar.

Referencias bibliográficas

Alparslan, E., Aydöner, C., Tufekci, V., Tüfekci, H. (2007). Water quality assessment at Ömerli Dam using remote sensing techniques. Environmental Monitoring and Assessment, 135 (1-3), 391-398.

Álvarez, O., Tejedor, B., Vidal, J. (2001). La dinámica de marea en el estuario del Guadalquivir: un caso peculiar de 'resonancia antrópica'. Física de la Tierra, 13, 11-24.

Antoine, D., Morel, A., Gordon, H.R., Banzon, V.F., Evans, R.H. (2005). Bridging ocean color observations of the 1980s and 2000s in search of long-term trends. J. Geophys. Res. 110, C06009.

Aranuvachapun, S., LeBlond, P. H. (1981). Turbidity of coastal water determined from Landsat. Remote Sensing of Environment,11,113-132.

Azumaya, T., Isoda, Y., Noriki, S. Modeling of the spring bloom in Funka Bay, Japan. (2001). Cont. Shelf. Res. 21, 473–494.

Baban, S. M. J. (1993). Detecting water quality parameters in Norfolk Broads, UK., Using Landsat imagery. International Journal of Remote Sensing, 14, 1247-1267.

Baban, S. M. J. (1995). The use of Landsat imagery to map fluvial sediment discharge into coastal waters. Marine Geology, 123 (3-4), 263-270.

Baban, S. M. J. (1997). Environmental Monitoring of Estuaries; Estimating and Mapping Various Environmental Indicators in Breydon Water Estuary, U.K., Using Landsat TM Imagery. Estuarine, Coastal and Shelf Science, 44, 589-598.

Babin, M., Stramski, D., Ferrari, G. M., Claustre, H., Bricaud, A., Obolensky, G., et al. (2003). Variations in the light absorption coefficients of phytoplankton, nonalgal particles, and dissolved organic matter in coastal waters around Europe. Journal of Geophysical Research: Oceans (1978–2012), 108(C7).

Bailey, S., Wang, M. (2001). Satellite Aerosol Optical Thickness Match-up Procedures. NASA Technical Memorandum, 2001-209982 , 70-72. Greenbelt, MD: NASA Goddard Space Flight Center.

Baldacci, A., Corsini, G., Grasso, R., Manzella, G., Allen, J., Cipollini, P., et al. (2001). A study of the Alboran sea mesoscale system by means of empirical orthogonal function decomposition of satellite data. Journal of Marine Systems, 29 (1), 293-311.

Behrenfeld, M.J. (2010). Abandoning Sverdrup's Critical Depth Hypothesis on phytoplankton blooms. Ecology 91 (4), 997–1021.

Behrenfeld, M.J., Falkowski, P.G. (1997). Photosynthetic rates derived from satellite-based chlorophyll concentration. Limnol. Ocean. 42 (1), 1–20.

Behrenfeld, M.J., O'Malley, R.T., Siegel, D.A., McClain, C.R., Sarmiento, J.L., Feldman, G.C., Milligan, A.J., Falkowski, P.G., Letelier, R.M., Boss, E.S. (2006). Climate-driven trends in contemporary ocean productivity. Nature 444, 752–755.

Behringer, D., Xue, Y. (2004). Evaluation of the global ocean data assimilation system at NCEP: The Pacific Ocean. Eighth Symposium on Integrated Observing and Assimilation Systems for Atmosphere, Oceans, and Land Surface, AMS 84th Annual Meeting, Washington State Convention and Trade Center, Seattle, Washington, 11–15.

Bhat, A., Blomquist, W. (2004). Policy, politics, and water management in the Guadalquivir River Basin, Spain. Water Resources Research, 40 (8).

Björnsson, H., Venegas, S. A. (1997). A Manual for EOF and SVD Analyses of Climate Data. Department of Atmospheric and Oceanic Sciences and Centre for Climate and Global Change, McGill University, Technical report, No 97 (1).

Boss, E., Behrenfeld, M.J. (2010). In situ evaluation of the initiation of the North Atlantic phytoplankton bloom. Geophys. Res. Lett. 37, L18603, doi:10.1029/2010GL044174.

Bouman, H.A., Platt, T., Sathyendranath, S., Irwin, B.D., Wernand, M.R., Kraay, G.W. (2000). Bio-optical properties of the subtropical North Atlantic. II. Relevance to models of primary production. Mar. Ecol. Prog. Ser. 200, 19–34.

Boyce, D.G., Lewis, M.R., Worm, B. (2010). Global phytoplankton decline over the past century. Nature 466, 591–596.

Bricaud, A., & Morel, A. (1987). Atmospheric corrections and interpretation of marine radiances in CZCS imagery: use of a reflectance model. Oceanologica Acta, SP, 7, 33-50.

Brickley, P. J., Thomas, A. C. (2004). Satellite-measured seasonal and inter-annual chlorophyll variability in the NorthEast Pacific and Coastal Gulf of Alaska. Deep Sea Research Part II: Topical Studies in Oceanography, 51 (1), 229-245.

Brodie, J., Schroeder, T., Rohde, K., Faithful, J., Masters, B., Dekker, A., et al. (2010). Dispersal of suspended sediments and nutrients in the Great Barrier Reef lagoon during river-discharge events: conclusions from satellite remote sensing and concurrent flood-plume sampling. Marine and Freshwater Research, 61(6), 651-664.

Bustamante, J., Palacios, F., Díaz-Delgado R., Aragonés, D. (2009). Predictive models of turbidity and water depth in the Doñana marshes using Landsat TM and ETM+ images. Journal of Environmental Management, 90, 2219-2225.

Caballero, I., Ruiz, J., Navarro, G. (2011). Dynamics of the turbidity plume in the Guadalquivir estuary (SW Spain): A remote sensing approach, IEEE Oceans 2011, Santander, Spain.

Caballero, I., Morris, E. P., Navarro, G. (2012). DEIMOS-1 Satellite Provides Imagery for Coastal Management, Sea Technology,53 (2),10-13.

Caballero, I., Gomez-Enri, J., Cipollini, P., Navarro, G. (2014a). Validation of High Spatial Resolution Wave Data From Envisat RA-2 Altimeter in the Gulf of Cadiz. Geoscience and Remote Sensing Letters, IEEE, 11, 371-375.

Caballero, I., Morris, E. P., Ruiz, J., Navarro, G. (2014b). Assessment of suspended solids in the Guadalquivir estuary using new DEIMOS-1 medium spatial resolution imagery. Remote Sensing of Environment, 146, 148-158.

Caballero, I., Morris, E., Prieto, L., Navarro, G. (2014c). The influence of the Guadalquivir river on spatio-temporal variability of suspended solids and chlorophyll in the Eastern Gulf of Cadiz. Mediterranean Marine Science, 15 (4) (en prensa).

Calbet, A., Landry, M. R. (2004). Phytoplankton growth, microzooplankton grazing, and carbon cycling in marine systems. Limnology and Oceanography, 49 (1), 51-57.

Carpenter, D. J., Carpenter, S.M. (1983). Modeling inland water quality using Landsat data. Remote Sensing of Environment, 13(4), 345-352.

Chavez, P. S. Jr. (1988). An improved dark-object subtraction technique for atmospheric scattering correction of multispectral data. Remote Sensing of Environment, 24, 459-479.

Chavez, P. S. Jr. (1989). Radiometric calibration of Landsat Thematic Mapper multispectral images. Photogrammetric Engineering and Remote Sensing, 55, 1285-1294.

Chavez, P. S. Jr. (1996). Image-based atmospheric corrections -revisited and improved. Photogrammetric Engineering and Remote Sensing, 62, 1025-1036.

Chen, Z., Hanson, J. D., Curran, P. J. (1991). The form of the relationship between suspended sediment concentration and spectral reflectance: its implications for the use of Daedalus 1268 data. International Journal of Remote Sensing, 12 (1), 215-222.

Chen, X., Li, Y., Liu, Z., Yin, K., Li, Z., Wai, O., King. B (2004). Integration of multi-source data for water quality classification in the Pearl River estuary and its adjacent coastal waters of Hong Kong. Continental Shelf Research, 24, 1827-1843.

Chen, T., Hu, C., & Muller-Karger, F. (2007). Monitoring turbidity in Tampa Bay using MODIS/Aqua 250-m imagery. Remote Sensing of Environment, 109, 207-220.

Chen, Z., Hu, C., Muller-Karger, F. E., Luther, M. E. (2010). Short-term variability of suspended sediment and phytoplankton in Tampa Bay, Florida: observations from a coastal oceanographic tower and ocean color satellites. Estuarine, Coastal and Shelf Science, 89(1), 62-72.

Cloern, J. E. (1987). Turbidity as a control on phytoplankton biomass and productivity in estuaries. Continental Shelf Research, 7 (11), 1367-1381.

Cloern, J. E. (1991). Annual variations in river flow and primary production in the South San Francisco Bay Estuary (USA) James E. Cloern US Geological Survey, MS-496, 345 Middlefield Road, Menlo Park, CA 94025, USA. Estuaries and coasts: Spatial and temporal intercomparisons, 19, 91.

Cloern, J. E. (1996). Phytoplankton bloom dynamics in coastal ecosystems: a review with some general lessons from sustained investigation of San Francisco Bay, California. Reviews of Geophysics, 34(2), 127-168.

Contreras, E., Polo, M. (2010). Propuesta metodológica para diagnosticar y pronosticar las consecuencias de las actuaciones humanas en el estuario del Guadalquivir. technical report, Group of Fluvial Dyn. and Hydrol., University of Córdoba, Córdoba, Spain.

Contreras, E. (2012). Influencia de los aportes fluviales en la calidad del agua del estuario del Guadalquivir. Tesis Doctoral. Universidad de Córdoba.

Contreras, E., Polo, M. J. (2012). Measurement frequency and sampling spatial domains required to characterize turbidity and salinity events in the Guadalquivir estuary (Spain). Natural Hazards and Earth System Science, 12(8), 2581-2589.

Contreras, E. (2013). Influencia de los aportes fluviales en la calidad del agua del estuario del Guadalquivir.

Costa, S., Gutiérrez Mas, J., Morales, J. (2009). Establecimiento del régimen de flujo en el estuario del Guadalquivir, mediante el análisis de formas de fondo con sonda multihaz. Revista de la Sociedad Geológica de España, 22(1-2), 23-42.

Criado Aldeanueva, F., García Lafuente, J., Vargas, J.M., Del Rio, J., Vázquez, A., Reul, A., Sánchez, A. (2006). Distribution and circulation of the water masses in the Gulf of Cadiz from in situ observations. Deep Sea Research II, 53 (11-13), 1144-1159.

Crowley, G. (2010). DMC Data Product Manual. 0115056, 02, DMC International Imaging Ltd., UK.

Cui, T., Zhang, J., Groom, S., Sun, L., Smyth, T., Sathyendranath, S. (2010). Validation of MERIS ocean-color products in the Bohai Sea: A case study for turbid coastal waters. Remote Sensing of Environment, 114(10), 2326-2336.

Darecki, M., Stramski, D. (2004). An evaluation of MODIS and SeaWiFS bio-optical algorithms in the Baltic Sea. Remote Sensing of Environment, 89 (3), 326-350.

Díez-Minguito, M., Baquerizo, A., Ortega-Sánchez, M., Navarro, G., Losada, M. (2012). Tide transformation in the Guadalquivir estuary (SW Spain) and process-based zonation. Journal of Geophysical Research: Oceans (1978–2012), 117(C3).

Díez-Minguito, M., Contreras, E., Polo, M. J., Losada, M. A. (2013). Spatio-temporal distribution, along-channel transport, and post-riverflood recovery of salinity in the Guadalquivir estuary (SW Spain). Journal of Geophysical Research: Oceans, 118(5), 2267-2278.

Díez-Minguito, M., Baquerizo, A., de Swart, H.E., Losada, M. A. (2014). Structure of the turbidity field in the Guadalquivir estuary: Analysis of observations and a box model approach (en prensa).

Doxaran, D., Froidefond, J. M., Lavenderb, S., Castainga, P. (2002). Spectral signature of highly turbid waters. Application with SPOT data to quantify suspended particulate matter concentrations. Remote Sensing of Environment, 81, 149-161.

Doxaran, D., Cherukuru, N., & Lavender, S. J. (2006). Apparent and inherent optical properties of turbid estuarine waters: measurements, empirical quantification relationships, and modeling. Applied Optics, 45 (10), 2310-2324.

D'Sa, E. J., Hu, C., Muller-Karger, F. E., Carder, K. L. (2002). Estimation of colored dissolved organic matter and salinity fields in case 2 waters using SeaWiFS: Examples from Florida Bay and Florida Shelf. Proceedings of the Indian Academy of Science, 111 (3), 197-207.

Dyer, K. R. (1997). Estuaries: a physical introduction.

Dzwonkowski, B., Yan, X.-H. (2005). Tracking of a Chesapeake Bay estuarine outflow plume with satellite-based ocean color data. Continental Shelf Research, 25(16), 1942-1958.

Eppley, R.W., Peterson, B.J. (1979). Particulate organic matter flux and planktonic new production in the deep ocean. Nature 282, 677–680.

Fauchot, J., Saucier, F. J., Levasseur, M., Roy, S., Zakardjian, B. (2008). Wind-driven river plume dynamics and toxic< i> Alexandrium tamarense</i> blooms in the St. Lawrence estuary (Canada): A modeling study. Harmful algae, 7(2), 214-227.

Fettweis, M., Sas, M., Monbaliu, J. (1998). Seasonal, neap-spring and tidal variation of cohesive sediment concentration in the Scheldt Estuary, Belgium. Estuarine, Coastal and Shelf Science, 47(1), 21-36.

Field, C.B., Behrenfeld, M.J., Randerson, J.T., Falkowski, P. (1998). Primary Production of the Biosphere: Integrating Terrestrial and Oceanic Components. Science 281, 237–240.

Fiúza, A.F.G.. (1983). Upwelling patterns off Portugal. p. 85-98. In: Coastal Upwelling Its Sediment Record. Suess, E., Thiede, J., Springer US, New York.

Forget, P., Ouillon, S. (1998). Surface suspended matter off the Rhone river mouth from visible satellite imagery. Oceanologica Acta, 21 (6), 739-749.

Fraser, R. S., Ferraze, R. A., Kaufman, Y. J., Markham, B. L., Mattoo, S. (1992). Algorithm for atmospheric correction of aircraft and satellite imagery. International Journal of Remote Sensing, 13, 541-557.

García, C.M., Prieto, L., Vargas, M., Echevarría, .F., García Lafuente, J., Ruiz, J., Rubín, J.P. (2002). Hydrodynamics and spatial distribution of plankton and TEP in the Gulf of Cadiz (SW Iberian Peninsula). Journal of Plankton Research, 24 (8), 817-833.

García-Gorriz, E., Carr, M.E. (1999). The climatological annual cycle of satellite derived phytoplankton pigments in the Alboran Sea. Geophys. Res. Lett. 26 (19), 2985–2988.

García-Lafuente, J., Delgado, J., Criado-Aldeanueva, F., Bruno, M., del Rio, J., Miguel Vargas, J. (2006). Water mass circulation on the continental shelf of the Gulf of Cadiz. Deep Sea Research Part II: Topical Studies in Oceanography, 53 (11-13), 1182-1197.

García-Lafuente, J., Delgado, J., Criado-Aldeanueva, F., Bruno, M., del Río, J., Miguel Vargas, J. (2006). Water mass circulation on the continental shelf of the Gulf of Cádiz. Deep Sea Research Part II: Topical Studies in Oceanography, 53(11), 1182-1197.

González-Mazo, E., Forja, J. M., Gómez-Parra, A. (1998). Fate and distribution of linear alkylbenzene sulfonates in the littoral environment. Environmental science & technology, 32 (11), 1636-1641.

Gordon, H. R., Morel, A. Y. (1983). Remote Assessment of Ocean Color for Interpretation of Satellite Visible Imagery. New York: Springer-Verlag.

Goslee, S. C. (2011). Analyzing Remote Sensing Data in R: The landsat Package. Journal of Statistical Software, 43(4), 1-25.

Granado-Lorencio, C. (1991). The effect of man on the fish fauna of the River Guadalquivir, Spain. Fisheries research, 12 (2), 91-100.

Gregg, W.W., Conkright, M.E. (2002). Decadal changes in global ocean chlorophyll. 29, 15, doi:10.1029/2002GL014689.

Gregg, W.W., Conkright, M.E., Ginoux, P., O'Reilly, J.E., Casey, N.W. (2003). Ocean primary production and climate: global decadal changes. Geophys. Res. Lett. 30, 1809, doi:10.1029/2003GL016889.

Hall, F. G., Strebel, D. E., Nickson, J. E., Geotz, S. J. (1991). Radiometric rectification toward a common radiometric response among multidate, multisensor images. Remote Sensing of Environment, 35, 11-27.

Hellweger, F. L., Schlosser, P., Lall, U., Weissel, J. K. (2004). Use of satellite imagery for water quality studies in New York Harbor. Estuarine, Coastal and Shelf Science, 61 (3), 437-448.

Henson, S.A., Robinson, I., Allen, J.T., Waniek, J.J. (2006). Effect of meteorological conditions on interannual variability in timing and magnitude of the spring bloom in the Irminger Basin, North Atlantic. Deep Sea Res. II. 53 (10), 1601–1615.

Henson, S.A., Thomas, A.C. (2007). Interannual variability in timing of bloom initiation in the California Current System. J. Geophys. Res. 112, C08007, doi:10.1029/2006JC003960.

Hijmans, R. J., Etten, J. (2011). raster: Geographic analysis and modeling with raster data. R package version 2.0-12. http://CRAN.R-project.org/package=raster

Hu, C., Carder, K. L., Muller-Karger, F. E. (2000). Atmospheric Correction of SeaWiFS Imagery over Turbid Coastal Waters: A Practical Method. Remote Sensing of Environment, 74, 195-206.

Hu, C., Chen, Z., Clayton, T., Swarzenski, P., Brock, J., Muller-Karger, F. (2004). Assessment of estuarine water-quality indicators using MODIS medium-resolution bands: Initial results from Tampa Bay, FL. Remote Sensing of Environment, 93, 423-441.

Hurrell, J. W. (1995). Decadal trends in the North Atlantic oscillation. Science, 269, 676-679.

Irigoien, X., Castel, J. (1997). Light limitation and distribution of chlorophyll pigments in

a highly turbid estuary: the Gironde (SW France). Estuarine, Coastal and Shelf Science, 44 (4), 507-517.

Jamet, C., Loisel, H., Kuchinke, C. P., Ruddick, K., Zibordi, G., Feng, H. (2011). Comparison of three SeaWiFS atmospheric correction algorithms for turbid waters using AERONET-OC measurements. Remote Sensing of Environment, 115 (8), 1955-1965.

Jerlov, N. G. (1968). Optical oceanography. Elsevier, New York.

Jerlov, N. G. (1976). Marine Optics. Elsevier, New York.

Jo, C.O., Lee, J.Y., Park, K.A., Kim, Y.H., Kim, K.R. (2007). Asian dust initiated early spring bloom in the northern East/Japan Sea. Geophys. Res. Lett. 34, L05602, doi:10.1029/2006GL027395.

Kara, A. B., Rochford, P. A., Hurlburt, H. E. (2000). An optimal definition for ocean mixed layer depth. Journal of Geophysical Research: Oceans, 105(C7), 16803-16821.

Kidd, P., Dominguez-Rodriguez, M., Diez, J., Monterroso, C. (2007). Bioavailability and plant accumulation of heavy metals and phosphorus in agricultural soils amended by long-term application of sewage sludge. Chemosphere, 66 (8), 1458-1467.

Kirk, J.T.O. (1983). Light and Photosynthesis in Aquatic Ecosystems. Cambridge University Press: Cambridge, MA, USA.

Koeve, W. (2001). Wintertime nutrients in the North Atlantic-new approaches and implications for new production estimates. Mar. Chem. 74, 245–260.

Lahet, F., Forget, P., Ouillon, S. (2001). Application of a colour classification method to quantify the constituents of coastal waters from in situ reflectances sampled at satellite sensor wavebands. International Journal of Remote Sensing, 22 (5), 909-914.

Largier, J. L., Lawrence, C., Roughan, M., Kaplan, D., Dever, E., Dorman, C., et al. (2006). WEST: A northern California study of the role of wind-driven transport in the productivity of coastal plankton communities. Deep Sea Research Part II: Topical Studies in Oceanography, 53(25), 2833-2849.

Lavery, P., Pattiaratchi, C., Wyllie, A., & Hick, P. (1993). Water quality monitoring in estuarine waters using the Landsat Thematic Mapper. Remote Sensing of Environment, 3, 268-280.

Le, C., Hu, C., English, D., Cannizzaro, J., Kovach, C. (2013). Climate-driven chlorophyll-a changes in a turbid estuary: Observations from satellites and implications for management. Remote Sensing of Environment, 130, 11-24.

Li, Y., Li, J. (2000). A suspended sediment satellite sensing algorithm based on gradient transiting from water-leaving to satellite-detected reflectance spectrum. Chinese Science Bulletin, 45 (10), 925-931.

Li, M. Z., Amos, C. L. (2001). SEDTRANS96: the upgraded and better calibrated sediment-transport model for continental shelves. Computers & Geosciences, 27(6), 619-645.

Li, Y., Smayda, T. (2001). A chlorophyll time series for Narragansett Bay: assessment of the potential effect of tidal phase on measurement. Estuaries, 24(3), 328-336.

Lobo, F., Sánchez, R., González, R., Dias, J., Hernández-Molina, F. J., Fernández-Salas, L., et al. (2004). Contrasting styles of the Holocene highstand sedimentation and sediment dispersal systems in the Northern shelf of the Gulf of Cadiz. Continental Shelf Research, 24 (4), 461-482.

Loisel, H., Bosc, E., Stramski, D., Oubelkheir, K., Deschamps, P. Y. (2001). Seasonal variability of the backscattering coefficient in the Mediterranean Sea based on satellite SeaWiFS imagery. Geophysical Research Letters, 28 (22), 4203-4206.

Longhurst, A.R., Sathyendranath, S., Platt, T., Caverhill, C. (1995). An estimate of global primary production in the ocean from satellite radiometer data. J. Plankton Res. 17, 1245–1271.

Lorenz, E.N. (1956). Empirical orthogonal functions and statistical weather prediction. Sci. Rep. Statist. Forecasting Proj., Department Meteor., MIT, No 1, 49 pp.

Lu, D., Mausel, P., Brondizio, E., Moran, E. (2002). Assessment of atmospheric correction methods for Landsat TM data applicable to Amazon basin LBA research. International Journal of Remote Sensing, 23 (13), 2651.2671.

Maritorena, S., Siegel, D. (2005). Consistent merging of satellite ocean color data sets using a bio-optical model. Remote Sens. Environ. 94, 429–440.

Maritorena, S., d'Andon, O.H.F., Mangin, A., Siegel, D.A. (2010). Merged Satellite Ocean Color Data products using a bio-optical model: characteristics, benefits and issues. Remote Sens. Environ. 114, 1791– 1804.

Martin, J. M., Windom, H. L. (1991). Present and future roles of ocean margins in regulating marine biogeochemical cycles of trace elements. R.F.C. Mantoura (Ed.), Ocean margin processes in global change, Wiley, New York , 45-67.

Martinez, E., Antoine, D., Fabrizio, D'Ortenzio., Gentili, B. (2009). Climate driven basin-scale decadal oscillations of oceanic phytoplankton. Science 326 (5957), 1253–1256.

May, C. L., Koseff, J. R., Lucas, L. V., Cloern, J. E., Schoellhamer, D. H. (2003). Effects of spatial and temporal variability of turbidity on phytoplankton blooms. Marine Ecology. Progress Series, 254, 111-128.

Mayer, L. M., Keil, R. G., Macko, S. A., Joye, S. B., Ruttenberg, K. C., Aller, R. C. (1998). The importance of suspended particulates in riverine delivery of bioavailable nitrogen to coastal zones. Global Biogeochemical Cycles, 12, 573-579.

McFeeters, S. K. (1996). The use of the Normalized Difference Water Index (NDWI) in the delineation of open water features. International Journal of Remote Sensing, 17 (7), 1425-1432.

Mendiguchía, C., Moreno, C., García-Vargas, M. (2007). Evaluation of natural and anthropogenic influences on the Guadalquivir River (Spain) by dissolved heavy metals and nutrients. Chemosphere, 69 (10), 1509-1517.

Mertes, L. A. K., Smith, M. O., Adams, J. B. (1993). Estimating suspended sediment concentrations in surface waters of the Amazon River wetlands from Landsat Images. Remote Sensing of Environment, 43, 281-301.

Miller, R. L., McKee, B. A. (2004). Using MODIS Terra 250 m imagery to map concentrations of total suspended matter in coastal waters. Remote Sensing of Environment, 93, 259-266.

Miller, R. L., Del Castillo, C. E., McKee, B. A. (2005). Remote sensing of coastal aquatic environments: Technologies, techniques and applications. Springer, Vol. 7.

Milton, E. J. (1994). Teaching atmospheric correction using a spreadsheet. Photogrammetric Engineering and Remote Sensing, 60, 751-754.

Mobley, C. D. (2004). Light and water-Radiative transfer in natural waters. CD Edition

Moran, M. S., Jackson, D., Slate, P. N., Teillet, P. M. (1992). Evaluation of simplified procedures for retrieval of land surface reflectance factors from satellite sensor output. Remote Sensing of Environment, 41, 169-184.

Morel, A., Prieur, L. (1977). Analysis of variation in ocean color. Limnology and Oceanography, 22, 709-722.

Morel, A., Gentili, B., Chami, M., Ras, J. (2006). Bio-optical properties of high chlorophyll Case 1 waters and of yellow-substance-dominated Case 2 waters. Deep Sea Research Part I: Oceanographic Research Papers, 53(9), 1439-1459.

Morel, A., Huot, Y., Gentili, B., Werdell, P. J., Hooker, S. B., Franz, B. A. (2007). Examining the consistency of products derived from various ocean color sensors in open ocean (Case 1) waters in the perspective of a multi-sensor approach. Remote Sensing of Environment, 111 (1), 69-88.

Morris, A. W., Allen, J. I., Howland, R. J. M., Wood, R. G. (1995). The estuary plume zone: Source or sink for land-derived nutrient discharges?. Estuarine, Coastal and Shelf Science, 40 (4), 387-402.

Navarro, G. (2004). Escalas de variabilidad espacio-temporal de procesos pelágicos en el golfo de Cadiz. MSc Thesis. University of Cadiz, Spain, 224 pp.

Navarro, G., Ruiz, J. (2006). Spatial and temporal variability of phytoplankton in the Gulf of Cádiz through remote sensing images. Deep Sea Research Part II: Topical Studies in Oceanography, 53(11), 1241-1260.

Navarro, G., Gutiérrez, F. J., Díez-Minguito, M., Losada, M. A., Ruiz, J. (2011). Temporal and spatial variability in the Guadalquivir estuary: a challenge for a real-time telemetry. Ocean Dynamics, 61 (6), 753-765.

Navarro, G., Caballero, I., Prieto, L., Vázquez, A., Flecha, S., Huertas, I. E., Ruiz, J. (2012a). Seasonal-to-interannual variability of chlorophyll-< i> a</i> bloom timing associated with physical forcing in the Gulf of Cadiz. Advances in Space Research, 50 (8), 1164-1172.

Navarro, G., Huertas, I. E., Costas, E., Flecha, S., Díez-Minguito, M., Caballero, I., López-Rodas, V., Prieto, L., Ruiz, J. (2012b). Use of a real-time remote monitoring network (RTRM) to characterize the Guadalquivir estuary (Spain). Sensors, 12 (2), 1398-1421.

Nechad, B., Ruddick, K., Park, Y. (2010). Calibration and validation of a generic multisensor algorithm for mapping of total suspended matter in turbid waters. Remote Sensing of Environment, 114(4), 854-866.

Neckel, H. (1984). The solar radiation between 3300 and 12500 Å. Solar Physics, 90 (2), 205-258.

Nezlin, N.P., Li, B.L. (2003). Time-series analysis of remote-sensed chlorophyll and environmental factors in the Santo Monica-San Pedro Basin off Southern California. J. Marine Syst. 39, 185–202.

Nezlin, N. P., DiGiacomo, P. M. (2005). Satellite ocean color observations of stormwater runoff plumes along the San Pedro Shelf (southern California) during 1997–2003. Continental Shelf Research, 25(14), 1692-1711.

Nezlin, N. P., DiGiacomo, P. M., Stein, E. D., Ackerman, D. (2005). Stormwater runoff plumes observed by SeaWiFS radiometer in the Southern California Bight. Remote Sensing of Environment, 98(4), 494-510.

North, G. R., Bell, T. L., Cahalan, R. F., Moeng, F. J. (1982). Sampling errors in the estimation of empirical orthogonal functions. Monthly Weather Review, 110 (7), 699-706.

O'Reilly, J. E., Maritorena, S., Siegel, D. A., O'Brien, M. C., Toole, D., Mitchell, B. G., et al. (2000). Ocean color chlorophyll a algorithms for SeaWiFS, OC2, and OC4: Version 4. SeaWiFS postlaunch calibration and validation analyses, 3, 9-23.

Ondrusek, M., Stengel, E., Kinkade, C. S., Vogel, R. L., Keegstra, P., Hunter, C., Kim, C. (2012). The development of a new optical total suspended matter algorithm for the Chesapeake Bay. Remote Sensing of Environment, 119, 243-254.

Otero, M. P., Siegel, D. (2004). Spatial and temporal characteristics of sediment plumes and phytoplankton blooms in the Santa Barbara Channel. Deep Sea Research Part II: Topical Studies in Oceanography, 51(10), 1129-1149.

Otero, P., Ruiz-Villarreal, M., Peliz, A. (2008). Variability of river plumes off Northwest Iberia in response to wind events. Journal of Marine Systems, 72(1), 238-255.

Patsch, J., Kuehn, W., Radach, G., Santana Casiano, J.M., Gonzalez Davila, M., Neuer, S., Freudenthal, T., Llinas, O. (2002). Interannual variability of carbon fluxes at the North Atlantic Station ESTOC. Deep Sea Res. II. 49, 253–288.

Parsons, T. R., Maita, Y., Lalli, C.M. (1984). A manual of chemical and biological

methods for seawater analysis. Pergamon Press, Oxford.

Pawlowicz, R., Beardsley, B., Lentz, S. (2002). Classical tidal harmonic analysis including error estimates in MATLAB using T_TIDE. Computers & Geosciences, 28(8), 929-937.

Peliz, A.J., Fiúza, A.F.G. (1999). Temporal and spatial variability of CZCS derived phytoplankton pigment concentrations off the western Iberian Peninsula. Int. J. Remote Sens. 20 (7), 1363–1403.

Pennock, J. R. (1985). Chlorophyll distributions in the Delaware estuary: Regulation by light-limitation. Estuarine, Coastal and Shelf Science, 21 (5), 711-725.

Pierson, D. C., Kratzer, S., Strömbeck, N., Håkansson, B. (2008). Relationship between the attenuation of downwelling irradiance at 490 nm with the attenuation of PAR (400 nm–700 nm) in the Baltic Sea. Remote Sensing of Environment, 112 (3), 668-680.

Piñones, A., Valle-Levinson, A., Narváez, D., Vargas, C., Navarrete, S., Yuras, G., et al. (2005). Wind-induced diurnal variability in river plume motion. Estuarine, Coastal and Shelf Science, 65(3), 513-525.

Platt, T., Sathyendranath, S., Caverhill, C.M., Lewis, M.R. (1998). Ocean primary production and available light: further algorithms for remote sensing. Deep Sea Res. I. 35 (6), 855–879.

Platt, T., Fuentes-Yaco, C., Frank, K.T. (2003). Spring algal bloom and larval fish survival. Nature 423, 398–399.

Platt, T., Sathyendranath, S., Fuentes-Yaco, C. (2007). Biological oceanography and fisheries management: perspective after 10 years. ICES J. Mar. Sci. 64 (5), 863–869.

Platt, T., White, G.N., Zhai, L., Sathyendranath, S., Roy, S. (2009). The phenology of phytoplankton blooms: Ecosystem indicators from remote sensing. Ecol. Model. 2220, 3057–3069.

Prandle, D. (2009). Estuaries: Dynamics, Mixing, Sedimentation and Morphology. University of Liverpool, Cambridge University Press.

Prieto, L., Navarro, G., Rodríguez-Gálvez, S., Huertas, I. E., Naranjo J. M., Ruiz, J. (2009). Oceanographic and meteorological forcing of the pelagic ecosystem on the Gulf of Cádiz shelf (SW Iberian Peninsula). Continental Shelf Research, 29, 2122-2137.

Rey, F., Skjoldal, H.R., Slagstad, D. (1987). Primary production in relation to climate changes in the Barents Sea. In: Loeng Bergen, H. (Ed.), The Effect of Oceanographic Conditions on Distribution and Population Dynamics of Commercial Fish Stocks in the Barents Sea. Institute of Marine Research. 29-46

Reynolds, C.S. (1998). What factors influence the species composition of phytoplankton in lakes of different trophic state. Hydrobiologia, 369/370, 11-26.

Ribas-Ribas, M., Gómez-Parra, A., Forja, J. M. (2011). Spatio-temporal variability of the

dissolved organic carbon and nitrogen in a coastal area affected by river input: The North Eastern shelf of the Gulf of Cadiz (SW Iberian Peninsula). Marine Chemistry, 126 (1), 295-308.

Richardson, A.J., Silulwane, N.F., Mitchell-Innes, B.A., Shillington, F.A. (2003). A dynamic quantitative approach for predicting the shape of phytoplankton profiles in the ocean. Prog. Oceanogr. 59, 301–319.

Ritchie, J. C., Schiebe, F. R., McHenry, J. R. (1976). Remote sensing of suspended sediment in surface water. Photogrammetric Engineering & Remote Sensing, 42, 1539-1545.

Ritchie, J. C., Cooper, C. M., Yongqing, J. (1987). Using Landsat multispectral scanner data to estimate suspended sediments in Moon Lake, Mississippi. Remote Sensing of Environment, 23 (1), 65-81.

Ritchie, J. C., Cooper, C. M. (1988). Comparison of measured suspended sediment concentrations with suspended sediment concentrations estimated from Landsat MSS data. International Journal of Remote Sensing, 9, 379-387.

Ritchie, J. C., Schiehe, F. R., Cooper, C. M. (1989). Landsat digital data for estimating suspended sediment in inland water. International Association of Hydrological Sciences, 182, 151-158.

Ritchie, J. C., Cooper, C. M., Schiebe, F. R. (1990). The relationship of MSS and TM digital data with suspended sediments, chlorophyll, and temperature in Moon lake, Mississippi. Remote Sensing of Environment, 33, 137-148.

Ritchie, J. C., Zimba, P. V., Everitt, J. A. (2003). Remote Sensing techniques to assess water quality. Photogrammetric Engineering & Remote Sensing, 69, 69-704.

Rochford, P.A., Kara, A.B., Wallcraft, A.J., Arnone, R.A. (2001). Importance of solar subsurface heating in ocean general circulation models. J. Geophys. Res. 106 (C11), 30923–30938.

Roegner, G. C., Hickey, B. M., Newton, J. A., Shanks, A. L., Armstrong, D. A. (2002). Wind-induced plume and bloom intrusions into Willapa Bay, Washington. Limnology and Oceanography, 47(4), 1033-1042.

Ruddick, K. G., Ovidio, F., Rijkeboer, M. (2000). Atmospheric correction of SeaWiFS imagery for turbid coastal and inland waters. Applied optics, 39(6), 897-912.

Ruhl, C. A., Schoellhamer, D. H., Stumpf, R. P., Lindsay, C. L. (2001). Combined Use of Remote Sensing and Continuous Monitoring to Analyse the Variability of Suspended-Sediment Concentrations in San Francisco Bay, California. Estuarine, Coastal and Shelf Science, 53(6), 801-812.

Ruiz, J., Garcia-Isarch, E., Huertas, E., Prieto, L., Juárez, A., Muñoz, J. L., Sánchez-Lamadrid, A., Rodríguez-Gálvez, S., Naranjo, J. M., Baldó, F. (2006). Meteorological and oceanographic factors influencing< i> Engraulis encrasicolus</i> early life stages and catches in the Gulf of Cadiz. Deep Sea Research Part II: Topical Studies in Oceanography, 53 (11), 1363-1376.

Ruiz, J., González-Quirós, R., Prieto, L., Navarro, G. (2009). A Bayesian model for anchovy: The combined pressure of man and environment. Fisheries Oceanography, 18 (1), 62-76.

Ruiz, J., Macías, D., Losada, M., Díez-Minguito, M., Prieto, L. (2013). A simple biogeochemical model for estuaries with high sediment loads: Application to the Guadalquivir River (SW Iberia). Ecological Modelling, 265, 194-206.

Ruiz, J., Polo, M.J., Díez-Minguito, M., Navarro, G., Morris, E.P., Huertas, E., Caballero, I., Contreras, E., Losada, M.A. (2014). The Guadalquivir Estuary: A Hot Spot for Environmental and Human Conflicts. Environmental Management and Governance: Advances in Coastal and Marine Resources, Springer International Publishing Switzerland, 8, 199-232.

Sá, C., Da Silva, J., Oliveira, P. B., Brotas, V. (2008). Comparison of MERIS (Algal_1 and Algal_2) and MODIS (OC3M) chlorophyll products and validation with HPLC in situ data collected off the Western Iberian Peninsula. Proceedings of the 2nd MERIS/(A) ATSR User Workshop, Frascati, Italy, 22-26.

Saldías, G. S., Sobarzo, M., Largier, J., Moffat, C., Letelier, R. (2012). Seasonal variability of turbid river plumes off central Chile based on high-resolution MODIS imagery. Remote Sensing of Environment, 123, 220-233.

Sánchez-Lamadrid, A., Ruiz, J., García, E., Juárez, A., Jiménez, T., Sobrino, I., Blanco, E., Jiménez, P., Bruno, M., Navarro, G. (2003). Estudio de los recursos pesqueros del Golfo de Cadiz. Consejería de Agricultura y Pesca, Junta de Andalucia.

Sarmiento, J.L., Hughes, T.M.C., Stouffer, R.J., Manabe, S. (1998). Simulated response of the ocean carbon cycle to anthropogenic climate warming. Nature 393, 245–249.

Sathyendranath, S. (2000). Remote Sensing of Ocean Colour in Coastal, and Other Optically-Complex, Waters. Reports of the International Ocean-Colour Coordinating Group, No 3, 140 pp.

Schiebe, F. R., Harrington, Jr., J. A., Ritchie, J. C. (1992). Remote sensing of suspended sediments: the Lake Chicot, Arkansas project. International Journal of Remote Sensing, 13 (8), 1487-1509.

Schoellhamer, D. H. (1995). Sediment resuspension mechanisms in old Tampa Bay, Florida. Estuarine, Coastal and Shelf Science, 40(6), 603-620.

Schoellhamer, D. H. (1996). Factors affecting suspended- solids concentrations in South San Francisco Bay, California. Journal of Geophysical Research: Oceans (1978–2012), 101(C5), 12087-12095.

Schott, J. R., Salvaggio, C., & Volchok, W. J. (1988). Radiometric scene normalization using pseudoinvariant features. Remote Sensing of Environment, 26, 1-26.

Schroeder, T., Devlin, M. J., Brando, V. E., Dekker, A. G., Brodie, J. E., Clementson, L. A., et al. (2012). Inter-annual variability of wet season freshwater plume extent into the Great Barrier Reef lagoon based on satellite coastal ocean colour observations. Marine pollution

bulletin, 65 (4), 210-223.

Sharples, J., Tweddle, J. F., Mattias Green, J., Palmer, M. R., Kim, Y.-N., Hickman, A. E., et al. (2007). Spring-neap modulation of internal tide mixing and vertical nitrate fluxes at a shelf edge in summer. Limnology and Oceanography, 52(5), 1735-1747.

Siegel, D.A., Doney, S.C., Yoder, J.A. (2002). The North Atlantic Spring Phytoplankton Bloom and Sverdrup's Critical Depth Hypothesis. Science 296, 730–733.

Song, C., Woodcock, C. E., Seto, K. C., Lenney, M. P., Macomber, S. A. (2001). Classification and Change Detection Using Landsat TM Data: When and How to Correct Atmospheric Effects?. Remote Sensing of Environment, 75, 230-244.

Sousa, F., Bricaud, (1992). A. Satellite-derived phytoplankton pigments structures in the Portuguese upwelling area. J. Geophys. Res. 97 (C7), 11343–11356.

Stevenson, R.E. (1977). Huelva Front and Malaga, Spain, Eddy Chain as defined by Satellite and Oceanographic Data. Deutsche Hydrographische Zeitschrift, 30 (2), 51-53.

Stumpf, R. P. Pennock, J. R. (1989). Calibration of a general optical equation for remote sensing of suspended sediments in a moderately turbid estuary. Journal of Geophysical Research, 94(C10), 14, 363-371.

Stumpf, R. P., Gelfenbaum, G., Pennock, J. R. (1993). Wind and tidal forcing of a buoyant plume, Mobile Bay, Alabama. Continental Shelf Research, 13(11), 1281-1301.

Sverdrup, H.U. (1953). On conditions for the vernal blooming of phytoplankton. Journal du Conseil Permanent International Pour L'Exploration de la Mer. 18, 287–295.

Tassan, S., Sturm, B. (1986). All algorithm for the retrieval of sediment content in turbid coastal waters from CZCS data. International Journal of Remote Sensing, 7, 643-655.

Tassan, S. (1994). Local algorithms using SeaWiFS data for the retrieval of phytoplankton, pigments, suspended sediment, and yellow substance in coastal waters. Applied Optics, 33(12), 2369-2378.

Teodoro, A. C., Veloso-Gomes, F., Gonsalves, H. (2008). Statistical Techniques for Correlating Total Suspended Matter Concentration with Seawater Reflectance Using Multispectral Satellite Data. Journal of Coastal Research, 24, 40-49.

Thomas, A., Carr, M. E., Strub, P. T. (2001). Chlorophyll variability in Eastern boundary currents. Geophysical Research Letters, 28 (18), 3421-3424.

Thomas, A.C., Townsend, D.W., Weatherbee, R. (2003). Satellite measured phytoplankton variability in the Gulf of Maine. Cont. Shelf. Res. 23, 971–989.

Thomas, A. C., Weatherbee, R. A. (2006). Satellite-measured temporal variability of the Columbia River plume. Remote Sensing of Environment, 100(2), 167-178.

Toole, D. A., Siegel, D. A. (2001). Modes and mechanisms of ocean color variability in the Santa Barbara Channel. Journal of Geophysical Research: Oceans (1978–2012), 106 (C11),

26985-27000.

Townsend, D.W., Cammen, L.M., Holligan, P.M., Campbell, D.E., Pettigrew, N.R. (1994). Causes and consequences of variability in the timing of spring phytoplankton blooms. Deep Sea Res. I. 41 (5-6), 747–765.

UNESCO (1994). Protocols for the Joint Global Ocean Flux Study (JGOFS) Core Measurements. IOC Manuals and Guides. Paris, UNESCO.

Valente, A. S., da Silva, J. C. (2009). On the observability of the fortnightly cycle of the Tagus estuary turbid plume using MODIS ocean colour images. Journal of Marine Systems, 75(1), 131-137.

Vanney, J. (1970). Lhidrologie du Bas Guadalquivir. Publicaciones del Departamento de Geografía Aplicada, CSIC, Madrid.

Vargas, J., Garcıa-Lafuente, J., Delgado, J., Criado, F. (2003). Seasonal and wind-induced variability of sea surface temperature patterns in the Gulf of Cadiz. Journal of Marine Systems, 38 (3), 205-219.

Volpe, V., Silvestri , S., Marani, M. (2011). Remote sensing retrieval of suspended sediment concentration in shallow waters. Remote Sensing of Environment, 115, 44-54.

Walker, N. D. (1996). Satellite assessment of Mississippi River plume variability: causes and predictability. Remote Sensing of Environment, 58(1), 21-35.

Wang, J., Lu, X., Zhou, Y. (2007). Retrieval of suspended sediment concentrations in the turbid water of the Upper Yangtze River using Landsat ETM+. Chinese Science Bulletin, 52 (II), 273-280.

Wang, H.Q., Hladik, C.M., Huang, W.R., Milla, K., Edmiston, L., Harwell, M.A., Schalles, J.F. (2010). Detecting the spatial and temporal variability of chlorophyll-a concentration and total suspended solids in Apalachicola Bay, Florida using MODIS imagery. International Journal of Remote Sensing, 31 (2), 1366-5901.

Warrick, J. A., Mertes, L. A. K., Washburn, L., &Siegel, D. A. (2004). A conceptual model for river water and sediment dispersal in the Santa Barbara Channel, California. Continental Shelf Research, 24 (17), 2029-2043.

Werdell, P. J., Bailey, S. W., Franz, B. A., Harding Jr, L. W., Feldman, G. C., McClain, C. R. (2009). Regional and seasonal variability of chlorophyll-a in Chesapeake Bay as observed by SeaWiFS and MODIS-Aqua. Remote Sensing of Environment, 113 (6), 1319-1330.

Wilson, C. (2003). Late Summer chlorophyll blooms in the oligotrophic North Pacific Subtropical Gyre. Geophys. Res. Lett 30, 1942, doi:10.1029/ 2003GL017770.

Wofsy, S. (1983). A simple model to predict extinction coefficients and phytoplankton biomass in eutrophic waters. Limnology and Oceanography, 28 (6), 1144-1155.

Wolanski, E., McLusky, D. (2011). Treatise on Estuarine and Coastal Science. Elsevier Inc, Amsterdam. ISBN: 978-0-08-087885-0.

Xu, Y., Chant, R., Gong, D., Castelao, R., Glenn, S., Schofield, O. (2011). Seasonal variability of chlorophyll a in the Mid-Atlantic Bight. Continental Shelf Research, 31 (16), 1640-1650.

Yamada, K., Ishizaka, J. (2006). Estimation of inter decadal change of spring bloom timing, in the case of the Japan Sea. Geophys. Res. Lett. 33, L02608, doi:10.1029/2005GL024792.

Zhang, C., Hu, C., Shang, S., Müller-Karger, F. E., Li, Y., Dai, M., et al. (2006). Bridging between SeaWiFS and MODIS for continuity of chlorophyll-< i> a</i> concentration assessments off SouthEastern China. Remote Sensing of Environment, 102 (3), 250-263.

Zhang, Y., Pulliainen, J., Koponen, S., & Hallikainen, M. (2002). Application of an empirical neural network to surface water quality estimation in the Gulf of Finland using combined optical data and microwave data. Remote Sensing of Environment, 81, 327-336.